UNIVERSITY OF SOUTHAMPTON

FACULTY OF PHYSICAL SCIENCE AND ENGINEERING

Optoelectronics Research Centre

Volume 1 of 1

EXPLORING OPTICAL NONLINEARITY IN GAS-FILLED HOLLOW CORE FIBRE

by

Seyed Mohammad Abokhamis Mousavi

Thesis for the degree of Doctor of Philosophy

May 2018

UNIVERSITY OF SOUTHAMPTON

ABSTRACT

FACULTY OF PHYSICAL SCIENCE AND ENGINEERING

Optoelectronics Research Centre

Thesis for the degree of Doctor of Philosophy

EXPLORING OPTICAL NONLINEARITY IN GAS-FILLED HOLLOW CORE FIBRE

Seyed Mohammad Abokhamis Mousavi

The growing need for novel light sources in variety applications increases the demand for laser sources operating in many different range of spectrum. Despite the success in development of mid-infrared (mid-IR) lasers, which are essential in many applications such as: environmental science, bio-science and physics, there are still lack of reliable lasers in this range with existing fibre laser technology compatibility. Meanwhile the nonlinearity in gases has been explored extensively from the very beginning of nonlinear optics, however, new developments in pulsed lasers and fibre design provide opportunities for more applications. The introduction of Hollow Core Photonic Crystal Fibres (HC-PCF) has revolutionised the area of nonlinearity in gaseous media by offering a single-mode confined light beam for very long distances. In this thesis, the focus was on mid-IR pulse generation by Raman frequency conversion in a gas-filled HC-PCF. Due to reliable performance and compatibility of fibre lasers with HC-PCFs, and towards fully fiberized source, an erbium-doped fibre laser (1.55 μm) has been selected as the pump for this project. In order to reach as far as possible into the mid-IR region, hydrogen has been selected as the filling gas of fibre, due to its large frequency shift and high Raman gain. The large frequency shift and mid-IR operating range required a new fibre design with a broadband transmission window and relatively low loss in mid-IR. After studying conventional HC-PCF structures, the recently proposed Nested Anti-resonant Nodeless Fibre (NANF) has been selected as the most suitable option for the purpose of this thesis [71]. Two NANFs, made of silica and tellurite, have been designed and optimized through the use of the developed Finite Element Method (FEM) toolbox in this thesis for operating wavelengths at pump (1.55 μm) and 1st Stokes (4.35 μm). A novel design has also been introduced in NANFs which shows polarization maintaining feature as good as the latest state-of-the-art HC-PBGF

type [77]. The proposed design also shows polarizing capability in addition to its polarization maintaining by presenting a large loss ratio (~30 dB) between different polarizations of propagating light through it. The pulse propagation throughout the hydrogen-filled NANFs has been investigated by modelling the Raman response of hydrogen and numerically solving the Generalized Nonlinear Schrödinger Equation (GNLSE). Simulations show promising results for frequency conversion towards mid-IR and the possibility of Raman lasers in this region by considering different gas and using the readily available air in HC fibres. Furthermore, in this work, the nonlinear dynamics of atmospheric air-filled HC fibres have been studied, ranging from Raman down conversion process to a high spectral power density supercontinuum spanning from 850 to 1600 nm. A semi-quantum model for air has been adopted and integrated into the GNLSE, which surpasses the limitations of simple model. Using the adopted model, the experimental results have been reproduced without any extra computational cost. A rigorous study has been performed on nonlinear dynamics of pulse propagation in air-filled HC fibres and the origin of many nonlinear phenomenon are identified.

Table of Contents

List of Tables

List of Figures

List of Accompanying Materials

DECLARATION OF AUTHORSHIP

I, Seyed Mohammad Abokhamis Mousavi declare that this thesis and the work presented in it are my own and has been generated by me as the result of my own original research.

EXPLORING OPTICAL NONLINEARITY IN GAS-FILLED HOLLOW CORE FIBRE

I confirm that:

1. This work was done wholly or mainly while in candidature for a research degree at this University;
2. Where any part of this thesis has previously been submitted for a degree or any other qualification at this University or any other institution, this has been clearly stated;
3. Where I have consulted the published work of others, this is always clearly attributed;
4. Where I have quoted from the work of others, the source is always given. With the exception of such quotations, this thesis is entirely my own work;
5. I have acknowledged all main sources of help;
6. Where the thesis is based on work done by myself jointly with others, I have made clear exactly what was done by others and what I have contributed myself;
7. [Delete as appropriate] None of this work has been published before submission [or] Parts of this work have been published as: [please list references below]:

Signed: .....

Date: .....

Acknowledgements

Working on this thesis has been a life changing experience for me, for which I am indebted to many people for their support. First and foremost, I would like to express my deepest appreciation and thanks to my supervisors Professor David Richardson and Professor Francesco Poletti for their patience, encouragement and continues advice. It has been a great honour to be their PhD student. My profound gratitude goes to Professor Francesco Poletti who has been a truly dedicated mentor and without his guidance and persistent help, this work would not have been possible.

I would also like to thank university of Southampton for providing funding for my PhD that allowed me to undertake this research. I would also like to acknowledge Dr Peter Horak, Professor Gilberto Brambilla, Professor Anna Peacock, Dr Eric Numkam Fokouaand and Dr Natalie Wheeler.

Special mention goes to my dearest fellows and friends, Dr Seyed Reza Sandoghchi and Dr Shahab Bakhtiari Gorajoobi for their unwavering support and understanding throughout.

Finally, but by no means least, I would like to thank my family and friends and the most specially my brother and my mother who supported me in every possible way with love and encouragement to see the completion of this work.

Definitions and Abbreviations

ABS-FDM	Fourier decomposition with adjustable boundary conditions
ARB	Anti-resonance band
ARF	Anti-resonant fibre
ARROW	Anti-resonant reflecting optical waveguide
BPM	Beam propagation method
CL	Confinement loss
CW	Continues wave
ECR	Error Check Routine
FDM	Finite difference method
FEM	Finite element method
FFT	Fast Fourier transform
FM	Fundamental mode
FROG	Frequency-resolved optical gating
FWHM	Full width at half maximum
FWM	Four wave mixing
GNLSE	Generalized nonlinear Schrödinger equation
GP	Gaussian pulse
GUI	Graphical user-interface
GVD	Group velocity dispersion
HC-ARF	Hollow core anti-resonant fibre
HCF	Hollow core fibre
HC-KF	HC Kagomé fibre
HC-PBGF	Hollow core photonic bandgap fibres
HC-PCF	Hollow Core Photonic crystal Fibre
HC-TF	Hollow core tubular
HHG	High-harmonic generation
HOM	Higher order mode
ICL	Interband cascade laser
IR	Infrared
IVP	Initial value problem
MI	Modulation instability
MM	Multipole method
MOF	Microstructured optical fibres
NANF	Nested anti-resonant nodeless fibre

NGS	Net gain of Stokes
NLSE	Nonlinear Schrödinger equation
ODE	Ordinary differential equation
OFM	Orthogonal function method
OPO	Optical parametric oscillators
ORC	Optoelectronic Research Centre (in University of Southampton)
PDL	Polarization differential loss
PLR	Polarization loss ratio
PMB	Polarization mode birefringence
PMC	Phase matching condition
PML	Perfectly matched layer
PWE	Plane wave expansion
QCL	Quantum cascaded lasers
QED	Quantum Electrodynamics
RCL	Raman conversion loss
RRS	Rotational Raman scattering
RS	Raman scattering
SBS	Stimulated Brillouin Scattering
SDO	Single damped oscillator
SEM	Scanning electron micrograph
SGP	Super-Gaussian pulse
SMF	Single mode fibre
SMT	Source-model technique
SNM	Suppressing nonlinearity method
SPM	Self-phase modulation
SQM	Semi-quantum model
SRS	Stimulated Raman scattering
SSFM	Split-step Fourier method
TB	Transmission band
TMM	Transfer matrix method
UPPE	Unidirectional Pulse Propagation Equation
VRS	Vibrational Raman scattering
XPM	Cross phase modulation
ZDW	Zero dispersion wavelength

Chapter 1: Introduction

1.1 Introduction

Nonlinear optics, dating back to the discovery of second-harmonic generation by Franken et al. (1961) shortly after the first working laser demonstrated by Maiman in 1960, has generated many applications that have changed the optical world in many ways [1]. Nonlinear optical phenomena occur as a consequence of modifications in the optical property of a material under the influence of light. The term "nonlinear" has been used to illustrate the fact that the material system responds nonlinearly to the strength of the optical field applied upon itself. During the last decades, nonlinear optics in solid, liquid and gas materials has been studied and lots of applications and devices have been developed based on it [2]. Although solid-state materials have shown great capability of tuning their nonlinear response through change of material composition, and a wide range of devices has been fabricated in the form of solid core fibres and integrated systems, all these nonlinear systems suffer from critical issues at high field intensities, as well as some fabrication limitations [3].

Gases, as an alternative material, can also support a variety of nonlinear processes and behave as nonlinear optical media. They are more reliable than solid-state materials at high intensity fields, where solid–state materials can be damaged permanently [4]. In addition, nonlinearity and dispersion of gases are tuneable by controlling the gas composition and pressure [5]. They also show a broader transparency spectrum than solid-state equivalents. During the last decades, a variety of nonlinear effects has been demonstrated in gaseous media such as, to name but a few: supercontinuum generation [6], high-harmonic generation (HHG) [7], filamentation [8], Raman frequency comb generation [9, 10]. However, gases inside conventional bulk glass cells have inherently lower densities than solids, even at high-pressures, which significantly influences their nonlinearity and imposes the necessity of very high laser power or very long light-matter interaction length for an efficient nonlinear response.

A long interaction length could be achieved through multiple passes in a resonant gas cell, but these are quite cumbersome to align and maintain. Hollow core photonic crystal fibres (HC-PCF) provide a practical alternative and some very useful properties for the generation of efficient nonlinear process in gases. For example, they provide confined single mode beam over very long interaction paths (1 to 1000 m), very high intensity per Watt (their small core radius increases the intensity), higher optical

damage threshold and superb control on the Group Velocity Dispersion (GVD) [11-14]. These characteristics of HC-PCFs have been employed in a variety of experiments [15, 16]. Furthermore, many other nonlinear processes have been demonstrated in these fibres such as: self-similarity and solitary waves in stimulated Raman scattering [17, 18], delivery of high-energy and intense optical solitons [19], ultrashort pulse supercontinuum generation [5], deep-ultra-violet (UV) generation [20], to name just a few. However, most of those activities in gas-filled HC-PCFs have been focused on UV to the near-infrared spectral range [5].

The mid-infrared (mid-IR) spectral region, comprising wavelengths between approximately 2 and 20 μm, is an interesting region for many areas in science and technology. Molecules shows strong vibrational transitions in this range [21], which makes mid-IR spectroscopy a unique way of identifying the type and quantifying the concentration of molecules in a given environment. Mid-IR spectroscopy can provide a powerful tool to understand the structure of molecules in materials and also gives the ability to perform non-destructive detection of composite chemical, physical or biological systems in solid, liquid or gas phase. Two important sections of this region, from 3-5 μm and 8–13 μm, are very important due to the transparency of the atmosphere, which allows the detection of small traces of toxic vapours with great sensitivity [22]. Also, as Rayleigh scattering loss is low in this region, the possibility of imaging in unclear media increases as well [23]. This wide range of applications emphasizes the necessity for reliable and high power laser sources in this region.

In the past decades, there has been an impressive growth in the number of compact and high power laser sources [24]. However, some of the regions in the spectrum, in particular at mid-IR frequencies, have not seen any dramatic progress due to fabrication, detection and material limitations. Recently, there has been some promising new development in the mid-IR light sources by new techniques and materials such as: quantum cascaded lasers (QCL) [25], optical parametric oscillators (OPO) [26], high-power fibre lasers with different host glasses (e.g. fluorides) and dopants [27] and gas-filled hollow-core lasers (population inversion lasers) [28-30]. However, each of these options has limitations that decrease its performance. For instance, QCLs are limited by their strong dependency of maximum power on the operating temperature [25]. Besides, state-of-art high power fibre lasers cannot go beyond certain wavelength (~3.9 μm) [27] and other types of lasers such as interband cascade lasers (ICLs) are mainly limited to 2-3 W for the range of mid-IR.

Unlike conventional population inversion lasers, frequency conversion lasers using nonlinear process such as stimulated Raman scattering (SRS) are not limited to transition levels, and as a result, they can present great tunability of their output wavelengths through a relative frequency shift of the input laser (i.e. pump laser). Gas-filled HC fibre lasers exploiting SRS for frequency conversion seem therefore a promising option to produce novel laser sources for the mid-IR region. They offer, in principle, the possibility of a fully fiberized system with a sharp emission linewidth and with the advantages of gases over solid-state materials already discussed. During the last decade, promising results have been achieved on Raman conversion processes in gas-filled HC fibres [31-34], and a very low threshold laser using a hydrogen-filled HC fibre has been demonstrated [35]. However, despite many successful experimental works in other regions of the spectrum (UV, visible, near infrared), there have been very few works towards the investigation of gas-filled fibre based mid-IR sources, mostly due to very large loss in the fibres at those wavelengths.

In this thesis, I have focused on studying the potential of devices that exploit Raman nonlinearity in gas-filled HC-PCFs to create efficient mid-IR laser sources. In particular, different ways of using Raman down-conversion processes in the gas have been studied to generate mid-IR laser sources from a well stablished near-IR fibre laser source. This configuration has great potential for integration with well-stablished ytterbium or erbium-doped fibre lasers, whereby, by adding a simple gas-filled hollow core fibre a fully fiberized mid-IR laser can be achieved [35].

1.2 Outline of the thesis

The main objective of this thesis is to generate a high power laser source in a gas-filled HC fibre at mid-IR wavelengths (4-6 μm) by means of Raman down-conversion. Therefore, this work can be divided into two main parts, HC fibres and Raman scattering in the gases. The thesis is structured as follows:

- In chapter 2, a brief background on different topics related to each part of this work (i.e. HC fibres and nonlinearity in gases) is covered. Starting from HC PCFs and their main guiding mechanisms, two main categories of these fibres will be reviewed. The advantages and disadvantages of each category for gas-filled applications will be briefly touched upon. Then, a brief introduction about optical nonlinearity in general, and more specifically on Raman scattering is presented, and a suitable light propagation model to include a wide range of nonlinear phenomena for this work is selected. The chapter ends by introducing

the advantage of gas-filled HC fibres over bulk implementation of the process and with an overview of recent works in this field.

- Chapter 3 is dedicated to the introduction of the numerical methods used and of the toolboxes developed in this work. At first, in order to model HC fibres, different numerical models are compared, and Finite Element Method (FEM) is chosen as the most suitable one to model and optimize the HC fibre. To achieve accurate results in fibre modelling, optimum parameters for modelling are calculated; a suitable Perfectly Matched Layer (PML) is implemented and a modelling toolbox is developed. Similarly, to study the pulse propagation in the gas medium, a symmetric split-step method was selected and programmatically implemented to solve the nonlinear pulse propagation model throughout the gas-filled HC fibre. In the end, to include all modelling methods and provide an integrated solution for design, modelling and simulation of the Raman laser in gas-filled fibre, an integrated software toolbox has been developed.

- In Chapter 4, HC fibres guiding through anti-resonance/inhabited coupling (called in the chapter HC-ARF) are reviewed as the most promising HC type for nonlinear applications in gases. While the loss of these fibres is identified as the most concerning problem, it is shown that the overlap of the air-guided field with the cladding glass is one of the main reasons of the high loss in these fibres. These findings shift the focus of this work towards different type of fibres called *tubular fibres*, which present a lower amount of field-glass overlap. These fibres have shown a very broad low loss transmission window. Meanwhile, a more sophisticated variation of these fibres called *nested antiresonant nodeless fibres* (NANFs) has been proposed in ORC. NANFs show very low loss while having similar broadband characteristics as tubular fibres. Therefore, by selecting the NANF as premier choice for this project, an optimization process has been performed on the main design parameters for a silica-based NANF and for a non-silica one with IR-transparent glass (tellurite) to achieve low loss operation at both the pump wavelength and at the first Raman Stokes (for example, 1.55 μm and 4.35 μm, respectively). The optimum NANF with silica has a loss of about < 1.2 dB/m at 4.35 μm with core radius of 35 μm despite the considerable material loss of silica at this wavelength (~3000 dB/m). Although the fibre has a large core size, it is designed to be effectively single mode regardless of its core size by out-coupling higher order modes. The optimised tellurite fibre could

achieve the similar loss with much smaller core radius of 15 μm at the Raman frequency.

- Considering the importance of polarization on the efficiency of vibrational Raman scattering, in Chapter 5, novel designs for birefringent NANFs have been studied, which are able to preserve linear polarization. I have proposed a novel way to achieve a fibre with high birefringence and at the same time polarizability. After exploring the possibly of introducing birefringence in NANF by introducing an elliptical core shape, it is shown that conventional methods to introduce birefringence in solid core fibres are not applicable on HC-ARFs. Using the effect of mode-crossing on the effective refractive index, combined with multi-layered loss control, a low loss and birefringence NANF structure have been achieved for the first time. The proposed design has the ability to introduce birefringence larger than 10^{-4} over a record bandwidth (~550nm) and loss extinction between orthogonal polarizations as large as 30 dB. A fibre with such a large polarization loss ratio can practically act as a polarizer, specifically for operation with high power lasers, where conventional polarizers reach their damage threshold limit. Besides, following the scaling law in NANF, the proposed design can be used for different wavelength ranges by simply scaling the structure in relation to the operating wavelength. The novelty in this design results a patent registration (patent number UK 1410100) and has already inspired other works.

- Chapter 6 is started by comparing different options for filling gas in the HC-fibre to fit the purpose of generating mid-IR laser. Then, the choice of H_2 is motivated as the most appropriate gas for this work. To achieve the highest possible Raman frequency conversion, the optimum core size for the NANF designed in Chapter 3 is calculated as a parameter in the optimization towards maximum Raman conversion. To properly model the pulse propagation in this designed fibre while retaining the ability of including different nonlinear phenomena in a unified simulation tool, a semi-classical model for Raman scattering in H_2 is considered. This can be fully integrated within a well-known generalized nonlinear Schrödinger equation (GNLSE). To test the reliability of the model, the effect of different parameters on the final Raman gain, from pulse length to waveguide dispersion contributions are reviewed. The model is shown able to reproduce accurately experimental results from literature. In the end, the efficiency of Raman conversion from pump to first Stokes has been studied

by using a GNLSE model in full frequency domain for different pulse lengths and shapes in the designed and optimised NANF. It is shown that the generation of 4.35 μm mid-IR laser with more than 68% of quantum efficiency from an erbium-doped laser at 1.55 μm with moderate power (10kW) is possible in silica NANF, despite its high material loss in the mid-IR. It is also shown that even higher efficiencies are possible by altering the pulse shape or changing the fibre material.

- In Chapter 7, the nonlinear dynamic of a different but more naturally occurring filling gas inside a HC fibre is considered. Atmospheric air existing in the core of the HC fibres shows interesting characteristics and has been studied in the last decades due to the increasing interest in HC fibres and high power lasers. In this chapter, the propagation of a picosecond pulse in different types of HC fibres (i.e. HC PBG, Kagomé and tubular fibres) have been studied, experimentally and theoretically. The choice of an appropriate pulse length (~6 ps at 1036 nm) has enabled the observation of a variety of nonlinear phenomena, from rotational and vibrational Raman scattering to a broad supercontinuum ranging from ~900 nm to ~1600 nm. To model the nonlinear phenomena, a semi-quantum model for air has been adopted, which can be fully integrated in the GNLSE and could reproduce well the experimental results in different fibres. By using the newly developed model and by integrating it in the developed nonlinear modelling toolbox in this work, the origin of initial broadening peaks are identified and the output spectrum for different input power levels are reproduced successfully, ranging from the initiation of vibrational Raman signature up to the generation of a double-pump feature supercontinuum, with good agreement. Generally, in previous works only one or two of such nonlinear phenomena have been observed. This is because they mostly operated with either very long or very short pulse lengths, while in this work the output can be tuned from single pulse Raman frequency conversion (from 1036 nm to 1354 nm) to a broad supercontinuum just by adjusting the input power and provide a high spectral density output.

- Chapter 8 summarises the results of this work and proposes a few suggestions for future works.

Chapter 2: Background

In this chapter, the key background information required to understand the primary content of this thesis is provided. By necessity, it is not possible to go into great depth on each topic given space constraint and in each section references are provided as a source of full details. In the following sections, the hollow core optical fibres, the general formulation of nonlinearity and more specifically Raman nonlinearity are briefly introduced as the key elements of this thesis. In the end, the advantage of gas-filled hollow core fibres (HC) with an overview of recent activities in this field is provided.

2.1 Introduction to Hollow core optical fibres

2.1.1 Historical perspective

Optical fibres have proven to be one of the best ways to transmit and guide light which provide great control and flexibility on the transmission path. From the first successful and reliable single mode fibre with 16 dB/km loss by Keck and Maurer at Corning [36] to the present matured form with a loss of ~0.18 dB/km at 1550 nm for SMF-28® [37] and the record loss of 0.149 dB/km at 1550 nm [38], solid-core optical fibres have been the backbone of telecommunication networks for many years. However, some of their limitations caused by the interaction of light and the solid material in the fibre core have not been yet addressed effectively in many sensitive or high intensity applications [39-41]. Guiding light through air/vacuum can overcome many limitations of solid material due to the ultra-low Rayleigh scattering loss and ultra-low optical nonlinearity of air/vacuum. This can consequently provide higher transmission speed (i.e. lower latency) and higher power delivery. However, simple replacement of the solid core with air in conventional forms of solid-core fibres cannot provide any light confinement because of the lower refractive index of air in comparison to the surrounding material, which breaks the guidance mechanism of total internal reflection [42]. Fortunately, a large body of studies and developments in the area of “Photonic crystals” pioneered by Yablonovitch [43] and John [44] opened up new opportunities to overcome this problem. From the first adaptation of the photonic crystal to the concept of out-of-plane propagation of light in a defect within a lattice (i.e. photonic bandgap guidance) by Birks and co-workers in 1995 [45] to the first working example of such structures in a solid-core fibre, photonic bandgap fibres (PBGFs) have shown promising results [46]. The ability to confine the light regardless of the core and cladding indices had brought the

possibility to guide the light in air with the help of the PBG mechanism and the first instance of HC-PBGFs was demonstrated by Cregan *et al* [14] as shown in **Figure 2.1**.

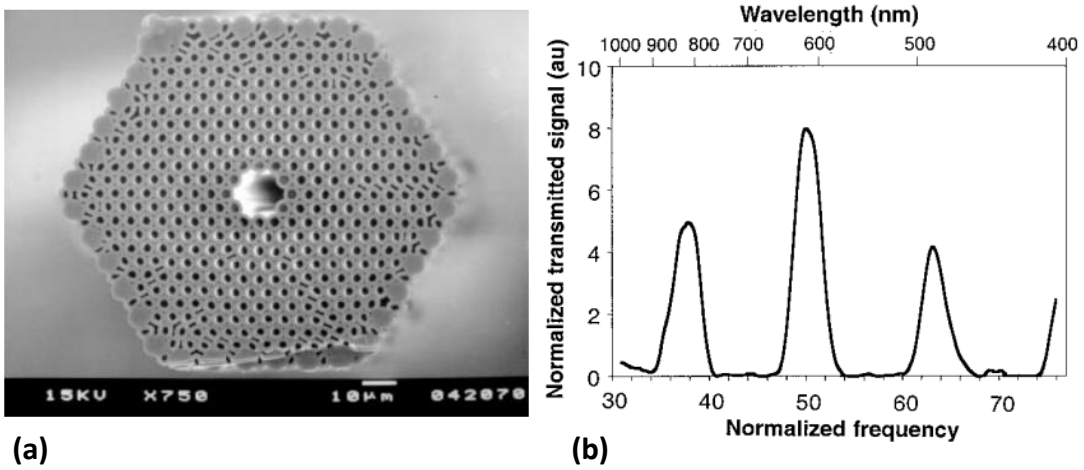

Figure 2.1. (a) the first demonstration of single mode air-guiding fibre, **(b)** the spectral transmission profile of the fibre (after [14]).

Since then, different hollow core optical fibres have been introduced and developed over the past decades. Not only have these fibres been used to address common problems in solid-core fibres and provide a larger damage threshold, robustness to mechanical and magnetic field perturbation as well as extending the operating wavelengths, but they have also opened up opportunities for new applications such as long path gas-light interactions, biophotonic applications, etc. [15, 47-49]. Although, at first, HC fibres are introduced by PBG mechanism, during the last decade many different other structures and forms of HC fibre have emerged offering some advantages over HC-PBGFs. Some of these alternative fibres types are discussed in the following sections.

2.1.2 Categories of hollow core fibres.

Despite the advantages of hollow-core fibres, they suffer from lack of total internal reflection guiding mechanism, which limits the guidance to the engineered low loss "leaky modes" instead of actual band "guided modes" as in solid-core fibres [42], which increases the structural complexity of the fibre and introduces different category of fibres. In general, there are two major HC photonic crystal fibre (HC-PCF) categories in terms of transverse modal control and guidance mechanism. HC photonic bandgap fibres (HC-PBGF), rely on the band gap property of the surrounding photonic structure (as discussed in the previous section) [50, 51] and anti-resonant fibres (HC-ARFs) that guide based on the reflection properties of cladding structure in the anti-resonance regime/inhabited coupling [52-55]. Although, the optimum design of HC-PBGFs can be

predicted by borrowing concepts and design tools from the mature field of solid-state physics [15, 43, 56], not all features of HC-ARF's guidance can be fully understood by the common picture of simple anti-resonant reflecting waveguides (ARROWs) and the search for optimum designs is ongoing. In practice, HC-PBGF shows a lower loss than HC-ARFs [51]. However, their narrow bandwidth (i.e. 10-30% of the central operating wavelength) and larger field overlap with the glass in comparison to HC-ARFs [48] make them less suitable for broadband applications (e.g. broadband nonlinear processes) and high power delivery. Furthermore, recent designs of HC-ARF [57] not only have a theoretical loss better than HC-PBGFs but also show the potential to achieve a loss as low as solid-core fibres across a wide range of wavelengths and they are less influenced by the intrinsic material loss unlike their solid-counterpart.

2.1.2.1 Photonic bandgap fibres

The guiding mechanism in the first group (HC-PBGFs) (also called PBG-guiding HC-PCFs) is based on confining the light in a low index core due to two-dimensional properties of a photonic bandgap. This type of HC fibre, which is a subclass of microstructured optical fibres (MOFs), can provide extremely low confinement loss (CL) in a narrow spectral region (the best reported case has a loss as low as 1.2 dB/km at 1620 nm [51]). The most common and efficient structure for these type of fibres is a hexagonal lattice of air holes. **Figure 2.2 (a)** shows the scanning electron micrograph (SEM) of an HC-PBGF which has been designed to operate at 800 nm. In general, the group velocity dispersion (GVD) of this fibre type has a steep slope at the two ends of the bandgap while passing through zero dispersion inside the transmission window, as shown in **Figure 2.2 (b)**. As has been mentioned, they have very low loss but only over a small transmission window (e.g. ~100 nm) for broadband nonlinear processes such as: supercontinuum generation and multi-octave frequency comb generation or large shift frequency conversion. Hence, in this thesis, the focus is on different types of HC fibres with more potential for nonlinear applications.

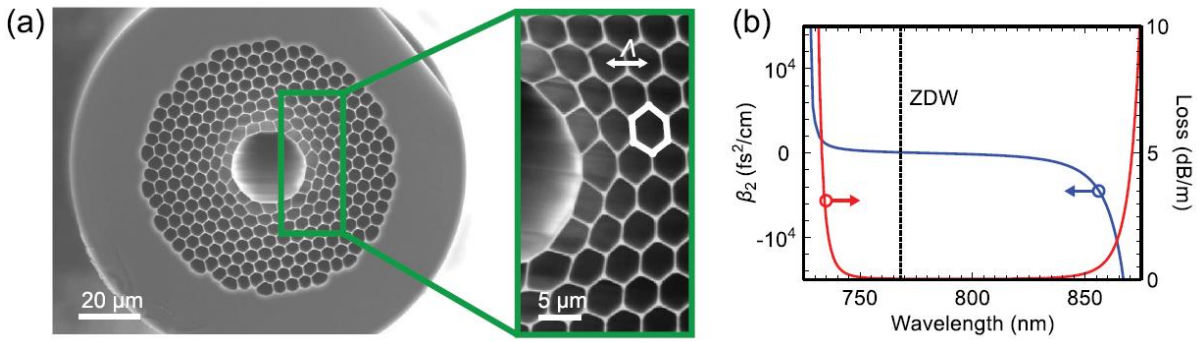

Figure 2.2. **(a)** SEM of HC-PBGF cross-section with an operating wavelength around 800 nm, 2·1 µm pitch (Λ) and 11 µm core diameter, **(b)** calculated GVD and loss for an idealized model of this fibre [after [5]].

2.1.2.2 Anti-resonant fibres

The second group of HC- PCFs, can in some way, be seen as a large pitch (i.e. $k\Lambda > 50$) type of HC-PBGF, and low loss air-core guiding from the absence of photonic states in the surrounding photonic crystal structure might be expected. However, this strong relation falls apart for the large pitches, and a wide range of low loss transmission windows, which are wider than a simple capillary, has been observed experimentally [34]. This specific property is very interesting for efficient broadband nonlinear effects that cannot propagate in HC-PBGFs. The most famous structure for this type is a Kagomé-lattice cladding, which was investigated for the first time in 2002 [34], and has a unit cell of glass webs with a star-of-David pattern. **Figure 2.3 (a)** shows the SEM of a Kagomé fibre designed to work around 800 nm and the UV region. As it is clear in **Figure 2.3 (b)**, this fibre has a broadband low loss transmission window, except for the anti-crossing (resonance) region, which occurs around 380 nm (resonance region repeats periodically across the spectrum). In terms of GVD, this fibre shows relatively small anomalous dispersion (in contrast to PBG-guiding HC-PCF) except in the anti-crossing sections. Although this anti-crossing in loss profile and GVD property of the fibre is disrupting, it can be tuned away by changing the thickness of the glass webs.

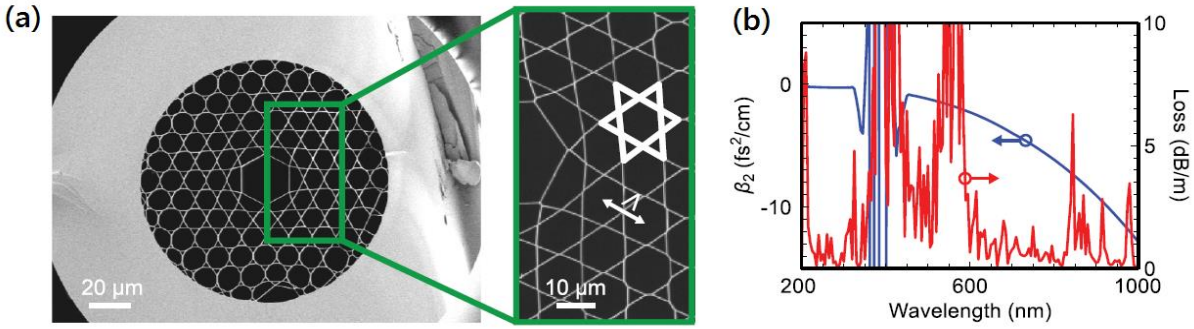

Figure 2.3. (a) SEM of Kagomé HC-PCF cross-section with an operating wavelength around 800 nm and in the UV, 15 µm pitch (Λ), 30 µm core diameter and 0.23 µm web thickness, **(b)** calculated GVD and loss for ideal model of this fibre [after [5]].

The guiding mechanism in Kagomé fibre was not well understood when it was reported for the first time [34]. One of the first attempts to explain the guiding property of these type of fibre was given by Benabid *et al* [34]. In this explanation, the guiding mechanism was related to the strong confinement of a low density of photonic states, which causes guidance only in the core of the fibre. In other words, the overlap integral between core modes and cladding modes are very low at guiding frequencies [58, 59]. In another attempt to explain the guiding process, the guidance was related to the washing-out of the overlap between the air-core modes and cladding modes due to the strong mismatch of fast and slow transverse-field modes in the cladding (glass webs) and air-core, respectively [60]. Although those explanations added a broad understanding of the guiding mechanism and provide an overview, they are too complicated for the design process of a fibre with desired characterizes.

On the other hand, it is possible to consider the guiding modes to be due to 'anti-resonant reflection optical waveguiding (ARROW). In this approach, which has been studied before [52] in the planar waveguide context, the glass webs can act as Fabry–Pérot structure and the transverse-field is reflected back at the core in the anti-resonance frequencies. In more detail, the constructive back reflection from layers of dielectrics in a specific range of frequencies can act like a mirror with a reflectivity related to the refractive index and thickness of those layers. This mirror effect is the working principle of many setups and structures such as Bragg mirrors or Fabry–Pérot structures. Similar mechanism has been used in simple micro cavities, however, in the case of fibres, the transverse-field with related wavevector plays the main rule. The simplest ARROW in the form of cylindrical geometry is a suspended dielectric tube, which can give a very good approximation of resonance and anti-resonance frequencies in most of the anti-resonant HC-PCF structures. The resonance and anti-resonance frequencies of the fundamental mode of a dielectric tube with tube thickness of t can

be calculated from the resonance /anti-resonance wavelength equation as [61] (for the fundamental mode):

$$\lambda_m \approx \frac{2\pi\sqrt{n_{clad}^2 - n_{core}^2}}{\sqrt{\left(\frac{C_m\pi}{2t}\right)^2 - \frac{U_0^2}{R^2}}} \tag{2.1}$$

where n_{clad} and n_{core} are the refractive index of tube dielectric and refractive index of core as well as surrounding material respectively, λ_m is the m^{th} resonance or anti-resonance wavelength of the tube with thickness of t. N_m is $2m+1$ or $2m$ based on anti-resonance or resonance condition if m is an integer value, respectively. U_0 is the value at which the first zero of Bessel function of the first kind ($J_0(U_0)=0$) occurs and R denotes the core radius.

Equation (2.1) can provide an accurate approximation for resonance frequencies even for multi-layered tubes, especially if they are designed to be at the optimum distance or in the optimum thickness, however in the complex air-glass structures similar to Kagomé fibres [15], due to the existence of the glass webs in different directions, there are small discrepancies between the calculated and measured resonance frequencies. In addition, the CL of HC-ARFs, which is represented as $\alpha(R,R_c,\lambda)$, strongly depends on the core radius (R), guiding wavelength (λ) and bend radius (R_c). This dependency of loss, in the case of a single tube fibre as the simplest form of ARROW fibre, is given by [62]:

$$\alpha(R,R_c,\lambda) \propto c_1\left(\frac{\lambda^3}{R^4}\right) + c_2\left(\frac{R^2}{\lambda R_c^2}\right) \tag{2.2}$$

where C_1 and C_2 are mode related constants. In general, a Kagomé structure has a lower loss than a single tube because the CL in the structure would be decreased by increasing the number of layers in the cladding, however, they have higher loss than ideal multi-layer tubes.

During the last decade, lots of work has been done to improve the loss in these fibres with early samples showing a limited loss of ~0.5 dB/m at 1.064 μm [60]. However, by introduction of the negative curvature core boundary in these fibres, the loss has significantly improved in a multi-layer Kagomé structure and reduced to 17 dB/km at 1064 nm [63], to 12.3 dB/km at 1010 nm [64] and finally and remarkably to 8.5 dB/km at 1030 nm [65]. In a separate work, I have also studied the loss mechanism in a much

simpler yet more reliable form of Kagomé structure called "hexagram" HC fibre. Studying this fibre helps to understand the effect of glass node on the loss mechanism of Kagomé structure [66]. More detail of study is provided in *appendix A*.

Figure 2.4 shows some of the recent ARFs. Since this type of HC fibre (i.e. HC-ARFs) has broadband low loss transmission windows and maintains a very small fraction of power in the cladding glass, they are the main focus of this work and are studied more extensively in the next chapters.

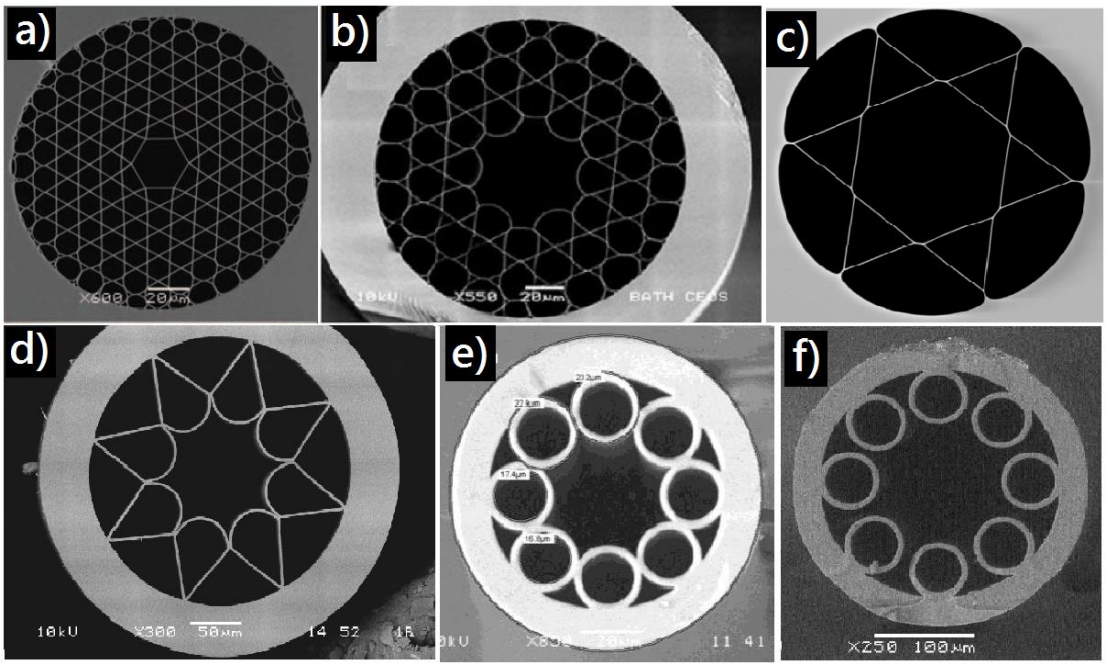

Figure 2.4. SEMs of some recent ARFs: a) Kagomé cladding with straight core surrounding [after [11]]; b) Kagomé cladding with hypocycloid core surrounding [after [67]]; c) simplified ARFs with a hexagram cladding [after [68]]; d) and e) are simplified HC fibres with negative curvature core surrounding [after d [69] , e [70]]; f) simplified nodeless tube-lattice ARF [after [71]]

2.2 Introduction to optical nonlinearity

When light passes through a material the behaviour of photons in space-time and in interaction with molecules of the material can be described by Maxwell's equations as electromagnetic waves in the limit of large quantity of photons. In this framework, which is called the "classical approach", the interaction between light and material is modelled through the modification of polarization density ($\vec{\boldsymbol{P}}$) of the material by electromagnetic waves. This approach has been studied very well in the past and

provides powerful tools to analyse the behaviour of light-matter interaction and doesn't carry the complexity of Quantum Electrodynamics (QED), which can provide very accurate but complex picture of interaction. In this work, the main focus is on classical approach while borrowing few aspects of QED where it is necessary.

To begin with, Maxwell's equations in the derivative form in SI units can be described as:

$$\begin{aligned} \vec{\nabla} \times \vec{\boldsymbol{H}} &= \frac{\partial \vec{\boldsymbol{D}}}{\partial t} + \vec{\boldsymbol{J}}, \\ \vec{\nabla} \times \vec{\boldsymbol{E}} &= -\frac{\partial \vec{\boldsymbol{B}}}{\partial t}, \\ \vec{\nabla} \cdot \vec{\boldsymbol{D}} &= \rho, \\ \vec{\nabla} \cdot \vec{\boldsymbol{B}} &= 0. \end{aligned} \tag{2.3}$$

where $\vec{\boldsymbol{E}}(\vec{\boldsymbol{r}},t)$ and $\vec{\boldsymbol{B}}(\vec{\boldsymbol{r}},t)$ denote the electric and magnetic field vectors, respectively, with $\vec{\boldsymbol{r}}$ as a spatial vector. $\vec{\boldsymbol{D}}(\vec{\boldsymbol{r}},t)$ and $\vec{\boldsymbol{H}}(\vec{\boldsymbol{r}},t)$ represent the electric displacement vector and magnetizing vector, $\rho(\vec{\boldsymbol{r}},t)$ and $\vec{\boldsymbol{J}}(\vec{\boldsymbol{r}},t)$ represent the free charge and the free current vector, respectably, which are assumed to be zero in the rest of this work due to nature of the material (e.g. dielectric and gas) and applications. The electronic displacement is described as $\vec{\boldsymbol{D}} = \varepsilon_0 \vec{\boldsymbol{E}} + \vec{\boldsymbol{P}}$ and, in a general form, $\vec{\boldsymbol{P}}$ can be an "arbitrary function" of electric field ($\vec{\boldsymbol{P}} = f(\vec{\boldsymbol{E}})$). However, in the range of common material and practical applications, a polynomial representation of such a function is a good approximation and provides relatively accurate results especially in the range of atomic potential in natural materials [72]. As a result, $\vec{\boldsymbol{P}}$ can be separated into $\vec{\boldsymbol{P}}_L$ and $\vec{\boldsymbol{P}}_{NL}$, where the former one represents the linear part of the relation between $\vec{\boldsymbol{E}}$ and $\vec{\boldsymbol{P}}$ which comes from the first term of the polynomial approximation ($\vec{\boldsymbol{P}}_L = \varepsilon_0 \chi^1 \vec{\boldsymbol{E}}$) with χ^1 as first order/linear susceptibility tensor of the material and the later one contains other nonlinear higher order susceptibilities. Accordingly, $\vec{\boldsymbol{D}}$ can be presented as $\vec{\boldsymbol{D}} = \varepsilon_0(1+\chi^1)\vec{\boldsymbol{E}} + \vec{\boldsymbol{P}}_{NL} = \varepsilon_0 \varepsilon_r \vec{\boldsymbol{E}} + \vec{\boldsymbol{P}}_{NL}$ where the linear part of $\vec{\boldsymbol{P}}$ and $\varepsilon_0 \vec{\boldsymbol{E}}$ are combined in the form of the permittivity of medium $\varepsilon_r(\omega, x, y, z)$. In the way that the dispersion and modal property of the electromagnetic wave manifest in the spatial and time dependency of ε_r, the complex value of ε_r expresses the linear loss of medium [72].

The general form of Maxwell's equations (Eq. (2.3)) can be summarized in a single wave equation by considering the relation between $\vec{\boldsymbol{H}}$ and $\vec{\boldsymbol{B}}$ as $\vec{\boldsymbol{H}} = 1/\mu \vec{\boldsymbol{B}}$ with $\mu = \mu_r \mu_0$

where μ_0 is permeability of vacuum (no magnetization field ($\vec{\boldsymbol{M}}$) in the material) and μ_1 is relative permeability of the material, which is $\mu_r \approx 1$ for nonmagnetic material (this assumption is used through this thesis). Assuming that $\vec{\nabla} \cdot \vec{\boldsymbol{E}} \approx 0$ which is widely correct in the transversal modal cases like optical fibres[1] [72]:

$$\nabla^2 \vec{\boldsymbol{E}} - \frac{1}{c^2} \frac{\partial^2 \varepsilon_r \vec{\boldsymbol{E}}}{\partial t^2} = \mu_0 \frac{\partial^2 \vec{\boldsymbol{P}}_{NL}}{\partial t^2}. \tag{2.4}$$

where $c = 1/\sqrt{\varepsilon_0 \mu_0}$. In general, the polynomial expansion of $\vec{\boldsymbol{P}}_{NL}$ has the following form:

$$\vec{\boldsymbol{P}}_{NL} = \varepsilon_0 \left[\chi^2 \otimes \vec{\boldsymbol{E}} \cdot \vec{\boldsymbol{E}} + \chi^3 \otimes \vec{\boldsymbol{E}} \cdot \vec{\boldsymbol{E}} \cdot \vec{\boldsymbol{E}} + \cdots \right]. \tag{2.5}$$

where $\otimes$ denotes the convolution operator in time domain and $\chi^n, n \geq 2$ are higher – order nonlinear susceptibility tensors. In most practical cases the effect of higher order susceptibilities are negligible and only χ^2 and χ^3 are considered. Moreover, the susceptibility has a direct relation with the profile of the molecule and in some conditions (e.g. lattice symmetry) the material may not exhibit χ^2 or χ^3. For instance, χ^3 is the dominant susceptibility in silica glass and common diatomic gasses (e.g. H_2). Therefore, in this work, the $\vec{\boldsymbol{P}}_{NL}$ can effectively be presented in the following form:

$$\vec{\boldsymbol{P}}_{NL}(\vec{\boldsymbol{r}},t) = \varepsilon_0 \iiint_{t_1,t_2,t_3=-\infty,t} \chi^3(\vec{\boldsymbol{r}}, t-t_1, t-t_2, t-t_3) \vdots \vec{\boldsymbol{E}}(\vec{\boldsymbol{r}},t_1) \cdot \vec{\boldsymbol{E}}(\vec{\boldsymbol{r}},t_2) \cdot \vec{\boldsymbol{E}}(\vec{\boldsymbol{r}},t_3)\, dt_1\, dt_2\, dt_3 . \tag{2.6}$$

In this approach (i.e. classical approach), χ^3 encapsulates the interaction of the electromagnetic field with bound electrons and the molecule or nuclei. The former one, which has a very short interaction time and is considered instantaneous, is known as the Kerr effect and manifests its effect in different forms such as self-phase modulation (SPM), four wave mixing (FWM), cross phase modulation (XPM) and etc. On the other hand, the interaction of the electromagnetic field on the nucleus has a noticeable time scale and should be treated as memory effect which is mostly demonstrated in Raman scattering (RS) or Stimulated Brillouin Scattering (SBS). Although the later effect can have a lower threshold and can have significant effects by coupling the acoustic waves to the electrical field, due to its dependence on phase matching and the power ranges in this work, it is not at the centre of attention of this thesis. On the other hand, Raman

[1] In general, the validity of such assumption may break down especially in highly anisotropic or highly nonlinear materials [72]. However, such assumption is valid for the range of material and applications in this work.

scattering, which represents the effect of vibration or rotation of molecules in the interaction with an electromagnetic field, can provide great possibility to transfer the energy of light from one frequency to another in an efficient and controlled way.

2.2.1 Raman scattering

Spontaneous Raman scattering was discovered independently and simultaneously by Krishnan and Raman in liquids [73] and by Mandelstam and Landsberg in crystals [74]. Although Stimulated Raman scattering (SRS) was predicted as a part of the general Placzek theory [75] shortly after the discovery of RS, it was only observed thirty years later by Ng and Woodbury during their work on a Q-switched ruby laser since this process needs high power lasers (e.g. megawatt) [76].

It is possible to explain the Raman scattering process either using a classical wave model or through a quantum behaviour interpretation. In the quantum point of view, which is easy to visualize, the scattering of the incoming photons with electrons in the media has two scenarios. In one scenario, if a molecule in an energy state is excited by the incoming photon (υ_0) and goes back to its previous energy level, the emitted photon has the same frequency/energy as the exciting photon and the process is called Rayleigh scattering. In another scenario, if the excited molecule loses its energy in order to reach a certain vibrational or rotational energy level (υ_R) at a higher or lower energy level than its initial energy level, the process is called Raman scattering and the generated photon in each case is called “Stokes” and “anti-Stokes”, respectively, as shown in **Figure 2.5**.

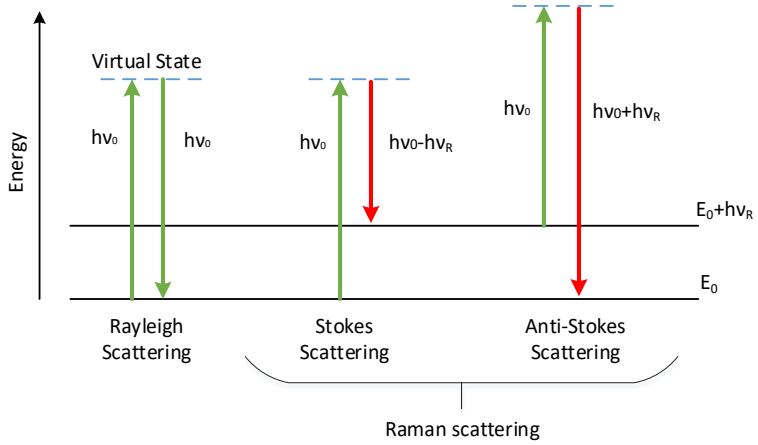

Figure 2.5. Quantum interpretation of Rayleigh and Raman scattering. When the excited molecule falls back to its previous energy level, it releases a photon with the same absorbed energy (Rayleigh scattering), or either goes back to a higher vibrational energy level (Stokes) or to a lower energy level (anti-Stokes), it emits lower or higher frequency photons (Raman scattering), respectively.

From the classical point of view, considering light as electromagnetic radiation, it is an oscillating electric field, which interacts with materials through their molecular polarizability (α). In an excited molecule by an external monochromatic electromagnetic field, the dipole momentum (μ), which act as the source of scattering, has an extra term in addition to the original exciting field:

$$\mu \propto q_0 I_0 \left(\frac{\partial \alpha}{\partial q}\right)_{q=0} \left\{\cos\left[2\pi(\upsilon_0 - \upsilon_R)t\right] + \cos\left[2\pi(\upsilon_0 + \upsilon_R)t\right]\right\}. \tag{2.7}$$

where I_0 and υ_0 are the intensity and frequency of the incident field, q and υ_R are molecular displacement with amplitude of q_0 and Raman vibrational/rotational frequency of molecule, respectively. μ in Eq. (2.7) has two different frequencies of scattering with $\pm\upsilon_R$ differences from the incident field which represents the Stokes $(\upsilon_0 - \upsilon_R)$ and Anti-Stokes $(\upsilon_0 + \upsilon_R)$ scattering, respectively, and gives a unique frequency shift signature to individual molecules. It is clear that only molecules with an anisotropic polarizability can show Raman activity. In other words, Raman vibrational or rotational activity is not available in molecules that cannot satisfy the polarizability change with displacement/time change ($\partial\alpha/\partial q = 0$), or that are formed by single atom such as noble gases [5].

In the steady-state regime and for undepleted monochromatic pump laser conditions, the intensity of the SRS Stokes field (I_S) passing through a Raman active medium with length L is given by [77]:

$$I_S(L) = I_S(0)e^{(g_R I_P L)} \tag{2.8}$$

where I_P is the intensity of the pump laser and g_R is the Raman gain coefficient which is defined by [72, 78]:

$$g_R = \frac{4\pi^3 N c^2}{\omega_L \omega_S^2 \hbar n_S^2 \Delta\upsilon_R}\left(\frac{d\sigma}{d\Omega}\right) \tag{2.9}$$

where λ_L and λ_S are the wavelengths of the Stokes beam and the pump laser beam, respectively; N is the density of scatterers (e.g. molecules); n_S is the refractive index at the Stokes frequency; $\Delta\upsilon_R$ is the Raman spectral line with the full width at half maximum (FWHM) definition; σ is Raman cross-section with laser frequency dependency of $\sigma \propto \omega_L^4$ [79] and Ω is the solid scattering angle. The gain coefficient is one of the most important parameters in Raman lasers applications and its magnitude is usually given in cm/GW. Equations (2.8) and (2.9) show that the intensity of the Stokes beam increases exponentially by increasing the intensity of the pump and the interaction length. It is also clear that materials with higher density of scatterers (N), larger differential Raman cross-section ($d\sigma/d\Omega$) and smaller linewidth ($\Delta\upsilon_R$) have greater Raman gain. From Eq. (2.9) and the frequency dependency of σ [79], it is clear that Raman gain has a direct relation with laser frequency ($g_R \propto \omega_L$), which reduces the Raman efficiency at longer wavelengths. Gases have usually smaller linewidth and larger Raman cross-section in comparison to silica or other solid-state materials but their low molecule density reduces the Raman gain significantly. It has been shown that in the steady-state regime in order to reach the threshold ($I_S \approx I_P$ at output), it is necessary to achieve $g_R I_P L \approx 25$, which in the case of gases with low Raman gain ($g_R = 1-3\,cm/GW$) in the visible range, solid-state materials have 10 times larger gain. Therefore, to reach the threshold either a very long path of gas-light interaction in comparison ($L = 0.5-3m$) to solid material or high pump intensity ($I_P > 1GW/cm^2$) are required [77].

In the two-state approximation for molecules in materials with narrow band Raman characteristic (e.g. gases), the evolution of the Stokes and pump field can be described in a more general and accurate form than Eq. (2.8) by a set of wave equations and a

material Raman coherence equation. These equations express the relation between the field dynamic and molecules dynamic in a coupled system and in the semi-classical approach. These coupled wave equations are known as the Maxwell-Bloch equations and here, without focusing on derivation and the mathematical aspect of the equations, a semi-classical form of them is presented as (for more detail refer to [80] [81]):

$$\begin{aligned}
&\left(\frac{\partial}{\partial z}+\frac{1}{c}\frac{\partial}{\partial t}\right)E_P(z,t)=-i(\frac{\omega_P}{\omega_S})\kappa_2 Q(t)E_S(z,t),\\
&\left(\frac{\partial}{\partial z}+\frac{1}{c}\frac{\partial}{\partial t}\right)E_S(z,t)=-i\kappa_2 Q^*(t)E_P(z,t),\\
&\frac{\partial}{\partial t}Q(t)=-\frac{1}{T_2}Q(t)+\frac{i\kappa_1}{4}E_s^*E_P.
\end{aligned} \tag{2.10}$$

where, E_P and E_S are the pump and Stokes component of the scalar form of the electric field for a plan wave defined as $E=1/2\left\{E_p\exp(i\omega_p t-ik_P z)+E_S\exp(i\omega_S t-ik_S z)+c.c\right\}$ [72]. $Q(z,t)$ is the slowly varying amplitude of the "atomic operator" which is called the "Raman coherence wave operator" in the quantum picture. It represents the coherent motion generated by the pump field and is the counterpart of the motion operator in the classical model of molecules [72, 80]. The coupling coefficients are defined as:

$$\kappa_1=\sqrt{\frac{2c^2 g_P T_2 \varepsilon_0^2}{N\hbar\omega_S}},\quad \kappa_2=\frac{N\hbar\omega_S\kappa_1}{2\varepsilon_0 c}. \tag{2.11}$$

where T_2 is the lifetime of the Raman coherency or in the classical approach the damping parameter of oscillating molecules, which has the relation with Raman linewidth $T_2=1/(\pi\Delta\upsilon_R)$. In the derivation of Eq. (2.10), the forward Raman scattering is assumed to be dominant and the molecules are mostly in the lowest state (valid for pulse power and repetition rates in the applications related to this work). Eq. (2.10) can provide useful information regarding the Raman operation regime and reduction in Raman gain, which is discussed in Chapter 6.

Although Maxwell-Bloch equations can describe the evolution of the Stokes and pump with a very good accuracy, they oversimplify the effect of other nonlinear processes (e.g. Kerr). Besides, adding different materials with different RS characteristics increases the number of coupled equations, which adds computational burden. Also in cases with multiple and broadband phenomena such as supercontinuum generation, the implementation of the coupling approach is not efficient (if not impossible). In the next

section, a more general form of pulse propagation is considered to cover the wider range of nonlinearities in a common formalism.

2.2.2 Nonlinear pulse propagation equation

In general, the Eq. (2.4) in conjunction with Eq. (2.6) can accurately model the interaction of electromagnetic field and materials in space-time if a proper expression for χ^3 is used (in the classical limit). However, calculating the full form of the wave equation (Eq. (2.4)) imposes a huge computational burden especially for cases with a long propagation distance. Fortunately, for a well-defined propagation direction (e.g. z-direction) such as optical fibres, there are different approaches that can benefit from the slowly varying feature of the electric field envelope in nonlinear materials and the paraxial approximation [82]. At first, in this approach, the transverse and longitudinal components of the electric field are separated in the form of:

$$\vec{\boldsymbol{E}}(x,y,z,t)=\int_{\omega}\sum_{m}\tilde{A}_m(z,\omega)\vec{\boldsymbol{E}}_m(x,y,\omega)e^{i(\omega t-k_m^z(\omega)z)}d\omega \tag{2.12}$$

where $\tilde{A}_m(z,\omega)$ donates the longitudinal amplitude of the electric field in the frequency domain, $\vec{\boldsymbol{E}}_m(x,y,\omega)$ is the transverse component of the field which represents the mode profile and k_m^z is the propagation constant in the z-direction for the mth mode, respectively. After calculating the transverse modes ($\vec{\boldsymbol{E}}_m(x,y,\omega)$) by solving the Eigenvalue equation (Eq (3.2)), the evolution of the longitudinal amplitude ($\tilde{A}_m(z,\omega)$) for the individual modes along the propagation direction can be obtained with less of a computational burden than using the full equation (Eq. (2.4)). Despite the fact that most of approaches rely on the slowly varying approximation (i.e. $\left|\partial^2\tilde{A}_m(z,\omega)/\partial z^2\right| \ll \left|k_m^z\partial\tilde{A}_m(z,\omega)/\partial z\right|$) to calculate the evolution of $\tilde{A}_m(z,\omega)$, their differences mainly come from the approximation used to calculate the dispersion or nonlinear operators [82]. While there are a few well-established equations to calculate $\tilde{A}(z,\omega)$, the Unidirectional Pulse Propagation Equation (UPPE) has less approximations and can provide very good results [82, 83]. However, its full implementation for MOFs needs substantial computational power [82]. In contrast, the Generalized Nonlinear Schrödinger Equation (GNLSE) provides a well-balanced approach in terms of computational cost and accuracy, which will be essential for the type of simulations in this thesis [1]. In general, these methods (i.e. UPPE and GNLSE) can be implemented in the multi-mode

scenario through mode coupling by the nonlinearity terms (i.e. $\vec{P}_{NL}$) [84, 85]. However, as most of the power is focused in the fundamental mode, in this study a single mode scenario (m = 1) is considered.

2.2.2.1 Generalized Nonlinear Schrödinger equation

Regardless of the differences between a gas and a solid-state medium, light propagation can be modelled with very good accuracy by the GNLSE under the slowly varying envelope approximation and single mode scenario, which is valid for purpose of this thesis, given by [1]:

$$\begin{aligned}\frac{\partial A(z,T)}{\partial z} = A(z,T)\left[-\frac{\alpha}{2}+\sum_{n=2}^{\infty}\frac{i^{n+1}\beta_n}{n!}\frac{\partial^n}{\partial T^n}\right]\cdots \\ +A(z,T)\left[i\gamma_0\left(1+\frac{i}{\omega_0}\frac{\partial}{\partial T}\right)\int_{-\infty}^{T}R(t')\left|A(z,T-t')\right|^2 dt'\right].\end{aligned} \tag{2.13}$$

here $A(z,T)$ is the slowly varying envelope of the electromagnetic field (Eq. (2.12)), ω_0 is the reference frequency which is normally chosen to be similar to the central frequency of the pump pulse. β_n is the n^{th} derivative of the mode propagation constant ($\beta(\omega)$) at ω_0. α is the total loss of the medium[1], z is the position in the propagation direction and $T = t - \beta_1 z$ is the relative time in a moving reference, respectively. γ_0 is the nonlinear parameter defined as $\gamma_0 = n_2\omega_0/cA_{eff}$ with n_2 the nonlinear index, A_{eff} is effective mode area and ω_0 is the reference frequency which is normally chosen to be similar to the central frequency of the pump pulse, respectively (more details can be found in [1]). $R(t)$ is the nonlinear response function which is defined by:

$$R(t) = (1-f_R)\delta(t) + f_R h_R(t). \tag{2.14}$$

Here, $\delta(t)$ is the Dirac delta function, $h_R(t)$ is the Raman response function of the molecule, f_R represents the fractional contribution of the delayed Raman response to the overall nonlinear response.

[1] In this formulation the loss is considered to be constant but in a more general form and in frequency domain form of GNLSE the full frequency dependent loss is used in this work.

The GNLSE (Eq. (2.13)) provides a unified equation that integrates the Kerr and RS processes along with the total chromatic dispersion of medium (i.e. material and waveguide dispersion), which plays a major role in defining many different nonlinear processes and effects such as: SPM, FWM, XPM, soliton (balance of nonlinearity and anomalous dispersion), dispersive wave generation, modulation instability (MI), SRS responses, and even supercontinuum generation (SG) [86]. In addition, Eq. (2.13) includes the nonlinear loss caused by energy transfer to the phonons in the RS process by introducing the self-steepening term in the nonlinear part. It is worthwhile to mention that ionization phenomena in gases can introduce extra effects such as high harmonic generation (HHG) and plasma associated blue-shift [5, 87], however, these effects are not included in Eq. (2.13) as the pulse energy in studies of this thesis are much lower than the ionization energy of the gases [88].

Among all the above-mentioned nonlinear processes with frequency conversion ability, Raman scattering has the best capability to fit the requirements of the main goal of the project in this thesis. First of all, Raman scattering in gas has a larger frequency shift than solid counterparts, which enables the generation of mid-IR output using near-IR excitation while the other counterpart, FWM, cannot perform such a large shift as Raman, and also FWM is influenced strongly by the dispersion of the material and waveguide. In addition, gases have very narrow Raman linewidth, which provides narrow bandwidth output. Although the study of each individual effect generated by nonlinear processes is possible by considering the physical origin of each one separately, nonlinear processes in light-matter interaction are coupled to each other and a broad understanding of their mutual effects is needed for more realistic and accurate results.

2.3 Nonlinearity in gas-filled fibres

In spite of all the positive aspects of gases for nonlinear optics applications, they suffer from lower Raman gain than solids (at moderate pressures and far from electronic resonances), which increases the required threshold to excite a particular nonlinear process. As a result, the use of long optical path lengths and high pump intensity to increase the light-matter interaction is necessary. However, for longer path lengths, in free space diffraction becomes a major problem. **Figure 2.6** shows the conventional free-space setup to increase the intensity at the focal point of a lens.

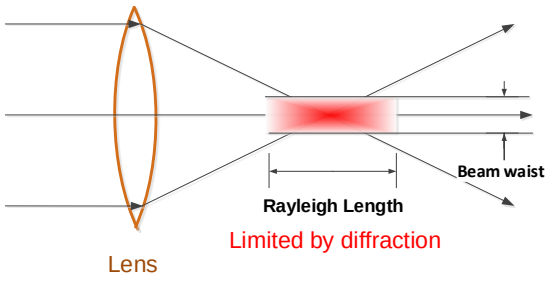

Figure 2.6. Conventional free-space setup for a nonlinear experiment in gases. The high intensity interaction length is limited by the Rayleigh length.

This setup suffers from a trade-off between spot size and Rayleigh length which is the effective length for the interaction. Although the use of a more powerful lens can produce higher intensities, in addition to reducing the Rayleigh length, it can also induce self-focusing or higher-order nonlinear effects such as photoionization of the gas and two-photon absorption. Many different attempts have been done to increase the length and intensity of the field by using a high-finesse Fabry–Pérot cavity. However, they are only effective over a narrow frequency range [48]. These limitations in free-space setups indicate the necessity of maintaining the intensity over a longer interaction length. Using a glass capillary as a solution for confining the light over a long distance was the first attempt. However, the large CL imposed by the cladding glass and lack of a total internal reflection mechanism in addition to a fixed dispersion profile have limited the application and interest in such a method. Alternatively, HC-PCFs with very low CL and a broad transmission windows are good candidates as an efficient gas-filled waveguide approach. **Figure 2.7** demonstrates the advantage of HC-PCF in contrast with a simple capillary [34].

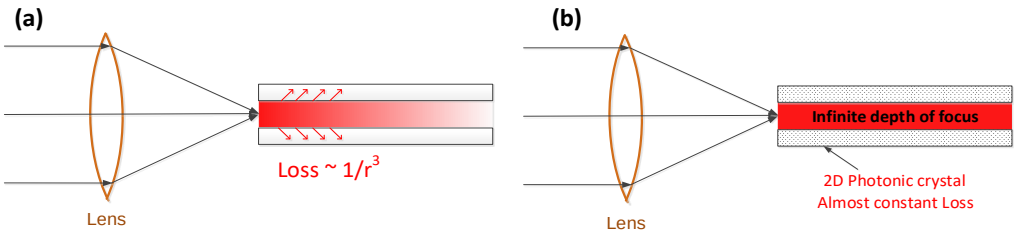

Figure 2.7. Increasing the interaction path length by using a waveguide: **(a)** The dependence of loss to bore size reduces the interaction path length in a glass capillary, **(b)** the HC-PCF can extend the depth of focus (interaction path length) to almost the full length of the fibre.

A quantitative figure of merit for comparing the nonlinear efficiency of different waveguides in terms of confinement of the light is defined by $f_{om} = L_{\text{int}} \lambda / A_{eff}$, where L_{int} is the effective constant-intensity interaction length ($L_{\text{int}} \approx 1/\alpha$), which is defined as the

length where the intensity drops to $1/e$ of its maximum [34]. **Figure 2.8** shows the figure of merit vs core radius for HC-PCFs and capillary fibres in contrast to a free-space beam, which indicates the significant advantage of HC-PCFs over a capillary [34].

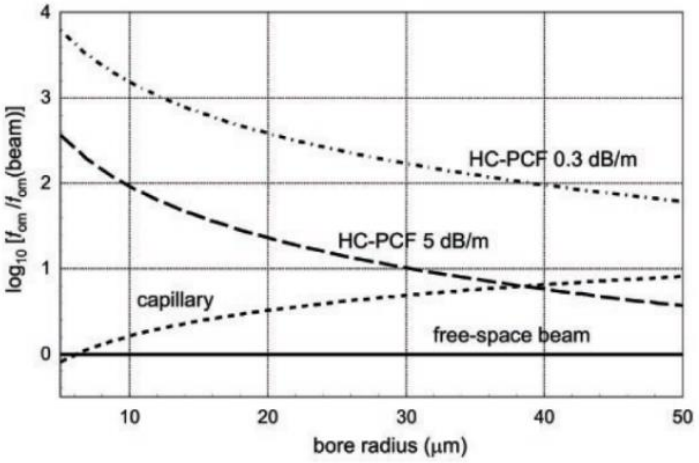

Figure 2.8. Relative figure of merit of hollow capillary and two HC-PCFs based on free-space beam. The HC-PCFs are at least 10000 times better for core radii < 5 μm at λ = 532 nm [after [34]]

Since the first demonstration of HC-PCFs a variety of attempts to explore nonlinear processes in gas-filled HC-PCFs have been reported [5]. For instance, it was reported, a decade ago, that air-filled HC-PCFs can offer soliton propagation at very high peak powers [19] and the possibility of soliton pulse compression was demonstrated in Xe-filled HC-PCF [89]. It is possible to give a long list of works that have been done in this field such as: Soliton-Effect Compression [89-91], adiabatic soliton compression [92], highly efficient deep-UV generation [93], etc. Recently, a few useful and comprehensive reviews have been published on this topic which are discussed in the following [5, 48].

2.3.1 Previous works on nonlinearity of gas-filled fibres

In general, the nonlinear dynamics of light in a gas can introduce many different effects depending on the gas mixture, dispersion, intensity and length of the pulse. On one side, the gas mixture and its pressure can have a direct effect on the strength of Raman (or even absence of Raman) and the chromatic dispersion. On the other hand, the intensity of the input pulse governs dominant nonlinear effects. Basically, the most important practical parameters, which can determine the dynamics of nonlinear pulse propagation in gas-filled fibres, are gas pressure, pulse intensity and pulse duration [5]. It is possible to relate these parameters to the parameters in Eq. (2.13). For example, it has been shown that dispersion profile of a gas-filled HC-ARF can be

modified and controlled, to some extent, by the pressure of the gas, and the intensity of the field can be related to the soliton order of pulse, which defines the relative strength of spectral/temporal broadening from nonlinearity and linear dispersion.

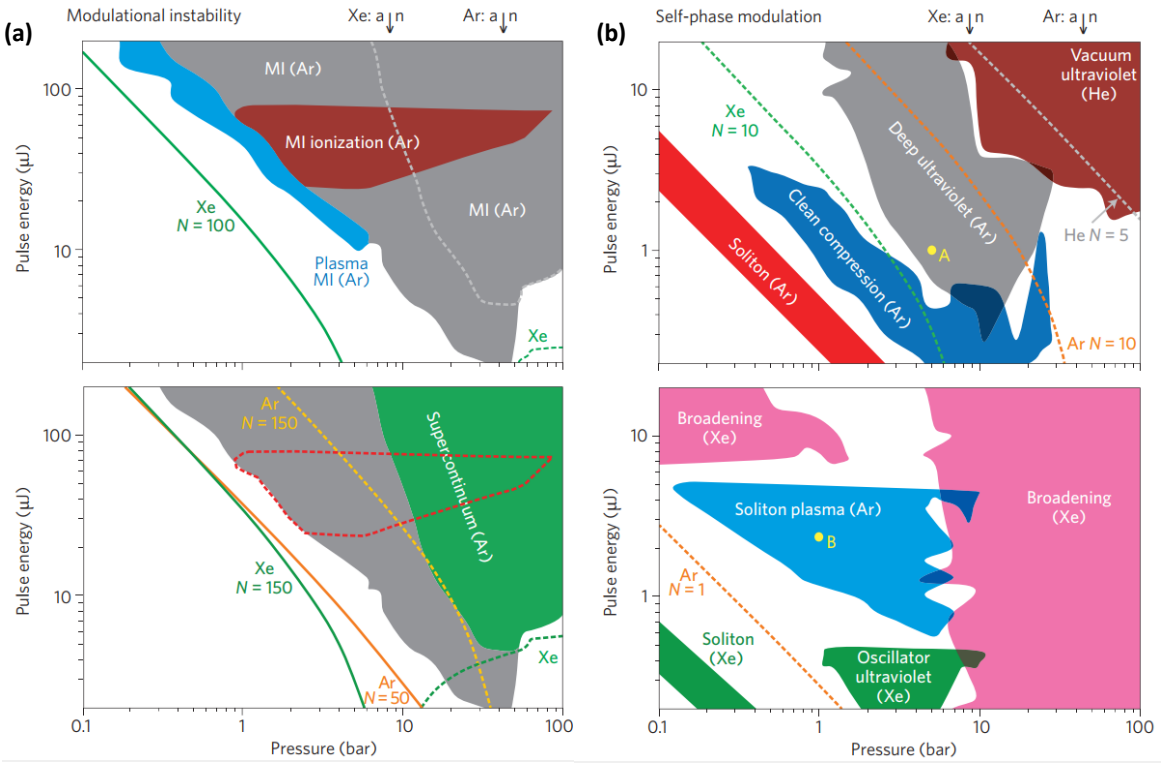

Figure 2.9. These maps show the variety of nonlinear phenomena and how they depend on pressure and pulse energy in a gas-filled Kagomé HC-PCF with a core radius of 13 μm and length of 50 cm at 293 K. Using pressure to switch from anomalous "a" to normal "n" dispersion occurs at 8.5 bar and 42 bar for Xe and Ar, respectively while the dispersion is always anomalous for He. The central wavelength of exciting laser pulse is in 800 nm. **(a)** The modulation instability map shows the effect of using fairly long pulses (600 fs), **(b)** The self-phase modulation map shows the effect of considerably shorter pulses (30 fs) (refer to [48] for details and discussion) [after [48]].

The dynamics of light propagation in the nonlinear regime have been summarized for long (600 fs) and short (30 fs) pulses depending on gas pressure (dispersion) and field intensity by Russell *et al* [48]. In this work, a wide range of nonlinear effects has been demonstrated for a visible selected range in the form of maps. Each map depends on the length of the pulse, relates each nonlinear effect to the pressure and pulse energy (~pulse intensity), as shown in **Figure 2.9**. Even though these maps are for special cases, as has been discussed earlier by having the relation between gas pressure /mixture and dispersion as well as the relation between intensity and soliton order for specific HC-PCF, to some extent it is possible to design or estimate the behaviour of the

light in gas-filled HC-PCF using these maps [5] (for more detail on nonlinear process on the map and experimental detail refer to [5, 48]).

Apart from the visible region, a highly significant work on UV and Deep-UV generation has been reported by Mak, K. F *et al* [94], which used different gas filling to generate a tunable UV light mainly based on dispersive waves generation. **Figure 2.10** shows the tunability of ultraviolet light generated in a gas-filled Kagomé.

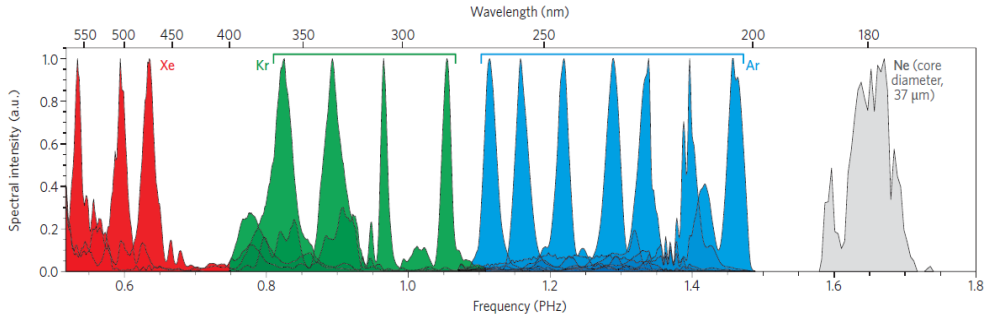

Figure 2.10. Tunable ultra-violate generation in a gas-filled Kagomé HC-PCF by using different gases and pressures. the fibre core diameter for all gases was 27 µm, except Ne which was 37 µm (refer to[94] for details and discussion) [after [94]].

In addition, many other phenomena ranging from pulse compression [95] to frequency comb generation [96] and even supercontinuum generation [5, 97] have been covered by many works on gas-filled HC-PCF. As it is clear, nonlinearity in gas-filled HC-PCF has been extensively explored up to near-infrared (near-IR) region, while mid-IR and IR regions have not been investigated as extensively as possible specifically in HC-PCFs (apart from very recent works [98] and population inversion laser-gases [99]) and need more study.

2.4 Conclusion

In this chapter, the background of major building blocks for exploring nonlinearity in gasses have been briefly touched. At first, hollow core fibres as an alternative to solid-core fibres are introduced to overcome some of the limitation raised from the direct interaction of light and material at the core of the fibre. After a very short introduction on their historical origin, according to their guidance mechanism, major categories of these fibres have been introduced and a few examples are provided to the reader. More details and analyses on HC-ARFs, as the main focus of this thesis, will be provided in the following chapters. In section 2.2, after a brief introduction on the classical formulation of optical nonlinearity, the main focus was concentrated on Raman scattering as the main objective of this thesis. Although Maxell-Bloch coupled equations

have been introduced for analysing solely the Raman scattering, a more general form of pulse propagation, which can include a wider range of nonlinear phenomena, has been explored. In section 2.3, by using the special potential of HC fibres to confine light in a long path with very low attenuation, gas-filled hollow core fibres have been introduced as an alternative solution to improve the low Raman gain of gases by increasing the interaction length of gas and light in a confined condition. In the end, as an overview of recent development, a few examples of recent works on gas-filled HC fibres have been presented. In the following chapters not only each element will be explored in more depth, to realize the goal of this project, but also new approaches and designs in some areas are developed.

Chapter 3: Modelling methods and Toolboxes

3.1 Introduction

In this chapter, the essential theory and numerical modelling toolboxes which have been developed and used throughout this study, are presented. This chapter is divided into two parts. In the first one, the modelling tools and numerical methods used for fibre modelling are discussed while in the second part, the numerical method to model the nonlinear dynamics of the pulse propagation by solving the GNLSE is presented. Together, these toolboxes can provide a unified solution for design and modelling the nonlinear gas-filled fibre applications. Although, for space constraint in this thesis, not all the detail of derivations could be presented, plenty of references have been provided where the reader can retrieve more in depth details.

3.2 The Maxwell's Eigen mode equation

One of the most essential steps towards implementing the nonlinear process in the gas-filled fibres is to design a suitable fibre with low loss at the working wavelengths. In general, by calculating the **"complex effective refractive index"** (N_{eff}) of a fibre it is possible to determine the combination of material and confinement loss as well as dispersion profile of a fibre regardless of its complex geometry. In principle, the transverse-field of electric or magnetic field has to satisfy a Mode Equation (ME). In fact, an Eigen-frequency problem in 2D space (e.g. fibre guiding mode in 2D cross section) can be formulated from Maxwell's equations (Eq. (2.3)) in the form of out-of-plane Eigen mode equation. Starting from the general form of the wave equation for electric field, and considering a nonmagnetic linear material:

$$\vec{\nabla}\times\left(\mu_r^{-1}\vec{\nabla}\times\vec{\boldsymbol{E}}\right)-k_0^2\varepsilon_r\vec{\boldsymbol{E}}=0 \tag{3.1}$$

Assuming $\vec{\boldsymbol{E}}(x,y,z)=\vec{\boldsymbol{E}}'(x,y)e^{(-ik_z z)}$ for 2D out-of-plane propagation, the Eigen mode equation for electric field can be expressed as:

$$\left(\vec{\nabla}-ik_z\vec{z}\right)\times[\mu_r^{-1}(\vec{\nabla}-ik_z\vec{z})\times\vec{\boldsymbol{E}}']-k_0^2\varepsilon_r\vec{\boldsymbol{E}}'=0 \tag{3.2}$$

where $\vec{\boldsymbol{E}}'$ is vectorial transverse electric field, $\vec{z}$ is the unit vector in the out-of-plane z direction, $k_0=\omega\sqrt{\varepsilon_0\mu_0}=\omega/c$ is the wavenumber of free space, k_z is the complex out-of-

plane wavenumber (i.e. in z-direction), ε_r and μ_r are the complex relative permittivity and permeability, respectively. The primary goal is to find the Eigenvalues (k_z) and Eigenvectors ($\vec{E}'$) by solving the Eq. (3.2) for an arbitrary $\varepsilon_r(x,y)$ at specific ω. In other words, the solutions of Eq. (3.2) provide the mode field profiles (i.e. $\vec{E}'(x,y)$) at the cross-section of waveguide (i.e. $\varepsilon_r(x,y)$) and the propagation constant (or wavenumber) of each mode (i.e. k_z). By considering a complex $\varepsilon_r(x,y)$, which includes the material loss in the model, and calculating the complex out-of-plane wavenumber (k_z) from Eq. (3.2), the complex N_{eff} for each mode can be obtained from:

$$N_{eff} = \frac{ik_z}{k_0} = \frac{\beta + i\alpha}{k_0} = n_{eff} + i\xi. \tag{3.3}$$

where β, as the real part of k_z, represents the propagation constant of the relative mode in the z-direction. n_{eff} is the effective refractive index of the relative mode (real part of N_{eff}) and has real value, which provides the dispersion characteristics of the mode with such relation $\beta = n_{eff}\omega/c$. ξ is the imaginary part of N_{eff}, which is related to α (the power loss in the fibre) by $\alpha = \xi\omega/c$. This power loss (α) stands for the combination of material loss as well as the waveguide confinement loss (CL) contribution if the field modes have leaky nature (i.e. leaky modes), which is an intrinsic condition in HC fibres due to lack of the total internal reflection. By looking more closely into the source of the loss in a fibre, it is possible to break it down into some major parts. Generally, the total loss in a fibre can be expressed as the collective form of major loss sources:

Total loss (TL) = *material loss (cladding material +gases trapped in core)* + *CL* + *surface scattering loss* (at the interface of glass and gas) + *defect induced loss (defect in the structure)* + *macro and micro bending loss*.

Among these loss sources, the material loss, CL and macro bend loss can be easily calculated by solving the Eq. (3.2) as discussed. The micro bend loss can be estimated statistically by considering an average spatial frequency of micro bends along the fibre and introduced mode coupling which can cause power loss by power transfer from lower order modes to higher order modes [100-102]. The defect loss has random distribution and cannot be modelled properly without accurate knowledge of the fabrication process and defects shape. The surface scattering loss is caused by inherent roughness of glass webs [103]. This roughness is typically caused by frozen thermally excited surface

capillary waves on the surface of glass during the fibre draw at the glass transition temperature. In this work, due to the range of operating wavelengths (mid-IR), the material loss, CL and bend loss are dominant loss sources while other loss mechanisms have negligible effect on the total loss in this regime.

3.2.1 Numerical mode solving methods

In its general form, Eq. (3.2) has no analytical solution for an arbitrary geometry/material properties or for complex structures like MOFs and it should be solved by numerical methods. Although there are many numerical methods that can provide approximate solutions to this equation with different accuracy and advantages, there are a few well-developed numerical methods that can solve the direct form or a modified version of Eq. (3.2) for complex structures like MOFs with acceptable accuracy such as: plane wave expansion method (PWE) [104, 105], beam propagation method (BPM) [106], multipole method (MM) [107], source-model technique (SMT) [108], finite element method (FEM) [109], orthogonal function method (OFM) [110] and Fourier decomposition with adjustable boundary conditions (ABS-FDM) [111], to name few.

In general, the accuracy and computational speed are the primary objectives for a numerical method. However, a versatile numerical method to tackle the complexity of MOFs needs to meet few more criteria such as:

- **Full vector implementation**: to provide an accurate result for high index contrast and arbitrary structure of MOFs.
- **Full material dispersion implementation**: the material dispersion can have significant impact on the characteristic profile of the HC-ARFs.
- **Confinement loss calculation**: a proper calculation of leaky modes is an essential capability for the numerical method to achieve accurate CL due to guidance mechanism in HC fibres.
- **Arbitrary cross section**: it is important to have freedom over fibre structure to compare the fabricated and ideal model of the fibres and explored variety of complex structures.
- **Symmetry exploitation**: this feature is essential to reduce the computational burden in symmetric structures, especially for complex MOFs.

Compiling these requirements in **Table 3.1** for above-mentioned methods, the FEM and SMT can clearly meet all the criteria. Thanks to the availability of a commercial FEM

solver, established and maintained by professional developers, in this study, FEM is chosen over other numerical methods.

Table 3.1: Capability comparison between different numerical methods in solving electromagnetic Eigen mode equation

Num Methods / Capibility	OFM	PWE	ABC-FDM	MM	BPM	SMT	FEM
Fully vectorial	✓	✓	✓	✓	✓	✓	✓
Full material dispersion	✓	✓	✓	✓	✓	✓	✓
CL calculation	✗	✗	✓	✓	✓	✓	✓
Arbitrary structure	✓	✓	✗	✗	✓	✓	✓
Symmetry exploitation	Partial	✗	Partial	✗	✗	✓	✓

3.2.2 FEM modelling toolbox

The FEM is a well-known and successful numerical method that in general is used for solving boundary value problems (BVPs) for partial differential equations (PDEs), or Eigen equations like the electromagnetic Eigen mode equation in this particular case of use. FEM is used in many areas of physics and engineering such as: structural analysis, mass transport, fluid flow, heat transfer, and electromagnetic potential and waves. In this method, the domain of the problem is discretized into a mesh and by defining basis functions (or shapes functions) for each subdomain of the mesh and solving the equation for each subsection of the mesh it can achieve a very good approximation of the exact solution to the equation with very low relative error[1] (for detail of FEM refer to [112]). As mentioned before, the main advantage of FEM comes from the fact that it can provide a full vectorial solution and the possibility of including the material dispersion and material loss in the calculation, which offers a comprehensive model of the waveguide. Moreover, in the FEM calculations, symmetric geometries can be solved in a reduced size symmetric unit cell, which saves a large memory and computational time.

[1] In principal, any numerical method provide an approximation of the actual solution to an equation.

In order to simulate and test the design concepts and fabricated fibres, in this work, a mode solver kernel from COMSOL Multiphysics® is used, which is a commercial FEM solver software. Although this kernel mode solver has been developed commercially, in order to extract the desired information, it is necessary to define the structure, boundary values, absorbing layers and many other parameters, along with proper post-processing methods to obtain correct results from the provided solutions. Despite the availability of an embedded graphical user-interface (GUI) in COMSOL Multiphysics®, the lack of advanced pre and post-data-processing in the GUI mode of this software as well as memory management problems for large parametric sweep simulations, have persuaded me to use more advanced script-based program instead. Therefore, as the first stage of this project, a complete and user-friendly toolbox has been developed for communicating to COMSOL Multiphysics® solver kernel (version 4.2 or later) via MATLAB® software.

This toolbox has been developed in Java based subroutines and is compatible with all Java versions of COMSOL Multiphysics®. The toolbox is in the form of MATLAB® functions which improves importing data as well as pre/post processing data efficiently into the MATLAB® environment. Although it is designed with mode calculation in MOFs and more specifically HC fibres in mind, because of its modularity, each function in the toolbox can be used for general-purpose mode calculation and can be applied to any form of mode solving problem.

Even though the accuracy of the results depends on the particular FEM solver (i.e. explicit or implicit), shape function (i.e. the shape of basis function for each subdomain defined in the FEM solving process) [112] or the relative tolerance, which are predefined in the solver, without proper mesh element type/size, boundary conditions and shape function, the results cannot be reliable and the accuracy of results reduces significantly. As a result, an Error Check Routine (ECR), which contains iterative sweeping simulation over specific parameter (e.g. mesh size) to reach a converging point in effective refractive index or CL, has been developed to find the optimum value for simulation parameters.

In general, the modelling process of a fibre by FEM solver toolbox can be described in few major steps. After a brief overview of these steps, the most important ones, which are necessary to achieve accurate simulation results, are discussed in more depth.

1. **Definition of Geometry**: the first step is to input the fibre structure into the modelling toolbox environment by defining the geometry of the fibre cross section in a 2D plane. The geometry is *usually* defined according to the boundary

of different materials in the fibre and creates different domains. Although, in general, each domain represent a material, there is not limitation on defining the structure of fibre or domain. This can be done manually through the provided GUI program by COMSOL or can be defined programmatically by MATLAB commands. The advantage of latter method is the flexibility in defining and controlling the geometry of the fibre programmatically and automation of parameter sweeping in different fibre structures but required complex and large coding. Therefore, to achieve the flexibility and speed in manipulating the geometry of the fibre, a library of MATLAB functions has been developed for this study that encapsulate the low level codes in a high level MATLAB functions. This library can be used to define different ARFs by breaking down their complex structure into smaller but simpler substructures. This library is a part of developed fibre modelling toolbox.

2. **Assigning the material**: at this stage, the profile of $\varepsilon_r(x,y)$ is determined for the mode solver to be used in Eq. (3.2) by assigning different material to each domain of structure defined in previous stage. Because dielectrics (e.g. glasses) are the most used material in the fabrication of optical fibres, the refractive index and loss (as the real and imaginary part of the complex refractive index) are the main material parameters at this stage. This process is also integrated in the developed MATLAB library.
3. **Selecting Solver module**: COMSOL is a modelling software that integrates many different physical models in one environment. To solve the mode equation (Eq. (3.2)), one needs to assign the "electromagnetic mode solver" module from COMSOL library to the defined geometry. This solver can be selected for isotropic and anisotropic materials. While in most cases the materials used in the structure of the fibre are assumed isotropic, as will be discussed later, for Perfectly Matched Layer (PML) one should select an anisotropic solver from the COMSOL library. This assignment and required coding are also integrated in the developed MATLAB library.
4. **Defining PML**,
5. **Meshing**,
6. **Post processing**.

The last three steps have very important roles in the process of simulation and need to be optimized for an accurate result. Therefore, they are discussed in more detail in the following.

3.2.2.1 Geometry meshing process

Meshing the geometry is an important process in the FEM and there are many available methods for implementation and optimization of this process [112]. Fortunately, the meshing process is handled very well in the COMSOL program. However, there are still a few parameters in the meshing process that need more attention to achieve accurate results. In the modelling of ARFs, the mesh size and its distribution have a big impact on the accuracy of the results, due to the unique resonance/anti-resonance features of the guidance mechanism in this type of fibres. It is shown that in such fibres very rapid field modulation phenomena such as Fano resonance [113] or resonant modes in the cladding [114] can impact the confinement of light and consequently affect the CL and dispersion property of the fibre. Hence, to model MOFs and specifically ARFs, not only the mesh size should satisfy the Nyquist rate for those rapid oscillating features of the field but also it should reconstruct the subwavelength spatial variants of the field due to very fine elements of the structures in ARFs. As a result, there is a trade-off between accuracy and simulation speed in the modelling process of ARFs. The key parameters of meshing in the COMSOL environment are maximum size of the mesh (*hmax*) and mesh resolution at narrow regions of geometry (*hnarrow*). A proper setting of these parameters can provide required balance between accuracy and simulation speed.

Here, the ECR process used for optimizing the above-mentioned parameters has been demonstrated in an example. A tube-jacket fibre, as the simplest form of ARF, can be modelled semi-analytically by the transfer matrix method (TMM) [115] with very high accuracy. Thus, it can be used as an example for ECR on meshing process of FEM. **Figure 3.1** shows the calculated loss and n_{eff} of a single tube in a jacket with t_s =0.83 μm, R = 15 μm and Z = 9.75 μm at λ = 1 μm (see inset of **Figure 3.1 (b)**) by TMM and developed FEM toolbox for different value of *hmax,* where *hnarrow* is not set to any specific value (i.e. minimum one grid point in each domain). With such setting, the meshing process in the narrow part of the geometry (i.e. glass ring of tube) is controlled by COMSOL internal routines. In another case, the fibre has been simulated with the previous condition but the *hnarrow* parameter is set to 5 point in narrow regions as shown in **Figure 3.1**. It is clear that by controlling the number of mesh points in the narrow domains of the geometry, which are an essential parts in the structure of ARFs, the simulation results converge faster and with smaller deviation from real value at larger mesh sizes (i.e. lower mesh number) than previous case (i.e. no setting for *hnarrow*).

An interesting property of HC fibres (with vacuum core) is their effective refractive index (n_{eff}) of less than one, which can be seen in **Figure 3.1 (a)**. As much as it looks counterintuitive, the basic principle of wavevectors in waveguides predicts such behaviour. From the conservation of wavevectors in any waveguide one has $k^2 = k_x^2 + k_y^2 + k_z^2$ where $k_{x,y,z}$ are the wavevectors in relative directions x, y, z, respectively and k is the wavevector amplitude. This relation also can be presented in the form of effective refractive index of propagation direction (i.e. n_{eff} in the z direction) and the absolute refractive index of medium (n), which the light is propagating through, as $n^2 = n_x^2 + n_y^2 + n_{eff}^2$. Here, in the case of HC fibres, the filling medium in the core of the fibre is considered vacuum (i.e. $n = 1$), which the relation between refractive indices enforces the effective refractive index (n_{eff}) of less than one, as shown in **Figure 3.1 (a)**.

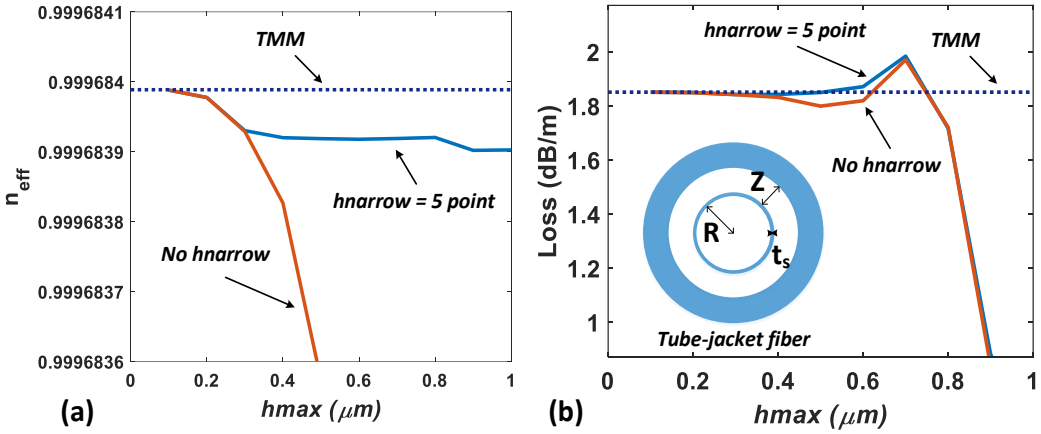

Figure 3.1. Simulation results of a tube-jacket fibre with t_s =0.83 µm, R = 15 µm and Z = 9.75 µm at λ = 1 µm by TMM, and FEM with and without *hnarrow* setting shown in the inset. **(a)** calculated effective refractive index (n_{eff}), **(b)** calculated CL.

Utilizing such ECR on many example of ARFs has shown that the maximum mesh size (*hmax*) in the range of $< \lambda_i / 5$ (see **Figure 3.1**) in individual material (λ_i is the wavelength in material i) and *hnarrow* = 5, can provide a good balance between accuracy and speed for the most cases.

3.2.2.2 Circular Perfectly Matched Layer (PML)

In order to reduce the special extent of the computational regions in problems with open boundaries, it is common to use artificial absorbing layers called Perfectly Matched Layer (PML) around the modelling area [112]. This feature is essential for simulating an infinite structure in the outer boundary sides to reduce the computational region.

Most importantly, the implementation of PML is an essential part of modelling the CL and leaky modes in MOFs. The important key difference of a PML from ordinary absorbing materials is the non-reflecting property of PML. PMLs can strongly absorb the outgoing waves without reflecting them back towards inside the computational region. This feature is due to impedance matching at the interface of the PML and modelling area, which can be expressed by:

$$\frac{\tilde{\mu}_{PML0}}{\tilde{\mu}_1} = \frac{\tilde{\varepsilon}_{PML0}}{\tilde{\varepsilon}_1}. \tag{3.4}$$

where $\tilde{\mu}_{PML0}$ and $\tilde{\varepsilon}_{PML0}$ denote the complex value of permeability and permittivity of PML layer at the interface with its neighbour material, while $\tilde{\mu}_1$ and $\tilde{\varepsilon}_1$ are the complex value of permeability and permittivity of the neighbour material next to PML layer at their interface.

In general, there are two main categories of PMLs. The first type is called Beranger's type [116], which is implemented in the form of coordinate-stretching method to virtually extend the PML layer and dissipate the field. This method needs changes in the definition of the main Eigen equation and adds extra calculation steps in the FEM. The other implementation of PML is represented in the form of an "*anisotropic*" PML by introducing anisotropic $\tilde{\mu}_{PML}$ and $\tilde{\varepsilon}_{PML}$, which can be simply implemented by readily available FEM solvers for anisotropic Eigen mode equation, and which has been shown to be more efficient [117, 118].

The standard PML has a rectangular shape, but by defining a cylindrical PML layer instead of regular rectangular shape, one can also save more simulation time in the simulation areas with cylindrical geometry (in 2D) similar to optical fibres due to reduction of wasted space between two rectangular PMLs and cylindrical geometry, as shown in

Figure 3.2.

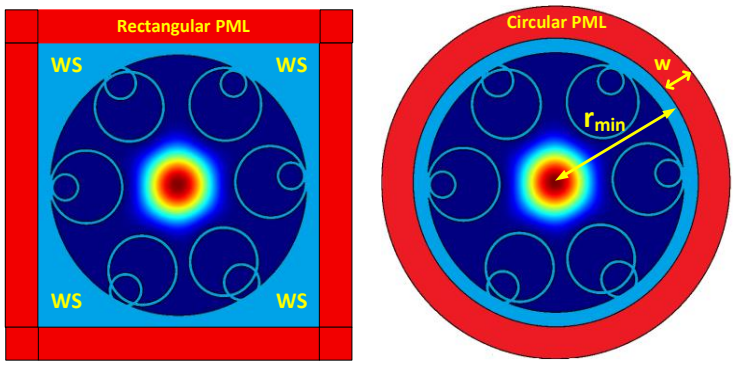

Figure 3.2. An example of rectangular PML (on the left) and circular PML (on the right) implemented for modelling a HC ARF. There are wasted spaces (WS) due to implementing rectangular PML.

In this form of "*anisotropic*" PML, $\tilde{\mu}_{PML}$ and $\tilde{\varepsilon}_{PML}$ are defined in the tensor form, which relate the coordinate of the simulation space (e.g. cylindrical coordinate) to an absorbing parameter S (refer to *appendix* ***B*** and [119, 120] for more details). The S parameter in the circular PML, which is developed in this study, is defined as (this definition does not depend on wavelength in the mode calculation):

$$S = 1 - i\varsigma\left(\frac{r - r_{\min}}{w}\right)^{m}, \quad r \geq r_{\min.} \tag{3.5}$$

where r is the length of coordinate vector (in the cylindrical case, it is the radial distance from the centre). $r_{\min}$ and w are the starting position of the PML and the thickness of the PML, as defined in

Figure 3.2, respectively. ς is a damping factor and must be positive number, m is the order of propagation loss in the PML, which typically is m = 2 [121]. In general, the damping or absorbing coefficient ς should be frequency dependent ($\varsigma \propto 1/\omega$) in time or frequency domain analysis, but in the mode calculation, it should be frequency independent as all mode solutions are calculated in the same frequency. For any simulation case, one needs to optimize w and ς parameters to reach convergence in the loss result. After running ECR for many different structures, I have found that a damping factor > 10, and PML thickness of > 5 μm can provide accurate results, which is consistent with results of [121]. Although these values may change slightly from geometry to geometry and an appropriate ECR can determine new values, it is found that changes are not significant for the cases in this study and these values are used through the simulations in this work.

3.2.2.3 Bend loss modelling and bend adaptive PML

In practical applications, fibres are very rarely used in a straight form and there is often a degree of macro bend imposed to the fibre. In its most general form, modelling of such bends need implementation of a 3D geometry. However, thanks to the symmetry of the problem, it is possible to reduce the problem to 2D geometry by modifying the refractive index profile of the fibre through a conformal transformation [122]. In this approach, the bend loss calculation can be performed by the developed modelling toolbox for straight fibres, but with a tilted spatial dependent refractive index profile, given by [122]:

$$n_{Rc}(x,y) = n_0(x,y)e^{\left(\frac{x}{R_{eff}}\right)}. \tag{3.6}$$

where $n_0(x,y)$ is the refractive index profile of the fibre, x and y are the coordinate displacement from the centre of the fibre, while in this example the bend direction assumed to be in x direction. R_{eff} is the effective radius of the bend, which is equal to the physical radius of curvature (R_C) for vacuum/gas, while for glass is approximately 1.28 times the physical radius to account for the elasto-optic effect [123]. Moreover, to model the bend loss, one must to modify not only the refractive index of the material, but also the discontinuity between PML and its neighbour material by suitably adapting the refractive index inside the PML layer to preserve non-reflecting property, which is implemented in the developed modelling toolbox (see *appendix* ***B***).

All of the above-mentioned points are implemented carefully in the developed modelling toolbox to achieve an accurate and realistic modelling environment for this thesis, which has been used for analysing a variety of fibre design ideas and modelling the fabricated fibres. To validate the developed bend adaptive PML, the analytical formula presented in [124] is used, as a well-known benchmark, to calculate the bend loss of a solid-core step index fibre. Considering a silica single mode fibre (SMF) with refractive index of the cladding n_{cl} = 1.444, NA = 0.117 and core radius of 4.1 μm, the bend loss of the fibre is calculated by FEM with the developed adaptive PML and the analytical formula in [124] at λ=1.55 μm. **Figure 3.3** shows the comparison between the results of analytical and FEM modelling with very good agreement.

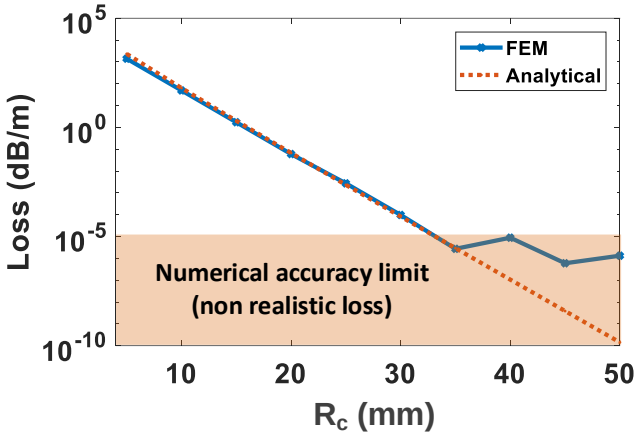

Figure 3.3. Comparing the calculated bend loss of silica SMF at λ =1.55 µm by developed FEM toolbox with bend adaptive PML and analytical formula [124].

3.2.2.4 Fibre modelling toolbox (GUI and Post-processing)

By developing a GUI based program, all of the modelling procedures have been organized and integrated such as: constructing the fibre geometry in the modelling environment, allocating all material properties and boundary conditions, implementing proper PML and meshing the geometry, all by a set of MATALB functions developed as a part of the developed modelling toolbox. This wrapper GUI based program has provide flexible environment to perform parameter sweep on any type of parameters in the model environment such as: geometrical parameters, mesh parameters, material parameters and most importantly, wavelength sweep for calculation of characteristic profile of the fibre. Although the FEM mode solver calculates the mode profile for a desired number of modes, without proper initialization, which is implemented in wrapper program, one may not find the desired modes (i.e. core guiding). Moreover, the provided data by solver require post processing to identify the relative effective index and field profile for fundamental mode and/or higher order modes and to extract the desired information from the data programmatically. Thus, a GUI based toolbox has also been developed that can provide verity of post processing facilities such as presenting mode profiles for each sweeping points and provides the ability to visually select the desire mode as well as categorizing the modes programmatically and represent relative loss and effective index profile.

Figure 3.4 shows the GUI of FEM modelling toolbox and the GUI of mode selecting utility alongside some examples of their outputs.

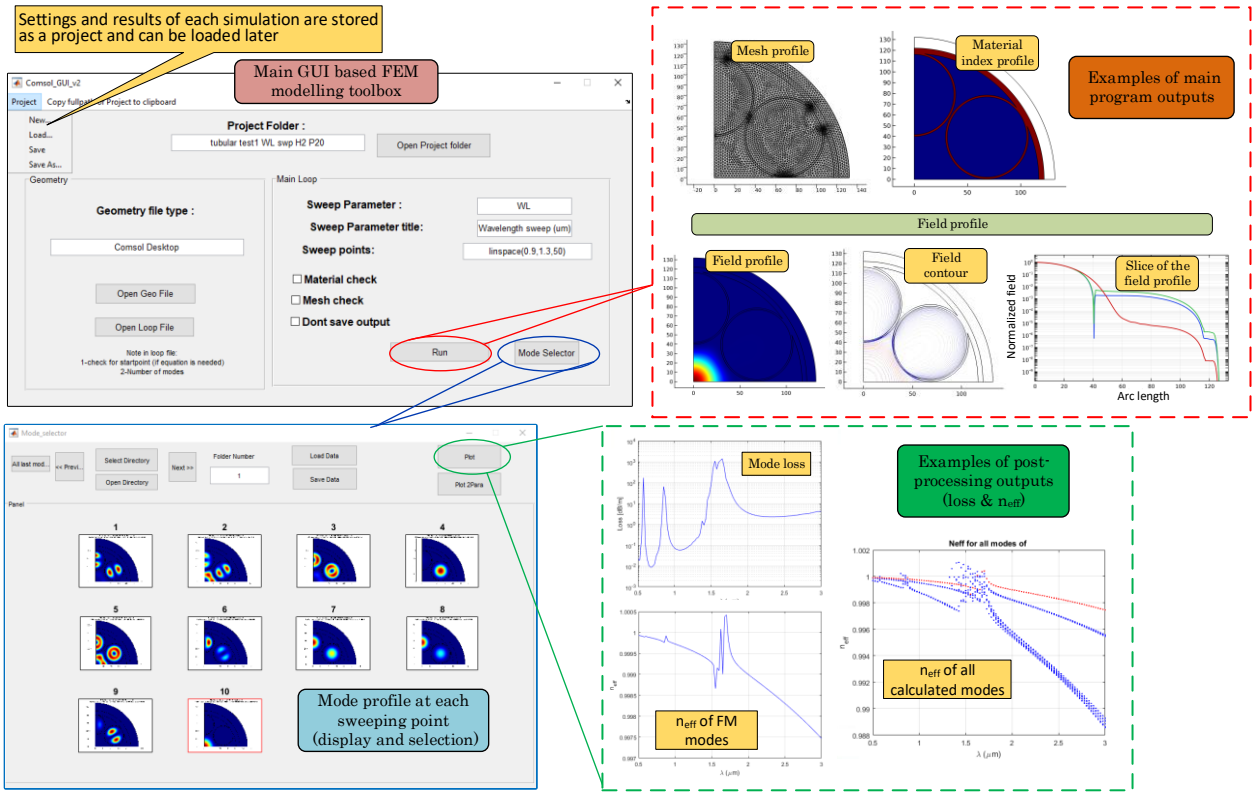

Figure 3.4. The GUI of FEM modelling toolbox and the GUI of its mode selecting utility. The FEM modelling toolbox provide a verity of implementation and presentation of mode profile, mesh profile and structure manipulation (few examples are presented). The mode selecting utility not only display and allow the user to select a specific mode, it can also present the loss and effective index profile of selected mode vs sweeping parameter, which can be wavelength or any design parameter.

3.3 Nonlinear modelling toolbox

As mentioned in Chapter 2, the solution of the GNLSE (Eq. (2.13)) represents the dynamic of mode evolution in time and throughout the waveguide. However, there is not an analytical or even semi-analytical method that can provide the solution in a general form. Therefore, numerical solutions are the only possible way to approximate the real solution similar to the Eigen equation problem (Eq. (3.2)). In principle, Eq. (2.13) is a partial differential equation with two dimensions (time and z direction), which can be simplified into a first order ordinary differential equation (ODE) in the space dimension. This ODE can be solved by numerical methods as an initial value problem (IVP) if the backward coupling is negligible (this is the case for most of single pass setups). To solve the GNLSE, apart from few numerical methods that are only suitable for a special form of the NLSE (e.g. no Raman, soliton) such as: Inverse

scattering method [125], there are few general purpose and accurate numerical methods that can be used to solve the GNLSE such as:

- **Direct Finite Difference Method (FDM)**: In this method the time and space domains are discretized and the derivatives in Eq. (2.13) (i.e. $\partial / \partial z$ and $\partial^n / \partial t^n$) are estimated by differential quantities. Depends on the explicit or implicit implementation of this method, the solution of the equation at the grid points can be calculated by numerically solving a large system of nonlinear equations. However, this method needs huge amount of memory to achieve accurate results in the applications considered for in this thesis (e.g. time grid (2^{24}) × space grid (10^5) for a simple example in this study).
- **FEM**: This method is a general numerical solver for nonlinear ordinary equations, which can solve most ODEs as a boundary value problem. Nevertheless, similar to FDM, it suffers from the impractical memory usage in this case and also both FEM and FDM suffer from numerical dispersion which can affect the results in high gain applications [126].
- **Split-Step Fourier Method (SSFM)**: This method is a forward solution method where the GNLSE is divided into two part of linear and nonlinear, and each part is solved separately in a sequential way for each step in space domain. In this method only the time information of the last step in space domain is preserved, therefore, the required memory is significantly reduced.

The SSFM is the most successful method in solving the GNLSE because of its ability to produce accurate results with less memory [1]. Therefore, the SSFM has been chosen as the main method for solving the GNLSE in this work.

3.3.1 Split-Step Fourier Method (SSFM)

The description of the SSFM can be started by rewriting the Eq. (2.13) in the form of a linear operator ($\hat{D}$), which includes dispersion and loss terms, and a nonlinear operator ($\hat{N}$), which includes the nonlinear part of the equation (FWM and Raman response). Therefore, different form of Eq. (2.13) and definition of each operator are given by [1]:

$$\begin{aligned} \frac{\partial A(z,T)}{\partial z} &= (\hat{D}+\hat{N})A(z,T), \\ \hat{D} &= -\frac{\alpha}{2}+\sum_{n=2}^{\infty}\frac{i^{n+1}\beta_n}{n!}\frac{\partial^n}{\partial T^n}, \\ \hat{N} &= i\gamma_0\left(1+\frac{i}{\omega_0}\frac{\partial}{\partial T}\right)\int_{-\infty}^{T} R(t')\left|A(z,T-t')\right|^2 dt'. \end{aligned} \tag{3.7}$$

The new definition of the GNLSE introduces the possibility of solving this equation in frequency and time domain separately. In SSFM, the length of propagation (L) is divided into N sections with arbitrary length of h_j, where the length of sections should not be necessarily equal but $\sum_{i=1}^{N} h_i = L$. In this case, the solution of Eq. (3.7) at length $z_j = \sum_{i=1}^{j} h_i$ can be found by:

$$A(z_j, T) = e^{\left[h_j\left(\hat{D}+\hat{N}\right)\right]} A(z_{j-1}, T). \tag{3.8}$$

It is more convenient to treat linear and nonlinear operators separately in the frequency and time domain, respectively. Therefore, in a specific method of SSFM, which is called the *symmetric* SSFM, the section h_j is divided into half and the following steps are implemented sequentially for each section through the entire length of propagation.

1. The dispersion effect over the first half ($h_j / 2$) is computed by:

$$A(z_j - h_j / 2, T) = \mathbb{F}^{-1}\left\{ e^{\left[h_j \tilde{D}(\omega)/2\right]} \mathbb{F}\left\{ A(z_{j-1}, T) \right\} \right\}. \tag{3.9}$$

where $\mathbb{F}\{\ \}$ and $\mathbb{F}^{-1}\{\ \}$ are the Fourier transform operator and inverse Fourier transform operators. $\tilde{D}(\omega)$ is the frequency domain of $\hat{D}$, given by:

$$\tilde{D}(\omega) = \mathbb{F}\left\{ -\frac{\alpha}{2} + \sum_{n=2}^{\infty} \frac{i^{n+1}\beta_n}{n!} \frac{\partial^n}{\partial T^n} \right\} = -\frac{\alpha(\omega)}{2} + i\sum_{n=2}^{\infty} \frac{\beta_n}{n!} (\omega - \omega_0)^n \tag{3.10}$$

where $\alpha(\omega)$ donates the loss profile in frequency domain. Recalling from Eq. (2.13), ω_0 and β_n are the reference frequency and the n^{th} derivative of the mode propagation constant, respectively. The requirement of higher order dispersion in this form of definition for dispersion limits its usage and accuracy, which is discussed in more detail in Chapter 6.

2. The nonlinear effect across the section h_j then is computed by numerically solving the differential equation and its initial conditions given by:

$$\begin{aligned} \frac{\partial A'(z,T)}{\partial z} &= \hat{N} A'(z,T), \\ A'(0,T) &= A(z_j - h_j / 2, T). \end{aligned} \tag{3.11}$$

In this thesis, 4th order Runge–Kutta method [127] is used with norm of the maximum estimated error between 5th order and 4th order method for the error

check and adaptive step size if the error is exceeded [128]. In order to calculate the time domain convolution in the nonlinear operator, a FFT circular convolution is used, which interprets the time convolution into a simple multiplication in frequency domain and returns the results in time domain by an inverse FFT. This method is the most efficient way for calculating the convolution, using the large speed advantage of FFT method, which is otherwise impossible to implement in direct convolution due to large set of data. However, it comes at the cost of generating artefacts in the case of aliasing, which will be discussed more and addressed in Chapter 6.

3. In the last step, the dispersion effect over the remaining half of the section (h_j) is computed similar to the first step, using the result from the second step.
4. Steps 1 to 3 are repeated throughout the fibre for each step in space and each calculation needs only the results from the previous step, which is a large memory saving.

Great care should be taken in selecting spectral/temporal grid size and resolution for preventing the aliasing effect and circulating convolution effect by FFT. For instance, the FFT method restricts the number of grid points into $n_t = 2^m$ in order to have efficient performance, which in the case of this study, due to large frequency shift and a very narrow Raman linewidth, a very large number of points ($n_t = 2^{24}$) are needed. In addition, the iterative nature of the SSFM needs carefully chosen step sizes for longitudinal sections (h_j) which is implemented by an adaptive step size method to keep the local error under a tolerance value. Taking to account all these considerations, a software toolbox has been developed in this work that implements the SSFM on the GNLSE with error control and an adaptive step method for efficient calculation. To validate the developed numerical modelling code, the simulation results, generated by developed toolkit, have been compared with reported ones in the literatures. For instance, the propagation of a femtosecond pulse in a microstructured fibre, as presented in figure 3 of [86], for the same parameters is modelled by the developed toolkit. This simulation result of a single femtosecond pulse accompanied by random noise are in a very good agreement with the presented results in [86], as shown in **Figure 3.5**.

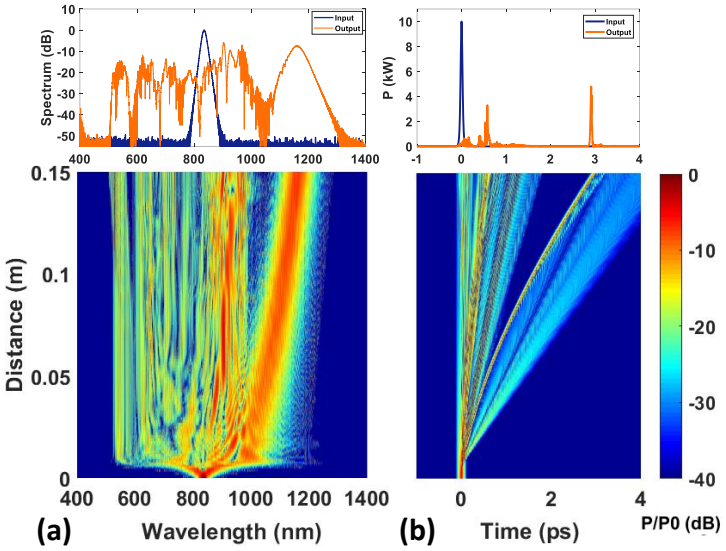

Figure 3.5. Simulation result by developed modelling toolbox for the similar parameters in figure 3 of [86]. The input sech² pulse at 835 nm has 10 kW peak power and 50 fs FWHM and the fibre has the parameters similar to table 1 in [86]. **(a)** frequency domain, **(b)** time domain.

3.3.2 GUI based nonlinear modelling toolbox

Although the SSFM process, described in previous section, seems straight forward, it requires data sets calculated in fibre modelling, initiating input plus and many parameters to describe the modelling environments such as grid size, initial step size, number of steps, fibre length and etc. It also involves many pre and post data processing to achieve reliable and accurate results. Therefore, as a part of this thesis, a GUI based toolbox has developed that not only provides a great control over a vast variety of input parameters such as: input pulse parameters, fibre parameters (e.g. dispersion, loss profile and Raman characteristic of the fibre), it also provide some utilities for pre-processing of data such as: fibre loss manipulation, dispersion and Raman response calculation and presentation, and etc. This GUI based program has also many options to represent the output in 2D and/or 3D format and also provides some post-processing utilities such as: output manipulation utility, spectrogram calculation and presentation. This toolbox not only implements SSFM very efficiently but also implements the anti-aliasing and anti-circular methods which are discussed in Chapter 6. **Figure 3.6** shows the GUI of the nonlinear modelling toolbox and its output alongside some of its utilities for data pre and post processing such as pulse and dispersion profile presentation, Raman response of the fibre and the GUI of spectrogram calculator utility. In addition to its standalone operation, this toolbox can be connected to the

developed FEM mode solver toolbox and provides an integrated modelling environment from fibre design to nonlinear pulse propagation modelling.

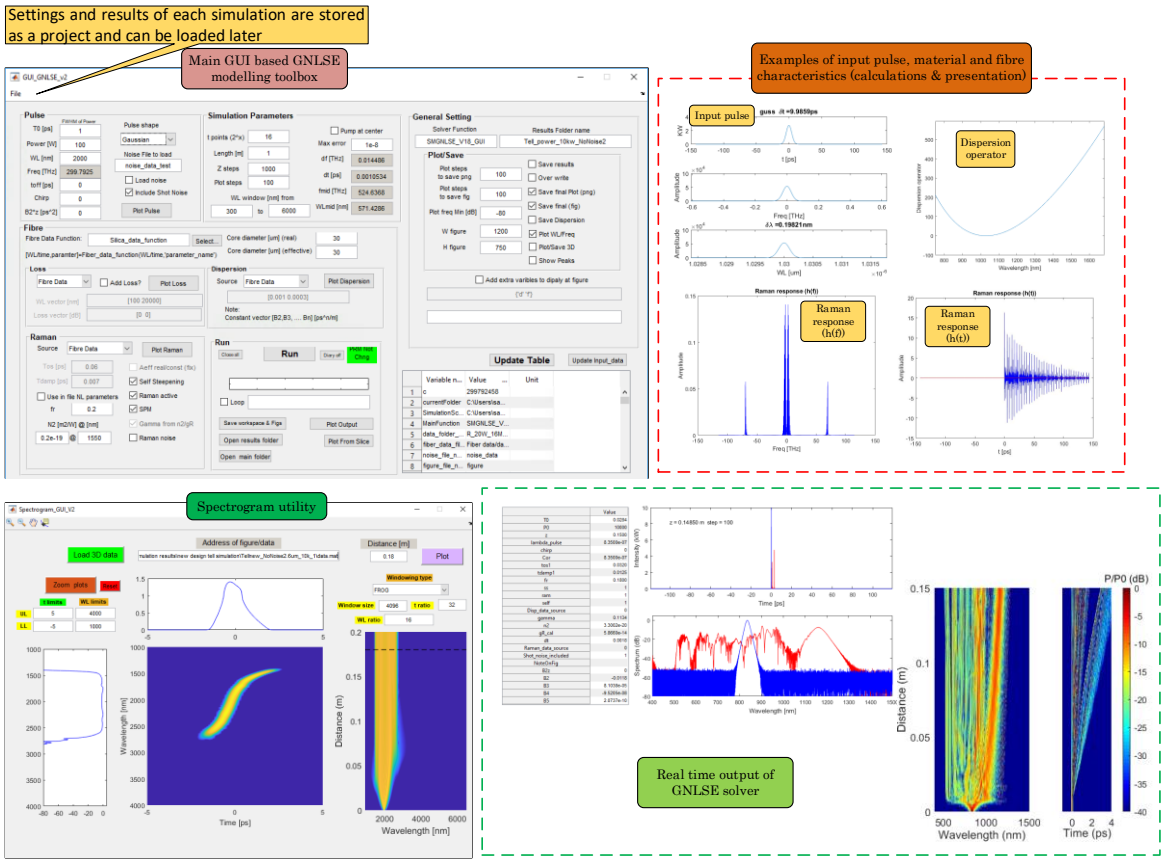

Figure 3.6. The GUI of nonlinear modelling toolbox (the GNLSE solver) and the GUI of Spectrogram utility. The GUI for nonlinear modelling toolbox provide a user friendly environment with broad range of control over a variety of modelling parameters. It also provides utilities to calculate and plot key parameters of modelling such as Raman response, dispersion operator and input pulse. It is also possible to include the simulation results from FEM solver toolbox automatically. The real time output of the solver provides a visual presentation of pulse evolution throughout the fibre and also presented in 3D format. The Spectrogram utility provides the short-time Fourier transform of the pulse at any point of propagation with variety of windowing options such as Frequency-resolved optical gating (FROG), Input gating, Hann, Hamming, Gaussian and etc.

3.4 Conclusion

In this chapter, an overview of the modelling tools and numerical methods used in this thesis has been discussed. The appropriate numerical methods have been implemented in a toolbox format. This facilitates the study of fibre design and nonlinear propagation dynamic modelling, which allows to perform a systematic study of gas-field HC fibres.

To design and model HC-fibres, after evaluating different numerical modelling methods, the FEM has been selected as the most effective numerical method. A commercial FEM mode solver (COMSOL Multiphysics®) has been used for calculating the mode profile, loss and dispersion of a fibre, which are essential parameters in nonlinear pulse propagation. In order to calculate the total loss of a fibre, a cylindrical PML has been implemented to include the confinement loss (CL) in the model. In addition a modified version of the PML and refractive index conformal mapping includes the fibre bend in the model, which allows bend loss calculations to be performed in 2D plane rather than modelling a full 3D structure. As the loss calculation in HC fibres is a very sensitive process, after performing many simulations, optimal ranges of mesh parameters and shape functions are determined to achieve a fast converging simulation.

To model the nonlinear dynamics of pulse propagation in HC fibres, a symmetric SSFM is chosen as the numerical method to solve the GNLSE. In this method, the linear and nonlinear operators are treated in frequency and time, respectively, to prevent time derivatives and to increase the computational speed by implementing the time convolution with an FFT method. To achieve reliable results, different approaches were implemented to eliminate the artefact effect and to improve the efficiency of the SSFM, which are discussed in the following chapters. In the end, all those numerical methods have been integrated in a user-friendly toolbox with a graphical user interface (GUI) for convenience.

Chapter 4: Hollow core fibres for nonlinear process in gases (selection and design)

4.1 Introduction

As it was shown in the previous chapters, to achieve practical levels of nonlinear optical conversion efficiency in gases, it is essential to increase the length of interaction between the gas molecules and light at high intensity. Although gas-filled capillaries can be seen as a simple choice to achieve reasonable nonlinear efficiency with moderate laser power, the laser intensity should be increased by reducing the effective mode area (i.e. decreasing the core size), which dramatically increases the attenuation of light in a simple capillary and demolishes the nonlinear process. In contrast, more sophisticated HC structures such as HC-PBGFs and HC-ARFs can provide fairly low loss with relatively small mode area, which provides a constant intensity profile of light over fairly long lengths (10-100s m). Although HC-PBGFs provide the lowest practical loss among other types of HC fibres, they mostly have a single narrow low loss transmission band in comparison to HC-ARFs. This significantly reduces their usefulness in the nonlinear applications involving broadband or large frequency shifts that require very wide profiles (or at least multiple low loss bands).

Most importantly, although the HC fibres can provide a consistent high intensity laser for a very long length to interact with gases, the gases still need higher power pulses due to their very low density, which manifests itself in a very low Raman gain, even at high pressures. Therefore, to achieve a reasonable level of nonlinear efficiency in gases, high power pulses are required, which increases the practical damage threshold that fibres should tolerate for gas-filled nonlinear applications. It has been shown through modelling and experiments that the fraction of power leaked from core to the surrounding glass for HC-PBGF is substantially higher than HC-ARF (an order of magnitude) [5], which is the result of differences in their guidance mechanism. On the other hand, HC-ARFs not only can provide the right transmission windows in terms of bandwidth but also they can tolerate higher intensity of light, which is essential in the mid-IR regime where the Raman gain is very low in gases. In addition, less power in the glass is crucial where the material loss of the glass plays a significant role at operating wavelengths like silica with a huge material loss in the mid-IR (>3 μm).

All of the aforementioned factors suggest that HC-ARFs are the best available options for the pursuit of mid-IR nonlinear process in the gases. However, in general, their larger loss in comparison to HC-PBGFs is the main drawback in practical applications and needs to be addressed. Therefore, in this chapter, I mainly focused on HC-ARFs and the means to improve their low loss performance in the mid-IR range. This chapter is divided into two main parts. In section 4.2, a simple tubular HC fibre is studied, which can fulfil the broadband transmission window and the higher power threshold criteria required for nonlinear applications in gases at the same time. Heading towards lower loss, this thesis is more focused on a recently proposed design called nested anti-resonant nodeless fibre (NANF) [57] with promising low loss features which opens up more possibilities in the nonlinear applications. In section 4.3, a summary of HC fibres is provided along with their advantages and disadvantages for the nonlinear applications.

As the second part of this chapter, in section 4.4, the NANF design is selected as the most promising candidate for nonlinearity in gas-filled fibres. After analysing the effect of each design parameter on its structural topology, the optimum value for each parameter has been calculated to achieve the lowest possible loss towards the mid-IR, considering silica and tellurite as the glass material for this type of fibre.

4.2 Anti-resonant hollow core fibres

4.2.1 Tubular fibre

Following the method of reducing the effect of connecting nodes and overlap modes on loss by introducing the negative curvature core walls in other ARFs such as Kagomé fibres (see Chapter 2), extensive studies have been done on the effect of nodes in a simple contacting tubular structure [70, 129]. This led to the introduction of a non-contacting design, to eliminate nodes while keeping the anti-resonance effect due to the glass webs [71, 130]. The new tubular structure consists of a few tubes that are attached inside the wall of a larger capillary in such a way that they do not touch each other, as shown in **Figure 4.1.** As was expected, due to the elimination of nodes, this structure shows a wide transmission window and a lower loss compared to similar type of fibres with contacting tubes [130]. The main advantages of such design are in its simplicity and the ability to control the parameters of each tube independently. Low CL in this type of fibres is not the only feature that makes them a desirable candidate for the nonlinear processes in gases. The fact that the core field overlaps much less with the

cladding material than in other types of fibres, can reduce the absorption loss from the cladding material at longer wavelengths (i.e. mid-IR range).

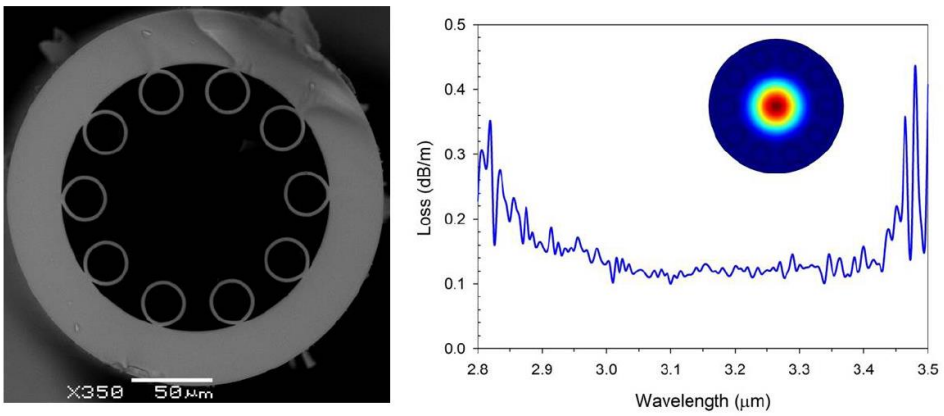

Figure 4.1. On the left hand side, SEM of the anti-resonant tubular fibre and on the right hand side, its measured spectral attenuation. The inset shows the power distribution profile at 3.1 µm in the fibre [after [130]].

Despite eliminating the nodes in tubular fibres, as the core size is reduced, the loss of the fibre increases dramatically. In general, the CL in HC-ARFs follows scaling rules inherited from capillary fibres. In fact, similar to the relation between loss and core radius in Eq. (2.2), it can be shown that, in general form, the trend of loss at the anti-resonant wavelengths for m nested tubes that are placed inside a capillary jacket, hereinafter called tube-jacket fibre, is proportional to $R^{-(2m+3)}$. According to this scaling feature of HC-ARFs, despite the significant improvement in the performance of proposed tubular fibre at [130], it shows loss dependency of $R^{-4.5}$, which is lower than single tube-jacket fibre. **Figure 4.2 (a)** represents the superposition of imaginary rings and the capillary jacket of tube-jacket fibre with red lines on top of the tubular configuration to present the similarity of both type of fibres. This representation of tubular fibre with an 1D anti-resonant Bragg structure (i.e. tube-jacket fibre) is a simple approximation and more in-depth studies have been done by different groups to identify the origin of the guidance and loss mechanism in this type of fibres [55, 131]. Yet, this simple approximation can help to grasp a simple yet powerful qualitative understanding over the loss trend in this type of fibres. To demonstrate the similarity of tube-jacket and tubular fibres, the CL of a tubular fibre with a tube thickness of 0.83 µm for different core radii is modelled at 1.1 µm (fundamental anti-resonance wavelength) alongside the CL of single, double and triple tube-jacket fibres (i.e. m=1, 2 ,3), as shown in **Figure 4.2**. This dependency of CL in ARFs on the number of rings and the high degree of similarity between tubular HC fibres and tube-jacket fibre, inspired

the design team in ORC to introduce a new type of fibre that is an improved version of tubular fibre with less CL for the same core size as described in the following section.

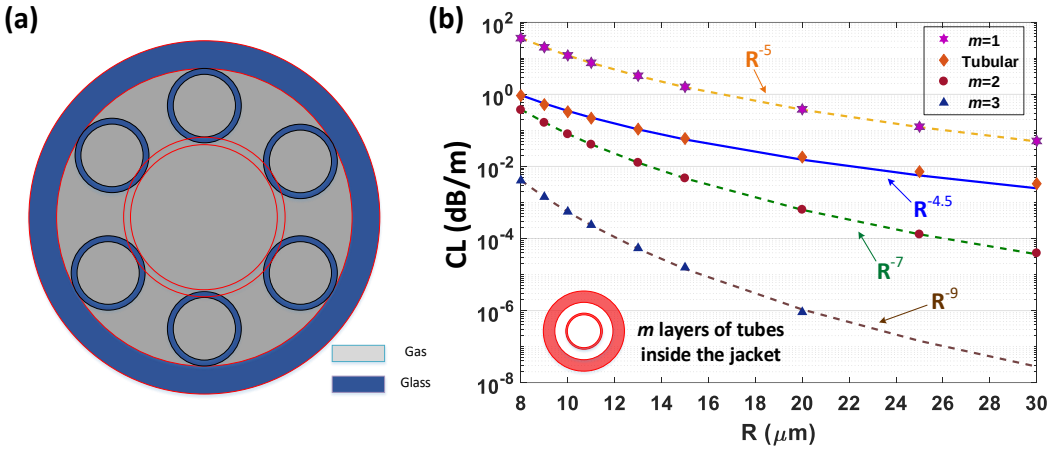

Figure 4.2. (a) demonstration of virtual ring and jacket (red lines) concept on top of tubular fibre**. (b)** the CL of the single, double and triple tube-jacket fibres as well as the tubular HC fibre with tube thickness of 0.83 µm vs core radius at their fundamental anti-resonance wavelength (1.1 µm). Although tubular fibre has lower loss than single tube-jacket fibre, its scaling order with core radius is lower.

4.2.2 Nested Anti-resonant Nodeless fibre (NANF)

Pursuing the idea of an additional ring in the simple anti-resonance model, a revolutionary Nested Anti-resonant Nodeless Fibre (NANF) was introduced by *Francesco Poletti*, as shown in **Figure 4.3**. The proposed structure not only benefits from the nodeless structure of the tubular fibre, it also has much lower CL due to the second tube inside the cladding tubes.

In this configuration, the wall of the larger cladding-tubes (i.e. nested tubes) collectively act as a single ring in the middle of the capillary and their thickness dictates the resonance and anti-resonance wavelengths of the structure. The smaller inner tubes mimic the second added tube around the first one in the tube-jacket fibre. Finally the jacket tube is the final piece of the anti-resonant structure as shown in **Figure 4.3 (a).** As it was shown, every extra tube in the tube-jacket fibre increases the loss scaling order by two ($R^{-(2m+3)}$), which improves the CL even in smaller cores. However, the NANF provides much better loss performance than the double tube-jacket fibre and has a much higher loss scaling order with core size (R^{-8}) [57]. Although, in general, many different studies have been done to identify the origin of the very low loss in "negative

curvature" category of fibres [54, 63] and more specifically on tubular fibres [113, 131], a full understanding of this ultra-low loss mechanism is yet to be achieved[1].

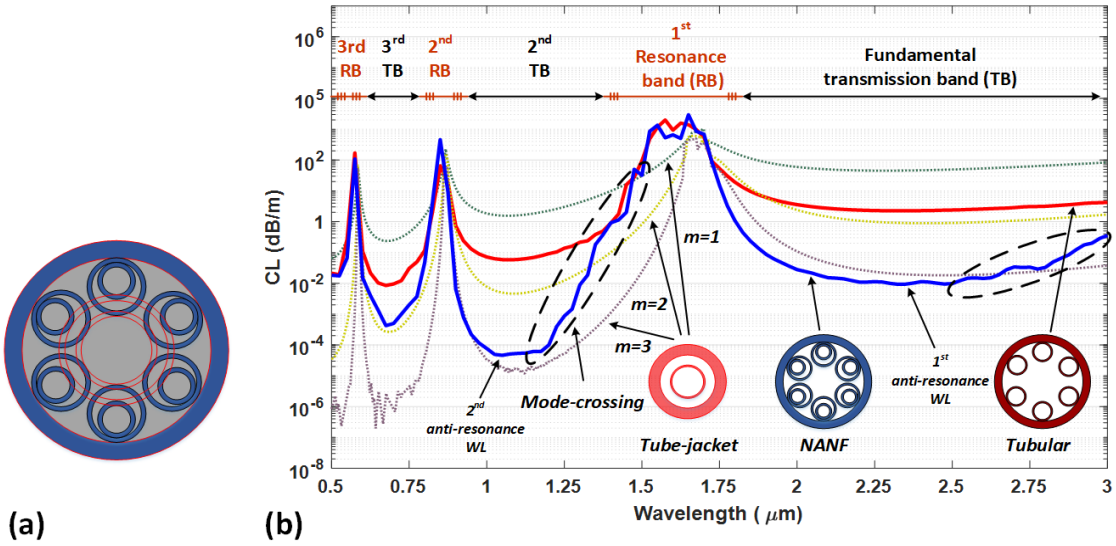

Figure 4.3. (a) the NANF structure with virtual tube-jacket structure (red lines) concept on top of it. Added inner tubes act as second tube in tube-jacket structure and reduce the CL. **(b)** the loss profile of a NANF, tubular fibre, single, double and triple tube-jacket (i.e. m=1, 2, 3) silica fibres with the same core size (R = 15 μm) and tube thickness (0.83 μm). The fundamental, 2nd and 3rd transmission bands, where loss is low, are marked alongside the resonance band with high loss. The loss is high and the loss profile is less smooth at "mode-crossing" reigns for NANF and tubular fibres due to closeness of effective index of cladding and core modes. The NANF has the lowest loss at its fundamental transmission band, even lower than tube-jacket fibre.

Figure 4.3 (b) shows the loss profile for a NANF, tubular fibre, single, double and triple tube-jacket silica fibres with the same core size (R = 15 μm) and tube thickness (0.83 μm). The tube-jacket fibres show larger loss in comparison to the tubular and NANFs but have a smoother profile at the longer wavelength side of each anti-resonance band. This effect can be explained by the core and cladding mode-crossing where the glass-modes of cladding tubes have a very close effective refractive index to the air-modes in the core and cause out-coupling of the core field to the outer jacket and increases the CL at anti-crossing wavelengths [131]. Furthermore, thanks to the

[1]There are many studies and also debates on the origin of loss mechanism in this type of HC fibres from anti-resonance feature of the structure [132-134] to inhibited coupling between core and cladding modes from lattice analysis of the tubes [55, 63]. However, here, without any intention to justify the anti-resonance mechanism, this scheme has been because of its simplicity and intuitive ability for this work.

additional nested element, NANF can be effectively single mode by out-coupling higher order modes (HOMs) to the cladding tubes [57] (explained more in the flowing sections).

The negative curvature and lower amount of glass in contact with core field in NANF can decrease the chance of surface scattering and also material absorption loss, which in this study has even greater priority. In fact, as the region of interest, in this study, is around 4 μm (mid-IR), the major drawback is the high material absorption in this spectral region (e.g. silica has loss of ~1600 dB/m at 4 μm), which makes the design of the fibre incredibly challenging. In principle, the loss in NANF can reach significantly lower values than presented ones in other HC-ARFs [57]. In fact, this is the first proposed HC fibre rather than HC-PBG fibres that in theory can reach a loss value below existing solid core fibres [57].

4.3 Comparison summary of HC fibres for nonlinearity in the gases

The most important characteristics of any HC fibre for Raman nonlinear applications are the loss and the core size of the fibre, which as above-mentioned, have strong dependency for HC-ARFs. In other words, on one hand one needs the smallest core possible for efficient nonlinear process, but on the other hand reduction in core size introduces large CL in ARFs.

In most cases, CL has been considered as the most dominant loss in HC fibres due to the lack of total internal reflection in their configuration. However, this argument cannot be valid anymore in high absorbing wavelengths of cladding glass, which in the case of silica are wavelengths above 3 μm (i.e. mid-IR). As a result, in order to reach proper and low loss waveguide structure for the nonlinear process towards the mid-IR regime, looking towards proper design/structure that can reduce the overlap of the field with glass alongside a reasonable CL is crucial.

Furthermore, in order to increase the Raman conversion efficiency a higher intensity is required, which can be achieved by decreasing the core size of the fibre. The trade-off between core size and CL may not be a big problem for normal power delivery or data transmission use of tubular fibres, but can be problematic in HC-ARFs. Therefore, the best design is the one with the lowest loss for the smallest possible core size.

Table 4.1: Advantage and disadvantage of different type of fibres for this project

Fibre type	Guiding mechanism	Advantages/Disadvantages	Possibility for this project/drawback
Photonic band gap fibres			
HC-PBG 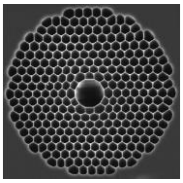	**Photonic bandgap:** fibre core has been placed as defect in the two-dimensional photonic crystal (PC) and introduces small guiding window in the bandgap of PC	**Advantages:** ● Very low loss (~ 4 dB/km), ● Small core size. **Disadvantages:** ● Very narrow transmission window (~100 ns) (impossible to perform broadband nonlinear process), ● Large overlap between field and clad-glass (high loss due to material loss in material absorbing range of WL) (field fraction ~ 5e-4), ● relativly large dispersion at the edge of bandgap.	Narrow transmission window and high loss at mid-IR
Anti-resonance fibres			
Kagome 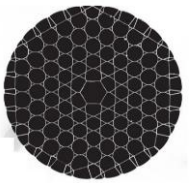	**Anti-resonance:** thin glass web around core area act as anti-resonance mirrors and confine the field in the core area	**Advantages:** ● Low loss (~ 10-1000 dB/km @ visible and near-infrared), ● Small overlap between field and clad-glass (field fraction ~ 5e-5), ● Wide transmission window (~1 µm) (many anti-resonance areas for guiding) (suitable for performing broadband nonlinear process), ● Dependency of operating wavelengths to web thickness instead of core diameter, ● Small core size (~7.5 µm diameter). **Disadvantages:** ● Exciting the glass nodes in the structure increases material loss in material absorbing range of wavelengths, ● Complicated structure for fabrication (specially with glasses other than silica), ● Non-smooth loss profile.	High loss at mid-IR
hexagram 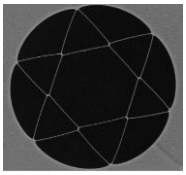		**Advantages:** ● Low loss (~ 10-1000 dB/km at visible and near-infrared) ● Small overlap between field and clad-glass (field fraction ~ 5e-5) ● Simple structure for fabrication and in-house (ORC) fabrication possibility, ● Wide transmission window (~700 nm) (many anti-resonance areas for guiding) ● Dependency of operating wavelengths to web thickness instead of core diameter **Disadvantages:** ● Although the loss has been improved by radially tilted nodes instead of azimuthal oriented nodes, still the existence of glass nodes in the structure introduce material loss in the range of material absorbing wavelengths.	High loss at mid-IR
tubular (nodeless) 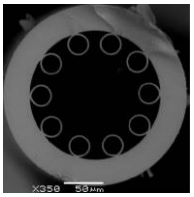		**Advantages:** ● Very low loss (~ 1-1000 dB/km @ visible to mid-infrared), ● Node less structure (reducing CL and material loss specially in mid-IR), ● Very small overlap between field and clad-glass (field fraction ~ 5e-5), ● Simple structure for fabrication and in-home (ORC) fabrication possibility, ● Very wide and smooth transmission window (~ 2 um) (many anti-resonance areas for guiding), ● Dependency of operating wavelengths to web thickness instead of core diameter. **Disadvantages:** ● High CL in small core sizes at mid-IR range due to single layer anti-resonance feature.	High CL at mid-IR for small cores
NANF 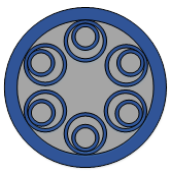		**Advantages:** ● Very low loss (~ 0.1-100 dB/km @ visible to mid-infrared), ● Node less structure (reducing CL and material loss specially in mid-IR), ● Very small overlap between field and clad-glass (field fraction ~ 3e-5), ● Very wide and smooth transmission window (~ 2 um) (many anti-resonance areas for guiding), ● Dependency of operating wavelengths to web thickness instead of core diameter. **Disadvantages:** ● Precise fabrication required (which is possible with existing fabrication facility).	Moderate Total loss at mid-IR

A summary of the main HC fibre categories are shown in **Table 4.1** alongside their advantages and disadvantages as have been mentioned in previous the sections. Among different type of HC fibres, the NANF is highlighted as the potential option for this work due to its advantages such as:

- Very low loss (~ 0.1-100 dB/km at visible to mid-infrared),
- Node less structure (reducing CL and material loss especially in the mid-IR),
- Very small overlap between the field and cladding-glass (field fraction < 10^{-5}),
- Very wide and smooth fundamental transmission window (width > 2 μm) and many anti-resonance bands that can be designed to cover a wide range of spectrum (0.2 μm to 10 μm),
- Dependency of operating wavelength to web thickness instead of core diameter.

4.4 Optimizing NANF design for mid-IR Raman conversion

As was mentioned before, the goal of this project is to generate mid-IR pulses ideally by using a near-IR fibre pump laser in order to achieve a fully fiberized mid-IR source. As will be discussed later in Chapter 6, the aim is to use an erbium-doped laser pump pulse at 1.55 μm (near-IR), which through the vibrational Raman process of hydrogen can be down-converted to the 1st Stokes at 4.35 μm (mid-IR). In principle, to achieve an efficient and practical conversion, it is necessary to have a reasonably low loss fibre at both the pump and Stokes wavelengths. For example, for a hydrogen-filled HC fibre with negligible loss at pump wavelength (1.55 μm) and core radius of 20 μm, the loss of the fibre at the Stokes wavelength should be less than 150 dB/m to achieve just above zero Raman gain with 10 kW input pump and with almost zero efficiency because of high loss (From Eq. (6.1), the unit net gain $Gn = g_R I_P - \alpha_s$ is above zero when the loss α_s is smaller than the production of Raman gain ($g_R = 0.45\,cm/GW$ for H_2) and pump intensity (I_p)). However, this is a marginal case and to achieve a reasonable Raman conversion efficiency, in practice, the loss at Stokes wavelength needs to be significantly lower than such limit. For instance, in the previous example, only if the Stokes experiences less than 25 dB/m loss, the pump power (10 kW) passes the Raman threshold (i.e. pump power and Stokes power are equal at the output) and the efficiency become ~50% of quantum conversion efficiency (refer to Chapter 6 for more details). This is worthwhile to mention that these values are calculated for continues wave (CW) laser and to apply the pulsed pump, one needs to take to account the effect of pulse length and Raman transient as well as pump loss where they can reduce the Raman gain substantially in hydrogen. Therefore, in practice, the upper limit for loss at the

Stokes wavelength would be much lower than 25dB/m, as will be discussed in more detail in Chapter 6. Thus, in this section the aim is to find an optimum NANF design to reach the lowest achievable loss at pump and Stokes wavelengths to achieve a high Raman frequency conversion.

Ideally, when it comes to selecting the glass material, silica is the most desirable material because of its favourable optical and mechanical characteristics that make it a suitable option for fabrication. Moreover, most fibre fabrication technologies and equipment have been developed around this material for years. However, silica has a large material absorption in the mid-IR range of this study (~3200 dB/m @ 4.35 μm). Therefore, at first, the design parameters of silica NANF has been optimized to reach the lowest possible loss and then a soft glass (i.e. tellurite) with lower material loss in the mid-IR regime has been used to achieve better results.

In the following sections, the process of designing silica and tellurite NANFs for mid-IR guiding are introduced, but at first, it is important to introduce the main design parameters of a NANF structure. For the sake of simplicity in fabrication, the NANF with a single nested element has been considered throughout this thesis unless otherwise said. The design parameters for such a NANF have been marked on **Figure 4.4**.

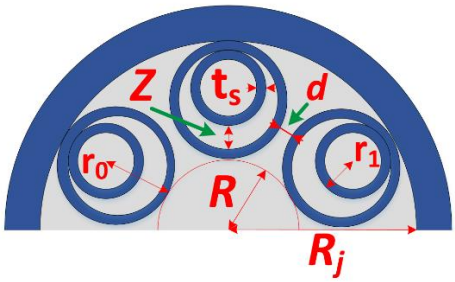

Figure 4.4. Design parameters of a NANF structure with a single nested element (half of the structure).

where t_s is the thickness of the glass web (consistent for all tubes), d is the distance between cladding tubes, R is the radius of the core. r_0 and r_1 are the core radii of nested and inner cladding tubes respectively and Z is the distance between them. Although there are many parameters in the NANF design, the number of independent parameters can be reduced by dependency of parameters due to topology of NANF. Thus, considering R, t_s, Z and d as independent parameters of the NANF design, the r_1 and r_0 can be calculated by the geometrical relation of parameters as:

$$r_0 = \frac{R\sqrt{2(1-\cos(\frac{2\pi}{n}))} - d}{2-\sqrt{2(1-\cos(\frac{2\pi}{n}))}}, \qquad r_1 = r_0 - t_s - \frac{Z}{2}. \tag{4.1}$$

where n is the azimuthal number of cladding tubes in the NANF structure (i.e. n=6 for NANF in **Figure 4.4**). In general, although a NANF can be designed with different azimuthal number of cladding tubes rather than six tubes, it has been shown that six tubes arrangement has the optimum results [57]. In more detail, the major advantage of the tubes in tubular fibres is to hold back the field from the jacket glass walls in order to reduce CL by reducing the field leakage throughout the jacket glass because the refractive index of the glass is higher than air and field tends to propagate though glass rather than air. Increasing the number of tubes for a constant core radius (R) reduces the distance of the core field from the jacket glass (i.e. R_j decreases as the number of tubes increase) which increases the CL. Therefore, the idea of using less tubes seems more appealing. However, for a smaller number of tubes (n < 6), the core size of tubes (r_0) becomes close to R and due to the anti-resonant feature of the tubes the probability of mode-coupling between tube air-modes and core modes dramatically increases. As a result, the loss of the fibre becomes more sensitive to fabrication tolerances, bend loss and other perturbations. According to these limitations, a six-tube configuration for the NANF design has been selected in this study. In this thesis the phrase "mid-IR NANF" might be used instead of "NANF" to emphasize the optimized loss of the fibre to operate in mid-IR range of this project.

4.4.1 Silica NANF

In this section, the main steps of designing a NANF from silica glass are explained. As a starting point, in order to realistically model the NANF, it is needed to include the material loss in the developed numerical modelling toolbox for a wide range of wavelengths since the desired Raman conversion process covers a broad range from 0.94 to 4.35 μm, if only one considers the 1st anti-Stokes, pump and Stokes wavelengths. Therefore, to cover such a broad range of spectrum in this study, the material loss for silica is obtained by combining two mostly used data sources in the literature. For the wavelengths between 0.4 and 2.4 μm, the loss of dry F300 fused silica in [135] is used, which is close to common silica glass used in fibre fabrication. For longer wavelengths, ranging between 2.4 and 15 μm, the data presented in [136] is used. The combination of both data sets is presented in **Figure 4.5**. The silica loss noticeably increases at

wavelengths above 2 μm, while this increase can be noticeable for solid core fibres, it is trivial for HC fibres due to the very small fraction of power in the glass in these fibres as well as the domination of CL in this range of wavelengths. However, the increase in the loss at wavelengths above 3 μm, especially the abrupt surge of the loss (inset of **Figure 4.5**) from 1500 dB/m at 4.2 μm to more than double (~3200 dB/m) at 4.35 μm (the Stokes wavelength) within a few nm wavelength changes, significantly impacts the loss in HC fibre and becomes dominant source of the loss in these fibres.

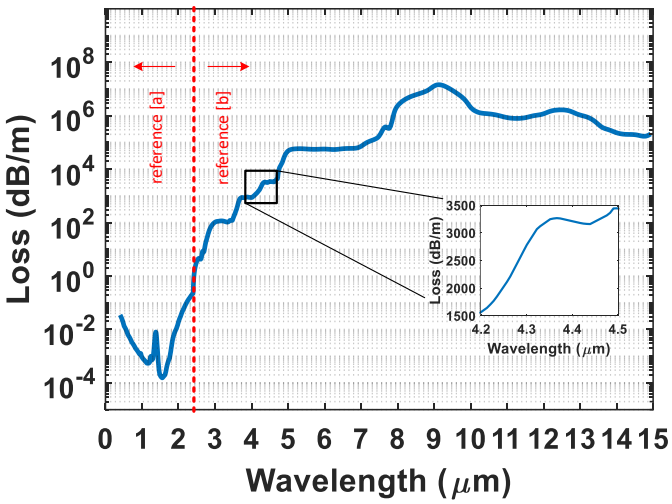

Figure 4.5. The material loss of silica obtained from [a][135] for wavelengths between 0.4 and 2.4 μm, while for wavelengths between 2.4 and 15 μm, it is obtained from [b][136].

In addition to material loss, the CL of ARFs strongly depends on the differences between core and glass refractive index due to the anti-resonance guidance mechanism. Therefore, to correctly model the loss and dispersion property of NANF, the dispersion profile of silica is modelled with a three resonance Sellmeier equation [1]:

$$n^2 = 1 + \sum_{i=1}^{3} \frac{B_i \lambda^2}{(\lambda^2 - C_i)} \tag{4.2}$$

where $B_1 = 0.6961663$; $B_2 = 0.4079426$; $B_3 = 0.8974794$; $C_1 = 0.0684043 \times 10^{-6}\ \mu m^2$; $C_2 = 0.1162414 \times 10^{-6}\ \mu m^2$; $C_3 = 9.896161 \times 10^{-6}\ \mu m^2$; while wavelength ($\lambda$) is in μm unit.

Unlike material loss, which depends on the glass material and is fairly constant for each wavelength, the CL depends on the structure of NANF and can be controlled and optimized to some extent for low loss by choosing proper design parameters. For NANF design, shown in **Figure 4.4**, the fibre design process relies on optimizing each of the four main structural tube parameters (t_s, d, Z, R) to achieve the lowest loss. Therefore,

in the following sections, each of these parameters is optimized to achieve low loss operation at 1st Raman Stokes wavelength (4.35 μm) and pump wavelength (1.55 μm).

4.4.1.1 t_s optimization

The thickness of the tubes is a key parameter for a NANF, because it determines the transmission bands and the low loss operating wavelength of the fibre through its anti-resonance feature. In an ideal Bragg anti-resonant tube-jacket fibre to have the lowest loss at specific wavelength (i.e. anti-resonance wavelength), the t_s can be determined analytically by Eq. (2.1) and the similarity between NANF and tube-jacket fibre allows us to approximate optimum t_s with the same equation. However, in order to obtain a precise results, it is important to calculate the optimum t_s by numerically solving the exact Eigen mode equation for the NANF structure due to differences between the perfect ring shape structure in the tube-jacket fibre and the nested tubular structure in the NANF. Here, the emphasis is on achieving the lowest possible loss in a silica NANF at 1.55 μm and 4.35 μm as the pump and first Raman Stokes wavelengths, respectively.

The most common practice to optimization a function with a limited number of free-parameters is to perform a parameter sweep within the free-parameter space (here are t_s, d, Z, R). However, the FEM simulation of a NANF structure for each set of parameters is a time consuming process[1] and a full parameter sweep in the entire free-parameter space (it is a 4D space) can be very time consuming. Thanks to effectiveness of each parameter on a specific characteristic of the loss profile, despite the mutual effect of design parameters on the fibre loss, the loss can be optimized for each individual parameter separately with very small deviation from the absolute minimum loss [57].

Therefore, in order to run a parameter sweep simulation on t_s by the developed FEM toolbox, some assumption on the other design parameters have been considered such as R = 20 μm (optimum value of R is discussed in Chapter 6), $Z = 0.65R$ (Eq. (4.3)) [57], d = 4 μm (based on further simulations which are consistent with [57, 66]). Using Eq. (2.1) and considering a fundamental anti-resonance wavelength around 4.35 μm, t_s is calculated to be ~1.6 μm as the initial value for the sweeping process over this

[1] For example, it takes 15 minutes for loss calculation at 1.55 μm for a NANF with R= 30 μm on machine with 16 core 3.4 GHz CPUs and 128 GB RAM

parameter. **Figure 4.6** shows the simulated loss profile of the NANF vs t_s over a broad range between 1 µm and 3 µm at 1.55 µm and 4.35 µm wavelengths (i.e. pump and 1st vibrational Raman Stokes wavelengths in hydrogen), respectively.

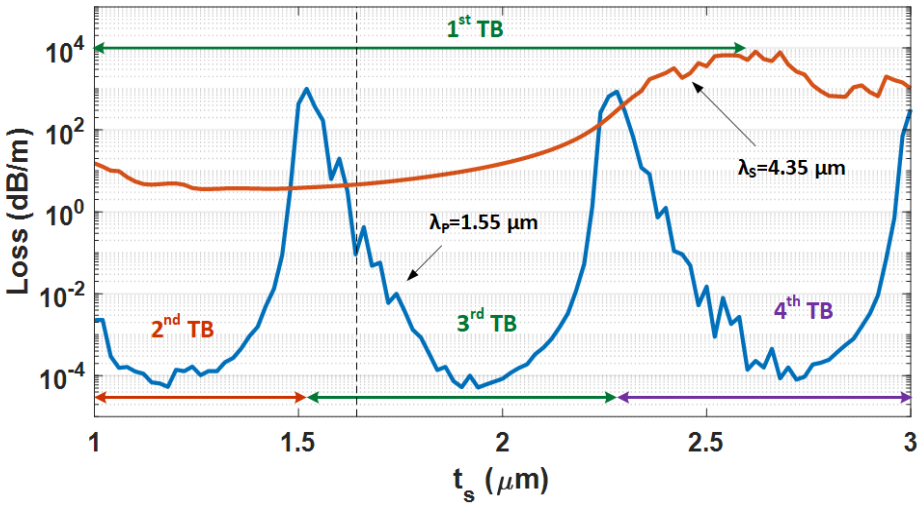

Figure 4.6. The FEM simulated loss of a silica NANF with R = 20 µm vs the thickness of tubes (t_s) at λ = 1.55 µm and 4.35 µm for d = 4 µm and $Z = 0.65R$. The $t_s \approx 1.66$ µm shows an optimum value for RCL as marked by dashed lines in the figure.

The different pattern of changes in loss profile for the two wavelengths shows the fact that wavelengths are in different transmission band of the fibre as expected from Eq. (2.1). In fact, while the Stokes is placed in the fundamental transmission band (1st TB) of the fibre for t_s < 2.5 µm, the pump wavelength is shifted from the 2nd TB to 4th TB of the fibre depending on the t_s value as can be seen in **Figure 4.6**. In the best scenario, achieving an optimum value of t_s, where the losses for both pump and 1st Stokes wavelength arWSOFe at their minimum value, is the desired goal. However, as a result of the difference between optimum values of t_s for each wavelength, it is necessary to choose a proper value for t_s that can provide a practical loss for both wavelengths. In fact, in the vicinity of the minimum loss at the Stokes wavelength ($t_s \approx$1.5 µm), the trend of the loss at both wavelengths are in opposite directions (i.e. the loss at Stokes wavelength inclines while the loss declines at pump wavelength) and achieving a minimum loss at both wavelengths is not simultaneously possible.

Therefore, to select the best option for t_s, I have defined a Raman conversion loss (RCL) for the fibre as $RCL = \sqrt{\alpha_P} + \sqrt{\alpha_S}$. In this definition, the effect of both losses at pump (α_P) and 1st Stokes (α_S) wavelengths are included for optimization, similar to the optimum loss in solid core Raman lasers [137]. Thus, considering the presented

simulation results, the fibre with $t_s \approx 1.66$ µm can provide the lowest RCL, as shown in **Figure 4.6**. Although in practice, the inaccuracy in fabrication process may alter the value of t_s, thanks to opposite trend of losses at pump and Stokes wavelengths, to some extent, the change in RCL is compensated.

Although the calculated optimum t_s from **Figure 4.6** is for a particular silica NANF with $R = 20$ µm, it can be shown that for $R > 15$ µm the optimum t_s is approximately similar. **Figure 4.7** shows the loss profile of silica mid-IR NANF for a few core radii at 1.55 µm and 4.35 µm. Except in very small core size of $R = 12$ µm, the optimum t_s is similar for other fibres, which can relax the optimization process for other parameters.

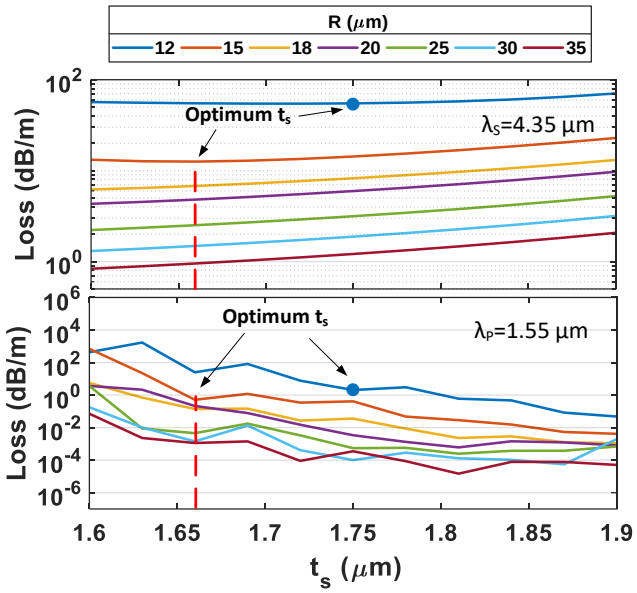

Figure 4.7. The calculated loss profile for silica mid-IR NANF similar to **Figure 4.6** for $R = 12, 15, 18, 20, 25, 30, 35$ µm. The optimum t_s for low RCL is marked on the figure.

4.4.1.2 *d* optimization

The azimuthal distance between cladding tubes (d), as shown in **Figure 4.4**, is another design parameter of a NANF structure, which is studied in this part. The effect of the d parameter has been investigated in several works and shown that the optimum value of d is unique for individual design parameters and configurations [57, 130]. This parameter controls the air gap between tubes, which allows the mode field to escape to the jacket tube for very large gaps (i.e. large d) or to couple into the lossy glass nodes that are created in the absence of such a gap. Therefore, an optimum value for d parameter is necessary to achieve a low loss operation at desired wavelengths. At two

extreme cases of $d < 0$, which means touching between the tubes and creating lossy nodes, and $d >> 0.5R$, which means the tubes are very far from each other and consequently have very small core sizes, the loss increases significantly and it is clear that neither of these cases are suitable for the d parameter. Therefore, in this study, a parameter sweep has been performed on this parameter for the optimum value of t_s = 1.66 µm over a reasonable range from $d = 0.005R$ to $0.5R$ at the Stokes wavelength (4.35 µm), as shown in **Figure 4.8 (a)**. Despite the different level of losses between the fibres, caused by different core sizes, each fibre has shown a flat loss profile across a large range of d. In order to visualize the minimum loss, the loss profiles have been normalized to the minimum loss of each fibre as shown in **Figure 4.8 (b)** (e.g. normalized loss for fibre with 20 µm radius = (the loss of the fibre with 20 µm)/ (the minimum loss of the 20 µm fibre)). It is clear that the minimum loss takes place at $d/R \sim 0.2$ for the modelled radii. However, as can be seen in the inset of **Figure 4.8 (b)**, the loss has less than 0.1 % change at $d = 4$ µm for all core sizes. As a result, selecting a fix value for d can relax the other parameter optimization processes and does not have a noticeable effect on the loss of the fibre. Consequently, $d = 4$ µm has been used for the rest of this work for the optimization process of silica mid-IR NANF. It is worth mentioning that the optimum value for d also depends on t_s, which has optimized and fixed at this stage of design [57] .

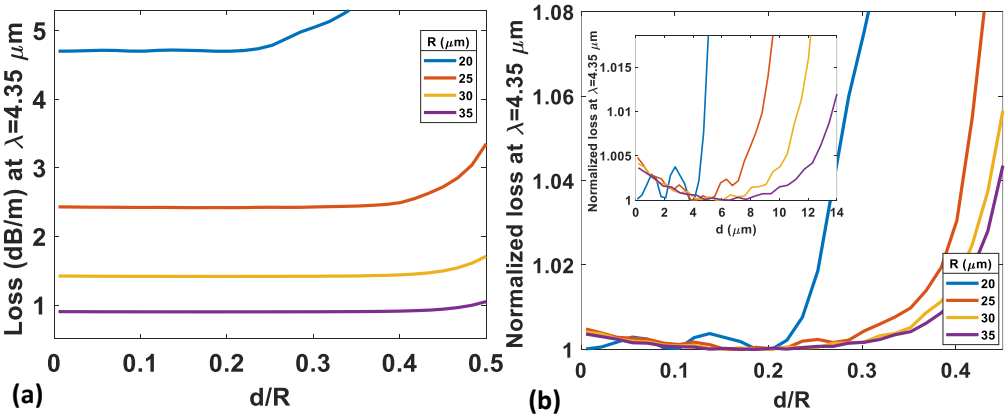

Figure 4.8. (a) the calculated loss of the silica mid-IR NANF (t_s =1.66 µm) vs the tube distance to core size ratio (d/R) at $\lambda = 4.35$ µm. **(b)** the normalized loss over the minimum loss for the same fibre shows the optimum $d/R \approx 0.2$. The inset of **(b)** shows the absolute value of d.

4.4.1.3 Z optimization

The low loss feature of NANF in comparison to a simple tubular fibre is the result of the inner tubes of the nested cladding tubes. Thus, the Z parameter, which dictates the size of these inner tubes, has an important role in the NANF design to achieve low loss performance. Recalling from the anti-resonance feature of a NANF, it is intuitive to consider the confinement mechanism of the fibre as the reflecting feature of surrounding tubes. In this model, the inner tubes of NANF act as the second reflecting layer similar to the second tubes in the tube-jacket fibres (see section 4.2.1 and Chapter 2) and their distance from outer tubes (Z) should follow Bragg's law to provide the maximum reflecting effect [52, 61]. Therefore, using Bragg's law and approximating the n_{eff} of the fundamental mode by the first zero of Bessel function of the first kind (i.e. U_0) [138], the optimum value of Z, represented by Z_{opt}, can be estimated by [66]:

$$Z_{opt} = \frac{\lambda}{4\sqrt{n_{gas}^2 - n_{eff}^2}} \approx \frac{\pi}{2U_0} R \cong 0.65R \qquad (4.3)$$

Although the Eq. (4.3) can provide an accurate value for Z in a simple tube-jacket fibres, the optimum value of Z for the lowest loss can deviate from the calculated value from this equation due to the complex structure of NANF in comparison to a simple tube-jacket fibre. Despite the structural complexity of NANF, the Eq. (4.3) can still provide a reasonable initial guess for Z parameter in NANF. In fact, it is shown in [139] and other studies [57] that for a NANF design the lowest loss typically lies in the range of $0.6 < Z/R < 0.8$, which is in good agreement with Eq. (4.3).

Therefore, to study the influence of the Z parameter on the loss of the fibre and more specifically at the Stokes wavelength, which is the dominant loss in the fibre, a parameter sweep has been performed on Z parameter for the silica mid-IR NANF with d = 4 µm and t_s =1.66 µm, while considering the material loss of silica in the simulation model. **Figure 4.9 (a)** shows the calculated loss for $0.1 < Z/R < 0.9$ and a few radii from R = 15 to 35 µm at λ = 4.35 µm. Due to differences in the loss level for each radius, the loss profiles have been normalized to the minimum loss of each fibre, as shown in **Figure 4.9 (b)**. The simulation results show different values for optimum Z/R across a wide range of R. Not only these values are different for each R, they are also far from the initial estimated value ($Z/R \sim 0.65$) by Eq. (4.3) or other studies on the NANF (0.6 <

$Z/R < 0.8$) [57]. However, as shown in the inset of **Figure 4.9 (b)**, the absolute value of the optimum Z parameter is fairly consistent (~ 7 µm) across the core radii apart from small radii where the CL becomes comparable to the material loss (i.e. R ~15 µm where the fibre loss becomes very high).

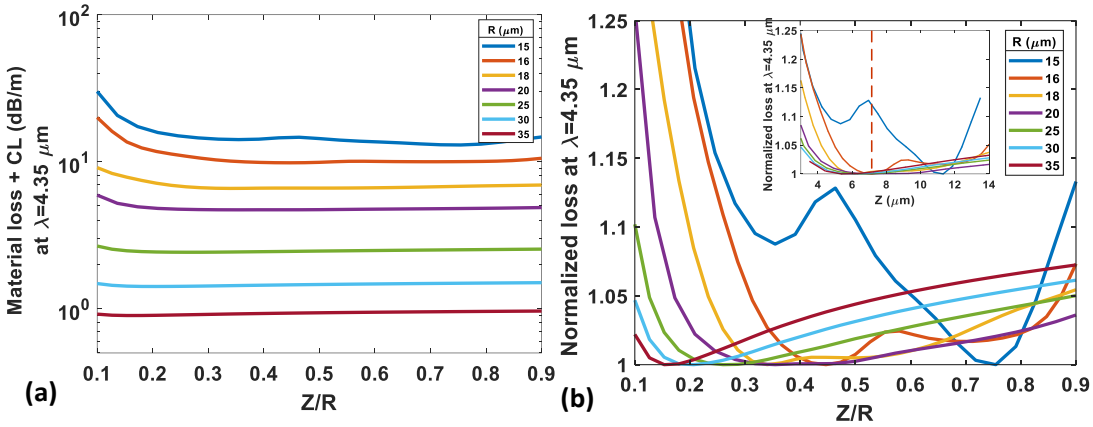

Figure 4.9. (a) the calculated loss of the silica mid-IR NANF (t_s = 1.66 µm) for Z/R ratio at λ = 4.35 µm. **(b)** the normalized loss over the minimum loss for the same fibre shows the change of optimum Z/R across different R. The inset of **(b)** shows the absolute value of Z where the $Z \approx 7$ µm is marked by a red dashed line as the selected option for optimum Z.

By studying the pattern of changes in optimum Z parameter, I believe such significant deviations from the predicted value from Eq. (4.3) is the result of the wavelength operation range (i.e. mid-IR) of the designed NANF as well as the high material loss of silica in the mid-IR. In principle, to achieve the lowest loss for a wavelength in a NANF the t_s should be chosen in a way that the operating wavelength is placed in the fundamental TB and more specifically in the anti-resonance wavelength of fundamental TB. This requirement, dictates thicker tubes in NANFs operating in the mid-IR range of wavelengths in comparison to NANFs designed to have low loss at much shorter wavelengths. For instance, the required t_s for a silica NANF to achieve the lowest loss at 1.55 µm is in the range of ~ 400 nm while to achieve low loss at 4.35 µm the t_s needs to be in the range of ~1600 nm, as seen in the t_s optimization section. This large thickness can have noticeable effect on the amount of captured field in the cladding glass, which can vary in different geometries. In addition, in conventional use of HC NANF for communication wavelengths (1.5~1.6 µm) or near-IR wavelengths (1~2 µm) the material loss has very small effect on the total loss of fibre and the minimum loss is mostly limited by CL or surface scattering loss. However, in

the mid-IR regime, the material loss has significant impact on the total loss and can shift the optimum design parameters significantly as seen in this case.

To study the effect of material loss in this case, a Z parameter sweep has been performed for similar fibres while the material loss is set to zero in order to observe the effect of CL in the fibre. **Figure 4.10 (a)** shows the calculated absolute CL of the fibres in **Figure 4.9** vs Z/R. As expected from Eq. (4.3) or other studies, the minimum losses for all fibres are in the range of ($0.6 < Z/R < 0.8$) and more importantly, as shown in **Figure 4.10 (b),** the CL is very sensitive to Z/R changes (e.g. more than 200% within $0.5 < Z/R < 0.9$) unlike the case with material loss. This shows that the large material loss in this fibre is altered the optimum value of Z/R toward lower values. However, when the CL loss becomes comparable to the material loss due to small core size, the Z/R ratio of minimum loss shifts towards the typical value of $0.6 < Z/R < 0.8$, as seen in the case of $R = 15$ µm (**Figure 4.9**).

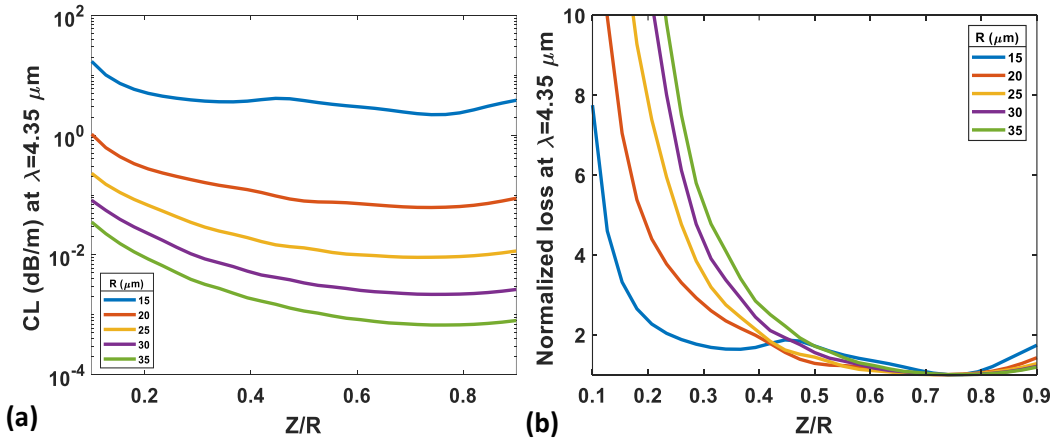

Figure 4.10. (a) the calculated CL (i.e. no material loss) of the silica mid-IR NANF (t_s =1.66 µm) for Z/R ratio at λ = 4.35 µm. **(b)** the normalized loss over the minimum loss for the same fibre shows very good agreement with the predicted optimum Z/R for all R.

Although, the optimum loss in silica mid-IR NANF is not achieved in the conventional range of Z/R, the flat distribution of the loss across board range of Z/R can be seen as an advantage for this fibre (less than 5% change in loss across $0.1 < Z/R < 0.9$, see **Figure 4.9**). To explain this, it is important to consider the fact that the distance between cladding tubes (Z), in addition to have an essential role on the loss of the fibre through the anti-resonance feature of NANF, it also has very important effect on imposing high HOM extinction. In more detail, according to [138], it is well-known that

the n_{eff} of the fundamental mode in a single tube fibre is proportional to the core radius of the tube. This means, the n_{eff} of higher order modes in a large tube can match the n_{eff} of the fundamental mode in the smaller tubes. In a similar scenario, in the structure of a NANF, the core size is larger than the core size of the inner cladding tubes or the air gap between inner and outer cladding tubes (i.e. the space defined by the Z parameter). Therefore, the index matching between the fundamental core mode and air-guided cladding modes (i.e. the modes in the air gaps of cladding tubes) is not possible at anti-resonance wavelengths (the wavelengths with the lowest loss in each TB). However, by adjusting the Z parameter, it is possible to match the index (i.e. n_{eff}) of HOMs in the core with air-guided modes in the cladding tubes [57, 140]. Using this method, a high HOM extinction can be achieved by small Z (i.e. $Z / R < 0.3$) via the air-guided modes of inner cladding tubes or by large Z (i.e. $Z / R > 0.9$) via out-coupling of HOMs into the gap between inner and outer cladding tubes. This method can effectively provide a single mode NANF regardless of the core size by introducing a significant loss difference between the fundamental mode and HOM. Therefore, such method can be implemented in the proposed silica mid-IR NANF especially where the loss of the LP_{11} is very high at $Z / R \sim 0.2$-0.4, which is at the range of Z / R that provides the minimum loss for designed mid-IR NANF (**Figure 4.9**). For instance, **Figure 4.11** plots the loss profile of the LP_{11} mode of a silica mid-IR NANFs with $R = 20$ μm, t_s =1.66 μm and d = 4 μm vs Z / R, alongside the effective index map of fibre (i.e. the effective index of a few cladding and core modes).

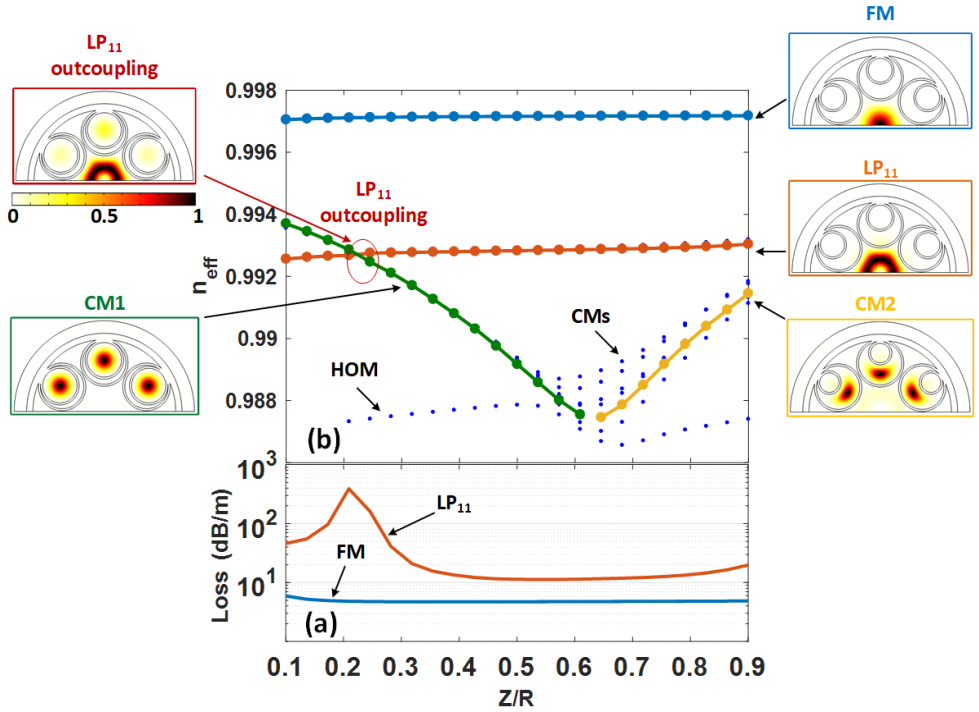

Figure 4.11. (a) the loss profile of the LP_{11} mode in silica mid-IR NANF vs Z/R. **(b)** the effective index profile of fundamental mode (FM), LP_{11} mode and cladding modes (CM1 and CM2) matched to LP_{11} alongside their normalized power distribution.

As it is clear, the loss of the LP_{11} mode significantly changes across different values of the Z parameter and has a large peak around Z/R~0.2 while the fundamental mode has an almost flat loss profile. Such a high HOM extinction ratio in the fibre provides an effective single mode operation. The large loss of the LP_{11} mode can be explained by the interaction of core and cladding modes (CM). **Figure 4.11 (b)** shows the evolution of n_{eff} for core and cladding modes due to changes of Z/R ratio. Starting from very small value of Z/R, inner tubes are large and, consequently, they have larger n_{eff} than the LP_{11} mode. By increasing the Z/R, while the n_{eff} of LP_{11} mode is almost constant, the radius of inner tubes becomes smaller and their n_{eff} becomes smaller too until the n_{eff} of LP_{11} and CM1 become very close at Z/R~ 0.2 (CM1 represents the inner tubes cladding mode). At this point the LP_{11} mode experience a large loss due to out-coupling to the CM1, as shown in **Figure 4.11 (b)**. Meanwhile, the n_{eff} of FM is far from the CMs and exhibits a flat loss profile. As the value of Z/R increases, the inner tubes become smaller and the difference between n_{eff} of LP_{11} and CM become larger, which reduces the out-coupling effect and loss of the LP_{11} mode. At larger values for Z/R ratio (Z/R>0.65), the gaps between inner and outer tubes become larger and their n_{eff} increases (marked as CM2 in **Figure 4.11 (b)**), which can reach the n_{eff} of LP_{11} at larger

Z/R (it is beyond the range of Z/R in **Figure 4.11**). Fortunately, as shown in **Figure 4.11** and **Figure 4.9**, the designed silica NANF has both the minimum loss and high HOM extinction ratio at the same range of Z/R. Therefore, the fibre operates in a single mode and low loss regime at the same time.

4.4.1.4 *R* optimization

In the previous optimization sections, it is shown that the optimum value of other design parameters in silica NANF has very low dependency on core size and can be fixed for a very broad range of R. Therefore, considering the optimized value for those parameters one needs to select the appropriate R for the best loss. In principle, the loss of HC ARFs decreases as the core size increases as shown in the previous sections through modelling results of optimization. Consequently, to achieve lower loss one should increase the R parameter until reaches the desired loss. However, in terms of Raman conversion application, the value of R not only impacts the fibre loss but also determines the intensity of the laser and consequently controls the Raman efficiency as well as effective nonlinear length of the fibre. Therefore, in Chapter 6, a detailed study is done on the effect of core size on loss and Raman conversion efficiency in order to achieve maximum efficiency of Raman conversion in gas-filled NANF.

4.4.1.5 Characteristics of the final silica design

By implementing the optimization process described in previous sections, the main design parameters for the lowest loss at pump and 1st Stokes wavelengths in a six-tube silica NANF are achieved as following: t_s =1.66 μm; d= 4 μm; Z = 7 μm. In this section, the characteristics of the final optimum design are studied in more detail. **Figure 4.12 (a)** shows the loss profile of the designed silica NANF with R = 20 μm alongside the normalized power distribution in fibre at the pump, 1st Stokes and two resonance wavelengths. While the field is properly confined in the core at anti-resonance wavelengths, the power distribution shows the core-cladding mode coupling and out-coupling of the field into the glass webs at anti-crossing/resonance wavelengths, which explains the high loss at these wavelengths due to leakage of field to the jacket tube. As it is clear from **Figure 4.12 (a)**, the pump wavelength is placed close to the edge of the second resonance wavelength, while the wavelength of the 1st vibrational Raman Stokes (122.9 THz shift) is very close to the 1st anti-resonance wavelength in the fundamental TB of the fibre. As discussed before, although neither wavelength is placed in the exact anti-resonance points due to the limitation by the periodic anti-resonance

feature of NANF, the best possible configuration has been chosen to reduce the RCL. With such configuration and for this specific core size (R = 20 μm), the total loss of 5.1 dB/m and 2.7×10^{-2} dB/m are achived at 1st Stokes and pump wavelengths, respectively. In order to show the material loss contribution on the total loss, the CL profile of the fibre has been shown beside the total loss in **Figure 4.12 (a)**. It can be seen that, due to small core size and high material loss in the mid-IR range, the CL and total loss have an order of magnitude difference (i.e. CL is 0.21 dB/m at 1st Stokes and wavelength). In this case even the CL of the fibre in the mid-IR range and particularly at 1st Stokes wavelength (4.35 μm) is high due to small core size in contrast to mode area. **Figure 4.12 (b)** plots the dispersion (D) profile of the fibre for different transmission bands. The dispersion profile has a similar pattern in each individual transmission window starting from a large normal dispersion value at the edge of the band at short wavelengths and becomes almost zero near the minimum loss point in each band. The dispersion becomes anomalous after passing the zero dispersion wavelength (ZDW) and increases significantly at the edge of the band at longer wavelengths. Although the dispersion is high at the edge of bands, it is relatively small in comparison to HC-PBGFs.

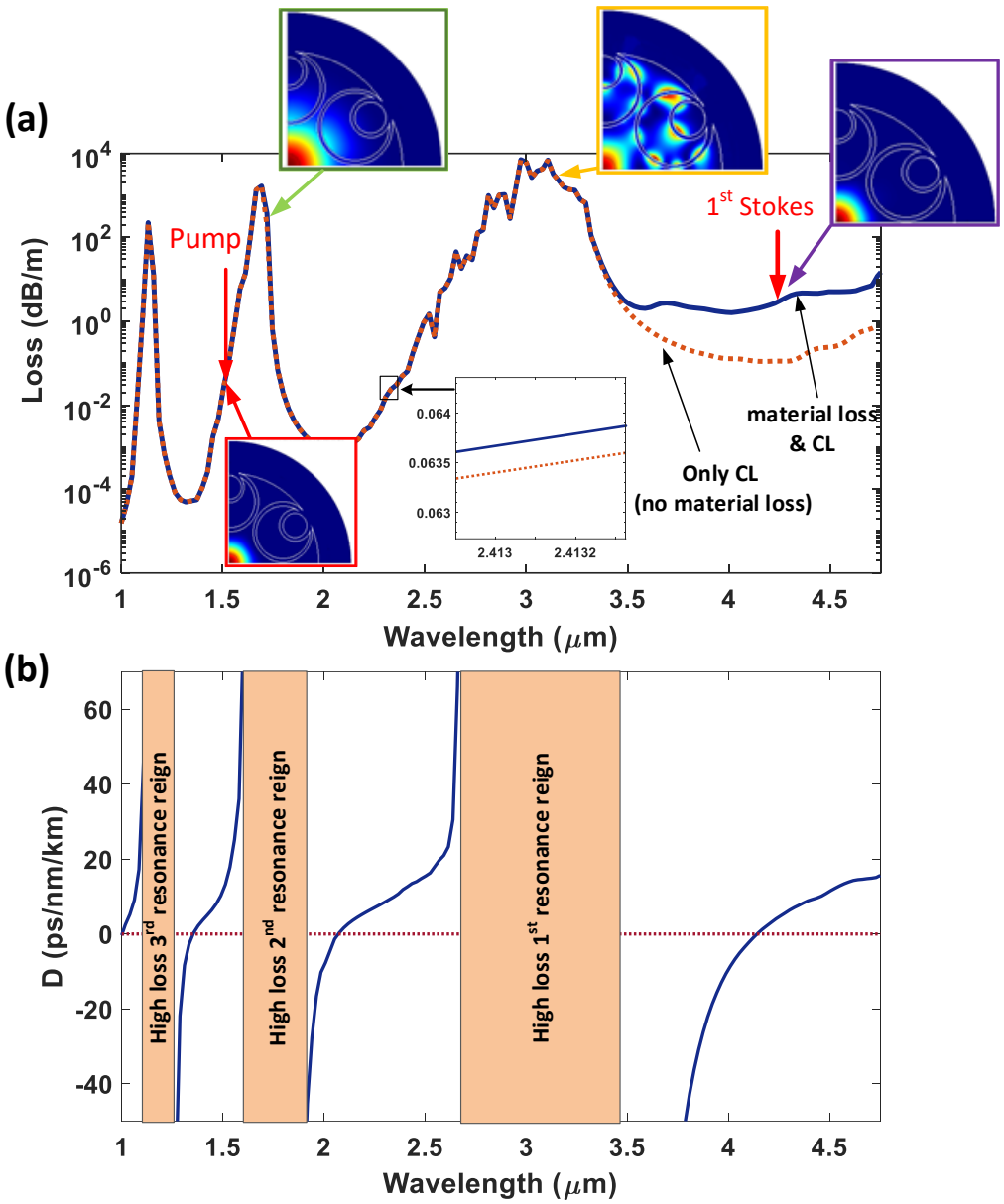

Figure 4.12. (a) FEM simulated loss profile of the silica NANF (t_s = 1.66 µm, R =20 µm, d = 4 µm and Z = 7 µm) with and without material loss. The normalized power distribution in the cross section of the fibre has been presented at pump, 1st Stokes and two resonance wavelengths. **(b)** The dispersion profile of the fibre at different transmission bands exhibits periodic pattern.

4.4.1.6 Bend loss analysis

Although the presented study of the designed NANF in the straight form shows promising performance, in practical applications the fibre would be used in a bent or coiled form. As a result, the performance of the fibre at the present of macro bend has been investigated by modelling the bend loss of the fibre, which is presented as loss change in the form of $Loss(R_c) - Loss(\infty)$, as shown in **Figure 4.13**. The bend loss

calculation has been performed by applying the tilted refractive index approach and bend sensitive PML in the developed FEM toolbox in this thesis (see Chapter 3 for more details).

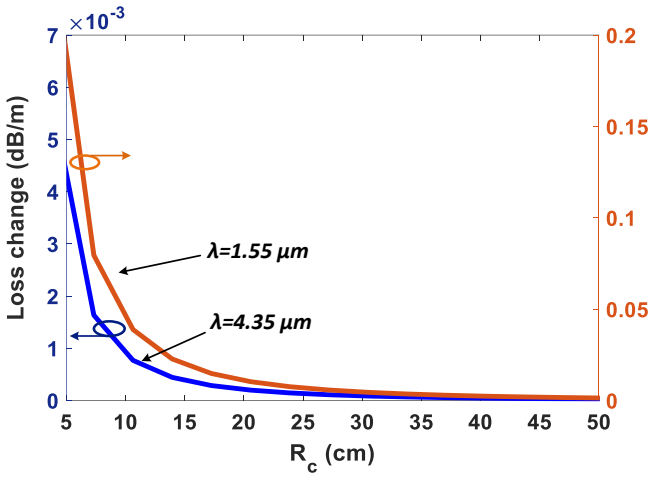

Figure 4.13. The simulated loss of the silica NANF for bend radii (R_c) at = 1.55 μm and 4.35 μm presented in the form of loss change.

Thanks to the inner tubes in the structure, the fibre shows very low bend loss even for a bend radius as small as R_c = 5 cm. The bend loss in HC-ARFs can be mainly related to two key mechanisms. Firstly, the anti-resonance effect of the web glass is reduced as the resonance wavelength is shifted towards the operating wavelength due to the modified refractive index profile of the web glass induced by the bending process. As a result, the reflection effect (i.e. mirror effect) of the webs reduces and the core field leaks into the jacket tube which increase the loss of the fiber. In a second mechanism, which can happen for very small bend radii, the n_{eff} of the core and the air-guided cladding modes (guiding modes in the core of surrounding tubes) become so close that coupling between them can cause significant leakage loss similar to the case seen in **Figure 4.11**. The latter effect in NANFs is less likely because of the aspect ratio and size difference between the inner tubes and core radius. In fact, using six tubes instead of four increases this mismatch by reducing the size of the cladding tubes (Eq. (4.1)) and reduces the chance of coupling.

4.4.1.7 Mid-IR NANF vs tubular fibre

The advantage of NANF for low loss application in comparison to tubular fibres at near-IR is proven through modelling in many works [57, 141, 142]. However, it is desirable to compare the results of optimized NANF in previous section for mid-IR with a similar counterpart in tubular form and study their low loss features. As the material

loss has large impact on the fibre loss in the mid-IR range, the question is raised about the advantage of using extra inner tubes in NANF in comparison to tubular fibre. As it is shown in the previous sections, the loss profile can be effected significantly by material loss in the mid-IR (comparing **Figure 4.9** and **Figure 4.10**), specially where the CL is negligible in the fibre. Similar to other ARFs, any NANF design has larger CL at smaller core sizes and the CL becomes significant, particularly when the core size (i.e. R) becomes comparable to wavelength. Although the material loss of the silica is high at 4.35 μm, the domination of CL has been seen in designed silica mid-IR NANFs with R = 15 μm (see **Figure 4.9**). However, for larger core sizes (R > 18 μm, see **Figure 4.9**), the material loss in the proposed designed NANF is dominant while the CL is very small (see **Figure 4.10**). Therefore, to justify the use of NANF over tubular fibre at larger core size in the mid-IR, a NANF and a tubular fibre with similar parameters (d = 4 μm, t_s =1.66 μm) and core size of R = 40 μm has been modelled at 4.35 μm. The NANF fibre has shown ~0.76 dB/m loss while the tubular fibre shows almost twice the loss of the NANF (~ 1.4 dB/m). Even though the NANF has more glass in its structure, it shows lower loss than tubular fibre. To study this effect, the power distribution in the propagation direction of light (i.e. P_z) for both fibres are presented in **Figure 4.14 (b)**. The distribution of "propagating power" in the cross section of the fibre shows far less power in the cladding area of NANF fibre, which decreases the CL in the fibre. This can be seen more quantitatively in **Figure 4.14 (c)**, where the power density drops significantly passing the first cladding tube at 40 μm for NANF due to the effect of the second tube (i.e. inner tube) while for tubular fibre the power density is almost constant after the first tube. Although studying the propagating power can be useful for understanding the CL behaviour of fibre, to appreciate and visualize the effect of inner tubes on material loss, the "outgoing power" of field has been presented in the X,Y direction (i.e. P_{out}) in **Figure 4.14 (a)**. From this figure, it is clearer that less power is confined in tubular fibre than NANF, as the outgoing field from cladding tubes to the jacket tube is far more than NANF fibre. More interestingly, the power leakage to the jacket tube in both fibres goes through the centre of tubes not the azimuthal gap between cladding tubes. Comparing the distribution of outgoing power for both fibres shows very large amount of power in the jacket tube for tubular fibre in comparison to NANF (Note: the power scale for both fibres is in dB and the dark red shows high power). Therefore, although NANF has more glass due to existence of inner tubes in its structure, the overall power in the glass in this fibre is far less than tubular fibre. In fact, due to inner tubes, less power reaches the inner and jacket tubes, which reduces the loss experienced by fibre from material loss. Therefore, even though the material

loss is the dominant loss source for large core silica mid-IR NANF, its low loss performance is better than tubular fibre with the same design parameters.

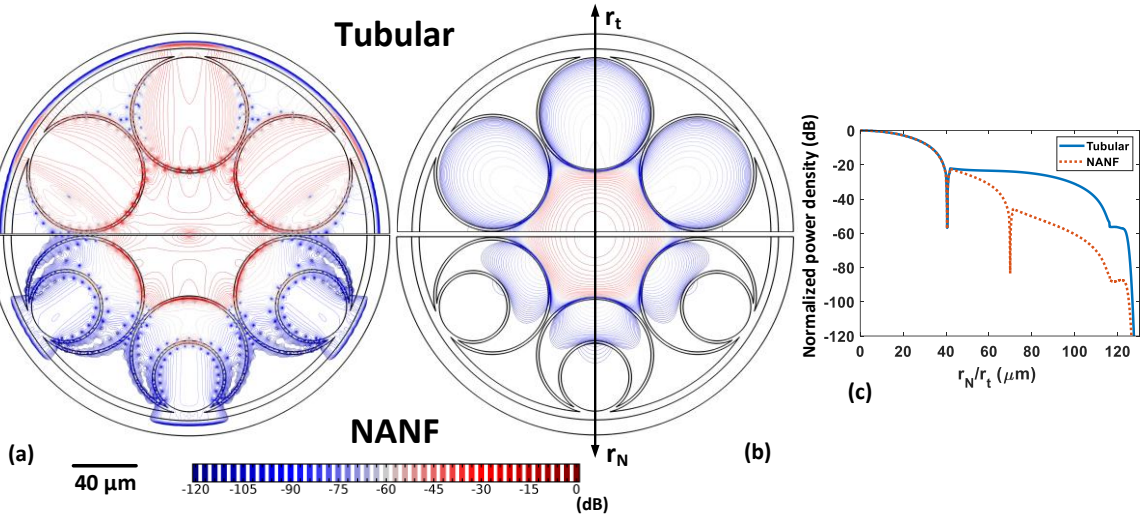

Figure 4.14. (a) distribution of normalized outgoing power (Pout) for Tubular fibre (top) and NANF (down) in dB scale. **(b)** distribution of normalized propagating power (P_z) for Tubular fibre (top) and NANF (down) in dB scale. **(c)** normalized propagating power density along $\mathbf{r_t}$ and $\mathbf{r_N}$ marked on figure **(b)** for tubular fibre and NANF, respectively.

4.4.2 Tellurite NANF

Despite using state-of-the-art design and optimization of the NANF fibre with silica, the high intrinsic material loss in the mid-IR introduces a large total loss in the silica NANF. Although silica is the most popular and dominant material for fibre fabrication due to existence of robust technology that has been developed around it to support the telecom industry, advances in the fabrication of soft glasses in recent years increase the possibility of shifting from silica to soft glass materials with lower intrinsic material absorption in the mid-IR regime. Among the many different form of soft glasses, tellurite (tellurium dioxide [TeO_2]) shows fairly low absorption in the mid-IR up to 5 µm. Previously, due to water contamination (OH) in this glass the absorption was very high, but recently the soft glass group in ORC[1] has developed a fabrication process which can reduce the OH content and allow fabricating a low loss fibre [143]. **Figure 4.15 (a)** shows the loss profile of an in-house-made halo-tellurite ($60TeO_2$-$20PbO$-$20PbCl_2$ [TLX] [mol.%]) with low OH concentration in the mid-IR region which shows material loss as low as 10 dB/m at 3-4 µm range [143]. Although the loss is high for

[1] ORC is the Optoelectronic Research Center of University of Southampton

fabricating solid fibres, in fact, it is reasonable for NANF due to the very small fraction of mode field inside the glass. **Figure 4.15 (b)** demonstrates the measured refractive index of Halo-tellurite which has been fitted by a three-term Sellmeier model (Eq. (4.2)) with following coefficients; $B_1 = 1.212$; $B_2 = 2.157$; $B_3 = 0.1891$; $C_1 = -6.068\times10^{-2}\ \mu m^2$; $C_2 = 7.068\times10^{-4}\ \mu m^2$; $C_3 = -45.19\ \mu m^2$.

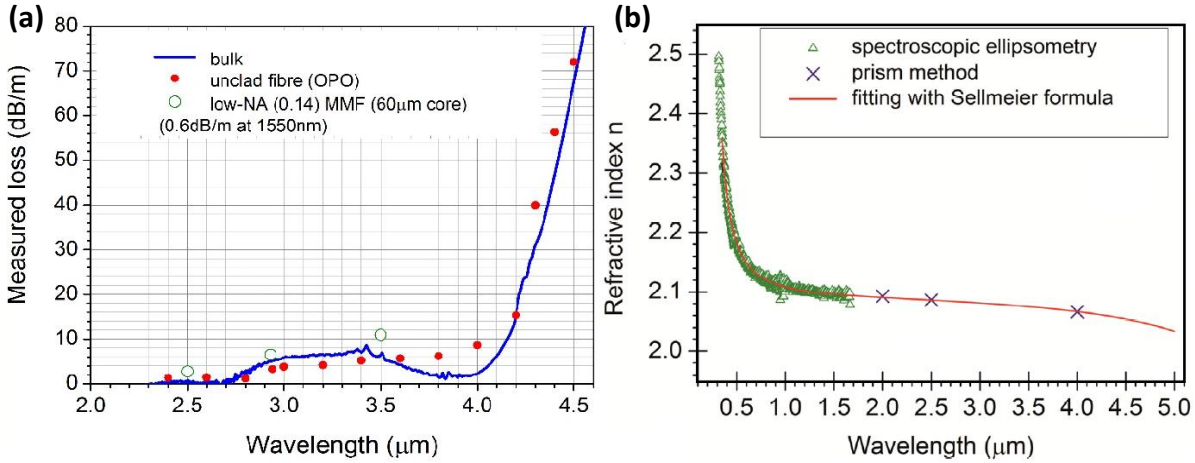

Figure 4.15. Refractive index and loss profile of Halo-tellurite (TLX) **(a)** loss profile of Halo-tellurite in different form, **(b)** Sellmeier model and measured refractive index of Halo-tellurite [after [143]].

4.4.2.1 Characteristic of the final tellurite design

As the fibre structure in tellurite design is similar to silica type, all optimization steps can be performed in the same way with related loss and dispersion profile of the Halo-tellurite. The final design for a six-tube tellurite NANF has the following parameters; $t_s = 2.01$ μm; $d = 2$ μm; $Z = 0.65R$ (because of lower material loss in comparison to silica, the CL loss controls the Z parameter). **Figure 4.16** shows the loss profile of the fundamental mode of the final design with $R = 15$ μm alongside the bend loss of the fibre at 1.55 μm and 4.35 μm in loss change. As it is clear, the tellurite fibre has an order of magnitude lower loss than silica NANF with similar core size due to significant lower material loss (i.e. the total loss of 1.1 dB/m and 3.3×10^{-3} dB/m at 1st Stokes and pump wavelengths, respectively). It is noticeable that the fibre in **Figure 4.12** has larger core size ($R = 20$ μm) thus should have lower loss but yet the loss of the tellurite fiber is lower. In fact, by using tellurite glass, the total loss reached the low loss limitation imposed by CL of fibre design. Thus, this fibre can be a very good candidate for nonlinear applications in gases because it can provide very small core size with lower

total loss than silica NANF and decreases the threshold power for Raman conversion significantly.

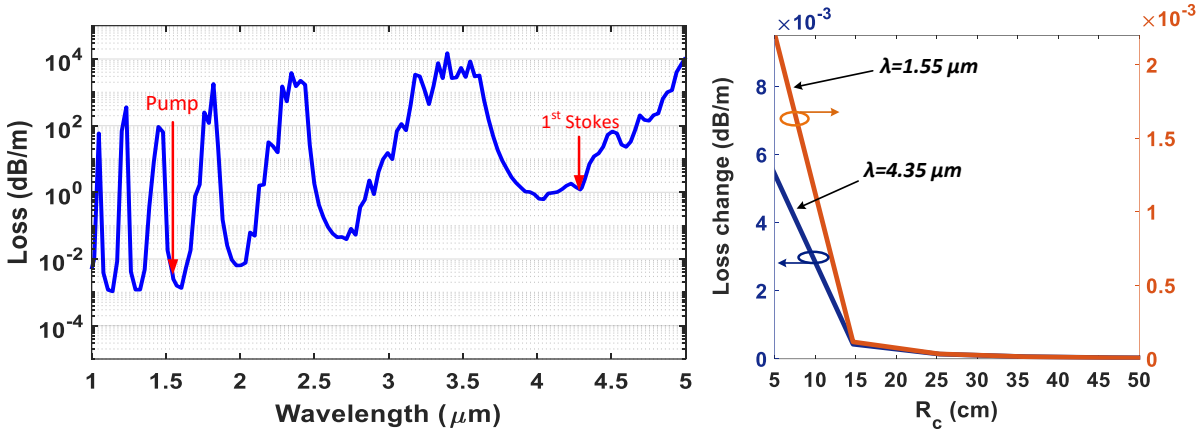

Figure 4.16. (a) FEM Simulated loss profile for tellurite NANF($t_s = 2.01$ µm, $R = 15$ µm, $d = 1$ µm and $Z = 0.65\,R$)). **(b)** Calculated bend loss in loss change of the silica NANF for bend radii (R_c) at 1.55 µm and 4.35 µm.

4.5 Conclusion

It is shown that by using HC fibres the length of light-matter interaction can be increased, and consequently the efficiency of the nonlinearity in the gas improved dramatically. The evaluation of the loss and group velocity dispersion profile of PBG-guiding and anti-resonant hollow core fibres, as the two main categories of HC-PCFs, shows that ARFs are good choices as HC waveguides for nonlinear process in gases due to their very broadband low loss transmission window, which is very important for broadband nonlinear effects, and also because of their almost flat GVD profile.

In this chapter, tubular HC fibres and more specifically a newly proposed nested anti-resonant nodeless fibre (NANF) are studied, as the best options for efficient nonlinear process in gas-filled HC-ARFs, due to their low loss in the mid-IR and high damage threshold. After comparing the low loss performance of both types of fibre, a summary of the advantage and disadvantage of HC fibres is presented. NANF design, as the best option for this project, has been selected, due to its very low loss performance at Mid-IR. Using the developed simulating toolbox, a silica NANF has been modelled and optimized, which despite its large material loss at mid-IR wavelength (~3000 dB/m at 4.35 µm), it shows total loss as low as < 0.9 dB/m at 4.35 µm for core radius of $R =$ 35 µm. This study has shown that due to high material loss the optimum values for

design parameters can deviate from other works reported on low loss regime [57, 142]. By studying the effective index of cladding and core modes, the optimum value for inner tube sizes have been identified in order to achieve high higher order modes (HOM) extinction ratio by out-coupling HOMs to the cladding modes while keeping the fundamental loss of the fibre low. Thus, the fibre not only has a very low loss in the mid-IR regime but also can be effectively single mode regardless of its core size. The bend loss analyses of the optimized NANF with $R = 20$ μm shows very low bend loss at both operating wavelengths (i.e. 1.55 μm and 4.35 μm) considering the straight loss of the fibre at those wavelengths.

The material loss of the fibre, as the main source of loss in the mid-IR reign, was reduced by using tellurite in a new optimized NANF design. Although the loss in NANF increases dramatically by reducing the core size (R^{-8}), similar range of loss as silica NANF with $R = 35$ μm has been achieved in a tellurite NANF with much smaller core size $R = 15$ μm. Apart from the core radius that needs separate optimization process due to its tight relation to Raman efficiency process, which is discussed in Chapter 6, in this chapter, the other design parameters have been optimized for low loss operation in pump and 1st Stokes wavelengths.

In addition to fibre loss and intensity of laser, the polarization of light is another interesting characteristic that can affect the Raman efficiency. Thus, in the next chapter a novel design for NANF is introduced with high birefringence and polarizing effect, which can provide constant linear polarization through interaction of light and gas.

Chapter 5: Broadband high birefringence and polarizing hollow core anti-resonant fibre

5.1 Introduction

Besides loss, bandwidth and modal properties, the ability to control and maintain the polarization state (e.g. by inducing a large birefringence or a differential loss between the two orthogonally polarized modes) is a key feature for a wide range of optical fibre applications, including precise interferometric sensing (e.g. fibre based gyroscopes [39]), quantum computing [144], atom spectroscopy [145], and polarization maintaining optical amplifiers [146]. Although conventional polarization-maintaining (PM) fibres have been around for many years, in which a high birefringence (Hi-Bi) is introduced by applying either stress (e.g. PANDA or Bow-tie fibres [147, 148]) or form anisotropy (e.g. elliptic core [149]), they face a few fundamental limitations associated with their solid core. For example, material absorption, low damage thresholds and optical nonlinearity fundamentally restrict their application to wavebands where the glass is transparent and to optical powers low enough not to cause undesired nonlinear effects and/or dielectric damage. Some of these limitations can be addressed by using hollow core optical fibres, which in addition can also enable interesting new linear and nonlinear applications exploiting long path lengths for gas-light interactions [15, 47-49]. Despite many potential advantages, hollow core fibres are a less mature technology than solid core versions, which still require physical understanding and new optical designs in order to achieve their full potential.

During the last decade considerable research has focused on lowering the loss in HC-ARFs and many different structures have been proposed based on: a Kagomé cladding [11, 67], a hexagram structure [66], a double anti-resonant layer [150], tubular "negative curvature" structure [71, 151] and nested tubular structure [152-154]. These have resulted in significant improvement of properties such as low bend-loss [130], ultra-large bandwidth [47], high damage-threshold [40, 41] and NANF [57].

Generating a birefringence of the same order of magnitude as in commercial solid core PM fibres (~10^{-4} for 1550 nm operation) in a hollow core fibre is however difficult. Conventional methods of using stress rods (and, as it shall be seen, elliptical shapes) are not applicable or effective. Besides, structural requirements to minimize confinement loss in hollow core fibres add additional limitations. Arguably, the best

result so far was achieved in a HC-PBGF with asymmetric rods in the core surround, presenting low loss (10 dB/km at 1.530 μm) and birefringence in the range of that of solid-core fibres, albeit over a narrow operating bandwidth (<10 nm) [155]. Achieving such a high birefringence in HC-ARFs is even harder since the field overlaps with glass and the resulting sensitivity of the birefringence to the core's geometry is even lower. Only recently, two theoretical Hi-Bi HC-ARFs based on modified NANF concepts were proposed which could address the problem by operating in the normal [156] or hybrid band transmission regimes [133]. Both show promising routes to achieve high birefringence ($\sim 10^{-4}$) in ARFs. However, the underpinning differences between the two approaches require detailed study, and further reduction of the loss and widening the Hi-Bi bandwidth are still possible and as targeted here.

In this chapter, a detailed study of the birefringence of NANF designs that have tubes with different membrane thicknesses along orthogonal axes (bi-thickness NANFs) is presented and a design procedure to maximize the bandwidth and minimize loss is proposed while maintaining high birefringence operation. In the following Section, it is demonstrated that unlike solid fibres, an elliptical core shape cannot provide a large enough birefringence in a hollow core fibre. In Section 5.3, a way to circumvent this problem is proposed using a bi-thickness NANF with a small core and 4 triple nested tubes. Also an approach for analysing the effect of the design parameters of the fibre on its loss, bandwidth and regime of operation is introduced, using this approach propose a new HC-ARF design is proposed providing the lowest loss and the widest bandwidth high birefringence operation ever reported, at the time of writing this thesis to the best of my knowledge. In Section 5.4, a novel method is proposed to out-strip a selected fundamental polarization mode to provide a hollow core fibre with an additional polarizing ability, in addition to a polarization maintaining behaviour. Finally the work is summarized in Section 5.5.

5.2 Birefringence by asymmetry

While the PM property of HC-PBGFs has already been investigated theoretically in various works [157, 158] and promising results have been achieved experimentally [155], extending these results to anti-resonant fibre types is not straightforward, and only recently the first designs have been proposed [133, 156]. In general, symmetrically arranged HC-ARFs can support degenerate polarization modes and polarization coupling due to random perturbations is inevitable. The idea of breaking the core symmetry and introducing ellipticity in the antiresonant reflecting optical waveguide

(ARROW)-guiding fibres has therefore been investigated in some of the simplest structures for terahertz applications [159], following the idea of exploiting form-birefringence that is used in solid core PM fibres. In this work, to study the potential of generating polarization mode birefringence (PMB) through core ellipticity in HC-ARFs, an ideal elliptical tube as the simplest possible HC-ARF structure has been considered as a starting point. The thickness of the tube needs to satisfy the resonance equation of ARROWs in order to support the leaky fundamental mode (FM) at frequencies f in the desired (m^{th}) anti-resonance band [57]:

$$\frac{c.(m-1)}{2t_1\sqrt{n_2^2-n_1^2}} < f < \frac{c.m}{2t_1\sqrt{n_2^2-n_1^2}}, \qquad m=1,2,.... \tag{5.1}$$

where c is the speed of light in vacuum. n_1, n_2 and t_1 are the refractive indices of core, cladding and the thickness of the tubes, respectively. Using Eq. (5.1) and choosing an operating wavelength (λ_0 =1.55 μm) in the second anti-resonance band, a thickness t_1 =1.172 μm is estimated to produce the lowest loss for a core radius of R =10 μm. In order to investigate the effect of the tube's ellipticity on its PMB, elliptical tubes with different major (***b***) to minor (***a***) axis ratios have been simulated by the developed FEM solver toolbox with optimized meshes and proper PML (see [57] and Chapter 3). **Figure 5.1** shows the simulated confinement loss and PMB (in this chapter $N_{V/H}$ are real part of effective index of vertical/horizontal polarizations) of the FM for different tube core dimensions. The simulation result shows that the PMB initially increases on increasing the ellipticity of the core, as shown in **Figure 5.1 (a)**. However, after a peak around ***b/a*** ~1.6, it decreases and settles to an almost constant value for further increase in the ellipticity, regardless of the core size. This indicates an optimum point for ellipticity. Additionally, it is seen that decreasing the core size to achieve a discernible PMB is necessary. However, as shown in **Figure 5.1 (c)**, reducing the core size results in impractically large loss, which in practice limits the minimum core size one can choose.

It is well known that loss in an antiresonant HC fibre can be reduced by designing the core surrounding membranes with negative curvature [67, 151, 160]. Amongst various designs, the NANF structure has shown the potential for very low optical loss, in principle comparable to that of solid silica fibres [57]. This structure consists of a number of equally spaced non-touching nested glass tubes, as shown in **Figure 5.2 (a)**, which are attached to the inner wall of a larger jacket tube. The nested tube

arrangement provides the anti-resonant cladding of the fibre, with the hole in the middle acting as the core. In this design, confinement loss is reduced dramatically due to the absence of nodes in the core surround, which can induce undesired coupling to lossy cladding elements (e.g. membranes) [66], and to the addition of coherent radially arranged reflecting layers. One might therefore want to consider whether a NANF with an elliptical cross section (and a small core) might provide a way to generate a significant PMB and low loss. The simulated loss and PMB of an elliptical core NANF obtained by rearranging and reducing the size of two opposite sets of nested tubes (see bottom structure in **Figure 5.1 (b)**) for different ellipticity is shown with markers in **Figure 5.1**, and compared with the behaviour of an elliptical tube. For both structures, a reduction in core size is helpful in increasing the birefringence, but at all core sizes the birefringence peaks around an optimum value of ellipticity for each core size. Larger ellipticities than that do not produce any higher birefringence.

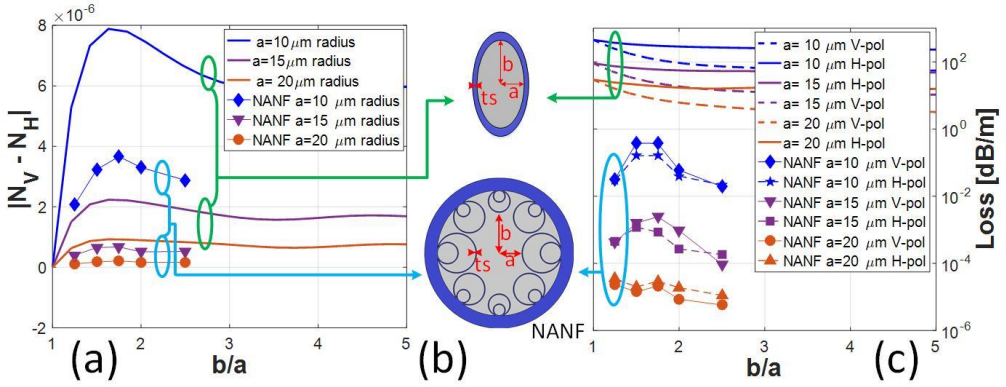

Figure 5.1. The characteristic profile of a single tube for different minor axis (**a** =10 µm, 15 µm, 20 µm) vs major axis b with t_s =1.172 µm at λ_0 =1.55 µm. **(a)** Birefringence of the fibres for different ellipticity, **(b)** tube structure (top) and NANF structure (bottom), **(c)** loss profile of fibres for horizontal and vertical polarization for different ellipticity. Properties of elliptical core NANF for **a** =10 µm, 15 µm at optimum ellipticity are provided for comparison.

As the results suggest, although the NANF structure can reduce the loss by many orders of magnitude in comparison to single tube, the resultant PMB of only $1-2\times10^{-6}$ is too low for PM operation. Additionally, to increase the PMB in NANF fibres by form-birefringence, other geometrical arrangements of the nested tubes are explored that provide a large core ellipticity, as shown in **Figure 5.2 (b)**. However, the simulations show that despite the fairly large core ellipticity achieved in these fibres (**b/a**> 2), the PMB remains below $\sim10^{-5}$ in all cases.

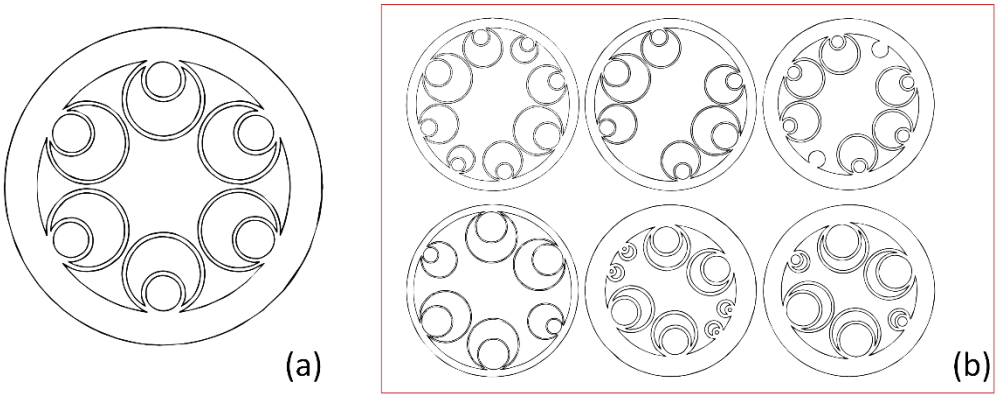

Figure 5.2. (a) 6 tube NANF design, **(b)** alternative NANF with elliptical core designs studied in this work, which are found to be unable to provide birefringence $>10^{-5}$.

In conclusion, the achievable PMB by making the air hole elliptical is not adequate to guarantee the HC-ARF a PM behaviour in the visible/infrared regions of the electromagnetic spectrum. However, there are some examples of multilayer ARROW fibres with large enough PMB factor at longer operating wavelengths (THz guidance) [159].

5.3 Birefringence in bi-thickness NANFs

In addition to elliptical core designs, another potential approach to induce significant birefringence in ARFs has been proposed and has previously been commercially exploited in HC-PBGFs [155] This relies on introducing a controlled anti-crossing between air-guided and glass-guided (surface) modes. By using glass elements of different thickness along orthogonal directions in the core surround, a significantly different effective index for the two polarizations of the FM can be achieved at the edge of an anti-crossing point [161]. In this way the birefringence is introduced by anti-crossing phenomena rather than by geometrical asymmetry [157].

Whilst this has only been experimentally applied to PBGFs so far, a couple of theoretical studies have explored the extent to which the concept can be applied to ARFs that guide light through a different physical mechanism [133, 156]. The main idea is to generate birefringence by introducing an asymmetry through modifying the thickness of selected core surrounding membranes in ARFs. Horizontal and vertical glass membranes can operate in either the same antiresonant window [156] or in a so called "hybrid" regime where they operate in different anti-resonance bands with opposite locked field phases at the outer boundaries [133]. In this work, a systematic study of both operating regimes is undertaken to highlight their benefits and drawbacks. Additionally, it is shown that by applying a suitable modification to the design of a

state-of-the-art NANF, not only it is possible to enhance its birefringence and therefore its polarization maintaining behaviour, but also to achieve a broad bandwidth that spans several 100s nm at a low enough loss for most device and power delivery applications.

5.3.1 The effect of thickness change on birefringent NANF

Following the abovementioned strategy (de-symmetrizing by an appropriate modification of the thickness of some glass membranes), one could think of a 6-tube low-loss NANF [57] and change the thickness of two oppositely located nested tubes with a different thickness than the remaining four. By simulating ANFs with 3 to 8-tubes of two different thicknesses, however, it is found that a structure with 4-tubes can achieve a considerably higher birefringence, as shown in **Figure 5.3**. According to simulation results, I believe the orthogonality of the core surrounding glass webs to the polarization of the core field is key to explain these effects. The fibre with 4-tubes is the only geometry able to guarantee membranes that are orthogonal to the mode polarization. This effect can also be explained by the tendency of each polarization of the FM at the edge of the anti-crossing frequency to couple preferentially to cladding tube modes with a similar polarization [133, 158].

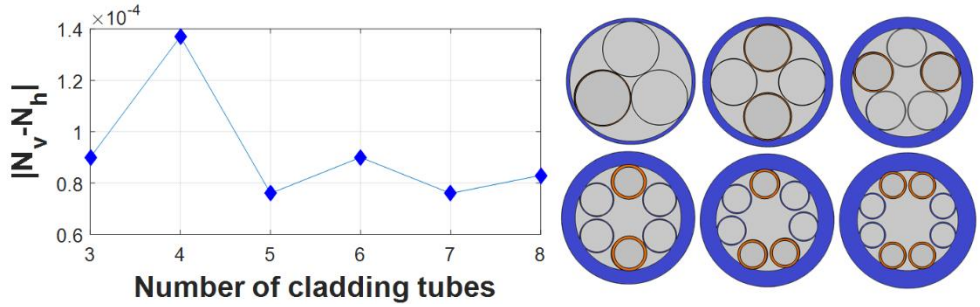

Figure 5.3. Birefringence (N_v-N_h) of 3-tube to 8-tube anti-resonant nodeless fibre design at λ_0 =1.55 µm alongside their structures with same core size (R =7 µm) and bi-thickness cladding tubes (thin tubes (blue)=0.372 µm and thick tubes (orange)=0.633 µm). The 4-tube structure shows maximum birefringence, and the structures with odd number of tubes show lower birefringence due to lack of 2-fold symmetry.

It is also noticeable that structures with odd number of tubes show lower birefringence, which can be explained by their lack of 2-fold symmetry, resulting in worse orthogonality between core boundaries and direction of polarization of the fundamental modes. I leave this topic open for further investigation in future works.

Since the 4-tube fibre was found to offer higher birefringence, the rest of this chapter will focus on this structure and further optimization of its performance.

The starting point in this study is a 4-tube NANF in which the tubes aligned along the vertical axis have a thickness t_1 which can be the same (normal operation) or different from that (t_2) of the tubes along the horizontal axis (i.e. a bi-thickness fibre). In order to minimize the loss while maintaining a small enough core to provide large birefringence in air (see section 5.2), a design with two nested tubes inside a larger external one is chosen, as shown in **Figure 5.4 (a)** with the details of all the relative design parameters. In order to optimize the confinement loss for a core radius of R =7 μm and an azimuthal tube distance d=1.5 μm, the distance between the inner tubes (Z) was calculated using the quarter wave condition which ensures the in-phase reflection of each layer towards the core [66]:

$$Z \approx \frac{\pi}{2U_0} R \approx 0.65R. \tag{5.2}$$

where U_0 is the solution of the first zero of the zeroth order Bessel function. Depending on the choice of t_1 and t_2, the fibre can operate in the following three regimes:

1. <u>Non-birefringent guiding</u> (standard operation, see **Figure 5.4 (b)**): $t_1 = t_2$ and the fibre shows no birefringence.
2. <u>Same band birefringent operation</u>: t_1 and t_2 are slightly different so that anti-crossing shifted birefringence is obtained whilst anti-resonance occurs in the same window for both FM polarizations.
3. <u>Different band birefringent operation</u>: t_1 and t_2 are considerably different, such that the anti-resonance in the orthogonal directions occurs in different bands and the FM polarizations have opposing locked field-phase at the outer boundaries (hybrid regime birefringence) [133].

As a starting point, the study is begun with a uniform NANF ($t_1 = t_2$). Using Eq. (5.1), a thickness $t_1 = t_2 = 0.6$ μm is selected such that the fibre operates in the first anti-resonance band around near-IR telecoms wavelengths (~1.55 μm). **Figure 5.4 (b)** shows the effective refractive index (n_{eff}) and loss profile of the designed fibre. The target operating wavelength of 1.55 μm has been placed within the first anti-resonance band but not at the lowest loss point, for the purpose of examining different scenarios. The

fibre, as expected, shows no birefringence. However, the fibre's polarization properties change dramatically when the thickness of all tubes along one axis is modified. **Figure 5.5** shows the evolution of the loss for each FM polarization and the difference between effective refractive index of vertical polarization (n_V) and horizontal polarization (n_H) at λ_0 =1.55 μm when t_2 is changed for a fixed t_1 =0.6 μm. It is worth mentioning that increasing t_2 causes the inner radii of the corresponding tubes to decrease, while the other parameters remain unchanged.

At $t_2 / t_1 = 1$ the fibre presents no birefringence and operates in the first anti-resonance band. As the thickness of the horizontal tubes (t_2) increases, the resonance region of these tubes start to shift towards the wavelength λ_0 =1.55 μm while the vertical tubes do not shift and still work around the original anti-resonance condition. The induced birefringence under this condition can be explained in various ways through:

a) the different behaviour between parallel and perpendicular polarization of core modes at the anti-crossing point [157];

b) the close relationship between the increase in n_{eff} and the sharp rise in CL based on the Kramers-Kronig relation, which is caused by the reduction in anti-resonance reflection of the glass membranes at the edge of the resonance frequency band [133];

c) the difference in confinement radius (not to be confused with the geometrical radius) of the individual fundamental polarization modes for different thicknesses, which cause a change in n_{eff} that can be explained by the well-known connection between mode radius and n_{eff} in an anti-resonant structure [133].

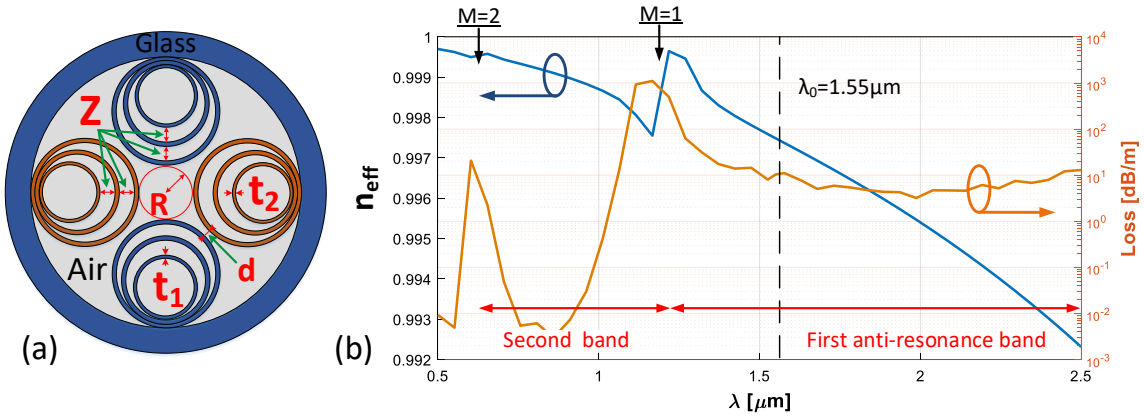

Figure 5.4. (a) Bi-thickness NANF and its design parameters, **(b)** simulated optical performance of a uniform NANF with $t_1 = t_2 = 0.6\ \mu m$, R=7 μm, d=1.5 μm and Z =0.65R.

As t_2 continues to increase, its associated resonance frequency reaches λ_0 , which induces a large loss, marked as "resonance region" in **Figure 5.5**. Beyond this point, the birefringence repeats the previous pattern, with fairly large ($>10^{-4}$) positive and negative values achievable. However, in this case the horizontal tubes operate in a higher anti-resonance band (second band when $t_2/t_1 = 1.5-2.3$, or third band when $t_2/t_1 = 2.7-3.6$). Moreover, a zero birefringence crossing is obtained for certain thicknesses. Interestingly, as **Figure 5.5 (a)** shows, while the vertical polarization (V-pol) experiences a similar loss as for $t_2/t_1 \approx 1$, the loss of the horizontal polarization (H-pol) decreases by as much as two orders of magnitude; a feature that can be exploited in a polarizing fibre design.

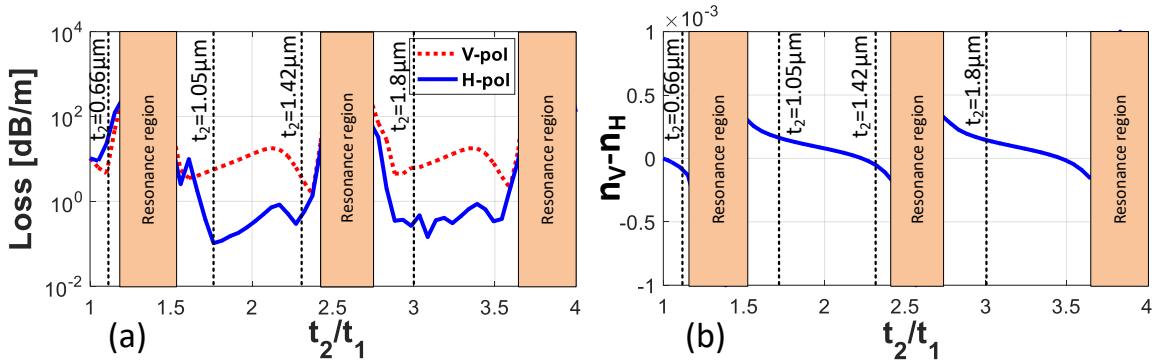

Figure 5.5. Optical properties of the NANF in **Figure 5.4 (a)** (t_1=0.6 μm, R=7 μm, d=1.5 μm, z=0.65R) at λ_0 =1.55 μm as t_2/t_1 varies between 1 and 4: **(a)** polarization mode loss, **(b)** birefringence (i.e. difference between effective refractive index of vertical polarization (n_V) and horizontal polarization (n_H)).

As shown above, sweeping t_2 provides a good design tool to find the highest possible birefringence at a single wavelength for a pre-determined t_1. However, the effect of the initial choice of t_1 on loss, and the mutual effect of t_1 and t_2 on the bandwidth over which

a large birefringence is achieved are not fully explained by the above picture. In the next section, the characteristic profile of different combinations of fibres are studied in order to draw a clearer picture of the role of each design parameter.

5.3.2 Bi-thickness NANF: a systematic study

In order to study the behaviour of the fibre for different combinations of thicknesses (t_1, t_2) and understand the working regimes in each case, the spectral characteristics (i.e. loss and birefringence vs wavelength) for the highlighted combinations of thicknesses (t_1, t_2) from **Figure 5.5** by vertical dashed lines are simulated. Each combination case represents a different working regime in order to highlight the mutual effect of t_1 and t_2 on loss, birefringence and bandwidth. **Figure 5.6** shows the results for fibres with t_1 =0.6 μm, and t_2 =0.66, 1.05, 1.42 and 1.8 μm, alongside the non-birefringent NANF case (**Figure 5.6 (a)**). In order to define the desired fibre characteristics, a practical working condition for the fibres has been defined, where the combination of birefringence and loss is reasonable. That is a loss lower than 1 dB/m (practical loss for most short length applications) and a birefringence with a beat length smaller than 15.5 mm (corresponding to a birefringence of 10^{-4} at 1.55 μm - the same order of magnitude as conventional solid-core PM fibres). These regions correspond to below the red dashed-line in the loss curve and outside the red dashed-line box in the birefringence plots.

Starting with the case t_2=0.66 μm, the loss shows only a slight difference for the perpendicular FM polarization and some birefringence starts to appear, although this is still rather modest in magnitude, as shown in **Figure 5.6 (b)**. The fibre therefore does not meet the defined loss and birefringence criteria.

Beyond a certain thicknesses, the resonance region of the horizontal tubes falls after λ_0. For t_2=1.05 μm, a large birefringence and acceptable loss can be observed as shown in **Figure 5.5**. **Figure 5.6 (c)** shows the optical properties of the fibre in this case. Here, the second resonance wavelength of t_2 has become large enough to reach the first resonance wavelength of the thinner tubes (t_1) ($m_{t_2}=2$ in **Figure 5.6 (c)**). The fibre has an acceptable low loss window in the Hi-Bi region between the two resonances $m_{t_2}=1$ and 2. In fact, as shown earlier, only one polarization of the fibre has a lower loss as compared to the symmetric fibre. This behaviour can be explained by the fact that the loss associated with each polarization of a FM is mainly controlled by the membranes perpendicular to the electric field of the mode, and operation in the second window

creates a lower leakage loss than in the first one. That is, in this case, the losses of the horizontal/vertical polarization modes, which are perpendicular to the thicker/thinner tubes (t_2 / t_1), are determined mainly by the anti-resonance condition of the perpendicular tube, respectively.

As a result, compared to the uniform NANF, the H-polarization experiences a lower loss as the thicker tubes (t_2) are working in the second anti-resonance band, while the loss of the V-pol is dominated by the thinner tubes (t_1), which operate in the first anti-resonance band and shows higher loss. In other words, the bi-thickness fibre operates on each individual polarization in the same way as a uniform fibre with tubes as thick as the tubes perpendicular to the electric field of that polarization.

Since the overlap between second and first anti-resonance bands of t_2 and t_1 respectively provides a good window of operation, a study is performed on the possibility to shift the first resonance wavelength of t_2 further towards longer wavelengths in order to widen its second anti-resonance band. To examine this approach, a bi-thickness fibre with t_2=1.42 μm is simulated (see **Figure 5.5**), with the results shown in **Figure 5.6 (d)**. At a first glance, the bandwidth of low loss operation has increased. However, the birefringence of the fibre has significantly reduced. A closer look reveals a zero birefringence crossing in this region. This is a characteristic feature of this region, which essentially limits the bandwidth of high birefringence achievable. It is caused by the fact that the second window is narrower than the first and hence has a steeper dispersion, which inevitably crosses that of the first window.

To include other possibilities and to study a broader span of thicknesses, t_2 = 1.8 μm is finally chosen from the third region of **Figure 5.5** with high birefringence and low loss. In this case, as it can be seen in **Figure 5.6 (e)**, three anti-resonance bands of t_2 overlap with the first anti-resonance band of t_1. While the first one (at λ > 3 μm, not shown) has a very high loss, the second and third bands show low loss operation. In this case, similar to the previous case (t_2=1.42 μm), a zero-crossing occurs in the second band which limits its bandwidth significantly. However, there is a small high birefringence window overlapping with a low loss band, which provides a good operational window in the third anti-resonance band, as shown by the green arrows in **Figure 5.6 (e)**. Here, some features are noticeable in the characteristic profile of this fibre. For instance, the third anti-resonance band shows almost identical birefringence and loss profiles to the second band in the case with t_2=1.05 μm, which demonstrates that it is possible to achieve Hi-Bi even in the same outer locked field phase condition (third band over first

band), see [29]. In other words, the existence of the "hybrid" regime [133] is not necessary to achieve Hi-Bi and low loss simultaneously. However, as the bandwidth of the third anti-resonance band is intrinsically smaller than the second one, the achievable birefringence bandwidth in this region is generally narrower.

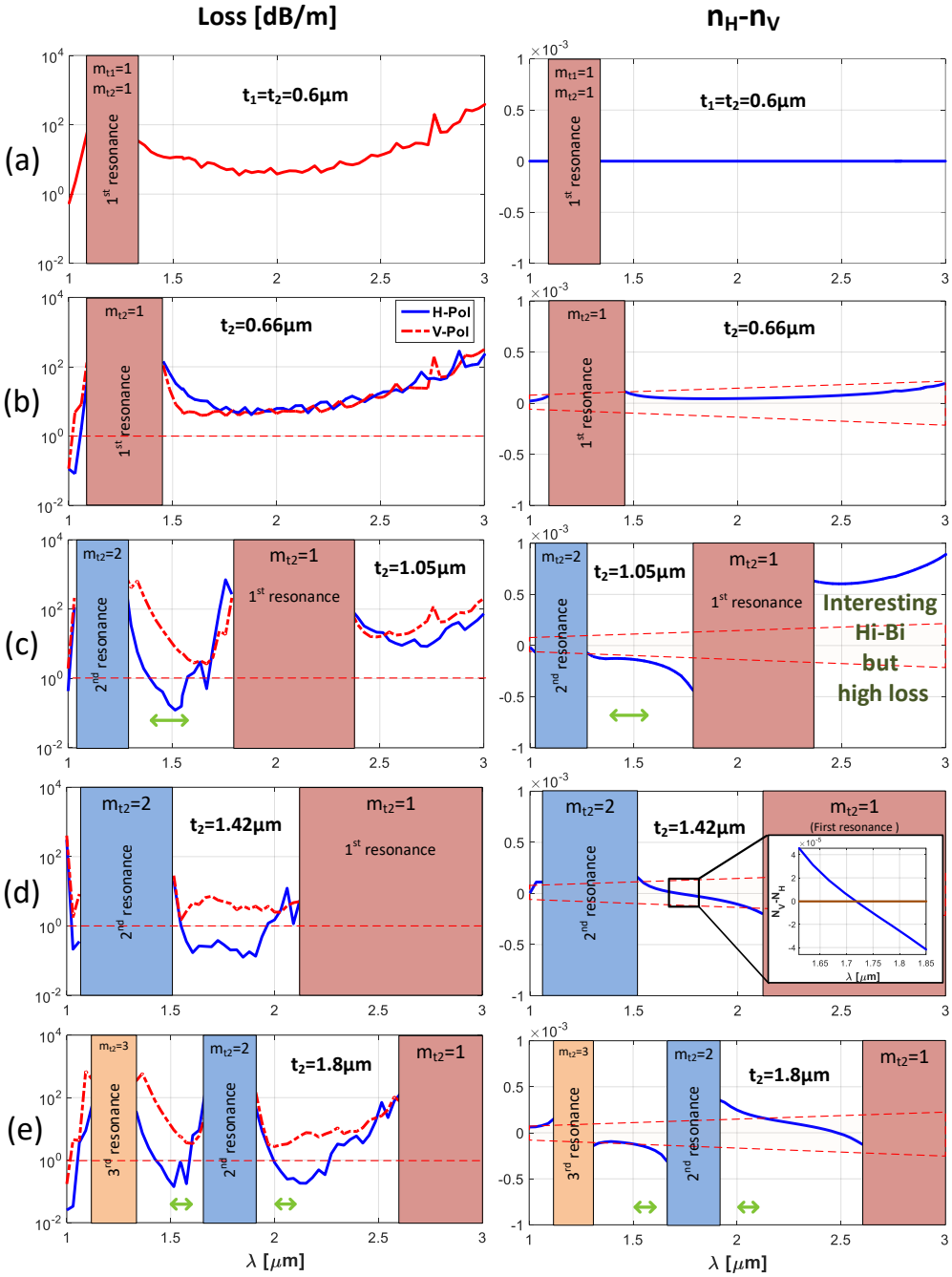

Figure 5.6. Simulated loss and birefringence profile of a bi-thickness 4 tube NANF with t_1=0.6 μm, R=7 μm, d=1.5 μm and t_2 = 0.6, 0.66, 1.05, 1.42 and 1.8 μm ((a) to (e) respectively). The red dashed line in the loss profile shows 1 dB/m and the red dashed lines in the birefringence profile indicates a beat length equal to 15.5 mm (roughly the birefringence of a conventional solid-core PM fibre). The green arrows show the defined practical operating window with loss lower than 1 dB/m and beat length larger than 15.5 mm.

Amongst all explored scenarios, just three practical regions can be used to simultaneously achieve Hi-Bi and low loss, as shown by green arrows in **Figure 5.6**. A) The region right after, where the second resonance wavelength of t_2 and the first resonance wavelength of t_1 overlap (case t_2=1.05 μm); B & C) The regions where the third and second anti-resonance band of t_2 and the first anti-resonance band of t_1 overlap (case t_2=1.8 μm). Although the regions of interest show high birefringence and low loss, their bandwidth is limited not only by the intrinsic bandwidth of their anti-resonance band, but also by the abrupt loss increases near the resonance regions. Additionally, it is shown in this study that shifting the second resonance wavelength away from the first one has some limitations due to the presence of a birefringence zero-crossing, which prevents ultra-broad band operation (**Figure 5.6 (d)**).

Figure 5.6 also shows another region of potential interest, the broad Hi-Bi region in the first anti-resonance band of the fibre with t_2=1.05 μm (**Figure 5.6 (c)**). This spectral range has intrinsically the largest possible bandwidth between all the cases as it is placed in the first anti-resonance band of both t_1 and t_2, simultaneously. However, despite its Hi-Bi and broadband feature, this region suffers from a high loss because it is close to the edge of the resonance wavelength of t_2 and operates in two different parts of the same anti-resonance band of t_1 and t_2. The next section focuses on improving the loss of this region.

5.3.3 Modified bi-thickness NANFs

In order to achieve broadband and large birefringence that benefits from the potential of the first anti-resonance band, its large loss needs to be overcome through a modified design. Here, I propose a structure that has reduced loss at the edge of an anti-crossing by eliminating the in-phase resonant layers. The proposed structure exploits anti-resonant inner tubes operating at the optimum point to minimize the loss in the first anti-resonance band, while the birefringence is still induced by the change in the thickness of the outer tubes. **Figure 5.7 (a)** shows the proposed modified structure and its design parameters. **Figure 5.7 (b, c)** show the performance of the proposed fibre with similar parameters as those presented in **Figure 5.6 (c)**, alongside the properties of a normal bi-thickness fibre with similar parameters, shown in **Figure 5.7 (d)** (a duplicate of **Figure 5.6 (c)** for ease of comparison).

A significant loss reduction is achieved in the first anti-resonance band of the new design, reducing the minimum loss below 1 dB/m, while the loss increases in the second

anti-resonance band compared to the previous fibre, as shown in **Figure 5.7 (c)**. Differently from the bi-thickness structure of **Figure 5.4 (a)**, in this arrangement, similar thickness t_1 of all the inner tubes guaranties an improved in-phase field confinement with lower loss in the first anti-resonance band, whilst a large birefringence through the outer tubes (t_2) is achievable. In the proposed structure, the dominant contribution to confinement is provided by t_1 for both polarizations, while in the original bi-thickness structure, t_1 and t_2 almost independently control the loss of the perpendicular polarization modes. This feature in the new design not only gives the ability to minimize the loss by optimizing only one thickness, but also increases the possible tuning range of t_2 to provide larger and broader birefringence outside its resonance wavelength by eliminating the strong dependency of loss on this parameter.

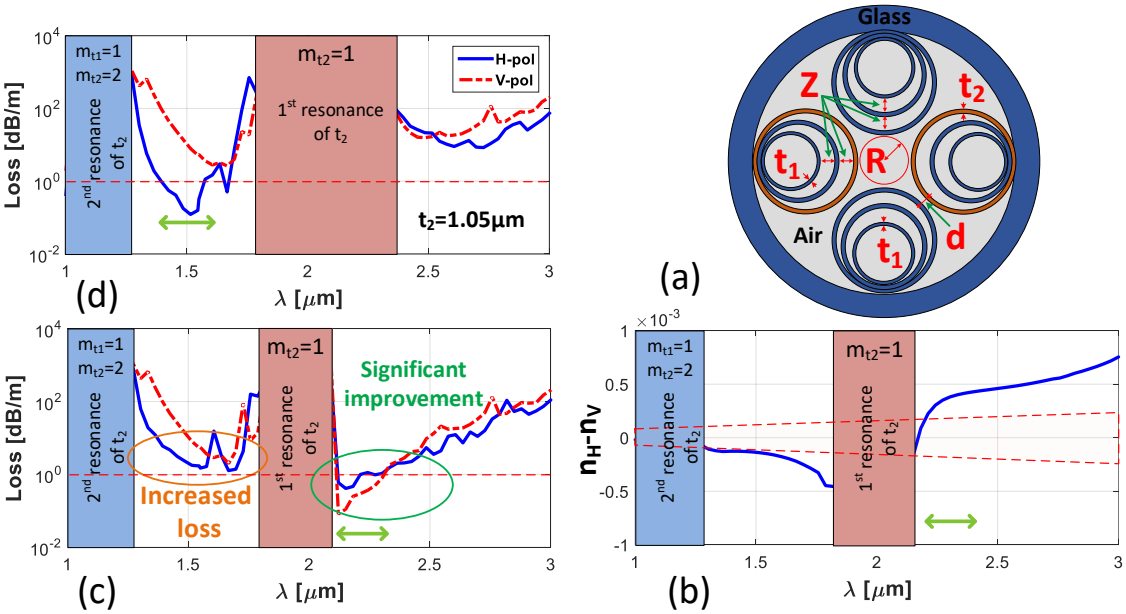

Figure 5.7. Proposed modified bi-thickness NANF: **(a)** structure; **(b)** birefringence; **(c)** loss of the proposed NANF with the same parameters as in **Figure 5.6 (c, d)** and **(d)** loss of standard bi-thickness NANF (duplication of **Figure 5.6 (c)** for comparison). Anti-resonant field confinement by inner tubes of thickness t_1 provides a significant improvement in the loss of the first anti-resonance region.

Although the design in **Figure 5.7** shows improvements in terms of loss and birefringence in the first antiresonant window, its parameters are not optimized for the lowest loss and largest operating bandwidth. To obtain the optimum design at the operating wavelength λ_0 =1.55 μm, the procedure is started by considering a uniform NANF with single thickness t_1. Eq. (1) is used to calculate a starting value for t_1. Then, the thickness t_1 is refined using a parametric sweep simulation to achieve the lowest loss at the first anti-resonance band, which resulted in t_1=0.372 μm. Then the thicker

tubes with thickness t_2 are introduced in the design. Using another parametric sweep similar to **Figure 5.5**, t_2 was optimized to provide the highest birefringence. The result is a bi-thickness 4-tube NANF with t_1=0.372 µm, t_2 =1.7×t_1, R=7 µm, d=1.5 µm and $Z = 0.65R$. **Figure 5.8** shows the simulated properties of the optimized Hi-Bi NANF with improved loss in the first anti-resonance band around λ_0 =1.55 µm.

This design and method, not only reduces the loss for both polarizations over several hundred of nm, but also increases the birefringence of the fibre simultaneously. Using this design strategy, an anti-resonant hollow core fibre with ultra-broadband high PMB and sub dB/m loss is achieved. The fibre has a birefringence of ~1.5×10^{-4} over a ~550 nm bandwidth (loss < 1 dB/m) with a minimum loss as low as 0.043 dB/m at λ_0. The proposed fibre is therefore ideally suited for ultra-broadband applications requiring polarization maintenance over almost all optical communication bands (E, S, C, L and U bands).

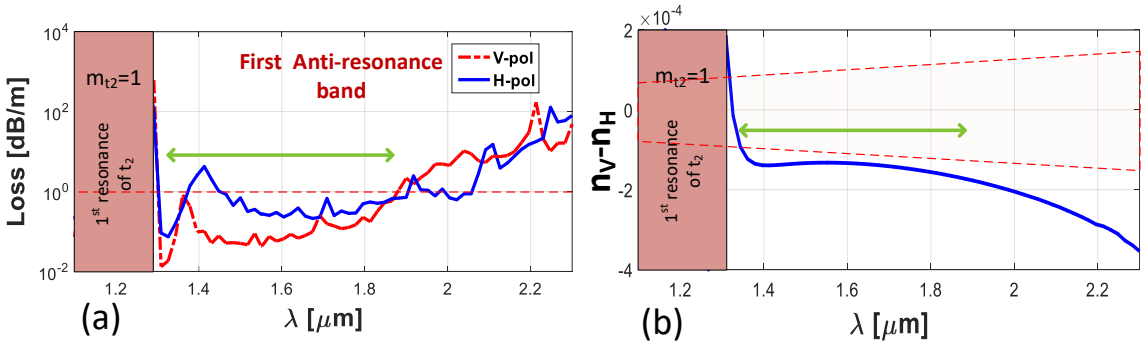

Figure 5.8. (a) Loss and **(b)** birefringence of the optimized new proposed design for λ_0 =1.55 µm with R=7 µm, Z=0.65R, d=1.5 µm, t_1=0.372 µm and t_2=0.633 µm. The fibre shows a very broad bandwidth (~550 nm) PMB =~1.5×10^{-4} with a loss <1 dB/m.

Figure 5.9 shows the mode profile of both FM polarizations at λ_0. As can be seen, the outer horizontal thicker tubes (t_2) provide lower reflectivity for the horizontal mode, as they operate at the edge of the resonance window, allowing some of the field to leak. However, the inner rings, which operate in perfect anti-resonance conditions, reduce the leakage of the field. As a result, the loss of the horizontal mode is only slightly higher than that of the vertical one whereas a large birefringence is obtained.

In practice, the thickness of tubes in the proposed design are achievable and have already been demonstrated in simpler single ring tubular fibres [162]. However, in order to relax the requirement for thin tubes and to allow easier fabrication, one can design the fibre to operate in the second anti-resonance window, if the full 550 nm of low loss PM operation is not strictly required. **Figure 5.10** shows the optical properties

of such an alternative fibre with thicker tubes operating in the second anti-resonance band (t_1=1.172 µm, t_2=1.42 µm).

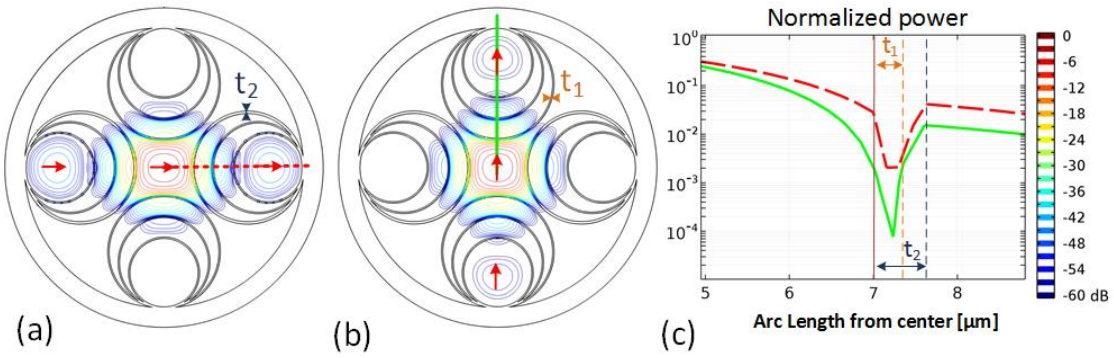

Figure 5.9. 3-dB contour plots of the normalized power of the fundamental mode with **(a)** horizontal and **(b)** vertical polarizations (red arrows indicate the direction of the electric field) at λ_0=1.55 µm for the optimum proposed design. **(c)** Cross-sectional profile of the normalized power in each polarization direction. A larger field penetration through the outer horizontal tubes (t_2) than the vertical ones (t_1) is clear while the horizontal inner tubes (t_1) play a critical rule in confining the field and reducing the loss.

This fibre shows an almost constant PMB value as large as ~1.45×10^{-4} with loss < 1 dB/m over a ~300 nm bandwidth covering the entire C, L and U optical communication bands. The loss in this design reaches its lowest value of 0.006 dB/m at λ = 1.57 µm, and is around 0.01 dB/m across the C+L bands. In comparison, based on the simulations, a fibre with a similar core size in the hybrid regime (see Section 5.3.2 and [133]) has a loss value that is more than 20 times larger due to the presence of leakier inner tubes and the close spectral proximity of the resonant edge of t_1 and t_2. Although the design of **Figure 5.10** shows a narrower bandwidth than the first band design (**Figure 5.9**), it presents some additional benefits, such as a lower minimum and polarization dependent loss, and likely greater mechanical robustness because of its thicker tubes.

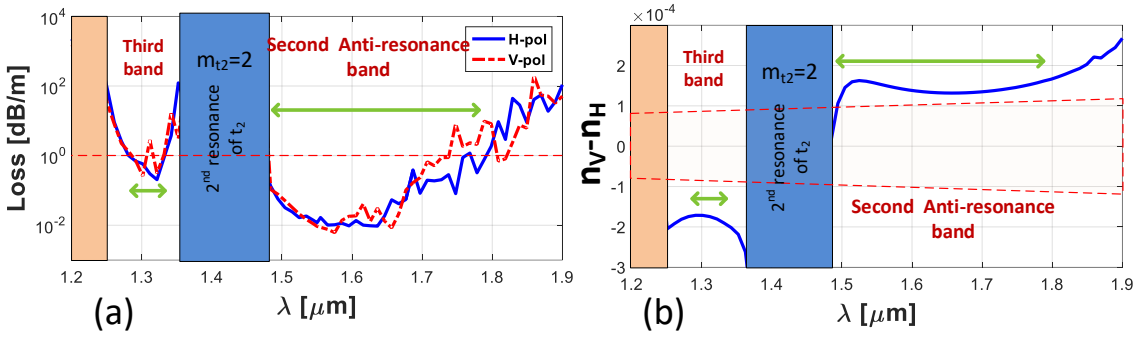

Figure 5.10. (a) Loss and **(b)** birefringence of the optimized new proposed design with thicker tubes at λ_0=1.55 µm with R=7 µm, Z=0.65R, d=1.5 µm, t_1=t_2=1.172 µm and t_2 = 1.42 µm. The fibre shows a large bandwidth (~300 nm) PMB = $\sim 1.45\times10^{-4}$ with a loss < 1 dB/m.

5.4 Single polarization designs

In addition to PMB, some applications like ultra-sensitive sensing or gyroscopes, or ultra-high power single polarization laser delivery may require a large polarization extinction ratio. The large birefringence in the fibre designs proposed so far decreases the beat length and reduces the possibility of coupling between polarization modes, which allows the input polarization state to be maintained. Here, I propose a modification to the abovementioned polarization maintaining Hi-Bi NANF to provide both PMB and a large polarization extinction ratio, which transforms it into a polarizing fibre. The new structure not only has the favourable Hi-Bi characteristic but also shows a very large polarization dependent loss (PDL) that can remove the unwanted polarization component of the input light, as well as limiting distributed inter-polarization coupling due to surface roughness and micro-bends [157].

The proposed modification is based on a well-known method used to strip higher order modes from a few moded fibre [163, 164], which is adapted to achieve "polarization dependent mode stripping". In this method, a specific polarization of the fundamental core mode is selectively coupled into a lossy cladding mode, while the orthogonal polarization experiences almost no change. Here, the two main structural features of the former proposed 4-tube NANF are fundamental.

First, the induced large birefringence in the fibre creates an opportunity to clearly separate the effective index of the two polarizations, of which only one is index matched and out-coupled to lossier cladding (i.e. guided inside the tubes) modes. Based on the similarity of the guidance mechanism in NANFs and in simpler hollow core fibres made of a borehole in glass, it is possible to calculate the necessary geometrical specifications

to match the index of the core and cladding modes [131]. n_{eff} of the FM in a single tube can be calculated with the following exact equation [138]:

$$n_{eff} = \sqrt{1-\left(\frac{U_0}{k_0 R}\right)^2}. \qquad (5.3)$$

where $k_0 = 2\pi/\lambda$, R is the core radius and U_0 is similar to Eq. (2.1). As it is clear from this equation, the effective index is related to the size of the tube. Therefore, in order to have index matching between the core mode and one of the peripheral tubes in a NANF, they must have approximately the same size.

Here, the second useful feature of the 4-tube NANF is the very large size of the nested tubes. This allows the described mode matching to be engineered in the design. In fibres with more than four nested tubes, although the cladding tubes are large enough to strip the higher order modes [57, 163, 164], they are too small to enable fundamental mode out-stripping. Following this idea, the radius of two opposite inner cladding tubes are modified in order to introduce index matching to the polarization with the highest loss in the Hi-Bi NANF of **Figure 5.8**.

Figure 5.11 shows the structure and mode profiles of both high and low loss polarizations of the proposed polarizing NANF (P-NANF). The modified nested structure with a different distance (Z_1) between the two innermost rings in the vertical direction opens up a matching window for vertical polarization to couple to the cladding mode. Consequently, vertically polarized light leaks through the outer tube. This does not occur for the light on the Horizontal polarization, **Figure 5.11 (b, c)**.

Figure 5.12 shows the simulated PMB, the loss of each polarization and the loss ratio between the two polarization for a fibre with R=7 μm, $Z = 0.65R$, $Z_1 = 1.74R$, d=1.5 μm, t_1=1.172 μm, and t_2=1.42 μm that has been designed for operation around λ_0=1.55 μm. Here, the polarization loss ratio (PLR) factor is plotted instead of the PDL as this ratio can provide a better measure of the effectiveness of the polarization stripping effect.

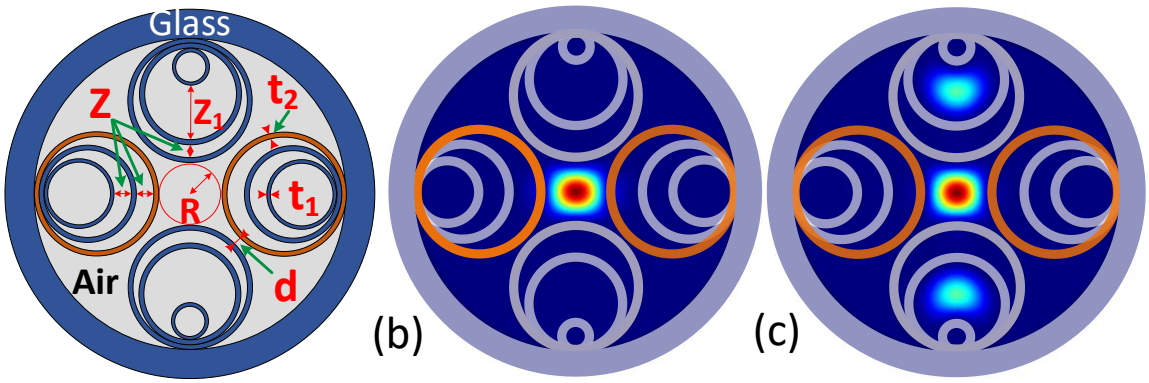

Figure 5.11. (a) The proposed structure for polarizing NANF (P-NANF) and its **(b)** low loss polarization (horizontal), and its **(c)** high loss polarization (vertical). The coupled field to the cladding tubes in the vertical polarization increases the loss significantly.

The modified design shows a relatively large bandwidth of ~100 nm with an almost constant PMB of $\sim 1.5\times10^{-4}$. The loss of the low loss polarization is less than 1 dB/m and the design exhibits a PLR of about 1000 at the wavelength of 1.55 µm. A polarizing window of ~10 nm with PLR > 100 can completely eliminate any undesirable cross-coupled polarization over a sufficiently long propagation distance. The fibre can therefore provide an almost pure polarized output, regardless of the input polarization state, which may have applications in, manufacturing and machining as well as in high precision gyroscopes that require modes with relatively pure linear-polarization.

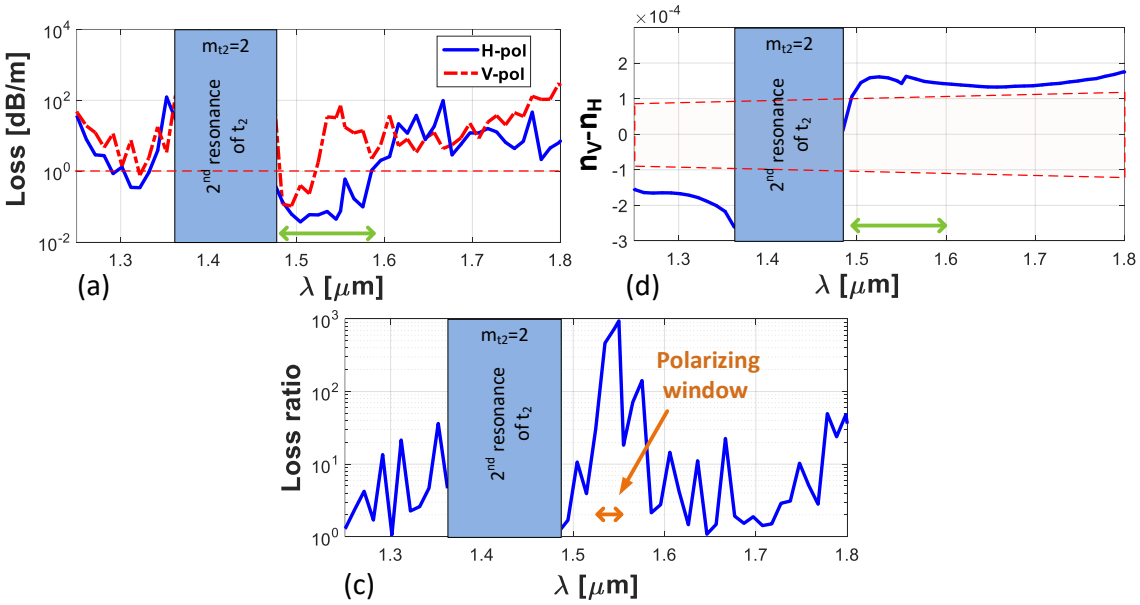

Figure 5.12. (a) PMB, **(b)** loss and **(c)** PLR (High-loss/Low-loss) of the optimized P-NANF at λ_0=1.55 µm with R=7 µm, $Z=0.65R$, $Z_1=1.74R$, d=1.5 µm, t_1=1.172 µm and t_2 =1.42 µm. The fibre has a bandwidth of ~100 nm with PMB ~1.5×10^{-4} and loss of the low-loss polarization <1 dB/m. The PLR at λ_0=1.55 µm is 1000 which gives the fibre a strong polarizing property.

5.5 Conclusion

In this chapter, a detailed study of various ways to obtain broadband polarization maintaining capability in antiresonant hollow core fibres was presented, in particular for the NANF structure. It was shown that achieving birefringence through asymmetric core designs adopted following the form-birefringence strategy in solid-core PM fibres is not effective in ARFs. Next, a different strategy, used in birefringent PBG fibres, was adapted where the geometrical symmetry of a 4-tube NANF is broken by introducing a bi-thickness design. To study the induced birefringence in this design, a decomposition analysis was introduced through which it was shown that the thickness of tubes along the horizontal and vertical directions control, almost independently, the properties of the two respective polarizations. This approach provides a better understanding of the role of the individual thickness parameters in this structure as well as a method for practical fibre design.

Using the developed method, a region with potential for ultra-broadband high birefringence was identified within the first antiresonant window of a bi-thickness NANF. By proposing a radical design, it is shown that the loss in this region can be mitigated, despite the small core size necessary for large birefringence. The proposed design not only offers a high birefringence ultra-broadband spectral window ~550 nm (that is almost 6 times boarder than ever reported in a birefringent HC-ARF [133]) with birefringence as large as 1.5×10^{-4} and a loss of less than 1 dB/m, but it also allows for losses as low as 0.04 dB/m at a wavelength of 1.55 μm. In addition, by sacrificing some bandwidth, an alternative design was proposed with thicker tubes operating in the second anti-resonance band that achieves an order of magnitude lower loss (0.004 dB/m at the wavelength of 1.57 μm) and a large bandwidth (~300 nm).

In order to add a polarizing effect into the design, a new polarization dependent mode stripping mechanism was introduced into the proposed bi-thickness NANF structure. The P-NANF structure offers a polarization dependent loss ratio of 30 dB at the operating wavelength of 1.55 μm with a minimum loss of 0.076 dB/m and a low loss bandwidth of 100 nm. With such a high loss ratio, the fibre can act as a polarizer for any unpolarized input over very short propagation distance, which would be of interest in applications requiring extremely high polarization extinction ratio.

Although the proposed fibres have been designed and optimized to operate in the telecommunication wavelength bands (i.e. around 1.55 μm), the geometrical scalability of ARFs with the operating wavelength allows a straightforward application of similar

design scenarios to other wavelengths more relevant to other applications, e.g. 1 μm for high power laser delivery or visible wavelengths for biomedical nonlinear endoscopy.

Chapter 6: Raman frequency conversion towards mid-IR in gas-filled NANF

6.1 Introduction

Generating high power lasers in the mid-IR, especially at longer wavelengths, is a challenging task mainly due to lack of rare-earth transition in this range of wavelengths. The typical sources in the mid-IR range are supercontinuum lights generated in soft glass fibres (e.g. chalcogenide) with fairly low to moderate power. On the other hand, gases with very high damage threshold and long-range Raman shift can be very good hosts for generating a long-range frequency conversion from high power conventional lasers to the mid-IR with fairly high power output. However, as mentioned before, the low Raman gain of gases required either a very high power excitation pump or long interaction path. Although the former has limited the use of gases for practical applications for many years, the development of hollow core fibres introduced a new opportunity by introducing a very long and confined light and gas interaction path.

This chapter focuses on studying the generation of mid-IR light in gas-filled hollow core fibre by Raman frequency conversion. In particular, the goal is to achieve efficient Raman conversion from 1.55 μm to mid-IR (i.e. 4.35 μm) within gas-filled optimized NANF, as presented in Chapter 4. Therefore, after selecting a proper gas as a filling material for the fibre, in order to achieve high Raman conversion efficiency in the designed silica NANF in Chapter 4, the final design parameter (R) requires optimisation. To correctly model the nonlinear pulse propagation in this gas-filled fibre, the nonlinear behaviour of the gas needs to be studied. Consequently, a general model for the Raman characteristic of the gas (i.e. H2), which can be embedded into the GNLSE, needs to be developed and verified. Finally, by means of the developed model, the influence of pulse characteristics, such as pulse length, pulse shape and power are studied on the efficiency of the process to achieve higher Raman conversion efficiency.

To achieve such targets, this chapter is structured as follow: in section 6.2, after studying different gases, hydrogen as a glass-friendly and accessible gas with the largest Raman frequency shift is selected in considering erbium-doped fibre laser (1.55 μm) as the pump. The proposed mid-IR optimized NANF in Chapter 4 has been optimised as hydrogen-filled fibre to maximise the frequency conversion towards the

mid-IR, in section 6.3.1. In section 6.3.2, to study the pulse propagation and different aspects of pulse properties on efficiency of conversion, a unified model is adapted for the GNLSE. After verification of the model, the optimised hydrogen-filled NANF has been studied for generating 4.35 μm laser. It is shown that, with an average peak power pump (10 kW) and duration of 6 ns, it is possible to achieve up to 68% of quantum efficiency at 4.35 μm and, with pulse shape modification, it is possible to achieve efficiency as high as 78%. Ultimately, although the fabrication of NANF is not yet fully developed, a first in-house-made prototype, which is not optimised for this purpose, has been modelled and more than 20% of quantum efficiency is predicted in this fibre. Moreover, the system can be fully fiberized, as both the pump laser and the Raman convertor are fibre-based.

6.2 Raman scattering and frequency shift in common gases

Considering the criteria and objective of this work, selecting a proper gas for this project is a challenging process. On one hand, the nonlinear optical property of the gas, in particular Raman characteristics, should be superior, such as: high Raman gain, absence of absorption lines at the operating wavelength and significant Raman shift. On the other hand, practical limitations reduce the options in selecting the proper gas for the purpose of this work, such as: availability (complexity of producing the gas), feasibility (some gases are not glass-friendly), operating temperature and pressure (some gases need very low or high temperature and very high pressure for reasonable Raman efficiency).

According to objective of the project, the desired filling gas is required to perform an efficient Raman frequency shift with as low pump power as possible to convert near-IR pulse into the mid-IR, while meeting feasibility factors, such as: glass-friendly (in particular there should not be any chemical reaction between gas and silica or tellurite); affordability (low fabrication and integration cost); and practicality (requiring medium pressure and room temperature operating condition). According to these expectations and also considering recent experimental results from other pioneering groups in this field [5, 31, 34, 35], a few options for the filling gas have been selected which can be considered as potential candidates.

Table 6-1 presents the selected Raman active gases with their Raman parameters, such as: Raman excitation mode, Raman gain in related excited state and Raman linewidth [165]. In order to use the presented data in this table, it is important to emphasize on dependency of Raman gain of gases on the wavelength of pump laser. In fact, while the

values for Raman gain have been presented at specific wavelength, their use can be extended to other wavelengths by considering the approximately inverse proportional relationship between wavelength of excitation laser and Raman gain($g_R \propto 1/\lambda$) [1, 79]. In addition to excitation wavelength, the values of gain and linewidth of Raman response are strongly dependent on the number of gas molecules involved in the Raman process. It is intuitive to relate the number of molecules in a constant volume of a certain gas to its pressure. However, the number of molecules or, in more precise form, the number density of molecules is described by "Amagat" unit (represented as "amg"). Amagat unit is defined as the number of ideal gas molecules per unit volume at 1 atm pressure and 0 °C, which can be presented as $1\ amg = 2.6867805\times10^{25}\ m^{-3}$ $= 44.615\ 036\ mol/m^3$. For an ideal gas, the number density of molecules (ρ) at temperature (T in Kelvin) and pressure (P in atm) can be describe by $\rho = PT_0/(P_0T)\ amg$ where $T_0 = 273.15\ K$ and $P_0 = 1\ atm$. Although this linear relation between pressure and molecule density can suggest the usage of pressure instead of Amagat unit (number density), in practice the gases are not ideal and such linear relation does not hold at high pressures or temperatures. Therefore, since the Amagat is the correct representation of number density of molecules and it is used in literature in relation to Raman gain and linewidth for gases [165], the presented values in **Table 6-1** are related to Amagat unit.

Table 6-1: Raman gain parameters of selected gases at 25^{0}C [165]

Gas	Mode	Frequency shift (cm^{-1})	Linewidth (MHz)	Gain (cm/GW)	ρ ($amagat$)	λ_0 (nm)
H_2	Q(1) Vibrational	4155	$309/\rho + 52.2\rho$	2.5 ± 0.4	20	532
	S(1) Rotational	587	119ρ	1.2	> 20	350
SiH_4	Q branch (v)	2186	15	0.19ρ	---	248
N_2*	Q branch (v)	2327	22.5	0.3ρ	---	248
O_2	Q branch (v)	1552	54	0.012ρ	---	248
GeH_4	V1	2111	15	0.27ρ	---	248
D_2*	Q(2)	2987	66ρ	1.9	> 60	350
CH_4	V1	2917	9000	0.12ρ	$1 < \rho < 10$	248
CF_4	V1	980	21	0.008ρ	---	248
SF_6	V1	775	30	0.014ρ	---	248

* The largest frequency shift

Although, some works involving CF_4 and SF_6 have been demonstrated with promising results in frequency conversion [31, 166], they are generally in the visible or near-IR range of the spectrum. However, in order to achieve practical results in this project, the chosen gas should have high Raman gain at mid-IR to compensate the intrinsic decrement in Raman gain at longer wavelengths (mid-IR) (Eq. (2.9)). Furthermore, to benefit from high power near-IR pump sources, the gas should have large frequency shift to be able to generate mid-IR range laser. Considering these two major criteria, hydrogen has the largest vibrational Raman gain and frequency shift among the listed gases in **Table 6-1** and it can satisfy both conditions simultaneously.

Although many Raman processes, such as frequency conversion, frequency comb generation and Raman lasers in hydrogen-filled hollow core fibres, have been demonstrated experimentally [15, 32, 35, 96, 167], the majority of works are in the visible or near-IR regions. **Table 6-2** presents Raman gain, 1st Stokes frequency shift and linewidth of these three gases for pump laser at 1.55 µm for comparison.

Table 6-2: Raman parameters of H_2, CF_4 and SF_6 for pump at 1.55 µm.

Molecule	Raman Gain (cm/GW) @ 1.550 µm for P = 20 bar	Linewidh (GHz)	Shift (cm^{-1})/ Freq (THz)	1st Stoke (µm)	Raman gain/H_2 (Vib) gain	Note
H2 (Vib)	0.86	1	4155 / 124.5	4.35	1	
H2 (Rot)	0.41	2.3	587 / 17.6	1.7	0.48	
CF4	0.026	0.25	908 / 27.2	1.8	0.03	Very small gain
SF6	0.045	0.25	775 / 23.2	1.75	0.05	There is no data for absorption in the mid-IR

The advantage of hydrogen-filled HC fibres with excitation at 1.55 µm is that by using an erbium-doped fibre laser as the pump laser, it is, in principle, possible to achieve a fully fiberized mid-IR source. Also, by choosing a linear or circular polarisation excitation of hydrogen it is possible to generate different frequencies. In principle, in order to have an efficient Raman conversion, the bandwidth of the pump pulse should be narrower than the Raman linewidth, which, in the case of hydrogen, a *ns* long pulse is required and easily achievable by existing erbium-doped fibre lasers. The general idea of the experimental setup is shown in **Figure 6.1**. Also, there is the possibility of using the pressurised splicing technique for commercialisation of the system, as described in [15].

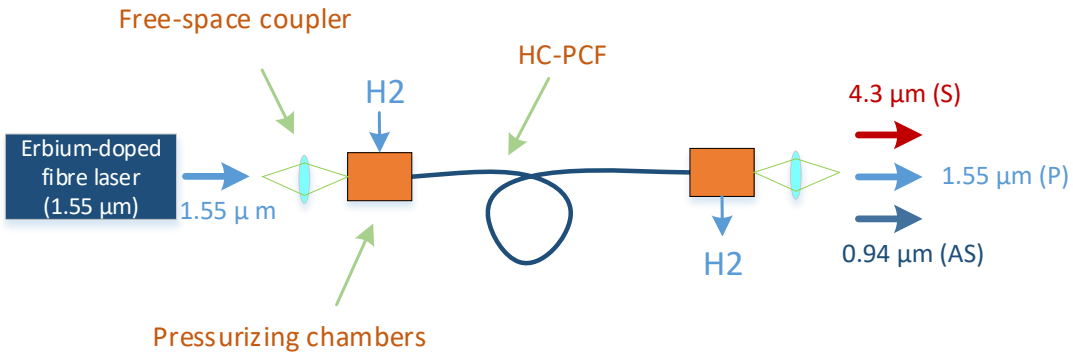

Figure 6.1. Schematic of experimental setup for frequency conversion in gas-filled HC-PCF with free-space coupling.

6.3 Exploring Raman frequency conversion in hydrogen-filled fibre

6.3.1 Efficiency analysis of designed NANF

To achieve optimum design for the highest Raman conversion in hydrogen-filled NANF, one may simply assume that, by reducing the core size of the fibre, the conversion gain will increase because of its inverse relationship with the square of core radius (i.e. increase of laser intensity). However, as presented in Chapter 4, the loss profile of the fibres with an anti-resonance guiding mechanism has strong relation with core size and dramatically increases as the core size is reduced. This can cancel out the high conversion gain achieved by reducing the core size. On the other hand, not only the fibre loss has direct effect on the net gain of the Raman conversion process, but also other factors, such as gas pressure and laser pulse intensity, have important effects on the Raman gain. Therefore, there is not a straightforward calculation for optimum core size and many factors need to be under consideration in the optimisation process, which are the main focus of this section and by taking all of the abovementioned factors in to account, an optimum design is proposed.

In general, the Raman frequency conversion in the simplest form and, in CW or quasi-CW regime, can be presented as a coupled equation of energy transfer from the main frequency of the pulse (pump) to the lower frequency part (Stokes), which at the steady-state regime, can be presented as (more detail [72]):

$$\frac{dP_P(z)}{dx} = -\frac{\omega_P}{\omega_S} g_R I_S(z) P_P(z) - \alpha_P P_P(z)$$
$$\frac{dP_S(z)}{dx} = g_R I_P(z) P_S(z) - \alpha_S P_S(z) \quad (6.1)$$

where, g_R is the Raman gain (m/W). $P_{P/S}$ and $\alpha_{P/S}$ are power and loss of the pump/first Stokes, respectively. $I_P(z)$ and $I_S(z)$ are the intensity of pump and 1st Stokes, respectively, defined by $I_{P/S} = P_{P/S} / A_{eff}$ with A_{eff} as effective fibre mode area. Although the Eq. (6.1) does not include other nonlinear effects and is a simplified form of the Raman process, it can provide a good starting point for optimization of parameters to achieve high conversion efficiency. Using this equation, in an undepleted pump approximation, the Stokes power at the end of the waveguide can be expressed as:

$$P_S(L) = P_{S0} e^{Gr(L)} \quad (6.2)$$

Here, P_{S0} is the initial power at the Stokes frequency at the input of the fibre, which can be vacuum noise in the absence of any input. $Gr(L)$ represents the 'net gain' of the Stokes (NGS) and is defined as: $Gr(L) = (g_R I_P - \alpha_s)L$. Here, the loss parameters are the collective loss of the waveguide and core material loss, which is dominated by waveguide loss (i.e. fibre loss) in the case of H_2-filled NANF. This definition highlights the dependency of NGS on characteristics of the waveguide, Raman gain of the gas and pump pulse intensity (I_P), which are important factors for the optimisation process. As a result, to achieve high NGS, one needs to have low loss, high gain and high pump pulse intensity (I_P). However, apart from pump power, which is generally limited by the laser source, the other two factors (gain and loss) are not entirely independent for a NANF design, and the fibre characteristics have a crucial effect on them.

As already discussed in the previous section, the loss of the NANF depends on many design parameters, such as: the tube thicknesses (t_s); distance of the nested tubes (d); number of nested tubes (n); the number of nesting elements (i.e. inner tubes) and their distance (Z); and, more importantly, the core radius (R) of the fibre. However, unlike core size of the fibre, which has direct impact on both the loss and nonlinear Raman gain, other design parameters (d, Z, t_s) have trivial effect on Raman gain while they can directly control the loss of the mid-IR NANF. The effect of these design parameters on the loss of the mid-IR NANF have already been discussed in detail and the optimised values for each parameter in mid-IR NANF made of silica and tellurite have been proposed in Chapter 4. Therefore, here, the focus is only on core size of the fibre, as a

key factor, to achieve higher NGS. Although loss of the designed NANF can be approximately calculated from previous results by scaling factor (R^{-8}) for large core radii ($>10\lambda$), the loss can be severely affected by overlap of the glass and core-mode field in small core sizes where the wavelengths become comparable with the core size or the fraction of power in the lossy glass become significant. Hence, a full FEM mode calculation of loss is needed to achieve accurate results at small core sizes. In addition, unlike the solid material, in gases, the number of molecules involved in the Raman process can be increased by increasing the pressure of the gas and cause Raman gain changes according to Eq. (2.9). Additionally, the increment of the molecules leads to larger refractive index, which is an important factor for the NANF guidance mechanism. Considering all these effects, the gas pressure should be included as a key parameter in the calculation of NGS and optimisation process.

In order to include the effect of the hydrogen refractive index in the loss calculation by the developed FEM modelling toolbox, the two term Sellmeier equation for hydrogen at fixed pressure and temperature (1 bar, 273 K) could be used as introduced in [168]. However, to include dependency of temperature and pressure in the refractive index of hydrogen, the presented model from [108] for other gases has been adopted and combined with the hydrogen dispersion equation at P_0=1 bar and T_0 =273 K (i.e. Eq. (7) from [168]) to achieve a more general form for refractive index of hydrogen:

$$n^2 = 1 + \frac{PT_0}{TP_0}\sum_{i=1}^{2}\frac{B_i\lambda^2}{\lambda^2 - C_i}. \tag{6.3}$$

where P and T are pressure in *bar* and temperature in *Kelvin* units, respectively. Here B_i and C_i are calculated by using data in [168] as: $B_1 = 1.6586\times10^{-4}$; $B_2 = 1.066\times10^{-4}$; $C_1 = 55.34\times10^{-4}\,\mu m^2$; $C_2 = 55.34\times10^{-4}\,\mu m^2$.

Although the range of experimental data used to extract this model is limited to 0.4-1.7 μm [168], due to lack of other data in the literature for higher wavelength, the same equation up to 4.5 μm has been used in this study. For the fibre itself, the relative Sellmeier model and material loss profile have been used, as presented in Chapter 4.

To study the effect of core size and pressure change on the loss of the fibre, the silica NANF is modelled by the developed FEM toolbox for optimum parameters from Chapter 4 by taking into account the hydrogen refractive index (Eq. (6.3)). **Figure. 6.2** shows loss of the silica NANF at pump (1.55 μm) and 1st Stokes (4.354 μm) of vibrational Raman in hydrogen vs core size of the fibre for a few gas pressures.

Unlike the loss at Stokes wavelength, the pressure change has noticeable impact on loss of the fibre at pump wavelength. This effect can be associated to the fact that the pump wavelength is at a region with high probability of the mode anti-crossing between core-mode and cladding-modes. This anti-crossing region is a characteristic of the NANF and exists at the longer wavelength side of the minimum loss in each anti-resonance transmission window of the fibre [169]. At this region, the guiding mode in the cladding tubes (cladding-modes) and leaky modes in hollow core share a very close wavelength-index space and the chance of their anti-crossing increases, which consequently increases the loss fluctuation, even for small change in wavelength or, in this case, core index change. It is worth mentioning that the presented loss in **Figure. 6.2** is the theoretical total loss considering confinement loss and material loss while, in practice, at very low end of the loss limit, which is at larger core sizes, other factors such as surface roughness scattering, bend loss, defect scattering, etc. become dominant. Moreover, as the core size increases, other air-gaps in the structure become larger and suitable for guidance and increases the chance of the mode coupling and the loss of the fundamental mode. Therefore, the calculated loss < 0.001 dB/m is not considered realistic and is indicated in **Figure. 6.2**

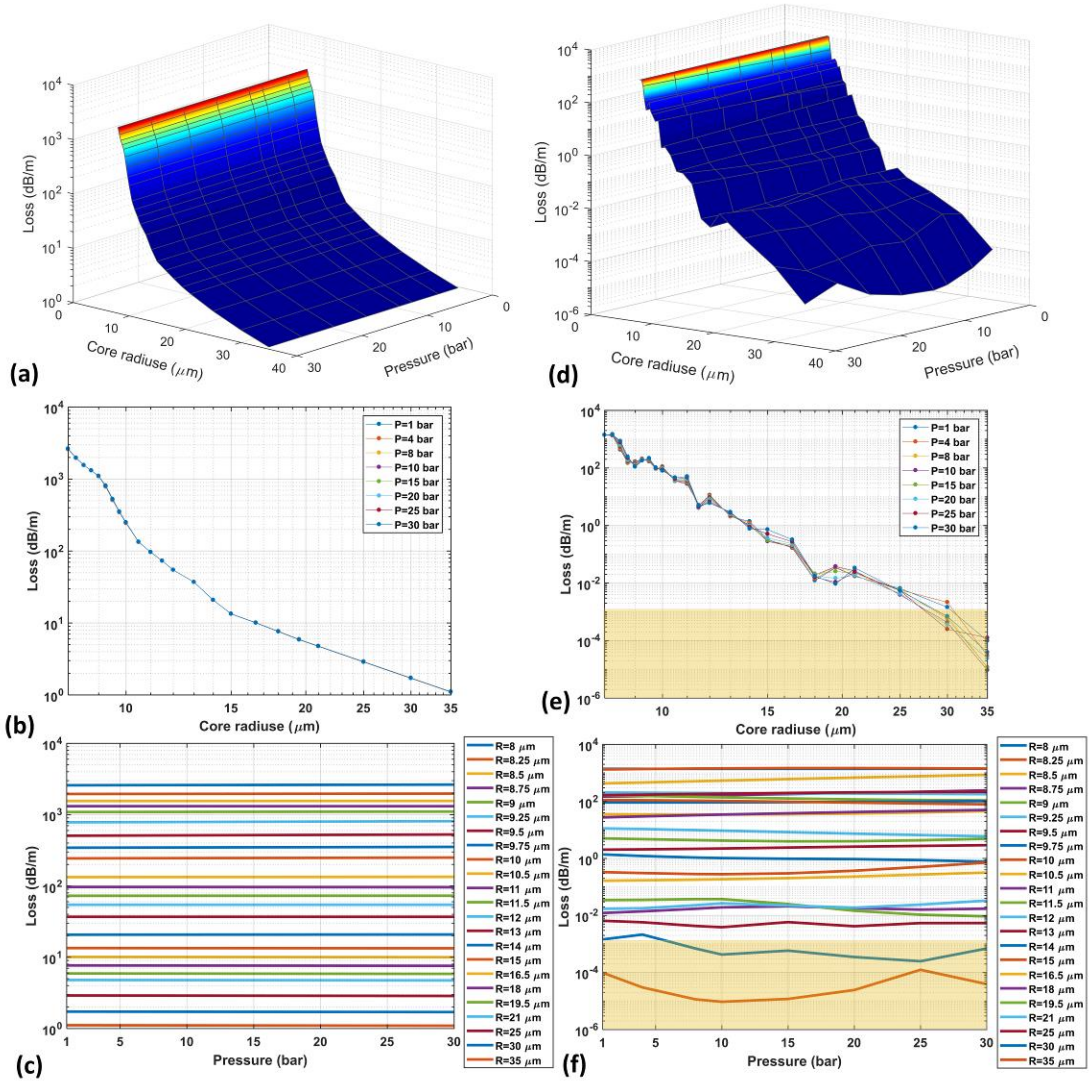

Figure. 6.2 Calculated loss of the hydrogen-filled NANF with n=6, d=4 μm, t_s=1.66 μm and optimum Z (**Figure 4.9**) at Stokes wavelength (4.354 μm) for **(a)** core radius and gas pressure. **(b)** and **(c)** represent the dependency of Stokes loss on core radius and gas pressure, respectively. **(d)** shows the loss of the fibre at pump power wavelength (1.55 μm) as a function of core radius and gas pressure, **(e)** and **(f)** representing the dependency of loss on core radius and gas pressure, respectively. The marked area in **(e)** and **(f)** shows the practical limit of low loss at 10^{-3} dB/m.

Another effect of pressure on NGS, in addition to the loss, comes from the pressure dependency of Raman gain of hydrogen, which should be considered in the calculation of the NGS. This dependency has been studied extensively and the wavelength, pressure and temperature dependent form of g_R is presented for hydrogen as [170]:

$$g_R = 9.37\times10^6 (52\rho/\Delta\upsilon)(K_B/0.658)(\upsilon_P - \Omega)(\upsilon_i^2 - \upsilon_P^2)^{-2}, \qquad (6.4)$$

$$\Delta\upsilon = (309/\rho)(T/298)^{0.92} + [51.8 + 0.152(T-298) + 4.83\times10^{-4}(T-298)^2]\rho. \qquad (6.4b)$$

where, $g_R(\upsilon_P, \rho, T)$ is the vibrational SRS gain of hydrogen at pump frequency (υ_P) in cm/W unit. Ω and υ_i denote vibrational and electronic resonance frequency equal to $4155\,cm^{-1}$ and $8.48\times10^4\,cm^{-1}$, respectively. ρ is the gas density in Amagat unit, which directly relates to pressure of the gas and T is the temperature of the gas in *Kelvin*. $\Delta\upsilon$ represents the vibrational Raman linewidth, which is of great interest and will be discussed in more detail in the following section.

Figure 6.3 shows the Raman gain of hydrogen at 1.55 μm for a range of pressures calculated by Eq. (6.4). At low pressure (< 5 bar), the gain has direct relation with pressure and increases relatively, while the gain saturates at pressures higher than 20bar to almost constant value. It is worth mentioning that, in addition to pressure, the temperature dependency of hydrogen is included in Raman gain and loss through Eq. (6.3)and Eq. (6.4). However, it does not change significantly enough to affect the results in the normal operating condition ($T \approx 25\,^{\circ}C$), and, therefore, is considered constant.

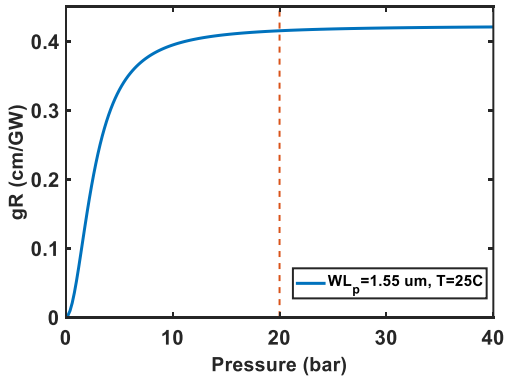

Figure 6.3. Vibrational Raman gain of hydrogen vs pressure of the gas at excitation wavelength of 1.55 μm, $T = 25\,^{\circ}C$.

In general, if the loss at pump wavelength does not surpass the Raman gain, as in solid core fibres with high gain, the effect of loss can be ignored because the Stokes amplification would be significant before the loss can have major impact on the pump. However, for gases with relatively low Raman gain, high loss can have an important role in the process. Although including the pump loss increases the complexity of the optimisation process, it can, in fact, introduce a good measure for maximum achievable Stoke power at optimum length.

To solve Eq. (6.1), there is an available analytical solution [171]; however, the essential approximation in this approach is not valid for the presented case because the loss of the pump and Stokes have large differences. In addition, there are plenty of efficient numerical solvers available for such initial value problem of an ODE. Hence, this equation can be easily solved for specific parameters with available numerical ODE solvers, such as MATLAB ODE113 or MATLAB ODE15s for stiff cases. **Figure. 6.4** shows an instance of the calculated evolution of pump and Stokes power throughout a silica NANF with loss profile as presented in **Figure. 6.2** and for P = 20 bar, R = 21 µm and 1 kW launched pump power (P_{P0}). This figure clearly shows three main stages of the Raman process. First, the pump power decreases under influence of the fibre loss while the amplification of Stokes is negligible (for the presented case, the pump change is small due to low loss). As the Stokes gains enough power, it rapidly grows by gaining power from the pump and this process continues until the rate of power transfer from the pump can no longer compensate the loss of the fibre at Stokes wavelength. At this point, the Stokes reaches its maximum value and starts to lose power due to the fibre loss. In this study, to characterize the Raman process, the maximum Stokes power and the relative length of fibre to achieve such power are defined as $P_{S\max}$ and $L_{S\max}$, respectively, as shown in **Figure. 6.4.** To find the optimum parameters for the highest power transfer to the Stokes wavelength in the shortest possible length, these two parameters ($P_{S\max}$, $L_{S\max}$) are of interest.

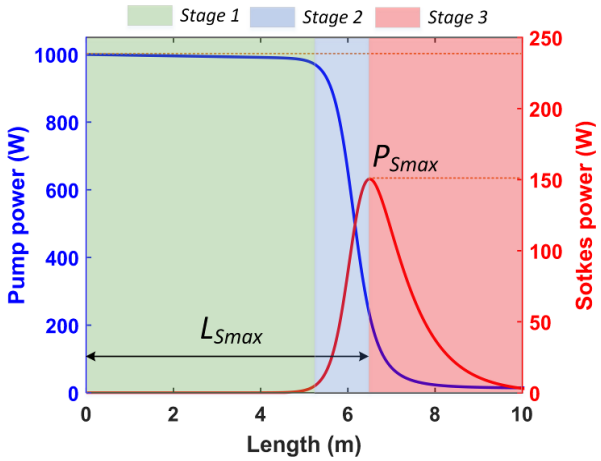

Figure. 6.4. Evaluation of pump power and generated 1st Stokes from vacuum noise. Numerical solution of Eq. (6.1). The maximum power of Stokes with relative propagation distance is marked as $P_{S\max}$ and $L_{S\max}$, respectively.

In general, to calculate $P_{S\max}$ and $L_{S\max}$ from Eq. (6.1), the independent variables form a five dimension set of (α_P, α_S, g_R, R, P_{P0}), considering no information about the fibre

and its characteristics except the mode area, which is represented by core size of the fibre (R) and launched pump power (P_{P0}). In this case, any combination of independent variables can generate an independent set of ($P_{S\max}$, $L_{S\max}$). The most importantly, while in this form, the core size of the fibre is used for calculation of effective mode area, the losses at both pump and Stokes wavelengths are considered independent from the fibre geometry and can be selected freely. Although a set of pre calculated ($P_{S\max}$, $L_{S\max}$) for any possible combination of independent variables can be used for optimisation of any fibre regardless of its structure or dependency of parameters, it is not feasible to calculate and search in such a large space of variables. Luckily, as presented in **Figure. 6.2** for NANF, the dependency of loss at Stokes wavelength, pump wavelength and g_R on pressure (P) and core size (R) can significantly reduce the number of independent variables to (P, R, P_{P0}). In addition, the saturation of Raman gain in hydrogen at higher pressures can limit the range of pressures in such set of parameters. However, as it will be discussed in the next section, in the pulsed pump operation regime, the pressure of hydrogen is one of the key factors that determines the transient or steady-state operating regime of Raman scattering, which significantly affects the Raman gain in the pulsed pump regime.

In addition to $P_{S\max}$, which is the actual output power of the fibre at Stokes wavelength, introducing a normalised quantum photon conversion (η) can be more useful since the efficiency of energy conversion is defined independent of P_{P0} in this form:

$$\eta = \frac{P_{S\max}}{P_{P0}} \frac{\omega_P}{\omega_S} \tag{6.5}$$

With this definition, η has the maximum value of one at 100% quantum efficiency. Using MATLAB ODE solvers, the η and $L_{S\max}$ are numerically calculated for the NANFs with the parameters used in **Figure. 6.2**. **Figure. 6.5** shows calculated η and $L_{S\max}$ vs R and P_{P0} for a few gas pressures ($P = 1, 15, 30$ bar). In order to present the results in a practical scale, the $L_{S\max}$ is limited to 40 m and, consequently, the η presents the achievable maximum efficiency up to this length.

Considering the relation of Gr with square root of core radius ($Gr \propto 1/R^2$), initially the smaller core size would be preferred for higher efficiency due to larger gain. However, the strong dependency of loss in NANF on core radius, as shown in **Figure. 6.5**, can significantly reduce the NGS to below zero. This is denoted as black areas in **Figure.**

6.5, where NGS is less than zero due to excessive loss. For instance, a NANF with 10 μm core radius would be desirable due to high intensity; however, the high loss of the fibre, particularly at Stokes wavelength, prevents any Raman process. In general, **Figure. 6.5** shows that the core size below 12 μm for the proposed NANF is not applicable for Raman conversion and, since this design has one of the lowest loss in HC-ARFs, the conclusion can be generalised to other HC fibres too. **Figure. 6.5 (d-f)** clearly shows that, for a constant pump power and regardless of gas pressure, $L_{S\max}$ is longer for larger core sizes while, for a constant core size, it declines as pump power increase. This might be supposed that fibres with smaller core size are more desirable in order to have shorter $L_{S\max}$. However, as can be seen in **Figure. 6.5 (a-c),** the efficiency of Stokes (μ) at smaller core sizes are very low for similar pump powers. On the other hand, although the increase of core size decreases the Raman gain, which manifests in longer $L_{S\max}$, in fact, the best efficiency can be achieved by larger core size, since the loss significantly decreases. In ideal NANF, the larger core sizes require higher Raman threshold power, but, as loss declines in larger core sizes, the $P_{S\max}$ increases and becomes closer to the quantum conversion efficiency limit. This effect can be seen in **Figure. 6.5** as the total ideal loss (confinement plus material loss) at pump and Stokes decrease monotonically with core size.

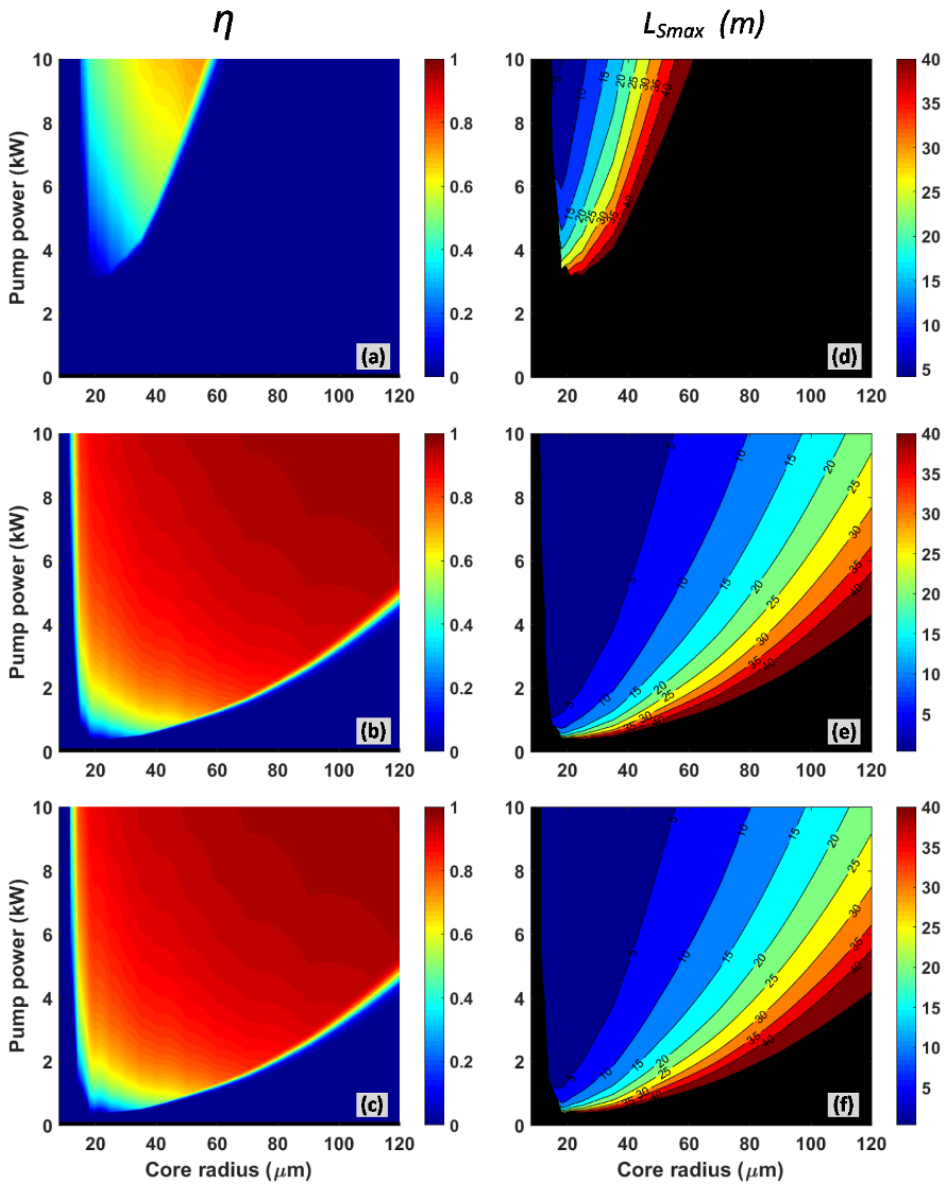

Figure. 6.5. Calculated η and $L_{S\max}$ for different pump power and core radius by numerically solving Eq. (6.1) for hydrogen-filled NANF with d = 4 μm, t_s = 1.66 μm and Z = 7 μm. **(a)**, **(b)**, **(c)** represent η for gas pressure of P=1, 15 and 30 bar respectively and **(d)**, **(e)**, **(f)** are relative $L_{S\max}$ (the black regions in the figure indicate out of range values where NGS < 0).

However, in practice, while the increase of core size in NANF decreases the CL and reduces the effect of material loss of the fibre due to very low overlap of field and glass (**Figure. 6.2**), the loss from other mechanisms, which are less sensitive to core size, such as surface scattering and structural deformation, become dominant factors in the total loss of the fibre. In fact, at very large cores, the loss can be higher due to higher possibility of mode coupling and bend sensitivity (see Chapter 4). Consequently, further increase in the core size not only may not be beneficial, but also can reduce the efficiency of the conversion, which is manifested as a decline in high efficiency at large core sizes

(R > 35 μm), as shown in **Figure. 6.6**. In **Figure. 6.6**, the lower limit of losses is fixed at certain levels (Stokes loss > 1 dB/m and pump loss >1 dB/km) to include the effect of other loss mechanisms in the fibre. Comparing **Figure. 6.5** and **Figure. 6.6** shows that, in the ideal silica NANF, the efficiency is limited just by the length of the fibre and pump power. Hence, theoretically, efficiency increases to its quantum level as core size increases. However, in practice, the factors that determine the minimum loss control the efficiency of Raman conversion.

In practice, in most setups, the fibre is coiled to keep the fibre in place and the bend loss can play an important role to limit the lower level of the loss in large core fibres. In fact, according to Eq. (2.2), the bend loss can be larger for larger core sizes and significantly affect the loss of the fibre. Therefore, the major advantage of NANF over simple tubular fibre in this application is its lower loss for a similar core size and less sensitivity to the bend, which increase the Raman gain and threshold. This allows NANFs with smaller core sizes to achieve the same level of loss as larger core size simple tubular fibres. **Figure. 6.6** can be a good guide for selecting the optimum core size and fibre length for desirable set of ($P_{S\max}$, $L_{S\max}$). While there is a trade-off between pump power, $P_{S\max}$ and $L_{S\max}$, at the powers above the Raman threshold level, the $L_{S\max}$ does not change significantly for different core sizes and choosing a large core size for larger $P_{S\max}$ is desirable. Here, a mid-IR NANF with R = 35 μm seems an appropriate choice. It is worth mentioning that fabrication limitations also play an important role in selecting the core size. It is very important to mention that, although the presented analyses of the efficiency are based on Eq. (6.1), which was originally for CW lasers, the relation between Raman gain (i.e. laser intensity) and core radius is the same for pulsed pump and similar optimum value can be used for pulsed pump as well.

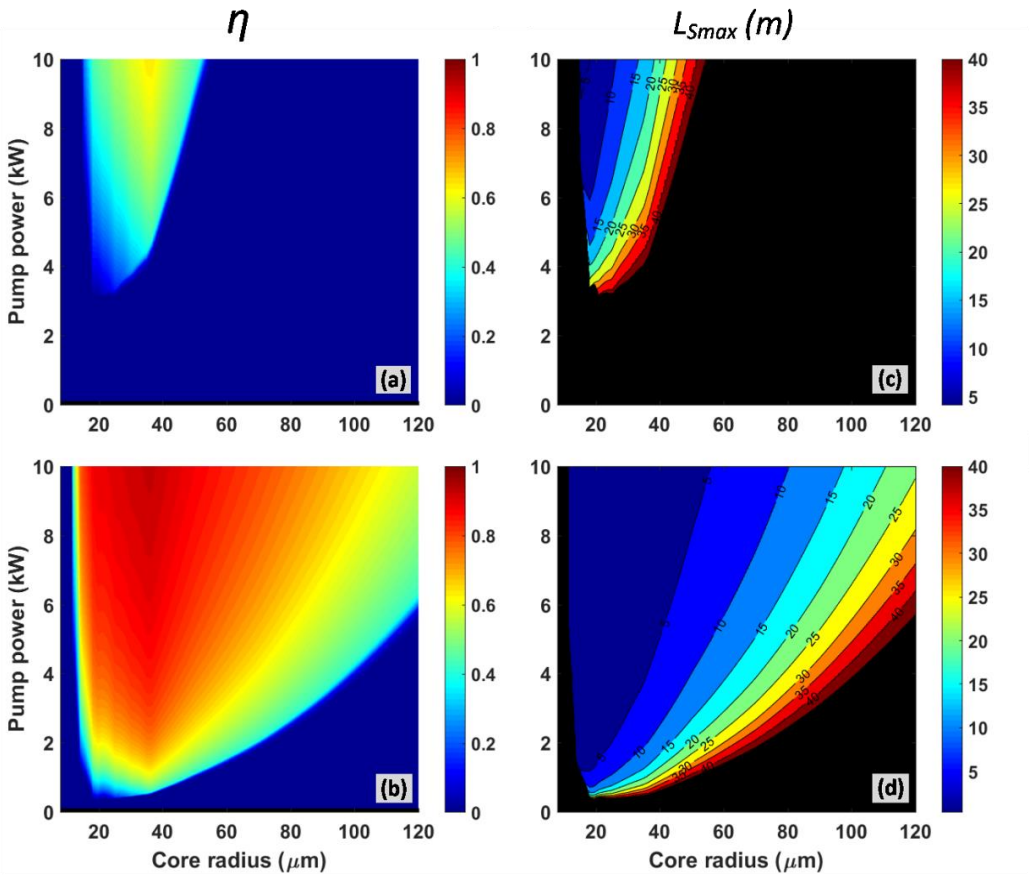

Figure. 6.6. Calculated η and $L_{S\max}$ by considering practical limitation on loss of the fibre for similar condition as Figure. 6.5. **(a)**, **(b)** represent η for gas pressure of P =1 and 30 bar respectively and **(c)**, **(d)** are relative $L_{S\max}$ (the black regions in the figure indicate out of range values where NGS < 0).

6.3.2 Full GNLSE simulations

From a modelling perspective, the majority of Raman coupled equations presented in the literature [1, 72, 80, 172] have been originated from the GNLSE with assumption of steady-state operation regime of Raman scattering or very limited number of nonlinear processes involved. In these approximations, the equations have been derived from the GNLSE by assuming a CW pulse in the time domain when the pulse duration is very large in comparison to the dephasing time scale of Raman response of the material. This assumption can transfer the time convolution between the pulse field and Raman response to a simple multiplication of the pulse in time domain with the Raman response at the Raman resonance frequency. Although this approach is very powerful for steady-state regime or CW operation, as the pulse duration becomes comparable to dephasing time the coupling equation overestimates the Raman gain, and the results become unreliable.

Moreover, the coupling equations are limited by the number of coupled equations and their complexity. Including multi-nonlinear effects, such as rotational-vibrational, Kerr nonlinearity and nonlinear broadening, in this from can produce a complex and impractical set of coupled equations that are difficult, if not impossible, to solve. On the other hand, improvement in computational power in recent years with state-of-the-art computers and deeper understanding and improvement in the NLSE to the GNLSE diminishes the necessity of such simplification and approximation of NLSE into coupled equations. It is worth mentioning that the coupled equations can provide a good insight about the physics and dynamics of the process, but, as the pulse duration starts to shrink and power exceeds a certain level, considering a full model of the GNLSE is a necessity for reliable results.

Although the discrete and narrow band feature of Raman scattering response of some gases, such as hydrogen, can be treated with coupled equations, implementing a method that can solve a general form of the NLSE is helpful to integrate broad and different nonlinear and linear phenomena in a uniform format. This can even simplify the integration of different gases and waveguide characteristics without adding any complexity to the equations or adding extra computational burden. In that regard, the ultimate way can be the direct numerical solution of Maxwell's equations, which is proposed and implemented in [173]. However, despite the precision of this method, its implementation for large or long waveguides, such as optical fibres, which are in the range of metres or even kilometres, is impossible due to the huge computational power and memory size required. In addition, achieving a steady-state solution with this method is beyond the practical time frame. Fortunately, thanks to the physical property of nonlinear and linear processes in common materials, GNLSE can be a middle way solution that, on the one hand, can overcome the computational problem in the Maxwell equation, and on the other, can hold the generality that limits the coupled equation usage.

Therefore, in this thesis, the GNLSE is used to study the dynamics of the pulse propagation in the hydrogen-filled hollow core fibres to create a general platform for analysing the behaviour of gases in more complex and general form in hollow core fibres. Meanwhile, the long-range Raman shift and very narrow band Raman gain in gases such as hydrogen can be challenging to model with the GNLSE due to handling the numerical problem and solving methods, which is addressed in this section followed by a few simulation results. Furthermore, the presented method not only applicable to hydrogen but also it can provide a powerful tool for other gases with a broader range of nonlinear process as presented in the next chapter.

6.3.2.1 Dispersion operator

It is well-known that total dispersion (chromatic dispersion) of any waveguide is a combination of geometrical and material dispersion [1]. In the case of study in this thesis, the total dispersion profile should be calculated by considering the effect of both gas and fibre simultaneously. In previous works on gas-filled fibres, due to the similarity of ARF's dispersion and the dispersion of the capillary, a modified analytical dispersion formula has been derived from the analytical formulation of capillary dispersion, which includes the index of gas at the operating pressure [5]. However, using this approach for the proposed NANF is not accurate due to two major limitations. First, the effective refractive index of NANF shows significant divergence from the standard capillary equation towards longer wavelengths (mid-IR) and also the large Raman frequency shift of H_2 requires a significantly broad spectral window that can extend over multiple transmission bands of an ARF and needs more precise calculation of dispersion. Therefore, to accurately model the total dispersion of the NANF, the pressure dependence refractive index of H_2 (Eq. (6.3)) is included in the calculation of $\beta(\omega)$ by the developed fully vectorial FEM mode solver toolbox (see Chapter 3 for detail of FEM solver).

It is important to indicate that time domain presentation of dispersion in Eq. (3.7) is the consequence of transferring the Taylor series of the propagation constant at frequency domain around central pulse frequency (ω_0) to the time domain [1]. This time derivative form needs many terms to provide an accurate result; however, it can be rearranged to include full dispersion instead of Taylor coefficients. Using the definition of Taylor series for a frequency-dependent propagation constant ($\beta(\omega)$) and rearranging the terms, the frequency domain of dispersion operator in the GNLSE can be replaced by:

$$\begin{aligned}\tilde{D}(\omega) &= -\frac{\alpha(\omega)}{2} + \mathbb{F}\left\{\sum_{n=2}^{\infty}\frac{i^{n+1}\beta_n}{n!}\frac{\partial^n}{\partial T^n}\right\} \\ &= -\frac{\alpha(\omega)}{2} + i\left[\beta(\omega) - \beta(\omega_0) - \beta_1(\omega_0)(\omega-\omega_0)\right].\end{aligned} \tag{6.6}$$

Here $\tilde{D}(\omega)$ denotes the frequency domain of $\hat{D}$ in Eq. (3.7). This form of dispersion operator contains a full range of higher order dispersions and can be implemented easily in the frequency domain form of the GNLSE. Moreover, in this form, not only the dispersion is not approximated by the common practice of truncating the higher order dispersions, but also the numerical error imposed on higher order derivatives is

eliminated. Moreover, the dispersion is not properly defined around resonance frequencies in NANF and Taylor series cannot represent the dispersion of these fibres across multiple anti-resonance bands with good approximation.

In Eq. (6.6), while $\beta(\omega)$ and $\beta(\omega_0)$ are the direct results of mode calculation, $\beta_1(\omega_0)$ needs special care. Although some simple numerical differentiation methods can be used to calculate $\beta_1(\omega_0)$, such as numerical differentiation on neighbour points of $\beta(\omega_0)$ or even polynomial fitting, the large number of required points for an accurate result and the intrinsic sensitivity of numerical differentiation to the accuracy of $\beta(\omega)$ can impose noticeable error. The large number of required points can also impose a significant calculation burden due to the high computational cost of the FEM mode solver (see Chapter 3). Alternatively, it can be shown that by using Chebyshev–Lagrange polynomial interpolation at a few specifically chosen values of $\beta(\omega)$ in the vicinity of ω_0, it can significantly increase the accuracy of $\beta_1(\omega_0)$ and considerably reduce the computational cost (see *Appendix C*). Besides, in this approach the $\beta_1(\omega_0)$ is calculated through simple matrix multiplication, which eliminates any form of numerical differentiation. Hence, this approach is used in this work to calculate the dispersion operator.

Another advantage of the dispersion operator in the represented form is the ability to introduce a simple yet powerful relation between the measured dispersion of the fibre in practice and the dispersion operator in the GNLSE (Eq. (3.7)). In practice, the measured dispersion ($D_{\exp}(\lambda)$) is in the form of:

$$D_{exp}(\lambda) = -\frac{2\pi c}{\lambda^2}\beta_2(\omega) \tag{6.7}$$

Although this form of dispersion can provide useful information regarding the fibre pulse propagation, it cannot be implemented directly into the GNLSE and the common practice is to extract higher-order dispersions from data by curve fitting and numerical differentiation. However, the number of measured data points is not large enough to create a reliable initial data set for accurate curve fitting to the required degree of accuracy for numerical differentiation. However, it is possible to calculate the dispersion operator (Eq. (6.6)) directly from the measured dispersion ($D_{\exp}(\lambda)$) or fitted curve on it by simply integrating the second derivative of propagation constant ($\beta_2(\omega)$), rearranging the results and using Eq. (6.6):

$$\tilde{D}(\omega) = -\frac{\alpha(\omega)}{2} - i\int_{\omega_0}^{\omega}\int_{\omega_0}^{\omega'} \frac{2\pi c}{\omega''^2} D_{\exp}(\omega'')\, d\omega'' d\omega' \qquad (6.8)$$

In this method, due to integration instead of derivation, it has less sensitivity to numerical error and represents a full form of dispersion operator in a closed form. Using a measured dispersion in Eq. (6.8) is especially useful for fabricated fibres with large pitch or complex multi-resonant structure, such as Kagomé fibres, where the FEM modelling of the cross-section of the fibre cannot accurately reproduce the experimental modal behaviour and dispersion profile of the fibre [54, 174].

6.3.2.2 Dispersion in gas-filled NANF

In section 6.3.1, it is shown that the loss of the NANF and ARFs in general can be affected by the pressure of the filling gas due to change of core refractive index (i.e. gas index). This effect can also alter the dispersion profile of an ARF. In general, the guidance mechanism in an ARF strongly depends on the reflectivity of the core boundary membranes, and according to Eq. (2.1) any change in material or thickness of either core or glass membranes can alter the behaviour of the fibre. The most important and unique consequence of such changes is the shift in ZDW (λ_0) [131]. Unlike HC-PBGF fibres, NANF usually has low dispersion in the anti-resonance bands (ARB) with a fairly flat profile. The GVD profile of NANF starts with normal regime at high frequency side of each ARB and becomes anomalous at the low frequency end of the band while crossing the ZDW at approximately the middle of the ARB, as shown in **Figure 6.7 (a)**. While it is generally accepted that pressure change can shift the ZDW in ARFs [5, 48], the significant changes take place at short wavelengths far from the operating point (1.55 μm) in this work. This is represented in **Figure 6.7 (a)**, where the dispersion profile of a hydrogen-filled silica NANF, covering the second and third ARBs, is calculated at various pressures. The results show very mild dispersion change in the designed NANF for the pressure change. In addition, because, in this work, the Raman conversion process covers multiple ARBs of the fibre, a more appropriate measure for the effect of pressure change would be phase mismatch parameter ($\Delta k = \beta(\omega_S) + \beta(\omega_{aS}) - 2\beta(\omega_P)$). As shown in the following section, the phase matching condition can severely affect the Raman process and needs to be studied in NANF. **Figure 6.7 (b)** shows the effect of pressure on Δk, calculated for silica NANF (d=1 μm, t_s =1.66 μm, R = 35 μm and Z = 7 μm). While, as expected, the absolute value of Δk is large ($\Delta k \sim 5.2\times10^3 (1/m)$ at $P = 1 bar$) because of the noticeable difference between n_{eff} at pump wavelength and longer wavelengths (Stokes wavelength), the change in Δk by

pressure change is not significant (~6% for $\Delta P = 70\,bar$). This assures that, unlike recent observations at shorter wavelengths [48, 175], increasing the pressure does not shift the ZDW towards pump wavelength and FWM does not suppress Raman scattering.

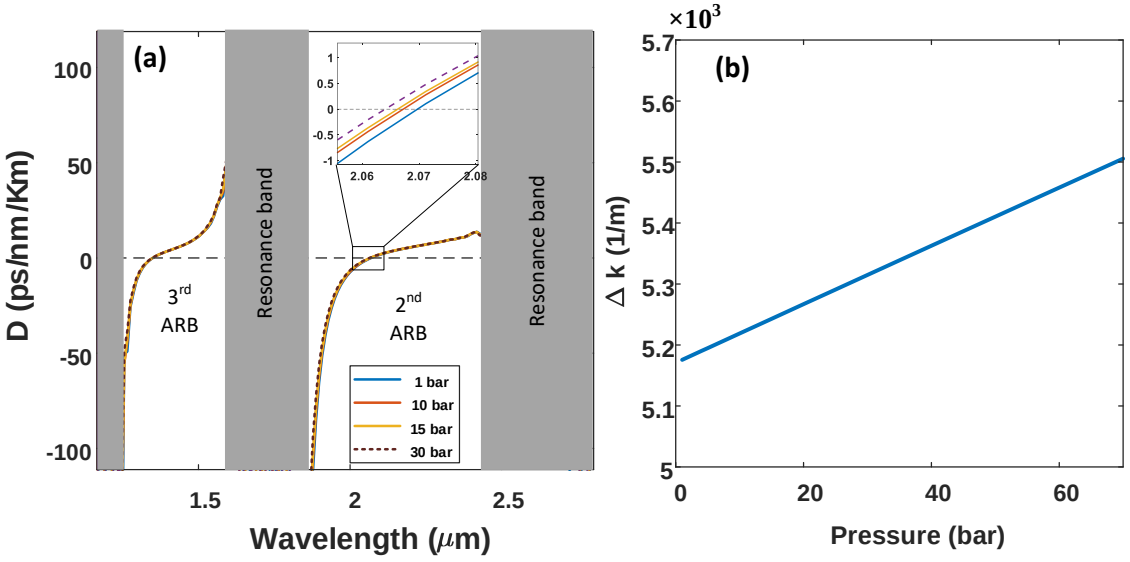

Figure 6.7. (a) The dispersion profile of hydrogen-filled designed NANF for various operating pressures at $T = 25\,^{\circ}C$. **(b)** The phase mismatch parameter of the fibre for pump, Stokes and anti-Stokes at 1.55 μm, 4.35 μm and 0.94 μm, respectively.

6.3.2.3 Raman response function of hydrogen (Raman operation regime)

As explained in Chapter 2, the nonlinear behaviour of a propagating pulse can be modelled properly by the GNLSE for the majority of the experimental environments in this work subject to providing a proper expression for both the nonlinear parameter ($\gamma(\omega)$)and Raman response function ($h_r(t)$), which includes the instant electronic response of the third order susceptibility (representing FWM, XPM and SPM) and the delayed Raman response of the molecule, respectively. Although hydrogen has been studied very well for many years, a straightforward and adaptive Raman response function to the GNLSE , similar to its solid counterparts, such as silica [176], is yet to be introduced. On the other hand, unlike the Raman response profile, as stated in section 6.3.1, the Raman gain ($g_R(\omega)$) has been studied and experimentally measured for different concentrations of gas [170], which can be a good starting point to introduce a model for the Raman response function of hydrogen.

It is shown that the Maxwell-Bloch equation (Eq. (2.10)), governing the evolution of the Stokes field, can be analytically solved by Laplacian transformation [80] in the absence

of loss and for an undepleted pump field. A simplified solution of Stokes field for flat-top pump pulse with the duration of τ_P is derived as:

$$E_s(L) = E_s(0)\left(1+\sqrt{\frac{Gr_0(L)T_2^{-1}}{2}}\int_0^{\tau_p} e^{-T_2^{-1}(\tau_P - t)}\frac{I_1\left(\sqrt{2Gr_0(L)T_2^{-1}(\tau_P - t)}\right)}{\sqrt{(\tau_P - t)}}dt\right) \quad (6.9)$$

where, $Gr_0(L)$ is the NGS in without loss term $Gr_0(L) = g_R I_P L$ (see Eq. (6.2)). I_1 is the first-order modified Bessel function and T_2 is the dephasing time as described in Chapter 2. At high gain regimes, where $Gr_0(L)\tau_P \gg T_2$, it is possible to reach a closed form for Eq. (6.9) depending on the value of normalized pulse duration $\tau' = \tau_P T_2^{-1}$ [80].

- **Steady-state regime**: for the case where $\tau' \gg 1$, the upper limit of integral in Eq. (6.9) goes towards infinity and the Stokes gain can be reduced to:

$$G_s(L) = \left(\frac{E_s(L)}{E_s(0)}\right)^2 \approx e^{Gr_0(L)} \quad (6.10)$$

  The results are similar to the solution of Eq. (6.1) where the system was treated in the CW condition.

- **Transient regime**: for the opposite end $\tau' \ll 1$ the Eq. (6.9) can be approximated by:

$$G_s(L) = \left(\frac{E_s(L)}{E_s(0)}\right)^2 \approx \frac{e^{\sqrt{8Gr_0(L)\tau'}-2\tau'}}{\pi\sqrt{8Gr_0(L)\tau'}} \quad (6.11)$$

In practice, the condition for transient regime can be relaxed to $Gr_0(L) \gg \tau_P$ [177]. According to Eq. (6.10) and Eq. (6.11), the Stokes gain not only depends on Raman gain of material, but also on the dephasing time and pulse duration. While the Raman gain becomes saturated at pressures above 20 bar and can be treated as constant, T_2 is related to linewidth of the Raman gain as $T_2 = 1/(\pi\Delta\upsilon)$. On the other hand, the Raman linewidth of the hydrogen ($\Delta\upsilon$) varies by pressure and temperature according to Eq. (1.4), and consequently, the dephasing time changes. **Figure 6.8** plots the linewidth and relative dephasing time of the hydrogen vs pressure at $T = 25\ ^\circ C$. The unusual behaviour of linewidth at different pressure can be explained with domination of Doppler broadening process at low pressures when the collisional broadening is negligible due to low density of gas [178]. As pressure increases, the majority of collisional processes become elastic with velocity-changing effect and *Dicke linewidth*

narrowing occurs, as shown in **Figure 6.8** [179]. Further increase in pressure causes more hard-collisional broadening and consequently increases the linewidth [178].

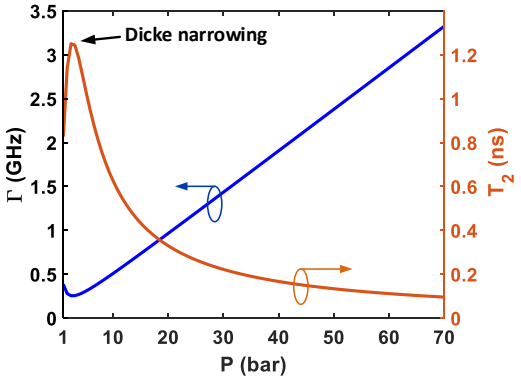

Figure 6.8. The linewidth and dephasing time of hydrogen vs its pressure. The Dicke narrowing occurs close to 1.25 bar pressure at $T = 25\ ^{\circ}C$.

The direct consequence of these changes in linewidth and dephasing time reflects on the Stokes gain ($G_S(L)$) as the Raman operating regime changes. **Figure 6.9 (a)** shows the marked regions for the transient and steady-state regimes in $Gr_0(L)$ vs τ_P chart as well as high gain condition. To study the behaviour of Stokes gain in different regimes, two pump pulses with duration of 20 ns and 1 ns at 532 nm with $I_P = 0.565\,GW/cm^2$ for steady-state regime (case A) and transient regime (case B) are considered for $L = 0.3$ m, respectively. This wavelength (i.e. 532 nm) has been selected for the purpose of demonstration of two different regime of operation for Raman process (case A and B) by single pump intensity because the Raman gain is much higher at shorter wavelengths than the pump wavelength of this project (i.e. 1.55 μm).

Figure 6.9 (b) plots the Stokes gain vs pressure calculated for each case by Eq. (6.9). Although both cases are in the high power region ($Gr_0(L)\tau_P \gg T_2$), as shown in **Figure 6.9 (b)**, the 1 ns pulse (case B) is in the transient regime with relatively low Stokes gain while 20 ns pulse is mainly in the steady-state regime with almost constant and relatively higher gain. Also, the solutions of Eq. (6.10) and Eq. (6.11) for each case show very good agreement with Eq. (6.9), as shown in **Figure 6.9 (b)**. It is noticeable that, in case A, even though $\tau_P > T_2$, due to large I_P, the Raman process is operating in transient regime. This gain reduction effect caused by pulse duration is not included in a simple form of coupled equation (Eq. (6.1)), which overestimates the Raman gain.

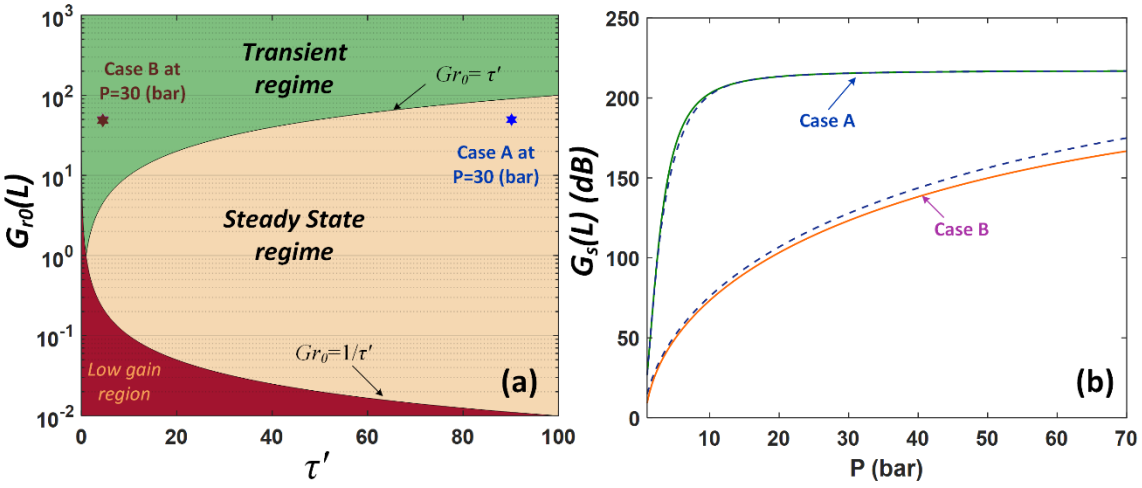

Figure 6.9. (a) Raman operating regime map where steady state regime (light brown area) and transient regime (green area) are marked above the low power region (red area). Cases A and B for $P = 30\,bar$ bar are marked. **(b)** The Stokes gain vs pressure is plotted for case A and B using Eq. (6.10) and Eq. (6.11) (solid lines), respectively, and by numerically solving Eq. (6.9) (dashed line) for both cases.

Considering different parameters involved in the final goal of this thesis, such as the pressure range of H_2 (P > 20), laser pulse duration, length and core size of NANF, the Raman process can be in either transient or steady-state regimes. Hence, as discussed before, while the lower limit of pressure is defined by Raman gain saturation in hydrogen (20 bar), to achieve as high as possible gain one has to increase the pressure (P) or increase the pulse duration (τ_p) to reach the steady-state regime. However, practical limitations, such as laser power at longer pulses or mechanical limitation of highly pressurised fibre, can push the Raman process into transient regime.

Therefore, to include this gain reduction effect and, most importantly, to achieve a comprehensive model for Raman, which can be integrated in the dynamic evolution of pulse propagation (i.e. the GNLSE), the Raman behaviour of molecules can be modelled as a dynamic system with a first-order impulse response. In this semi-classical approach, the motion equation for $Q(z,t)$ (Eq. (2.10)) can be treated as the characteristic equation of a linear system with intensity of the electric field ($|E(t,z)|^2$) as the input of the system. It is well-known that the time domain output of such a system for arbitrary input can be calculated through convolution of the input signal and impulse response of the system in the time domain [180]. From comparing the classical definition of nonlinear susceptibility [72] and the quantum model of motion equation in Maxwell–

Bloch for a two-level system with negligible population inversion [80], a simple impulse response can be introduced with the form of a single-Lorentzian model [172]. In this approach, the Raman response of the molecule (e.g. hydrogen) is modelled by a single oscillator with resonance frequency of "molecules" (Ω_v) and damping effect (e^{-t/T_2}), which mimics the linewidth of the response. Hence, the time response of the Raman process ($h_R(t)$) can be presented as:

$$h_R(t) = \frac{1+T_2^2\Omega_v^2}{T_2^2\Omega_v} e^{-t/T_2} \sin(\Omega_v t) U(t). \tag{6.12}$$

where $U(t)$ is Heaviside step function which implements causality in this equation. Also, the dephasing time (T_2) assures the implementation of transient regime. Although the Raman frequency shift of hydrogen (Ω_v) is relatively constant in the range of experimental environment for this study (e.g. pressure, temperature and pulse intensity range), as described previously, the dephasing time of hydrogen dependes on the pressure of gas and is a key factor in regulating the regime of Raman operation.

In Eq. (6.12), the Raman response function of hydrogen cannot be implemented correctly into the GNLSE without the introduction of a proper nonlinear coefficient and Raman fraction factor (f_R). Although some experimental values for $\gamma(\omega)$ are provided in the literature [165], to achieve reliable values and preserve the consistency between all parameters in the GNLSE, in this study, the nonlinear index ($n_2 = A_{eff}\gamma(\omega)c/\omega$) for hydrogen is calculated by its relation to the Raman gain (g_R)[1]:

$$n_2 = \frac{g_R}{2\max\left[\tilde{h}_{Ri}(\omega)\right] f_R} \tag{6.13}$$

where $\tilde{h}_{Ri}(\omega)$ is the imaginary part of Raman response in the frequency domain, max[] is maximum operator and A_{eff} is the effective mode area of the fundamental mode. Using Eq. (6.4) for g_R, considering the core size of 35 μm and calculating maximum of $\tilde{h}_{Ri}(\omega)$ from Eq. (6.12), the calculated value for n_2 is $1.2\times10^{-7}\ mW^{-1}$ for VRS. In this study $f_R = 0.25$ is chosen in order to achieve similar values for n_2 from Eq. (6.13) and experimental value in [165].

6.3.2.4 Pulse specification

Apart from the nonlinear parameters of the gas, simulating the Raman conversion process along the fibre requires proper parameters of the launched pulse in terms of peak power, pulse length and pulse shape. Considering the fully fiberized mid-IR goal architecture for this project, an erbium-doped fibre laser at 1.55 μm with a Gaussian linewidth profile has been considered. It has been experimentally observed that, above certain energy level of pulses in the hydrogen-filled fibres, the nonlinear loss increases due to self-focusing as well as higher mode coupling [34]. As a result, in this study, the peak power is considered in a practical range between 2 and 50 kW to achieve reasonable results while higher peak powers are achievable by state-of-the-art lasers [181]. In terms of pulse length, in order to achieve an efficient conversion, the pulse linewidth should be narrower than the Raman linewidth and satisfy the steady-state condition for maximum gain achievement. Although longer pulses are more desirable, the practical limitation to generate long pulses with high peak power restricts the options. Therefore, here, the effect of pulse length up to 10 ns is studied while longer pulses can be treated as quasi-CW, for which simple coupling equations can provide accurate results in that regime. It is worth mentioning that recently a high power source by Raman conversion from 1060 nm to 1550 nm in hydrogen-filled HC tubular fibre reaching 400 kW has been demonstrated [182]. Using such high power source can provide significant output at 4.35 μm. However, in this thesis, the focus is on a design considering available solid-core fibre lasers (e.g. erbium-doped fibre laser) with lower output power.

6.3.2.5 Modelling the noise sources

In practice, the SRS process is seeded by many different sources, such as quantum fluctuation (vacuum noise), noise from pump source, phase fluctuation noise or vibrational/rotational Raman noise in the molecules [183, 184]. Although I have calculated and used Raman noise in addition to vacuum noise in the simulations by using some of the existing models [184], the results have not shown significant difference from considering just vacuum noise, which indicates its dominance in the process. Therefore, only vacuum noise is used by calculating the average power of the noise in the frequency window and randomly distributed in the bits of time grid (points of time grid).

6.3.2.6 Dispersion-dependent Raman gain reduction effect

In addition to reduction of Raman gain at transient regime, the chromatic dispersion can also impose Raman gain reduction and dramatically reduce the frequency conversion. It is well-known that the Raman process does not intrinsically depend on the dispersion of the media nor does it rely on phase matching due to it is inelastic scattering nature [72]. However, in a nonlinear medium, it is not possible to completely isolate the physical processes from each other. It is clear that the nonlinear section of the GNLSE contains two parts: a third order electronic nonlinearity (phase matching required) and a Raman delayed part (no phase matching required). On the one hand, the Raman process acts by transferring the energy from pump pulse into the lower frequency (Stokes), while, on the other hand, FWM, as an energy transferring process, conveys energy from lower frequency to the upper one. Therefore, under proper phase matching condition, these two processes can mutually affect each other. In fact, if the condition for phase matching between pump, Stokes and anti-Stokes is satisfied, FWM can suppress the Raman process and either kill it completely or reduce its efficiency dramatically. However, in some cases, the Raman anti-Stokes can also be boosted significantly in proper phase matching [172]. This mutual effect between FWM and SRS has been well-known for more than three decades and there are many experimental and theoretical works in this area [185, 186] even in HC fibres [175]. To include this mutual effect in the form of a general gain, a modified version of Eq. (6.13) has been introduced as [185]:

$$g = 2\gamma\Re\left[\sqrt{K(2q-K)}\right] \tag{6.14}$$

where $\Re[]$ is real operator and $q = 1 - f_R - if_R \max\left[\left|\tilde{h}_{Ri}(\omega)\right|\right]$. $K = -\Delta k/(2\gamma I_P)$ is the normalised phase mismatch where $\Delta k = \beta(\omega_S) + \beta(\omega_{aS}) - 2\beta(\omega_P)$. By defining a gain reduction factor as $R_g = g/g_R$, the effect of parametric process (FWM) on Raman gain for different dispersion values (K) in hydrogen has been studied, as shown in **Figure 6.10.** The clear dependence of K on power and dispersion is an important point for optimising the efficiency of conversion.

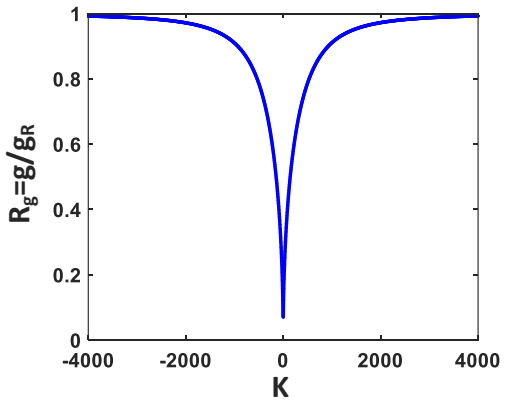

Figure 6.10. Raman gain reduction factor vs normalised phase mismatched. In a complete phase matching case, the effective Raman gain theoretically is zero.

Equation (6.14) shows that the Stokes gain becomes zero at $K = 0$, which indicates the complete absence of Stokes and anti-Stokes at this point, despite a large Raman gain in the material. Although in bulk materials the ZDW is far away from the typical operating wavelengths, the combination of waveguide and material dispersion (chromatic dispersion) can shift the ZDW closer to the pump wavelength. In fact, as shown previously (**Figure 6.7 (a)**) not only a gas-filled NANF has multiple ZDW across its dispersion profile, but, also, they can be adjusted to some extent by tube thickness to increase or decrease the gain reduction factor (R_g). This effect also is not included in the simple form of coupled Raman equation (Eq. (6.1)), but can be approximated by replacing the steady-state gain (g_R) in the equation by reduced gain (g), which includes the reduction factor.

This effect is modelled in the hydrogen with the GNLSE using the Eq. (6.12) for Raman response function ($h_R(t)$), nonlinear coefficient ($\gamma(\omega)$) and Raman fraction ($f_R = 0.25$). **Figure 6.11** shows propagation of 1 kW pump Gaussian pulse (GP) at 1.55 μm in a lossless hydrogen-filled NANF with R =15 μm, and fixed $\beta_2 = 0$ and $\beta_2 = -0.042\ ps^2/m$ for a 3 m long fibre, respectively. It is clear that in the absence of dispersion (i.e. $\beta_2 = 0$) the Raman Stokes and anti-Stokes are clearly suppressed by FWM.

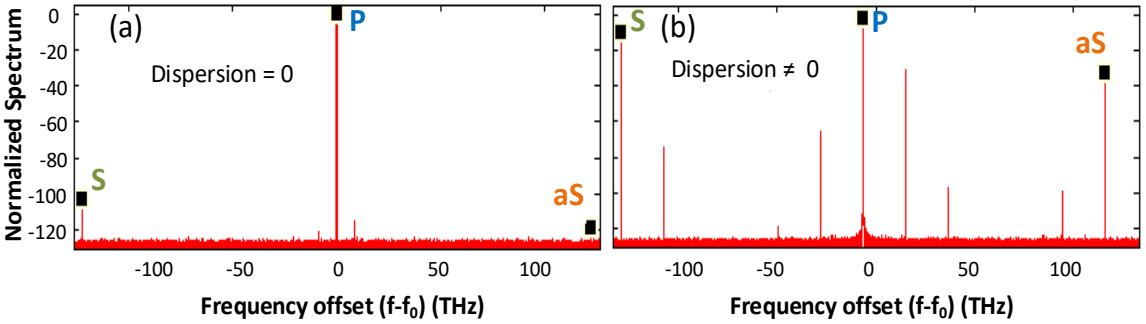

Figure 6.11. Simulated spectral profile of a Gaussian pulse at 1.55 μm with 2 kW peak power and 2 ns length after passing through 3 m of hydrogen with **(a)** $\beta_2 = 0$, **(b)** $\beta_2 = -0.042\ ps^2/m$. There is not any Stokes (S) and anti-Stokes (aS) amplification due to effect of FWM on Raman process at zero dispersion.

6.3.2.7 Simulation challenges and strategies

Having developed an appropriate Raman response function and nonlinear parameters for hydrogen, essentially, it is possible to model the pulse propagation through numerical calculation of the GNLSE. Nevertheless, the combination of very narrow Raman linewidth (~1 GHz) and large vibrational frequency shift (124 THz) in hydrogen requires a very wide frequency grid (at least twice the frequency shift) with a large number of grid points (to cover ns pulses and the hydrogen narrow linewidth simultaneously). Usually, the central frequency of the pump is chosen as the centre frequency of the simulation grid (zero frequency) and, consequently, the Stokes/anti-Stokes fields are generated from the vacuum noise at the side bands. At first, this approach was implemented for lossless silica NANF with 15 μm core radius, in a grid size of 2^{22} points for a 2 ns pulse, as shown in **Figure 6.12 (a)**. Simulation results show pump, 1st Stokes and 1st anti-Stokes fields as expected alongside other peaks in-between. These peaks turned out to be the higher order Stokes and anti-Stokes, but displaced due to a liaising effect and the circulating effect of FFT method for calculating the convolution part of the GNLSE. In addition, some artefact peaks are also generated by displaced Stokes and anti-Stokes, such as higher order Stokes, which, practically, do not exist in this particular case because there is not enough energy in photons to pass to the second vibrational level (second Stokes). Most importantly, the coupling effect between artefact peaks and legitimate ones can affect the conversion rate and generate unreal results. Thus, it should be eliminated by either changing the solving method or simulation parameters.

To eliminate such specious and undesirable effects, in principle, different strategies can be followed:

- **Direct time domain convolution** (*non-circulating*): in this method, direct implementation of non-circular convolution is implemented. However, the computation time and memory usage for even moderate grid size (2^{15}) put this method beyond computational possibilities in state-of-the-art systems.
- **Non-circulation convolution by FFT**: this method has the advantage of high speed calculation of FFT. However, in order to implement such a method for each iteration one needs to double the length of time grid by adding zero at the end of the grid (zero padding), which doubles the memory usage and rapidly increases as calculations continue.
- **Absorbing boundary:** This method is well-established for solving the wave propagation problems in a limited calculation window [187]. The PML presented in Chapter 3 is an instance of such methods, which can be implemented in the frequency or time domain to eliminate the back-reflected energy in the GNLSE. However, these methods not only increase the complexity of the problem, but also cannot solve the circulating effect of FFT properly and do not conserve the energy.

In contrast, in this thesis, simpler yet efficient methods have been explored to overcome the problem, which do not increases the complexity and time of simulation, while addressing the problem properly. In the first attempt, a very large loss has been artificially introduced at misplaced second Stokes and anti-Stokes to eliminate their effects, as shown in **Figure 6.12 (b)**. However, this method of suppression of anti-Stokes cannot reproduce the correct energy transfer rate between frequencies. For example, second Stokes can act as anti-Stokes and vice versa, which can affect the final conversion results. After trying different approaches, it is finally decided to increase the grid size and place the pump frequency off-centre of grid to create enough room for higher order anti-Stokes. **Figure 6.12 (c)** shows the off-centred simulation for the previous parameters. Clearly, a larger frequency window means more grid points ($n_t = 2^{24}$) for covering the 2 ns pulse in the time domain. Although the off-centred method could solve the problem of coupling and interference of anti-Stokes, circulated higher order Stokes, as can be seen in **Figure 6.12 (c)**, in fact, the 1st Stokes is under the influence of artefact second Stokes and cannot experience any growth larger than pump pulse. This effect is due to parametric back-coupling of energy from second Stokes while the second Stokes experience higher gain than actual gain due to its displacement at higher frequencies (higher frequencies have larger Raman gain). Finally, second Stokes has been eliminated by applying local loss at this frequency, as shown in **Figure 6.12 (d)**. Similar growth in 1st Stokes and pump depletion has been demonstrated

experimentally in different frequency by placing second Stokes in the high loss band of HC-PBGF [15, 188]. It is important that implemented extra loss does not interfere with the time domain field in a distractive way. In fact, any abrupt artificial change in loss profile manifests itself as ripples in the time domain, which can be reflected back into the frequency domain as rapid phase or amplitude oscillations. This is due to multiplication between the field ($E(t)$) and other time domain terms in GNLSE, which can be interpreted as convolution in the frequency domain. These effects create instability in the calculation and generate unreliable results. Therefore, to prevent such effects, large losses with Gaussian profile have been implemented at the circulated peaks, which has very little effect on time domain while suppressing the SRS process at these frequencies.

At first glance, the suppression effect caused by imposing loss at artefact higher order Stokes peaks is similar to the suppression effect experienced by higher order Stokes in a fibre with high loss at actual wavelengths of those higher order Stokes and one should expect to achieve correct results. However, as mentioned before, the energy transfer from 1st Stokes to the artificial higher order Stokes is incorrectly reproduced, because the experienced Raman gain by these artificial higher order Stokes is higher at misplaced frequencies (the Raman gain is higher for lower frequencies). In addition, in some cases, the higher order Stokes does not exist simply because the vibrational energy is higher than the photons in 1st Stokes (similar the case in this study). Therefore, a closer look at the GNLSE and the coupling mechanism at which the energy transfers to each Raman Stokes/anti-Stokes suggests a different approach to eliminate artificial circulating peaks in the first place without the need to dissipate the transferred energy later by loss, especially for the cases where the higher order Stokes are not allowed. The energy transfer in each frequency component of the GNLSE through propagation can be presented in a set of coupled equations in the form of:

$$\frac{\delta \tilde{A}(\omega_k, z)}{\delta z} = \tilde{D}(\omega_k)(\tilde{A}(\omega_k, z)) + \gamma(\omega_k)\mathbb{F}\left\{A(t,z)\left(R_n(t) \otimes |A(t,z)|^2\right)\right\}. \quad (6.15)$$

where $\tilde{A}(\omega_k, z)$ is the longitude amplitude of the electric field at frequency ω_k (e.g. Stokes) and $\otimes$ denotes the convolution of nonlinear response of the material ($R_n(t)$) and the field in the time domain. The second term on the right side of Eq. (6.15) shows that the energy transfer from other frequencies to the specific frequency (e.g. Stokes frequency) happens through nonlinearity of the material. Therefore, it is possible to exclude a specific frequency from this process by eliminating the nonlinearity at that frequency.

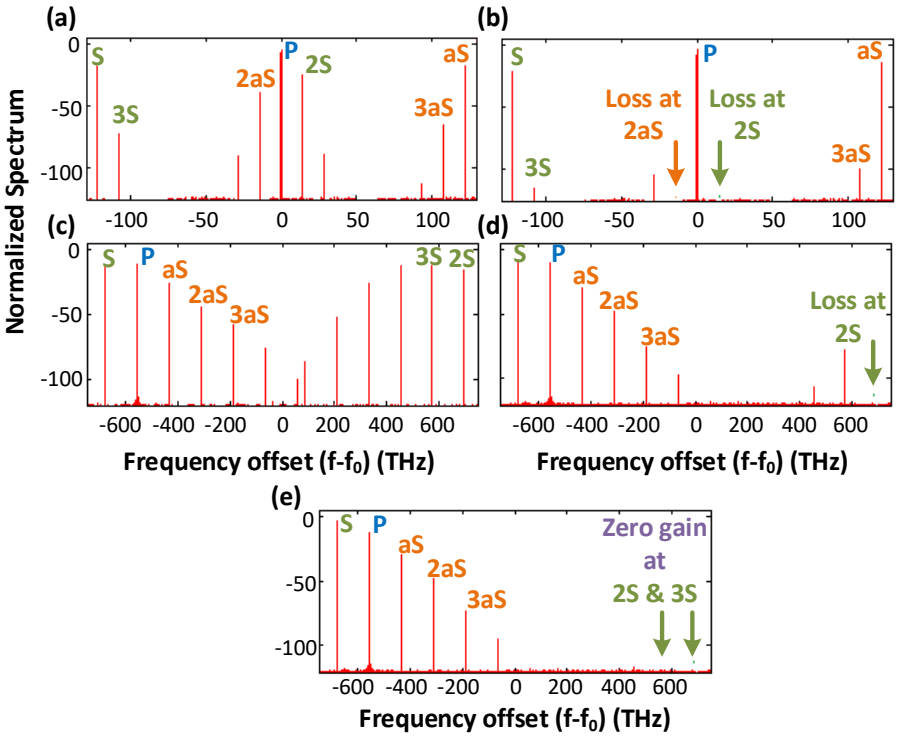

Figure 6.12. Simulated normalised spectral profile in dB for a 2 ns pulse at 1.55 μm with 2 kW peak power after passing through a hydrogen-filled lossless designed silica NANF (R =15 μm) with 5.8 m length for **(a)** pump placed at the centre of a small spectral grid (aliasing and FFT circulating effects); **(b)** pump placed at the centre of a small spectral grid and artificial loss applied on second Stokes and anti-Stokes (eliminating real coupling of second anti-Stokes); **(c)** pump has been shifted to the corner of the extended spectral grid (aliasing and FFT circulating effects); **(d)** pump has been shifted to the corner of the extended spectral grid and artefact second Stokes has been eliminated by artificial loss; **(e)** the SNM method is implemented by assigning zero gain to second and third circulated Stokes peaks.

Thanks to the definition of the GNLSE in the frequency domain, the implementation of this *suppressing nonlinearity method* (SNM) is as simple as defining the $\gamma(\omega_k)=0$ at generated peak (ω_k) by circulating effect. Here, also, a smooth change in $\gamma(\omega)$ is essential to prevent any problem in the time domain; hence, a similar Gaussian profile has been used. **Figure 6.12 (e)** shows the results of implementing the SNM and the complete elimination of circulating effect without need for losses at these peaks. With this method, it is also possible to reduce the size of the frequency domain without sacrificing the generality or observing artificial peaks. It is important to note that eliminating the gain is essential for modelling the Raman conversion from 1.55 μm to 4.35 μm because the transfer of energy to the higher order Stokes does not happen in practice, because the photon energy at 4.35 μm (0.2848 eV) is lower than vibrational energy level of H_2 (0.5151 eV) to generate second Stokes.

6.3.2.8 Verification of model

To verify the developed GNLSE-based numerical model, first, the behaviour of SRS for Raman transient and steady-state regimes was modelled to confirm the ability to reproduce such effects, and finally, an experimental result was reproduced by the developed models in this thesis. As a benchmark, the experimental setup and ARF (Kagomé fibre) in [34] are considered for the validation of the model, since the hydrogen–filled NANF is not yet experimentally explored. To demonstrate the behaviour of Raman conversion in different regimes of operation, a hydrogen-filled fibre with R =15 μm and gas pressure of $P = 50\,bar$ is considered. The fibre was assumed to be lossless while the pump wavelength and power ($\lambda_P = 532\,nm$, $P_P = 933\,W$) were chosen according to [34]. A super-Gaussian pulse (n=5) (SGP) was used to simulate a flat-top pulse while preserving the smoothness in the frequency domain. The pulse propagation was simulated in the fibre for different pulse lengths, 10 ns, 3 ns and 1 ns, to represent the steady-state, transient and deep transient regimes of SRS, respectively, as shown in **Figure 6.13 (a)**. The result does not only show the expected Raman gain reduction in the transient regime, but also a maximum quantum conversion achieved at steady-state regime as a result of lossless fibre, which indicates the proper modelling of vibrational loss. The simulation results at longer pulses (i.e. steady-state regime) approach the results of coupled equations (Eq. (6.1)), which represent the CW limit.

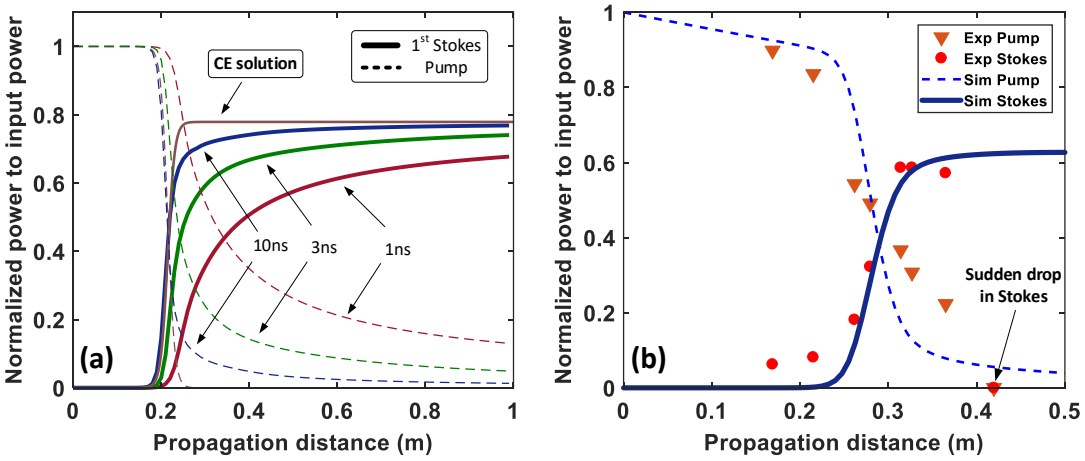

Figure 6.13. (a) Stokes and pump evolution of 1 ns, 3 ns and 10 ns SGPs are simulated using the developed model for H_2 (Eq. (6.12)) integrated in the GNLSE vs coupled equation (CE) solution. **(b)** Experimental (Exp) results from [Fig. 4(d) of [34] and simulation (Sim) results by the GNLSE. Sudden drop of Stokes in the experimental results is explained by self-focusing and coupling to higher order modes in [34].

The experimental results (Fig. 4(d) of [34]) are reproduced by simulating the propagation of ~6 ns pulse in the hydrogen-filled fibre with 17 bar pressure. **Figure 6.13 (b)** shows the comparison between experimental and simulation results by taking into account the loss of the fibre. The sudden drop in Stokes, as noted in **Figure 6.13 (b),** is associated to the self-focusing and higher order mode coupling that increase the loss at Stokes wavelength in [34], which is not included in the model. However, the peak of Raman conversion has been modelled with a very good approximation.

6.3.2.9 Efficient Raman conversation in NANF

Finally, having a reliable developed model for pulse propagation in hydrogen-filled NANF, in this section, the performance of Raman conversion is studied in an optimum NANF design. Considering the parametric analyses of NANF design in Chapter 4 and including the effect of pressure and radius of the fibre (**Figure. 6.6**) on the Raman conversion towards mid-IR, the optimum parameters for a hydrogen-filled NANF are chosen as d=4 µm, t_s=1.66 µm, R=35 µm, Z=7 µm, P=50 bar. Although, as discussed in section 6.3.2.4, it is possible to choose different pulse specifications within the practical range, here, for the sake of simulation, a ~6 ns pulse with 10 kW power is chosen as middle range power pulse and well above the Raman threshold. Although the random excitation of Stokes and anti-Stokes in the RS process generates slightly different results for each run of the simulation, practical results can be easily achieved by averaging over several simulation results with random noises.

Figure 6.14 (a) shows the spectrum of the pulse as it propagates through the fibre (in logarithm scale) alongside the power evolution of pump and 1st Stokes in the fibre, as shown in **Figure 6.14 (b)** (in linear scale). For the chosen pump power (10 kW), it is possible to reach more than 68% of the quantum limit in ~3.4 m, while the VRS is in the transient regime and also the fibre loss limits the maximum achievable conversion in this case. However, it is possible to achieve an even higher conversion efficiency by using longer pulses towards the steady-state regime, or higher pump power to overcome the loss of the fibre at Stokes wavelength. In regards to the former, using laser pulses with flatter peak power profile, such as SGPs, can increase the efficiency of conversion by increasing the effective pulse length for the same FWHM of pulse.

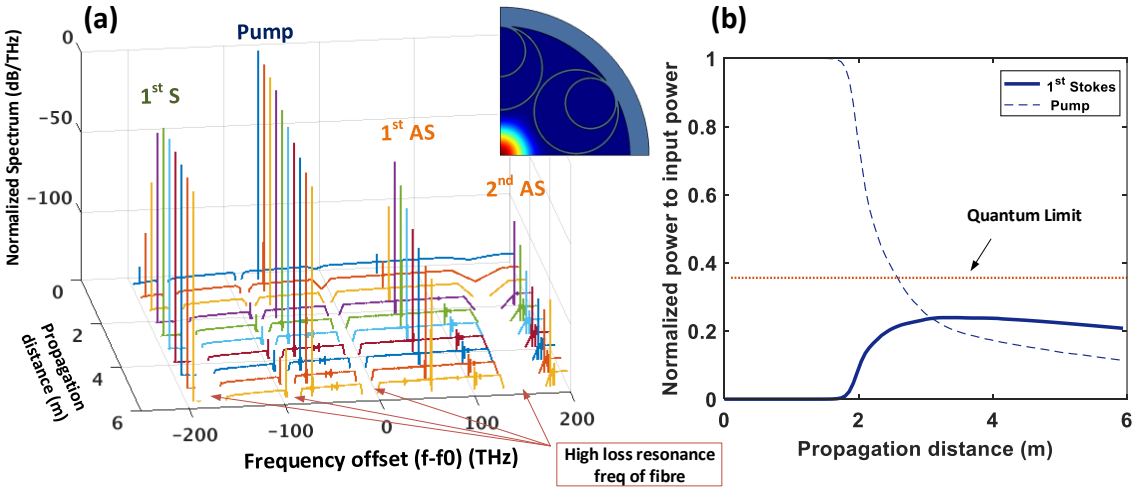

Figure 6.14 : (a) The normalised calculated spectrum of 6ns pulse with 10 kW at 1.55 µm propagating through hydrogen-filled NANF with design parameters in the text. **(b)** The evolution of normalised power of pump and 1st Stokes.

Figure 6.15 (a) compares the simulated power evolution of 1st Stokes for a 6 ns third order SGP and 6 ns GP alongside a 3 ns GP launched in the above-mentioned hydrogen-filled NANF. Using a flatter pulse with the same FWHM (i.e. SGP), it is possible to achieve as high as 78% of quantum limit within ~3 m of fibre. The results are consistent with the gain increase effect towards steady-state regime presented in the previous section. On the other hand, increasing the pump power overcomes the loss of the fibre and increases the conversion efficiency, as shown in **Figure 6.15 (b)** for different pump powers. Although by increasing the pump power it is clearly possible to diminish the effect of loss, self-focusing effects associated with high power pulses can introduce nonlinear loss by coupling the field to higher order modes [34].

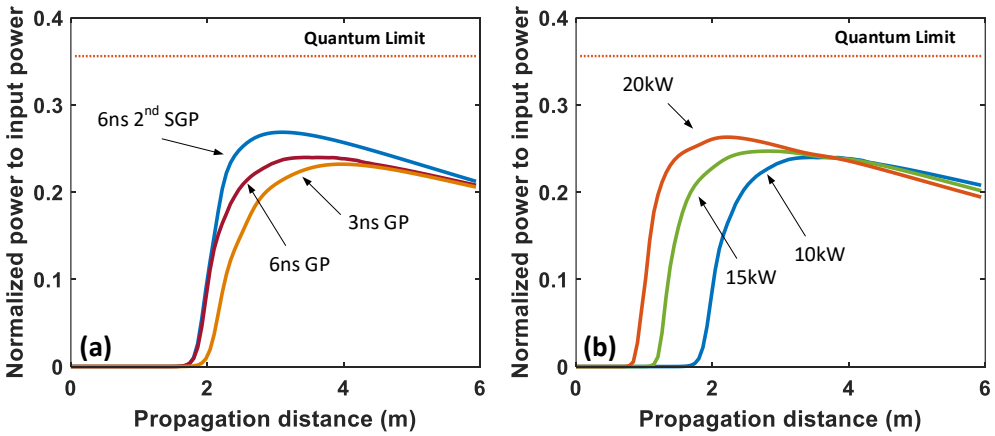

Figure 6.15: (a) The evolution of 1st Stokes of a 6 ns third order SGP, 6 ns GP and a 3 ns GP launched within the hydrogen-filled NANF with gas pressure of 50 bar. **(b)** Comparing the simulated evolution of 1st Stokes of a 6 ns GP with 10 kW, 15 kW and 20 kW along the same fibre as Figure (a).

6.3.2.10 Simulation of fabricated silica NANF

In the previous section, the potential of an appropriately designed NANF has been demonstrated which leads to high efficiency Raman conversion. At the time of writing this thesis, the fabrication technology of NANF was under development and a few examples of NANFs have been fabricated in fabrication group in ORC with close specification for the considered application in this thesis. Here, the simulation of Raman generation towards mid-IR in one of the early in-house-made prototypes has been presented. It is worth mentioning that the fabricated fibre is not optimised particularly for the purpose of this work, but, along with ongoing improvement in the fabrication technology, it is possible to achieve optimum design for high performance Raman generation. The fabricated NANF has seven nested cladding tubes with R =17.5 µm (the core size is not at the optimum according to **Figure. 6.6**). **Figure 6.16** shows the optical microscopy image of the cross-section of the fibre alongside its recreated structure used to model in the developed FEM toolbox. Its average tube thicknesses of $t_s \approx 1.14$ µm places the fundamental transmission band at wavelengths larger than 2.2 µm, which is compatible with the desired range of Stokes wavelength (4.35 µm), but does not provide the lowest loss at this wavelength. Consequently, the pump pulse (1.55 µm) propagates through the second ARB of the fibre. Although the fibre is one of the first fabrication attempts, it preserved a good balance in its structure with a few deviations from ideal structure. **Figure 6.17 (a)** shows the measured and realistic modelling of loss for the NANF. Despite the effect of distortion on the loss

profile of the fibre, it has an acceptable level of loss thanks to the robustness of NANF design to dimension tolerance. Although the loss measurement is not performed at the fundamental band, it is shown that the practical loss profile of a tubular fibre (consequently NANF) can be accurately reproduced by modelling, especially at long wavelengths [189]. The larger loss at shorter wavelength can be associated to micro-bend loss, surface scattering loss and structural inconsistency throughout the fibre, which are not included in the modelling.

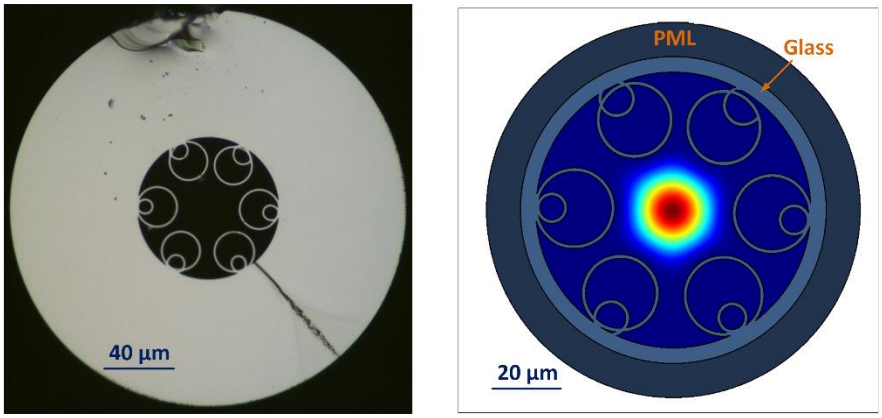

Figure 6.16. On the left: the optical microscopy image of the cross-section of a fabricated prototype NANF on the left with (R =17.5 µm, t_s≈1.14 µm). On the right: the realistic structure used to model the fibre in FEM toolbox and normalised power in the core modelled at 1.55 µm. Note: figures are in different scales.

Using both experimental and modelled loss (the modelled loss has been used where the measured data was not available) in conjunction with dispersion of the fibre, the propagation of a 6 ns pulse with 10 kW peak power in a 5 m hydrogen-filled fibre with 50 bar pressure has been modelled similar to the previous section. **Figure 6.17 (b)** shows the evolution of pump and Raman peaks along the fibre. As predicted in section 6.3.1, because of the high loss at the Stokes wavelength, the efficiency of the conversion is low (~21% of quantum efficiency). However, the optimum loss can be reached by improving the fabrication process for more uniform structure, larger core size and optimised tube thickness. Although, the efficiency of conversion is lower than ideal case, it occurred in shorter fibre length (~0.78 m).

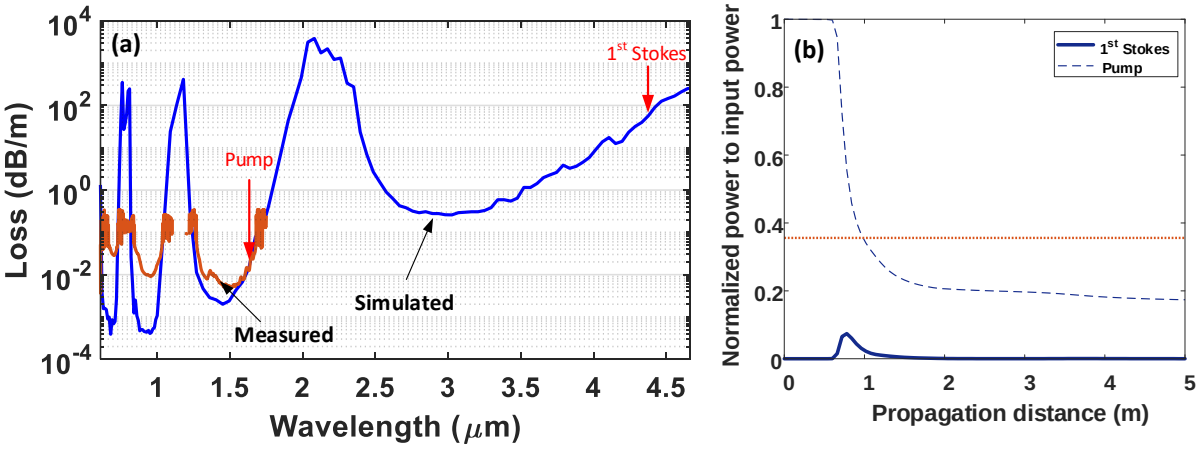

Figure 6.17. (a) The measured and simulated loss profile for fabricated NANF (R =17.5 μm, t_s≈1.14 μm). **(b)** The calculated evolution of normalised power for a 6 ns pulse with 10 kW at 1.55 μm and its 1st Stokes, propagating throughout the modelled hydrogen-filled NANF (**Figure 6.16**).

6.4 Conclusion and discussion

In this chapter, the Raman frequency conversion towards mid-IR in gas-filled hollow core fibres has been studied. Initially, hydrogen has been selected as a suitable gas from those available and glass friendly gasses with long Raman shift to access the longest possible wavelength range of mid-IR with available pump lasers at near-IR. Following the study of HC fibres in Chapter 4, a suitable mid-IR silica NANF with optimum parameters, as presented in Chapter 4, is selected and the effect of its core size and gas pressure on the efficiency of conversion is studied. It have been shown that, unlike solid core fibres, having smaller core size to achieve larger Raman gain is not a valid argument in HC-ARFs. Considering different parameters, such as gas pressure, core size and bend loss mechanism in HC-ARFs, an optimisation design parameter map for NANF as a function of pulse power and gas pressure is proposed and the optimum design to achieve the goal of this work is selected. To study the pulse propagation in hydrogen-filled NANF, a unified model of the GNLSE is adopted and different problems in numerical modelling are addressed and discussed. After verification of the model via comparison between results of model and experimental results in the literature, the efficiency of the proposed hydrogen-filled NANF is studied. It has been shown that it is possible to achieve up to ~68% of quantum efficiency for Raman conversion towards 4.35 μm by an erbium-doped fibre laser with moderate peak power (10 kW) and 6 ns pulse length as pump and without laser pulse modification (assuming GP for laser). Different approaches to achieve even higher efficiency are discussed, which shows that,

with modified pulse, it is possible to achieve as high as ~78% quantum efficiency for the same peak power. While the fabrication team is working on delivering an optimum designed NANF, an early prototype version has been modelled and showed up to ~20% quantum efficiency for GP laser with previous specification, despite the huge loss of the fibre at Stokes wavelength.

The proposed system, by using a conventional fiberized pump laser and hydrogen-filled NANF, can introduce a fully fiberized mid-IR laser with high power output in a demanding wavelength range in industrial and scientific applications. For example, using pulse lasers (e.g. Er:Yb-doped fibre lasers) in the range of C and L-band (~1530-1625 nm) as pump, the output wavelength can be in the range of ~4.2-5 μm. This broad range in mid-IR can be achieved simply by tuning the pump wavelengths and is on demand for many applications, such as biomedicine, laser detection, hydrocarbon processing and environmental monitoring. The simple structure of this laser, using available technology in HC-fibres and the independency of the fibre in any complex material processing, is a very important advantage, which can provide a cost-effective solution for high power mid-IR. In addition, unlike solid-core Raman fibre lasers, the output power is manly limited by the pump power not the Raman active material, which is a huge advantage for this laser.

Note: At the time of preparing this manuscript (a couple of months before submission), a similar experimental work in tubular fibre had been presented in [190], which is in good agreement with simulation results in this chapter. However, the loss in optimised NANF is lower than the tubular fibre used in [190] and, consequently, the modelled conversion efficiency in hydrogen-filled NANF is much higher.

Chapter 7: Nonlinear dynamic of air-filled hollow core fibre

7.1 Introduction

In this chapter, the focus is on the air as the most common gas available for filling the HC fibres (HCFs). Atmospheric air-filled HCFs, representing the simplest yet reliable form of gas-filled HCFs, show remarkable nonlinear properties and have several interesting applications such as pulse compression, frequency conversion and supercontinuum generation. Although the propagation of sub picosecond and a few hundred picosecond pulses are well-studied in air-filled HCFs, the nonlinear response of air to pulses with a duration of a few picoseconds has interesting features that have not yet been explored fully. Here, the nonlinear propagation of ~6 ps pulses in three different types of atmospheric air-filled HC fibre are studied experimentally and theoretically. This particular pulse length provides the ability to explore different nonlinear characteristics of air at different power levels. Using in-house-fabricated state-of-the-art HC photonic bandgap (HC-PBGF), HC tubular (HC-TF) and HC Kagomé fibres (HC-KF), it was possible to associate the origin of the initial pulse broadening process in these fibres to rotational Raman scattering (RRS) at low power levels. Due to the broadband and low loss transmission window of the HC Kagomé fibre it is used to observe the transition from initial pulse broadening (by RRS) at lower powers, through long range frequency conversion (2330 cm^{-1}) with the help of vibrational Raman scattering, to broadband (~700 nm) supercontinuum generation at high power levels. In this study, to model such a wide range of nonlinear processes in a unified approach, a semi quantum model for air is developed and implemented into the modified version of the GNLSE, which surpasses the limits of the common single damping oscillator model in this pulse length regime. The variety of nonlinear process in this case from Raman frequency conversion (in near-IR) to supercontinuum is a very good validation test for the developed numerical toolbox in this thesis while representing an integrated model for air in the GNLSE. In fact, the model has been validated by comparison between its results and experimental results, and provides a powerful tool for the design, modelling and optimization of nonlinear processes in air-filled HC fibres.

The ambient air that can be found in the core of HCFs, has an almost two orders of magnitude lower nonlinearity ($\sim 6\times10^{-23}\ m^2/W$) than silica glass ($2\times10^{-22}\ m^2/W$) [191-193]. However, its nonlinearity can still have significant effects on the propagation of high peak power pulses, that can lead to spectral broadening, pulse distortion and ultimately loss of power, all of which are typically detrimental in power delivery applications. For some applications, however, the nonlinear processes can be exploited for pulse modification [95, 194], new frequency generation [195], or even broad supercontinuum generation (SG) with a very high power density due to the very high damage threshold of HCFs and the confined gas within the core [48, 196]. The simplicity of air-filled HCFs, combined with their very long light-matter interactions, motivated the exploration of potential applications in recent works [197, 198]. To support such experimental works there is a clear need for appropriate tools for modelling the pulse propagation in air-filled fibres.

In recent years, there have been several experimental studies on pulse propagation in air-filled HCFs in different pulse regimes, ranging from a few femtosecond to nanosecond pulses [197, 199-202]. Each experiment has shown a specific characteristic of the nonlinear processes in air. Yet, to the best of my knowledge, a study that illustrates a broad range of nonlinear phenomena and observes clear fingerprints of both vibrational Raman scattering (VRS) and rotational Raman scattering (RRS) has not yet been reported. The ultra-short pulse regime (sub-ps duration) can introduce a broad supercontinuum expanding through many fibre transmission bands, as demonstrated in different types of HCFs including HC-KFs and HC-TFs [196, 197]. Although, in this regime, very interesting results are obtained through a variety of nonlinear processes, the clear signature of Raman scattering is absent. In this case, the mixed effect of four wave mixing (FWM) and SRS in the output pulse, and more specifically the lack of a clear sign of VRS, significantly reduce the ability to study in detail the RRS and VRS processes. Furthermore, it is challenging to resolve the evolution from an initial single dominant Raman/FWM excitation to a broad supercontinuum spectrum.

In contrast, long pulses (e.g. hundreds of picosecond to nanosecond pulses) show much more detail in terms of Raman scattering and can produce sharp and clear Raman peaks even at very high powers [197]. In this regime, not only can VRS be observed distinctively, but the RRS peaks corresponding to higher order Stokes can be distinguished, in contrast to the broadening effects seen with femtosecond pulses. However, to achieve broad SG in this regime, impractically high power input pulses are

necessary, which limits the understanding of the broadening process and practicality of the system. Recently, the dynamics of pulse propagation in both regimes has been experimentally demonstrated in two separate atmospheric air-filled HCFs (negative-curvature HC-KFs) pumped by 100 fs and 300 ps pulses in different setups [197]. Here, the nonlinear evolution dynamics for pulse durations has been studied in the middle of the aforementioned range, which complements existing results and helps constructing a comprehensive picture of the nonlinear response in air-filled HCFs.

Here, by selecting appropriate pulse parameters, a variety of nonlinear processes have been experimentally observed (the experimental part has been performed by Hans Christian Hansen Mulvad). In addition to variations in the pulse characteristics (e.g. pulse length and peak power), different types of HCFs (i.e. HC-PBGF, HC-KF and HC-TF) have experimentally compared, in order to provide insight into the influence of the HCF itself. Furthermore, in order to be able to theoretically reproduce the results over a broad spectral range, a semi-quantum model of the roto-vibrational Raman process in bi-atomic molecules has been implemented to simulate the nonlinear behaviour of air with a sufficiently good precision. Using this model, the nonlinear dynamics of pulse propagation have been simulated in different scenarios yielding a very good agreement with experimental results. This provides a useful tool for analysing the nonlinear behaviour of air-filled HCFs.

7.2 Experimental setup and results in HC fibres

7.2.1 HC fibre characteristics

In addition to their ability to confine gas, guide light for a long distance and therefore provide long gas-light interaction lengths, HCFs can profoundly influence the pulse propagation dynamics. Thus, their optical and geometrical characteristics are of critical importance in determining the pulse propagation dynamics, as exemplified in this study. Recall from Chapter 4, based on their guidance mechanism, HCFs can be categorized into two major types: photonic bandgap fibres (PBGFs) and anti-resonant/inhibited coupling fibres (ARFs). In this work, to study the effect of the fibre characteristics on the nonlinear behaviour of air, the pulse propagation dynamics has been experimentally explored in three different designs of in-house-fabricated HCFs, more specifically: HC-PBGF [203], HC negative-curvature Kagomé (HC-KF) [64] and HC nodeless tubular (HC-TF) fibres. All the fibres used in this study represent, or are similar to, the state-of-the-art in their respective categories. While the guidance

mechanism is clear in the first type (HC-PBGF), in the last two cases the guidance mechanism has been associated either to anti-resonance effects from glass membranes adjacent to air-core [114, 139, 204], or to inhibited coupling effects between the core mode and cladding modes [55, 63, 205]. Here, without any intention to dive into any explanation of their guidance mechanism, the fibres have been chosen for their great potential to generate gas-based nonlinear processes and for the sake of studying the effects, challenges, and performance of the developed model in this work.

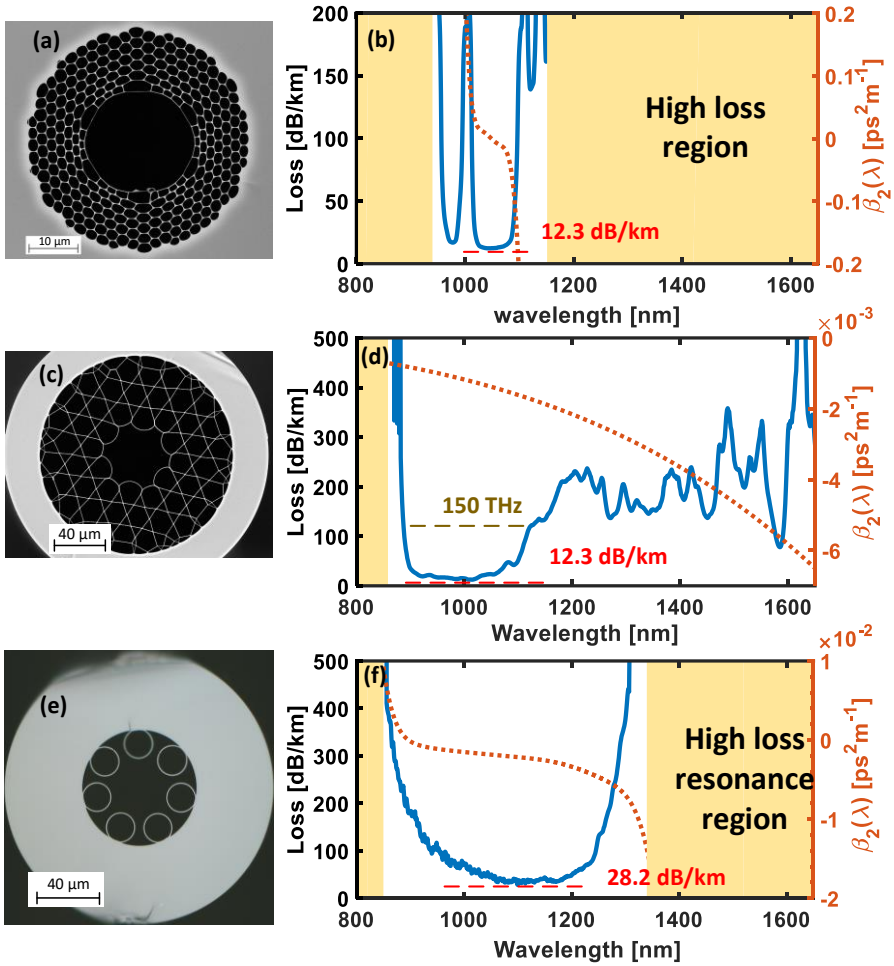

Figure 7.1 Scanning electron micrographs (SEMs) of the cross-section of fabricated **(a)** HC-PBGF, **(c)** HC-KF, **(e)** the optical microscopic image of the cross-section of fabricated HC-TF. The loss and dispersion profile of **(b)** HC-PBGF, **(d)** HC-KF, **(f)** HC-TF.

HC-PBGFs, despite their narrow transmission window, have shown the lowest experimental loss among any other type of HCFs [46]. Here, an in-house-fabricated 37-cell HC-PBGF has been used to achieve very low loss in the loss range of HC fibres (< 100 dB/km); the fibre cross section is shown in the scanning electron micrograph (SEM) image in **Figure 7.1 (a)**. The fibre has a core diameter of ~21.5 µm and a main low loss transmission window from 1010 nm to 1096 nm. Its average loss is 13.6 dB/km and the lowest loss is 12.3 dB/km at 1046 nm (one of the best values ever reported for

this kind of fibre). The measured cutback loss and calculated dispersion profile (found using commercial finite element (FEM) mode solver (COMSOL®)) are shown in **Figure 7.1 (b)**. Although the HC-PBGFs have a very low experimental loss, the significant overlap between the air-guided field and the cladding glass and their narrow transmission window limit their usage for high power applications and broadband nonlinear processes.

On the other hand, HC-KFs with higher damage threshold and broad multiband transmission windows can overcome the limitations of HC-PBGFs. Here, an in-house-fabricated 7-cell HC-KF has been used with low loss and low bend loss (in comparison to other ARFs) [64]. The fibre has a large bandwidth cantered around a wavelength of 1 μm, which is perfectly matched to the ps source of this experiment. **Figure 7.1 (c)** shows an SEM image of the cross-section of the fibre, which has a core diameter of 43 μm and an average core wall thickness of ~375 nm. The minimum loss of 12.3 dB/km is at 1010 nm and the 3 dB bandwidth is 150 nm. Its transmission window spans from 850 nm to 1700 nm, with an average loss of less than 200 dB/km as shown in **Figure 7.1 (d)**. This broad transmission window makes the fibre a suitable host for the observation of wideband nonlinear processes. To simulate its dispersion, a well-developed, suitably modified model based on the analytical dispersion of a hollow capillary has been used, which was proven to be accurate enough for the spectral range of this work [206]:

$$\beta(\omega) = \frac{\omega}{c}\sqrt{n_{gas}^2(\omega, P, T) - \left(\frac{2.4048c}{\omega \cdot a(\omega)}\right)^2} \tag{7.1}$$

here c is the speed of light, $a(\omega) = a_{AP} / (1 + 0.065(2\pi c)^2 / (\omega^2 a_{AP} t))$ where a_{AP} is an area-preserving core diameter of the HC-KF and t is the thickness of the core-surrounding glass membranes [206]. $n_{gas}(\omega, P, T)$ is the refractive index of the gas inside the fibre core and is a function of pressure (P) and temperature (T). Using Eq. (7.1) and a known model for air [207], the dispersion of the HC-KF has been calculated at experimental conditions ($T \approx$ 290 K, $P \approx 1\ atm$) as presented in **Figure 7.1 (d)**. According to performed simulations in this study, the percentage of air-guided field in the cladding glass for this fibre is of the order of 10^{-5}, which leads to a high damage threshold (approximately two orders of magnitude higher than that of HC-PBGF [48]). Although this fibre has a higher order transmission window below 800 nm in addition to the fundamental one that would make it possible to explore inter-transmission band

nonlinear processes, this work only focuses on the study and observation of nonlinearity in the fundamental transmission window.

Another type of HC negative-curvature fibre, with a reasonably low loss and ultra-broad multiband transmission windows, is HC-TF. Recent studies have shown the potential of these fibres to ultimately achieve a lower level of loss and greater polarization control than HC-PBGFs [55, 57, 140] and an octave-spanning version has been demonstrated recently with loss compatible with short range data transmission applications [189]. Here, an in-house-made 7-tube silica HC-TF with a core diameter of ~35.8 μm and an inner jacket tube diameter of ~76.7 μm is used. **Figure 7.1 (e)** shows an optical microscopic image of the fibre cross-section. With an average tube thickness of ~775 nm, the second low loss antiresonance band of the fibre is located between 850 and 1355 nm. The fibre loss in this transmission window is shown in **Figure 7.1 (f)** alongside its simulated dispersion profile using the developed FEM mode solver toolbox as mentioned in Chapter 3.

7.2.2 Experimental setup

In this study, a commercially available Trumpf TruMicro 5050© [208] laser has been used to perform the experiments. This source produces ~6 ps pulses with a 200 kHz repetition rate at 1030 nm and variable energy of up to 250 μJ per pulse (average power ≈ 50W). The output is a collimated beam of diameter 5.4 mm, and the M^2 value is 1.08. To couple t he laser pulses into the fibre, a coupling system composed of a variable beam expander (Jenoptik 1x-4x, AE 1614, 1030-1080 nm, transmission ≥ 97%) followed by a focusing lens (Thorlabs LA4148-B-ML, fused silica plan-convex lens with 50mm focal length, Broadband anti-reflection coating 650-1050nm) are used, as shown in **Figure 7.2**.

To maximize the power launched into the fundamental mode of the fibre, the fibre input facet is positioned using a micrometer positioning stage at the focal point of the focusing lens. The beam expander is used to adjust the width of the collimated beam (here operated in reverse to reduce the beam diameter), such that a beam waist with the optimum width for a fundamental mode launch of each fibre is obtained at the position of the fibre input. The beam expander is fine-tuned by monitoring and maximizing the output power of the fibre (measured using a Gentec UP55N-300F-H9-D0 power meter) which indicates an optimum fundamental mode launch due to the substantially higher propagation losses of higher-order modes. As an additional precaution, a camera is used to monitor and detect scattered light from the fibre input facet. The amount of scattered

light from the glass microstructure is minimized by fine-tuning the fibre input position, which further reduces the risk of damage to the input facet. The fibre under test is loosely coiled to approximately 30-40 cm coil diameter. The output power of the fibre is measured using a power meter (Gentec UP55N-300F-H9-D0). To measure the optical spectrum, a small portion of the output beam is reflected off a glass wedge and coupled into an optical spectrum analyser (OSA, Ando AQ6317B, 600-1750 nm).

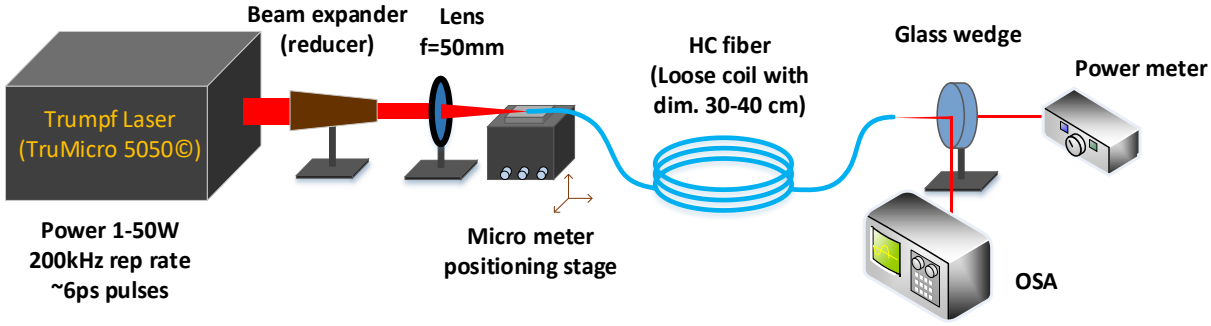

Figure 7.2. Experimental setup including free space launching mechanism and measurement systems.

7.2.3 Experimental results

In this section, a range of experimental results for different pulse powers launched into a sample of each fibre will be presented and studied. To start with, the experiments are conducted with low power pulses, launched into 5m and 9.6m of atmospheric air-filled samples of HC-PBGF and HC-TF, respectively, to cover two different categories of HCFs and to study the effect of the fibre characteristics on the optical output. The measured output spectra for both fibres are shown in **Figure 7.3**, for different average laser output power (P_{avg}). Coupling losses were ~0.3 dB and ~0.6 dB for the HC-TF and HC-PBGF respectively. In both cases, the measured output spectra show broadening around the pump wavelength caused by SPM, while sidebands start to appear at higher powers with consistent frequency detuning from the pump in both cases (as noted in **Figure 7.3 (a,b)**). The presented power levels in figures are measured at OSA and not representing the actual output power of the fibres.

Sidebands at 1036 nm and 1023 nm could in principle be caused by FWM, however, according to $2\gamma P_0 \approx -\beta_2\Omega^2 - (\beta_4/12)\Omega^4$ [209], the dependency of detuning on pulse power and dispersion should clearly affect the position of the peaks in both experiments, when dissimilar pulse powers and fibres are used. Here γ, β_n, P_0, Ω are the nonlinear coefficient, nth derivative of β, pump power, and phase matching detuning of Stokes respectively. To distinguish the FWM peaks from RRS peaks, in **Figure 7.3 (c,d)**, the

phase matching condition (PMC) detuning for each P_{avg} are plotted. The phase matching condition for HC-PBGF would be out of the range of the plotted spectrum. The clear difference between the phase matching wavelengths and the actual peaks confirms the influence of RRS. In more detail, the 1st Stokes (1036 nm) and anti-Stokes Raman peaks (1023 nm) appear at $P_{avg} > 2$ W and $P_{avg} > 5$ W for HC-TF and HC-PBGF, respectively. These frequency shifts are in a very good agreement with the rotational Raman shifts of nitrogen (J = 6) and are consistent with the nitrogen concentration in air (80%), while the different threshold powers at which the peaks begin to emerge can be explained by the difference in length and core size of each fibre. Meanwhile, the clear influence of nonlinear Kerr effects on the pulse and on the RRS peaks can be seen in the shape of the pump and sideband spectra [172]. Here, comparing two different categories of fibres has enabled us to understand the effect of fibre characteristics (primarily dispersion) on the emergence of broadening effects at their initial stages.

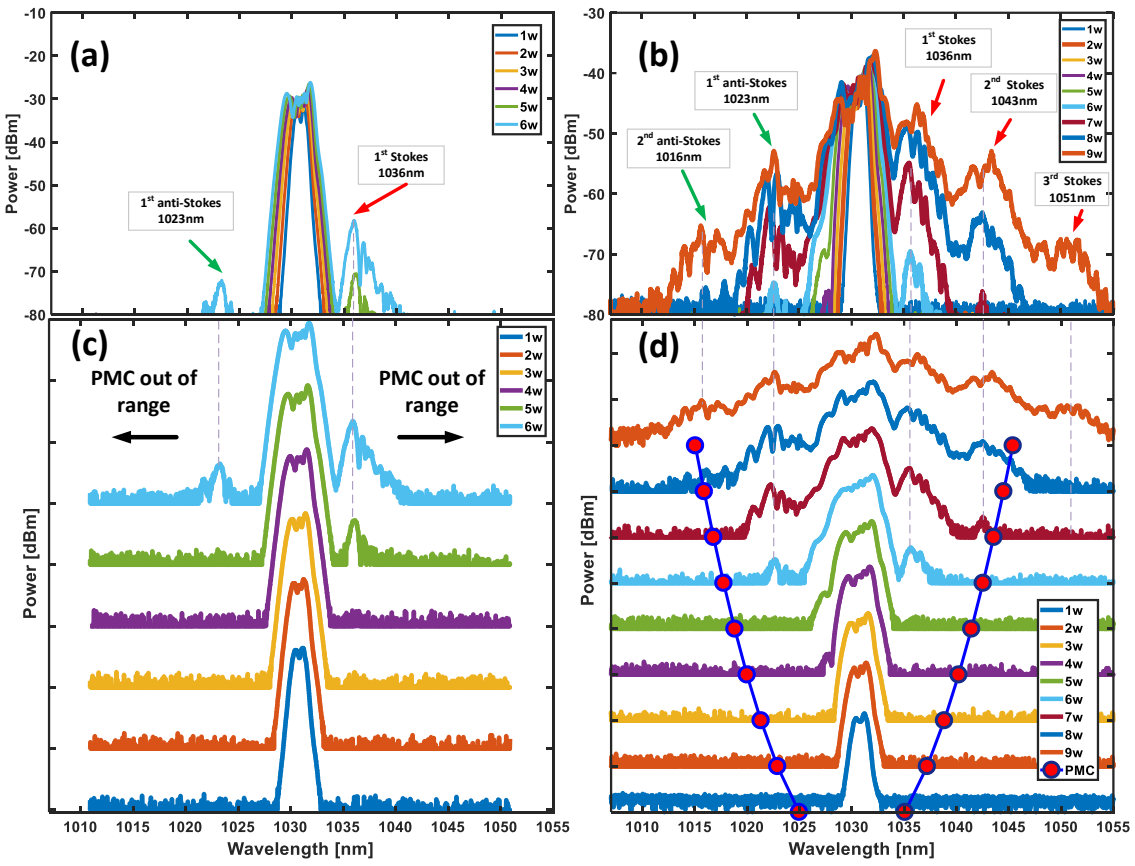

Figure 7.3. The measured output spectrum of the pulsed laser with ~6 ps pulse length at 1030 nm launched in **(a)** 5 m of HC-PBGF with average laser power (P_{avg}) range of 1 – 6 W and **(b)** 9.6 m of HC-TF with P_{avg} of 1 – 7 W. The phase matching condition (PMC) detuning wavelengths are superposed over the experimental results for **(c)** HC-PBGF and **(d)** HC-TF with 10 dBm shift for each plot (10 dBm/div). The PMC is out of the plot range for HC-PBGF **(d)** due to the higher nonlinear coefficient of this fibre.

As the power increases (P_{avg} > 7 W) for the HC-TF, higher orders of Stokes appear at 1043 nm, 1051 nm and for anti-Stokes at 1016 nm with clear signs of the combined effect of Kerr and Raman nonlinearities introduced in the form of broadening at the sideband peaks, which is distinguishable in the output spectra. Although both fibres presented similar nonlinear outputs despite the markedly different dispersion properties, it is found that their damage thresholds are considerably different. In the HC-TF, up to 50 W (P_{avg}) is transmitted, limited by the maximum power of the available source, without observing any damage. In the HC-PBGF, however, sudden damage to the end facet was observed at a much lower input power level, resulting in the partial or complete destruction of the microstructure extending from the end-facet and several mm into the fibre as shown in **Figure 7.4**. Repeated trials resulted in such damage occurring in a range of input power levels between 5 W and 9 W under similar coupling conditions. The end-facet damage is attributed to power leakage into the cladding-glass beyond the damage threshold of the glass.

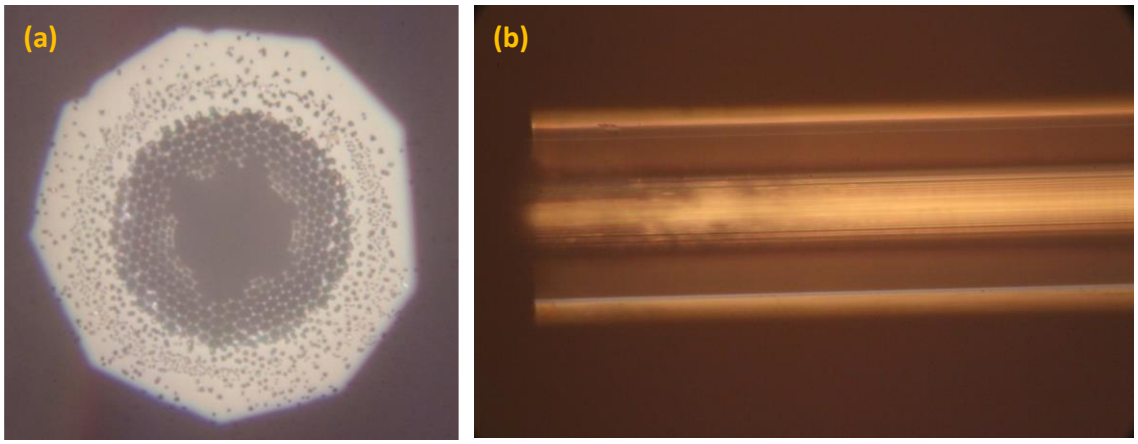

Figure 7.4. Damaged HC-PBGF by lunching the laser pulse with ~ 6 ps, 200 KHz and 7 W average power at 1030 nm. **(a)** Damaged cross-section of the fibre, **(b)** structural damage along the fibre.

Similar to the HC-TF, HC-KF has 2-3 order of magnitude lower power fraction in the glass than HC-PBGF and can tolerate higher power pulses. Therefore, to study nonlinear effects at higher powers, the results from HC-TF are compared with results obtained from a 13.8 m sample of the HC-KF (**Figure 7.1 (c)**). The wider transmission window with low loss profile in this latter fibre facilitates the study of VRS when the pulse power reaches the threshold for the first vibrational Stokes. **Figure 7.5 (a,b)** show the output spectrum of the HC-TF and HC-KF for P_{avg} =10, 15, 20 W and P_{avg} = 2, 5, 10, 15, 20 W, respectively. As the power increases, the main pulse experiences broadening from a mixture of nonlinear phenomena initiated by RRS (e.g. higher order

RRS, FWM, SPM, etc.) and long before any sign of VRS at P_{avg} = 20 W for HC-TF (**Figure 7.5 (a)**).

On the other hand, in the HC-KF, similar to the previous cases, sideband peaks with the same frequency shifts grow around similar input power (~5 W); this again confirms the insensitivity of the process to the fibre characteristics and the dominance of RRS. However, there is a clear sign of a 2330 cm^{-1} shifted peak (at ~1355 nm) associated with VRS of nitrogen at P_{avg} =5 W.

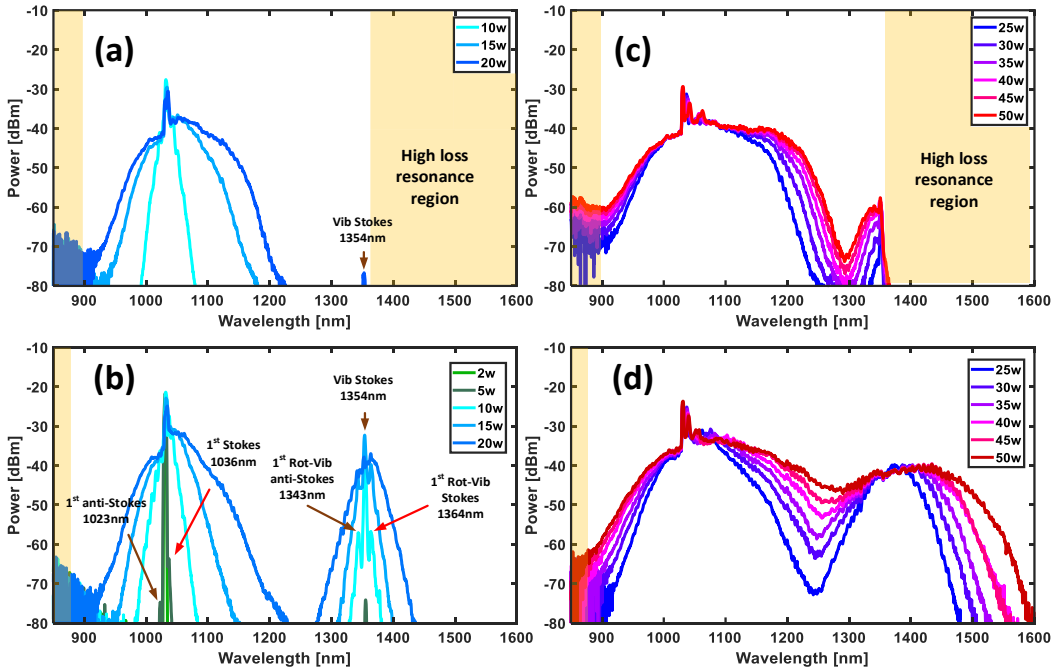

Figure 7.5. The output spectrum of the pulsed laser with ~6 ps length at 1030 nm launched in to **(a)** HC-TF with average laser power (P_{avg}) of 10, 15, 20 W and **(b)** HC-KF with P_{avg} of 2, 5, 10, 15, 20 W. The higher power output spectrums from overlapping sidebands to broad supercontinuum are presented for P_{avg} = 25, 30, 35, 40, 45 and 50 W in **(c)** HC-TF and **(d)** HC-KF.

The difference of the VRS threshold in both cases mainly comes from the high loss of the HC-TF at the VRS wavelength (**Figure 7.1 (f)**) in comparison to that of the HC-KF, with minor effects arising from their characteristic differences (i.e. fibre length and core size). It can be seen how the pulse duration in this experiment results in a good balance between pump broadening and energy transfer to the vibrational levels, making it possible to distinguish the signature of VRS very clearly [197]. This effect is modelled in the following sections. Furthermore, the first sign of roto-vibrational Stokes and anti-Stokes scattering are clear around the main peak of VRS as labelled in **Figure 7.5**

(b) at P_{avg} = 10 W. This initiates the broadening effect of the VRS sidebands and which is similar to that at the main pump wavelength. At powers above ~20 W, the pump and vibrational Raman peaks experience a rapidly-growing broadening effect, which is initiated by the RRS lines of nitrogen and is accelerated further by the Kerr nonlinearity with a similar pattern in both fibres, as seen in **Figure 7.5 (c,d)**. These broadening processes from pump and VRS peaks continue until they start overlapping and create a broadband supercontinuum extending over a bandwidth of ~750 nm in the HC-KF. In the case of the HC-TF, the high loss of the fibre outside the anti-resonance window reduces the bandwidth of the supercontinuum to only ~400 nm. On the other hand, the HC-KF output shows a very broad supercontinuum with a fairly flat feature (~10 dB over 500 nm). In fact, such a broadband output is generated with the help of the spectral wings from the main pump and VRS peak (second pump) in the form of a 'dual pump' SG scheme. This, in principle, can decrease the required launched power to achieve a similar bandwidth in conventional 'single pump' broadening schemes for the same initial pulse width, since the necessary broadening in each 'pump' can be achieved with lower power.

The consistency in the position of the initial sideband peaks in all three fibres at low input power and the appearance of similar vibrational peaks followed by spectral broadening (in two of the fibres) confirms that the detailed nonlinearity of air has a more significant effect than the dispersion related to waveguiding effects due to the fibres. The possibility of observing the dynamics of the nonlinear process in this setup by only tuning the pump power ranging from control of the Stokes and anti-Stokes sidebands, large Raman frequency down conversion (VRS) to broadband SG, introduces a powerful and tuneable source with high spectral power density and broadband spectral output for many applications. Moreover, the complex nonlinear evolution provides a good test and means of verifying the developed numerical model which is described in the next section.

7.3 Modelling high power pulse propagation in air-filled HC fibre

In order to model the observed phenomena by high-power pulse propagation in air-filled HCFs a robust method is needed to handle both the linear and nonlinear phenomena. Among many different methods and equations (e.g. coupled-mode Raman-FWM, Beam propagation method, etc.) [209], the Generalized nonlinear Schrödinger equation (GNLSE) is one of the most common, reliable and accurate equations to model the

dynamics of pulse propagation in a nonlinear waveguide (i.e. optical fibres). The GNLSE can model a range of phenomena by including key elements from linear chromatic dispersion to delayed molecular nonlinear effects. Despite its success, the most of common models for air are not suited for the GNLSE and the most recent studies on air-filled HCFs used a very simplified model for nonlinearity of air [196, 199, 210, 211], which struggles to correctly model the detailed nonlinear behaviour of air. Here, I address this problem by adopting a more comprehensive model, which is validated through comparison with experimental results.

In general, it would be challenging to model the optical behaviour of a gas mixture, due to the multi-molecule nature of the gas. However, in case of air, it can be significantly simplified by considering the diatomic model of nitrogen (~80%) and oxygen (~20%) as the dominant gases involved in the optical process. Although this can reduce the complexity of the process, including proper details in the model of each gas is crucial to produce realistic and reliable results, since oversimplification can generate discrepancies between simulations and experimental results.

Here, to present a comprehensive model for the nonlinear behaviour of air in the adaptive form with the GNLSE and to also include propagation of the pulse throughout the air-filled fibres, the dynamics of the pulse is assumed to be governed by the GNLSE in a co-moving frame with the central frequency of the pulse. This formulation includes the loss, dispersion and nonlinear properties of air, as well as all the waveguiding properties of the fibre. It can be represented by:

$$\begin{aligned} &\frac{\partial \tilde{A}(z,\omega)}{\partial z} - i\tilde{D}(\omega)\tilde{A}(z,\omega) = \cdots \\ &i\sum_{j=1}^{2} K_j \gamma_j(\omega)\mathbb{F}\left\{ A(z,t)\int_{-\infty}^{+\infty} R_j(T)\left|A(z,t-T)\right|^2 dT \right\}, \quad j=1,2. \end{aligned} \tag{7.2}$$

It is a modified version of the GNLSE (Eq. (2.13)) in frequency domain and $\tilde{A}(z,\omega) = \mathbb{F}\{A(z,t)\}$ denotes the slowly varying envelope of the electromagnetic field in the frequency domain. Recall from Eq. (6.6) that $\tilde{D}(\omega)$ is the linear/dispersion operator of the GNLSE with the definition $\tilde{D}(\omega) = \beta(\omega) - \beta(\omega_0) - \beta_1(\omega_0)(\omega-\omega_0) + i\alpha(\omega)/2$, where $\beta(\omega)$ represents the frequency-dependent propagation constant of the fundamental mode in the air-filled fibre and $\beta_n(\omega_0)$ is the nth derivative of the propagation constant at the central frequency of the pulse (ω_0). $\alpha(\omega)$ is the loss operator, which contains the contribution of fibre loss and the Rayleigh absorption of air. The right hand side of the

equation represents the nonlinearity originating from the interaction of the pulse with the multi-material waveguide, which here has two elements of air and glass represented by $j=1,2$, respectively. In order to model the relative contribution of glass and air in the nonlinear response, a contribution coefficient (K_j) is introduced, which represents the power fraction in the j^{th} material (i.e. K_1 for air and K_2 for glass) and satisfies the condition $\sum K_j = 1$. The frequency dependent nonlinear coefficient for each substance has been defined as $\gamma_j(\omega) = \omega \bar{n}_j(\omega) / cA_{eff}$ with $\bar{n}_j(\omega)$ as the nonlinear refractive index of the j^{th} substance and A_{eff} as the effective mode area.

Recall from Eq. (2.14) that $R_j(t)$ represent the nonlinear response of the medium labelled by *j*, as each term of summation in Eq. (7.2) stands for the nonlinear effect of the related material. In this definition, the nonlinear response ($R_j(t)$) contains both the electronic response, with instantaneous action on the pulse (Kerr effect), and the slower molecular response (Raman response) [209]:

$$R_j(t) = (1-f_{r_j})\delta(t) + f_{r_j} H_j(t), \quad j=1,2. \qquad \int_{-\infty}^{+\infty} R_j(t)dt = 1. \tag{7.3}$$

Here, $H_j(t)$ is the Raman response of the molecules and f_{r_j} is the fractional contribution of the Raman response to the total nonlinear response. In the regime of moderately high pulse power (but still far from the ionization energy of the material), $H(t)$ is the most important function, that includes almost all nonlinear effects at the molecular level and that needs to be properly defined to achieve accurate results.

Considering the causality for the Raman response and using the Kramers-Kronig principle, the simplest form of nonlinear response can be defined in the well-established form of a single damped oscillator (SDO) [212], which is defined as $H(t) \propto u(t)e^{-t/\tau_d}\sin(t/\tau_o)$ where $u(t)$ is the Heaviside function, τ_d is oscillator damping time, and τ_o is time constant controlling the oscillation period. This simple SDO with τ_d = 32 fs, τ_o =12.5 fs and f_{r_2} = 0.18 can successfully model a variety of nonlinear effects in silica glass by reproducing its broad Raman gain. In extreme cases a more precise model is needed, as suggested in [193]. Extending this approach to the study of RRS in gases, can only provide an overall approximate response, which accounts for all RRS lines as one broad continuous response. This simplification replaces the effect of individual lines in favour of one simple overlaying envelope. In previous works on

air-filled HCFs, the response of air in the GNLSE has been modelled mainly by considering nitrogen as the dominant gas with τ_d = 77 fs, τ_o =62.5 fs and f_{r1} = 0.5; this only takes into the account the 8th rotational transition in RRS of nitrogen [192, 210]. To illustrate some disadvantages of the SDO model for air in the pulse length regime of this study, a few experimental results of air-filled HC-KF (**Figure 7.5 (b)**) were simulated using the SDO and are shown in **Figure 7.6**. Here, not only the SDO was unable to correctly model the initial position of the sideband peaks and broadening effects at low power, but it also completely omits VRS, which is vital in this pulse duration regime, and therefore the SDO produces incorrect results. In the following, I describe the implementation of a comprehensive model of the air response using the GNLSE, which reproduces well the experimental results of different air-filled HCFs.

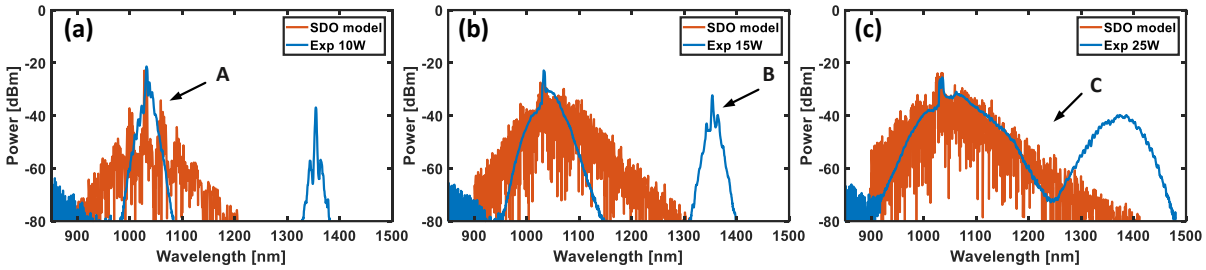

Figure 7.6. Comparison between experimental results of air-filled HC-KF (**Figure 7.5 (b)**) and the GNLSE simulation results using SDO model for air **(a)** P_{avg} = 10 W, **(b)** P_{avg} = 15 W, **(c)** P_{avg} = 25 W. The SDO model cannot properly predict A. the position of the RRS at low power. B. VRS is not reproduced at all. C. The broadening effect is not correctly reproduced due to lack of VRS.

7.3.1 Semi-quantum model for nonlinear scattering of air

Unlike solid materials, where molecules are limited to vibrational states, it is well known that gases can also have rotational states, which can be involved in RRS (subject to their Raman activity). Although general modelling of rotational states and rotational scattering can be challenging for complex molecules, a semi-quantum model (SQM) for simple diatomic molecules, such as nitrogen and oxygen (most frequent molecules in air), can provide enough information and accuracy to model the behaviour of the molecule in interaction with high power pulses. Generally, the full rotational Raman response of each gas is a collective response of transitions from individual rotational states, which depend on the energy level and population of each rotational state, as introduced in [213-215]. Although the quantum Schrödinger equation can be used to calculate the rotational states and their energy levels, thanks to a much less onerous

classical approach to calculate the angular momentum and energy of rotational levels, the implementation of their quantum mechanical property is straightforward [216].

For linear diatomic molecules such as nitrogen and oxygen by considering a rigid linear rotor as their molecular model and implementing the angular momentum principle, the energy of an individual rotational state (J) can be calculated as $E_J = J(J+1)Bhc$, where B is the rotational constant of the rotor and h is Planck's constant. In this representation, RRS arises from rotational level changes caused by an excitation field. The excitation/ relaxation of rotational states creates rotational Raman Stokes/anti-Stokes, respectively, with a frequency shift proportional to the energy difference between the initial and final states of the molecule. However, the change in energy levels is not arbitrary, but determined by the selection rule of $\Delta J = \pm 2$ [216], which implies a rotational Raman frequency shift of $\omega_J = 2Bc(2J+3)$. **Figure 7.7** shows the rotational energy level diagram of a diatomic molecule with Stokes and anti-Stokes frequency shifts.

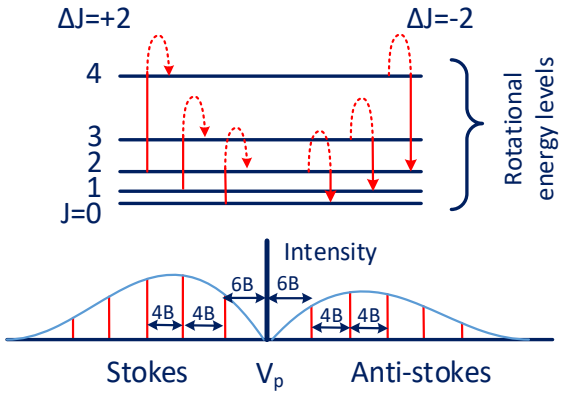

Figure 7.7. Demonstration of Rotational energy level diagram and intensity of each scattering transition.

In addition to the frequency shift, the intensity of each individual transition is also needed to complete the model. For each Raman transition (ω_J), the intensity is proportional to the population of the initial state and the Placzek-Teller coefficient of transition from the initial to final state [217]. In more detail, the population of each state is defined by the Maxwell-Boltzmann thermal distribution, the quantum degeneracy of the initial state ($2J+1$) and the isotopic effect. Taking all these factors into account, the total rotational Raman response of the diatomic gas ($H_{rot_k}(t)$) is ($k = 1,2$ for N_2 and O_2) [191, 217, 218]:

$$H_{rot_k}(t) = u(t)C_{rot_k}\sum_J e^{(-t/\tau_{rot_{k_J}})}A_{k_J}\sin(4\pi B_k c(2J+3)),$$
$$A_{k_J} = (N_{k_{(J+2)}} - N_{k_J})q_{k_J}\frac{(J+2)(J+1)}{(2J+3)}, \quad (7.4)$$
$$N_{k_J} = \exp\left[-hcB_k J(J+1)/KT\right]. \quad k = 1, 2.$$

where K, T are Boltzmann constant, and gas temperature, respectively. The rotational constants are $B_1 = 1.99\ cm^{-1}$ and $B_2 = 1.44\ cm^{-1}$. The quantum effects are $q_{1_J} = 1$ and 2 for odd and even J due to nuclear statistics (Isotopic effect), while $q_{2_J} = 1$ and 0 for odd and even J, respectively. In this approach, A_{K_J} represent the intensity of the Raman transition for frequency shift ω_J, which includes the effect of temperature by considering the temperature dependence of the population of molecules (N_{K_J}) for each rotational level. The normalization coefficient (C_{rot_k}) is defined to normalize the Raman response by Eq. (7.3). The relaxation factors ($\tau_{rot_{k_J}}$) are on average 61 ps and 68 ps for N_2 and O_2, respectively [216] while the measured values in [219] are used for this study. Here, for the sake of simplicity, a few factors such as centrifugal force, Stark effect, etc. are not included in the model, which have a very small effect on the results in the experimental environment (i.e. temperature and pressure stability).

Figure 7.8 (a) shows a comparison between the time domain rotational Raman response for nitrogen using the SDO and Eq. (7.4) as SQM. Although the SDO can mimic the first oscillating part of the response (t < 1 ps) (inset of **Figure 7.8 (a)**), which may be enough to model the SG process initiated by high-power short pulses [196, 197], the lack of the other oscillating peaks affects the accuracy of the model in reproducing the mutual effects of the Raman and Kerr processes. This can be seen more clearly in the frequency domain, as shown in **Figure 7.8 (b,c)**. The essential difference between the real and imaginary parts of both responses sets the major imbalance between the Raman and parametric gains in each model.

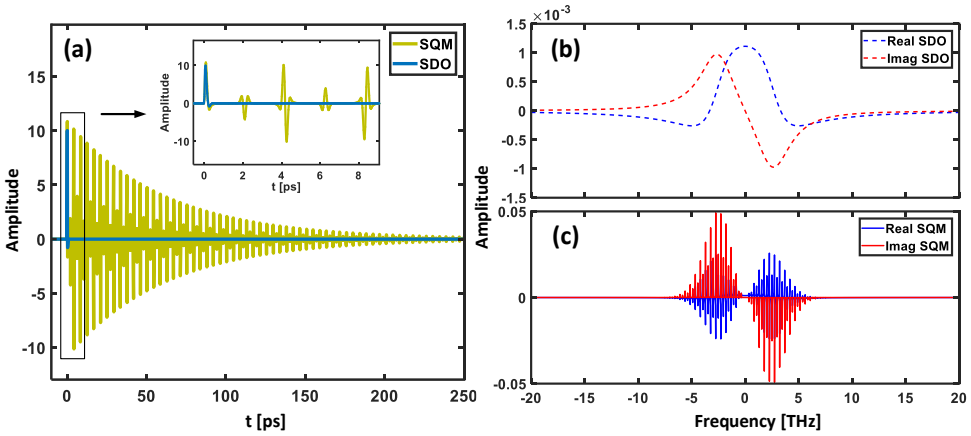

Figure 7.8. (a) Comparison between the time domain rotational Raman response for nitrogen by the SDO model and SQM, **(b)** real and imaginary parts of the frequency response of the SDO model for nitrogen, **(c)** real and imaginary parts of the frequency response of SQM for nitrogen.

Besides, the SDO model, not only cannot recreate the full rotational Raman response of the system, but it also fails to model the mutual interaction of rotational and vibrational states (roto-vibrational Raman scattering). Here, to achieve a full Raman response of the molecule, a similar approach as for the rotational states is followed and the roto-vibrational Raman transitions are included in the model. The vibrational Raman response $H_{vib_k}(t)$ in the Q branches are:

$$\begin{aligned} H_{vib_k}(t) &= u(t)C_{vib_k}\sum_J e^{(-t/\tau_{vib_{k_J}})}M_{k_J}\sin(\omega_{k_J}t), \\ \omega_{k_J} &\approx 2\pi c\left(\bar{\Omega}_k - \eta_k J(J+1)\right), \\ M_{k_J} &= q_{k_J}(2J+1)\exp\left[-hcB_k J(J+1)/KT\right], \quad k=1,2. \end{aligned} \tag{7.5}$$

where $\bar{\Omega}_k$ is the central wavenumber of the roto-vibrational transition ($\bar{\Omega}_1 \approx 2330\ cm^{-1}$ and $\bar{\Omega}_2 \approx 1556\ cm^{-1}$) and η_k are the rotational and vibrational interaction constants ($\eta_1 \approx 0.0173\ cm^{-1}$ and $\eta_2 \approx 0.0159\ cm^{-1}$). C_{vib_k} is the normalization coefficient and the average value for τ_{vib_k} is considered to be 10 ps [220].

Finally, to complete the Raman response function of air, the rotational and vibrational response of individual gases are combined and their concentration in air are included in the model:

$$H_1(t) = \sum_{k=1}^{2}\frac{\sigma_k}{\bar{n}_1}\left[\mu_{rot_k}H_{rot_k}(t) + (1-\mu_{rot_k})H_{vib_k}(t)\right], \tag{7.6}$$

where $\bar{n}_1$ is the nonlinear refractive index of air. σ_k is the product of molecular concentration (80% for N_2 $(k=1)$ and 20% of O_2 $(k=2)$) and their nonlinear refractive index [191]. This represents the contribution of the individual gas molecules to the Raman response. μ_{rot_k} is the contribution of rotational response to the full response of the molecule, since the collective form of the response function should satisfy the normalization requirement (Eq. (7.3)) as much as the individual rotational and vibrational Raman response functions. Eq. (7.6) contains all the necessary elements for a complete Raman model for air, from high order rotational transition for short frequency shifts to roto-vibrational phenomena for much higher frequency shifts, in a compatible form with use in a GNLSE.

7.3.2 Numerical modelling of pulse propagation

To numerically model and reproduce the experimental results through the use of Eq. (7.2), a set of parameters are needed. To begin with, for each fibre the linear operator in Eq. (7.2) ($\tilde{D}(\omega)$) must be calculated from the experimental and simulated data in Figure 7.1. In addition, the contribution of each individual effect must be tailored to the air nonlinearity through an experimental fitting process for (μ_{rot_k}, f_{r_k}).

Although the nonlinear part of Eq. (7.2) includes all the relevant effects, by assuming the frequency independence for $\bar{n}_j$ in the frequency range of experiment, one can significantly increase the numerical calculation speed by unifying separate convolutions in Eq. (7.2) into one as:

$$\frac{\partial \tilde{A}(z,\omega)}{\partial z} - iD(\omega)\tilde{A}(z,\omega) = i\gamma_{total}(\omega)\mathbb{F}\left\{A(z,t)\int_{-\infty}^{+\infty} R_{total}(T)\left|A(z,t-T)\right|^2 dT\right\}. \qquad (7.7)$$

Here $R_{total}(t) = (1-f_{r_{total}})\delta(t) + f_{r_{total}} H_{total}(t)$, $H_{total}(t) = 1/(\bar{n}_{total} f_{r_{total}})\sum_{j=1}^{N} K_j \bar{n}_j f_{r_j} H_j(t)$, $\bar{n}_{total} = \sum_{j=1}^{N} K_j \bar{n}_j$, $f_{r_{total}} = \sum_{j=1}^{N} K_j \bar{n}_j f_{r_j} / \bar{n}_{total}$, and $\gamma_{total} = \omega_0 \bar{n}_{total} / cA_{eff}$.

By using this form of the GNLSE, any number of materials can be included in the simulation without adding any extra computational burden. Also, despite its complex look, once Eqs. (7.4)-(7.6) are calculated using commonly accepted values in the literature for $\bar{n}_j$ at the experimental condition (i.e. $T = 300\,K$, $P = 1\,atm$) [191, 193] and at the initial time grid points of the simulation, they can be included in the GNLSE without any extra computational cost, like one does with the SDO.

To model the pulse propagation dynamics, the modified GNLSE (Eq. (7.7)) was solved numerically by the toolbox mentioned in Chapter 3 and special care was taken to eliminate the spurious Raman peaks that might otherwise reappear at short wavelengths due to periodic boundaries of the FFT by the method described in the Chapter 6. To fit the parameters of the model, the experimental data of the HC-KF transmission experiment are used. The best fit was obtained for μ_{rot_1} = 0.986, f_{r_1} =0.75. Here, also the condition of μ_{rot_2} = 1 is imposed due to the absence of VRS for oxygen in the experimental data. **Figure 7.9** shows a comparison of experimental and simulation results for the HC-KF experiment, where the sensitivity of the simulations to stochastic noise is reduced by averaging over 20 simulations for each spectrum.

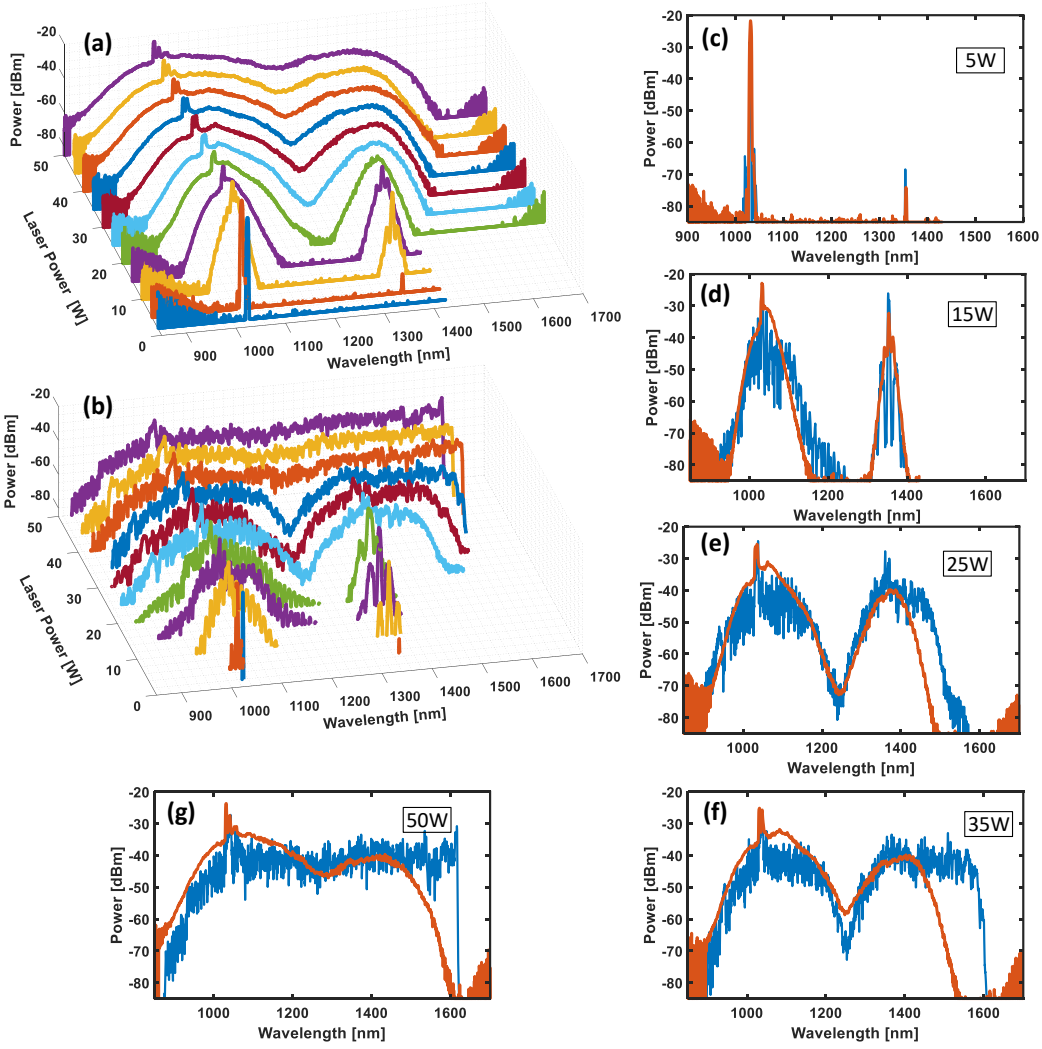

Figure 7.9. (a) Experimental output spectra for HC-KF at different P_{avg} (**Figure 7.5 (b,d)**), **(b)** simulation results using SQM in the GNLSE for the HC-KF (averaged over 20 shots). The comparison of simulation and experimental results for **(c)** 5 W, **(d)** 15 W, **(e)** 25 W, **(f)** 35 W, **(g)** 50 W.

Excellent agreement can be seen at low input powers, where the simulations reproduce well both the RRS and VRS dynamics, **Figure 7.9 (c)**. As the power increases the signature of higher order RRS, alongside the roto-vibrational Raman scattering is also well-reproduced (**Figure 7.9 (d)**). As discussed previously, increasing the input power not only stimulates higher order Raman peaks, but it also produces noticeable broadenings from the Kerr nonlinearity, which plays a key role in the sideband expansion. This broadening process is well reproduced, as shown by the snapshots at which the input laser and VRS bands start to overlap (**Figure 7.9 (e, f)**, at ~1250 nm). Such an accurate simulated behaviour can only be possible thanks to the implementation of the full Raman response described above. As the input power increases further, the dynamics of the process become more sensitive to the parameters of the fibre. I believe that some of the discrepancies at the highest peak powers are mostly due to inaccurate modelling of the dispersion in the vicinity of the VRS wavelength, which is close to the cladding-core mode crossing of the fibre (~1360 nm).

To further verify the model and the fitting values (μ_{rot_k}, f_{r_1}) mentioned above, the pulse propagation also is simulated in the HC-TF. Selected comparisons between experimental and simulation results, showing again excellent agreement, are shown in **Figure 7.10**. Key to obtaining such a good match was the careful reproduction of the loss profile of the fibre at VRS wavelengths. Such a good agreement of the model, with the same fitted parameters, for such different fibres, indicates the robustness of the modelling approach proposed here.

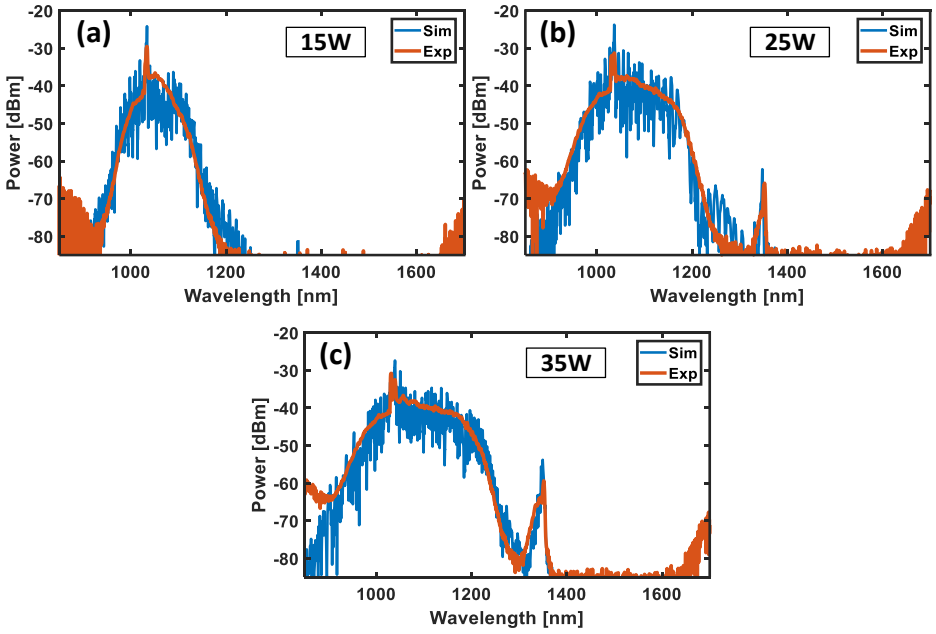

Figure 7.10. Comparison of experimental output spectrum and simulation results using the SQM in the GNLSE for HC-KF for P_{avg} of **(a)** 15 W, **(b)** 25 W, **(c)** 35 W.

In these experiments, as previously discussed, the pulse duration plays a major role in the pulse evolution dynamics, and in particular on the observation or not of the VRS peak in the output spectrum. To demonstrate this point, the developed model for air is used to model the pulse propagation along the same 13.8 m of HC-KF discussed above, for shorter (0.8 ps) and longer (50 ps) pulse durations. In both cases, the launched pulse energy is conserved at 200 μJ, equivalent to the P_{avg} = 40 W for the 6 ps pulse above (i.e. 6 ps at 200 KHz repetition rate).

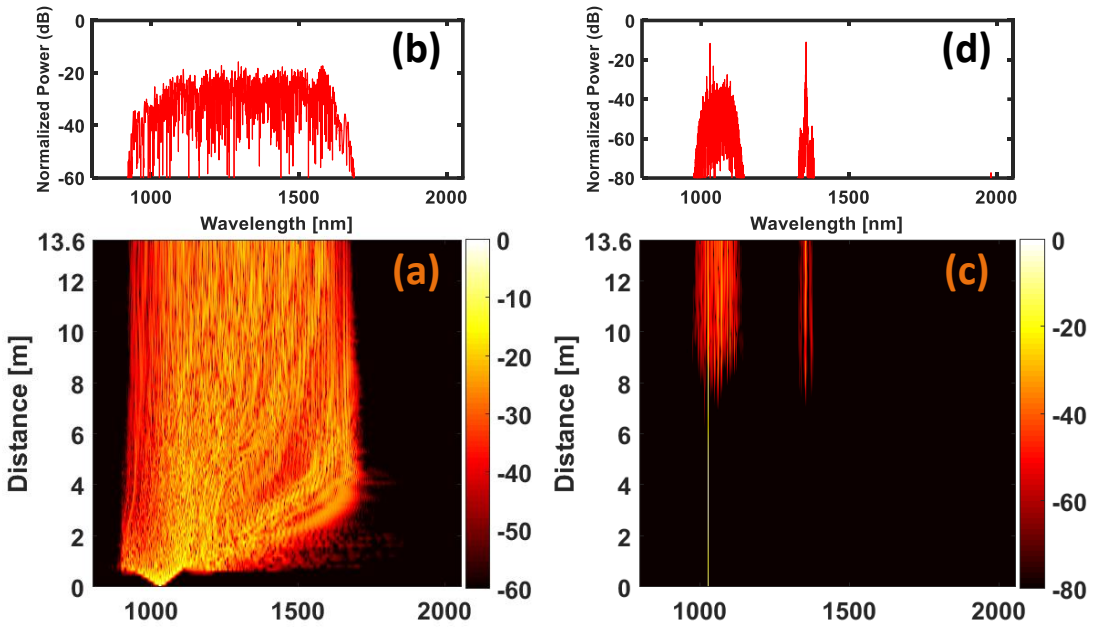

Figure 7.11. Power spectrum evolution of a 800 fs pulse **(a)** propagating along HC-KF at 1030 nm with 200 μJ energy, **(b)** at the output of the fibre; **(c)** Power spectrum evolution of a 50 ps pulse propagating along HC-KF at 1030 nm with 200 μJ energy, **(d)** the power spectrum of the 50 ps pulse at the output of the fibre.

Figure 7.11 (a) shows that for an 800 fs pulse, unlike the 6 ps pulse, the appearance of VRS features are masked by the faster broadening of the pulse due to soliton fission, soliton frequency shifting and other Kerr nonlinearities. The resulting output spectrum is a wide supercontinuum without any sign of VRS, which agrees with experimental observations [196, 197, 199]. In contrast, in the 50 ps case, **Figure 7.11 (c,d)**, shows the clear appearance of a VRS peak, but the broadening of both the pump and the VRS bands are considerably less than in **Figure 7.9**.

7.4 Conclusion

In this chapter, the nonlinear evolution of a picosecond pulse laser in state-of-the-art air-filled hollow core fibres has been studied. Three different fibre types, HC-PBGF, HC-TF and HC-KF are tested to explore the different behaviours and examine the influence of fibre characteristics on the results. In order to observe simultaneously Kerr and Raman effects and extensively model the nonlinear dynamics in air, input pulses of a few picosecond pulse duration has been selected; 6 ps pulses with a maximum energy of 250 μJ at 1030 nm from a commercial tabletop laser (TruMicro 5050©) were launched into the individual fibres. By comparing results from the HC-PBGF and HC-TF with very different fibre characteristics (i.e. dispersion and loss profile), the origin of certain sidebands were attributed to rotational Raman scattering in nitrogen. By switching from HC-PBGF to HC-KF, necessary for the exploration of higher input powers, the generation of a new band around VRS frequencies are observed. At even higher powers, the bands around pump and VRS frequencies merged and a high spectral power density supercontinuum spanning is achieved from 850 to 1600 nm. The presented experimental setup is therefore not only a valuable platform to study the pulse propagation dynamics in air-filled HCFs, but potentially also a technologically relevant high power source with power-selectable tuneable outputs, ranging from a highly efficient short/long range frequency conversion to broad supercontinuum generation.

To model the experimental results, it is shown that the well-established single damping oscillator (SDO) model is inadequate due to the lack of VRS and an oversimplified RRS interpretation. I have therefore adopted a semi-quantum model for air that not only includes the detailed RRS and VRS responses but that can also be used in conjunction with a standard GNLSE to simulate, very accurately, the broad dynamics of pulse propagation in the air-filled fibre. Using this model, the experimental results for HC-KF and HC-TF are simulated with very good agreement, and studied the effect of pulse length on the nonlinear propagation dynamics. The model presented here can be used to precisely tailor the fibre design for either maximizing a specific nonlinear phenomenon, or to reduce the pulse distortion and energy dissipation caused by nonlinearity in pulse delivery applications. It can be the matter of future works, to investigate the discrepancy between the model and experimental data for even higher peak power pulses and rotational Raman frequency shifts.

Chapter 8: Conclusion and future work

8.1 Summary

The significant improvement on HC-fibres on one hand, and the demand for reliable laser sources to cover extended range of spectrum on the other hand, persuade us to explore new possibilities and adapt the available concepts in the HC fibres and gas lasers towards a practical laser system in the mid-IR. From the first gas lasers that the potential of gases as a powerful source of coherent lights were demonstrated, they have been used for many applications. However, their low density nature demands a bulky pressurized housing and long light-matter interaction length to compensate their low density (i.e. low nonlinear gain). For many years, the lack of effective mechanism to provide such confined and long interaction condition for efficient light generation in gases limited their usage to either large and bulky cavities or required enormous exciting power to compensate the small interaction length provided by free-space focusing systems. The introduction of HC fibres with low loss, however, attracted research interest to bring back the gases in the field of laser generation and harness their huge potential in this field. In the last decade, along with improvement in the loss characteristic and durability of HC fibres, successful examples of gas-filled HC fibres have been introduced with various light generation mechanisms ranging from population inversion gas lasers [99], Raman frequency conversion to broad supercontinuum generation [5, 196, 197]. However, most of these works are generally done in the UV to near-IR regime [48] while the mid-IR and IR range of spectrum are still in their early stages due to fibre limitation.

In this work, the main focus is on exploring the light generation in gas-filled HC fibres with emphasis on Raman nonlinearity of gases. As mentioned before, the most important limitation in gases comes from very low density, and as a result, they exhibit low nonlinear gain (at low pressure) in comparison to solid or liquid form of matter. This limitation can be improved by increasing the intensity and/or length of laser-gas interaction. In this regard, HC fibre plays an important role to provide such conditions and unveil the potential of gases. Therefore, considering the key role of HC fibre in the nonlinear process, this thesis is divided into two main parts: (a) study, design and optimization of a HC fibre for gas-filled nonlinear application towards the mid-IR, (b) study of the optical nonlinearity in gases (more specifically Raman scattering) and provide a modelling tool for nonlinear phenomena in gas-filled HC fibre towards the

mid-IR. In the first part of this thesis, the focus was on HC fibres and their characteristics to identify the most suitable type of HC fibre to meet the goal of this project and optimize the fibre design to achieve high nonlinear efficiency in the form of gas-filed HC fibre. In the second part, the nonlinear dynamic of gases in interaction with light have been studied by adopting nonlinear models for a few gases (i.e. hydrogen and air) and integrating these models into the GNLSE to cover a large range of nonlinear phenomena. The results of my work on these topics have been presented in the form of chapters following an introduction in Chapter 1.

In Chapter 2, a brief background review on history and type of HC fibres is provided with the main focus on HC-ARFs due to their broadband transmission window and very high damage threshold. The optical nonlinearity, in general, and more specifically the Raman scattering process have been briefly introduced. The most common and general form of the GNLSE has been described for modelling the nonlinear dynamics of pulse propagation throughout a long light-matter interaction. The advantage of HC fibres to increase the interaction length of gas and light as a container and waveguide has been presented. In a brief overview, the recent works on nonlinearity in gas-filled HC fibres has been provided which shows the necessity of more studies on gas-filled HC fibre towards the mid-IR range.

In Chapter 3, the numerical modelling methods and the developed software toolbox to implement such numerical methods are discussed. To model the characteristics of fibres in general and specifically the HC fibres, after considering the advantages and disadvantages of available numerical methods, FEM has been selected from a list of available candidates as the most versatile and efficient numerical solver for the electromagnetic Eigen mode equation. A commercial FEM mode solver (i.e. COMSOL Multiphysics®) has been selected for its robust and up-to-date feature to minimize the implementation errors and maximize the efficiency of solving process. Although the FEM mode solver kernel is commercial, without correct initialization of essential parts and parameters in the solver and correct definition of fibre domains and boundaries the modelling results are not reliable. In this chapter, it was shown that unlike solid core fibres, HC fibres are very sensitive to mesh size, and the loss calculation process in these fibres needs a correct implementation of PML due to the leaky nature of their guidance mechanism. Therefore, I developed a MATLAB toolbox with a commercial FEM solver at its heart, which optimized for accurate design and modelling processes such as automatic parameter sweeping and effective meshing. Also, by implementing a circular bend adaptive PML, the computation time was reduced by reduction of wasted space between the structure and rectangular PML. This modelling toolbox has been

implemented in the form of modular multipurpose MATLAB functions and integrated with a graphical interface (GUI) to model any type of fibre from solid to HC-ARFs which has been used for modelling in this thesis. On the other hand, to model the nonlinear pulse propagation throughout the gas-filled fibre, the SSFM was chosen in this study to numerically solve the GNLSE because of its flexibility and performance advantages (i.e. it can handle the large grid size needed for the simulation in this thesis). The SSFM was implemented in MATLAB environment and a toolbox with GUI has been developed for the nonlinear solver code in this study. At the end, the fibre and nonlinear modelling toolboxes were connected within MATLAB for a fully integrated toolbox.

Chapter 4 is devoted to select and optimize the loss of HC fibre to reach desire values for the project. At first, tubular fibre and NANF were reviewed as the two most promising HC-ARFs having in mind the goal of the project, which is defined as generating a mid-IR (4.35 μm) laser light by Raman conversion from a pump laser at the near-IR (1.55 μm). After providing a brief summary of different category of HC fibres, NANF has been selected because of its advantages. To achieve the lowest loss at the operating wavelength for higher Raman conversion efficiency (i.e. 1.55 μm and 4.35 μm), each design parameter of a six-tube silica NANF were optimized. The optimization process for each parameter has been described in detail. The effect of material loss on optimization process was studied and it was shown that due to huge material loss of silica in the mid-IR, the optimum size of inner tubes in NANF design deviates from the previous works with low material loss [57]. By analysing the core and cladding modes in this study, an effectively single mode optimized fibre were achieved regardless of core size of the fibre by effectively outcoupling the HOMs and introducing a high HOM extinction ratio. The focus of the optimization process was on achieving the lowest Raman conversion loss (RCL) while, at the same time, low loss performance at both operating wavelengths was achieved. After optimizing the silica NANF for low RCL, in theory, a loss of ~0.9 dB/m at 4.35 μm with a core radius of R = 35 μm was achieved, where the material loss of silica is > 3000 dB/m at such wavelength. Also, by changing the fibre material to tellurite, the same order of magnitude loss with R = 15 μm has been achieved due to its low material loss.

In Chapter 5, the main focus was on introducing a novel NANF with high birefringence and polarizing effect simultaneously. This new design, in addition to its applications in many other areas of fibre optics, can improve the vibration Raman conversion efficiency required for this work by maintaining the linear polarization of the field throughout the fibre and reduces the waste of pulse energy on generation of rotational Raman conversion, which is mostly relies on circular polarization. In this chapter, as first

attempt, the asymmetric approach was implemented, similar to solid core fibres to introduce birefringence in NANF. However, it turns out due to very small overlap between the glass and the field, this method does not produce noticeable birefringence in the HC-ARFs. Borrowing the well-known anti-crossing concept in HC-PBGFs, a bi-thickness NANF was introduced which not only can provide a birefringence as high as commercially available solid core fibres ($>10^{-4}$), but also has a very broad high birefringence operating spectrum range (> 550 nm). In addition to birefringence, by adapting the out-coupling method for HOM (see Chapter 4), a novel polarization dependent out-coupling process was introduced, which induced more than 30 dB of orthogonal polarization loss ratios in the proposed fibre structure. Even though the presented fibre in this section is designed for a specific wavelength range, due to scaling law in NANFs, the design can be scaled to the desired wavelength operation. This work inspired many other design structures in other works.

In Chapter 6, the focus was on the main goal of generating light in the mid-IR from a near-IR laser source by Raman conversion process in gas. To achieve this objective, different materials were studied as filling gas for HC fibres. Hydrogen, in addition to its feasibility and glass friendly feature, shows the highest Raman gain and longer vibrational Raman frequency shift among other options. In this study, an erbium-doped fibre laser (1.55 μm) was considered as a reasonable option for the pump and due to its capability for integration with HC fibres in a fully fiberized mid-IR source. Therefore, to achieve a high conversion from 1.55 μm to 4.35 μm by vibrational Raman process in the hydrogen-filled NANF, the core size of the designed silica NANF were optimized in Chapter 4. It was shown that, unlike solid core fibres, the strategy of reducing core size for higher intensity and higher conversion efficiency is not applicable to HC-ARFs, due to the dependency of fibre loss to core size. In fact, it was shown that by increasing the core size, it is more likely to achieve high efficiency at the cost of longer fibre. Considering the practical limitations on loss of a large core NANF, an optimum core size of R = 35 μm is selected.

In the second part of the Chapter 6, to model the laser pulse propagation in the hydrogen-filled NANF, an adaptive model with the GNLSE for nonlinear response of the hydrogen has been adopted by combining the classical and quantum approaches. Using the developed modelling toolbox in Chapter 6, in conjunction with the adopted hydrogen model, the well-known effect of pulse length on Raman gain has been reproduced and validated by the experimental results from the literature. Furthermore, the numerical challenges in the modelling of such broadband nonlinear process were

addressed in this chapter. After validation of the model, the pulse propagation was modelled in the optimized hydrogen-filled NANF from previous chapters. The result showed ~68% of quantum efficiency within ~3.4 m of silica NANF for 10 kW peak power pump. It has also shown that by modifying the pulse shape, it is possible to achieve as high as 78% quantum efficiency with the same input power in the shorter length of fibre (~3 m). At the end, the vibrational Raman conversion was modelled in the first fabricated NANF prototype from ORC fabrication team. Although the fibre was not optimized for this project and had as high as 55 dB/m loss at the Stokes wavelength, it showed more than 20% of quantum efficiency with a 10 kW peak power pump due to its small core size.

In chapter 7, the nonlinear behaviour of different material were studied as the filling gas in the HC fibres. In fact, available atmospheric air in the HC fibres exposed to high power pulses shows remarkable nonlinear properties and has several interesting applications such as pulse compression, frequency conversion and supercontinuum generation. Although the propagation of sub-picosecond and a few hundred picosecond pulses are well-studied in air-filled fibres, the nonlinear response of air to pulses with a duration of a few picoseconds has interesting features that have not been fully explored yet. In this chapter, the nonlinear propagation of ~6 ps pulses in three different types of atmospheric air-filled HC fibres was studied experimentally and theoretically. With the help of this pulse length, different nonlinear characteristics of air at different power levels were explored. Using in-house-fabricated, state-of-the-art HC photonic bandgap, HC tubular and HC Kagomé fibres, it was possible to associate the origin of the initial pulse broadening process in these fibres to rotational Raman scattering at low power levels. Due to the broadband and low loss transmission window of the used HC Kagomé fibre, it was possible to observed the transition from initial pulse broadening (by Raman scattering) at low powers, through long range frequency conversion (2330 cm^{-1}) with the help of vibrational Raman scattering, to broadband (~700 nm) supercontinuum generation at high power levels. To model such a wide range of nonlinear processes in a unified approach, a new semi-quantum model for air has been implemented in the GNLSE, which surpasses the limits of the common single damping oscillator model in this pulse length regime. The model can be fully integrated into the developed GNLSE solver toolbox in this thesis and not only reproduces the experimental results with good agreement but also provides a powerful tool for design, modelling and optimization of the nonlinear processes in the air-filled HC fibres. Moreover, the presented atmospheric air-filled HC fibre can provide a powerful (i.e.

high power spectrum density) and tuneable source with a range of outputs from a single Raman peak source to a broadband supercontinuum in the near-IR regime.

In summary the key contributions of this thesis in both aspect of fibre design/optimization and nonlinear modelling of the gases can be listed as:

- A software toolbox has been developed covering both aspects of fibre design/modelling and nonlinear pulse propagation modelling in general, and specialized for gas-filled fibre modelling in a fully integrated form. The multipurpose and modular characteristics of this toolbox enable the user to model any type of fibre (e.g. solid, asymmetric cross section and even 3D structures) as well as general forms of the nonlinearity in material separately or as an integrated toolbox. This toolbox covers from fibre design/modelling to modelling the dynamic of nonlinear pulse propagation throughout the fibre. By implementing a circular and bend adaptive PML, the computation speed has been increased as well as accuracy.
- Selecting the NANF design as the best available low loss candidate for broadband nonlinear processes in gases (e.g. Raman conversion), a silica NANF has been optimized to achieve the lowest loss at mid-IR (i.e. 4.35 μm) despite the huge silica loss at this reign. It has been shown that, the optimum value of design parameters for NANF with high material loss (e.g. silica loss at mid-IR) can be different from the conventional optimum values previously reported [57]. The presented silica mid-IR NANF not only can provide very large core size and low loss, but also is effectively single mode due to high HOM extinction ratio.
- A novel design for high birefringence and polarizing operation in NANF has been introduced (the design is patented). The presented design not only exhibit birefringence as high as commercial solid core fibres ($>10^{-4}$), but also has a very broad birefringence spectral window (~550 nm). Moreover, a new the polarization out-coupling mechanism in NANF design has been introduced for the first time and are able to reach an orthogonal polarization loss ratios of 30 dB.
- A nonlinear optical model for hydrogen molecule has been introduced, which can be fully integrated into the GNLSE and is validated by reproducing the experimental results and integrated into the developed modelling toolbox in this thesis. It is shown, through modelling, that using the optimized silica NANF design, it is possible to achieve more than 68% of quantum efficiency of Raman

conversation in hydrogen-filled silica NANF towards mid-IR and even ~78% by pulse modification.

- A rigorous study on the nonlinear dynamics of a picosecond pulse propagating in atmospheric air-filled HC fibres has been performed. A semi-quantum model for air has been adopted, which is fully adaptive to the GNLSE and the developed modelling toolbox. This model could reproduce a wide range of phenomena observed in experiment which was not possible by conventional model without adding extra computational burden.
- The adopted model for hydrogen and semi-quantum model for air in conjunction with the developed toolbox can provide a powerful tool for modelling of nonlinear processes with broad and complex phenomena, which is not possible/feasible to model with conventional coupled equations.

8.2 Applications and future work

The proposed Raman laser in this work can find different applications in the interesting and demanding Mid-IR range of optical spectrum with focus on variety of topics from material processing to spectroscopy. The output wavelength of Raman lasers, unlike conventional population inversion lasers, by nature, are not bound to electronic states of the gain material and their output wavelength can be tuned directly by choosing proper pump wavelength. Although the proposed design in this study is optimized for single wavelength output (~4.35 μm), the tunability of Raman process and the loss characteristic of the designed NANF in conjunction with well-developed high power laser technology at the pump wavelength can provide a good combination for a tunable high power mid-IR laser. Therefore, available lasers in the range of 1430-1560 nm can be used with the proposed hydrogen-filled NANF design to generate a wide band tunable high power Raman laser ranging from 3500-4500 nm which can satisfy a wide range of atmospheric spectroscopy [221].

Furthermore, the proposed laser can achieve higher level of power than conventional method in mid-IR (the output power is limited mostly by pump power not the fibre damage threshold), which makes this option more attractive for remote sensing and military applications where reaching to far distances is necessary but cannot be achieved by other low power solutions. This combination of high power output (> 100 MW peak power) and tunable mid-IR range operation is also very appealing for many other applications such as material processing, nonlinear optical researches in mid-IR (e.g. mid-IR FWM or supercontinuum generation) and free space communication where

high power is required at mid-IR [26, 77]. In general, the proposed system can transfer, to some extent, the capability and tunability of the readily available high power lasers in near-IR to the challenging mid-IR range of spectrum with fully fiberized capability. In addition to the proposed NANF design for mid-IR laser, the developed theoretical framework in this thesis to analys the nonlinear behaviour of the gases in HC fibres also can be used to achieve high degree of flexibility in designing and modelling different type of gas-filled HC fibres.

The next step to complete this study would be the experimental exploration and reproduction of the simulation results as soon as a reasonable NANF has been fabricated. Although similar results in tubular fibre has been demonstrated very recently, I believe, due to lower loss in NANF, it is possible to achieve higher efficiency with lower input power or can achieve higher output power in the mid-IR with the same amount of input power. In general, a very high power laser source in the mid-IR range can open up many opportunities in many research areas. The idea of fully fiberized laser can be a future work where an erbium-doped fibre laser as the pump can be fully integrated with the hydrogen-filled NANF. Also to achieve very high power output using a high power laser at 1064 nm can be used to pump a hydrogen–filled NANF and through cascade Raman conversion the 2nd Stokes can be generated at the wavelength similar to this work in the mid-IR range (i.e. ~4.4 μm).

Appendices

Appendix A

Hexagram hollow core fibres

In this appendix, I have presented my study [66] on Hexagram fibres and the effect of glass nodes on the fibre loss.

A Hexagram HC fibre is a type of ARFs that consist of a single star-of-David shape in the centre of the structure as shown in **Figure A.1**. The guidance mechanism in this fibre is very similar to a Kagomé structure where the core surrounding glass webs acts as an anti-resonate reflector to confine the light at the core area. Hence, studying such fibre with a simple structure can help to understand better the influence of the different structural elements on the loss in a more complex structure (i.e. Kagomé fibres).

While the web thickness in this structure ("Hexagram") determines the resonant/anti-resonant wavelengths (i.e. the bandwidth of the transmission windows), which can be calculated by Eq. (2.1), the intersection of the webs creates glass nodes, as shown in **Figure A.1 (a, b),** that can noticeably affect the minimum achievable loss. Therefore, the effect of glass nodes formed in the structure have been extensively investigated as the key factor determining the loss and performance of anti-resonant hexagram HC fibre in [66]. In this work, the effect of node direction in relation to the cylindrical coordinate Eigen directions (i.e. radial and azimuthal directions) have been investigated experimentally, and through modelling the effect of the node dimensions on the loss of the fibre have been studied. **Figure A.1** shows an SEM of two Hexagram HC fibres with core surrounding web nodes aligned in either azimuthal or radial coordination direction alongside their loss profile. Although the experimental results show the clear advantage of radial nodes over azimuthal nodes identifying the source of the higher loss in azimuthal nodes requires more study.

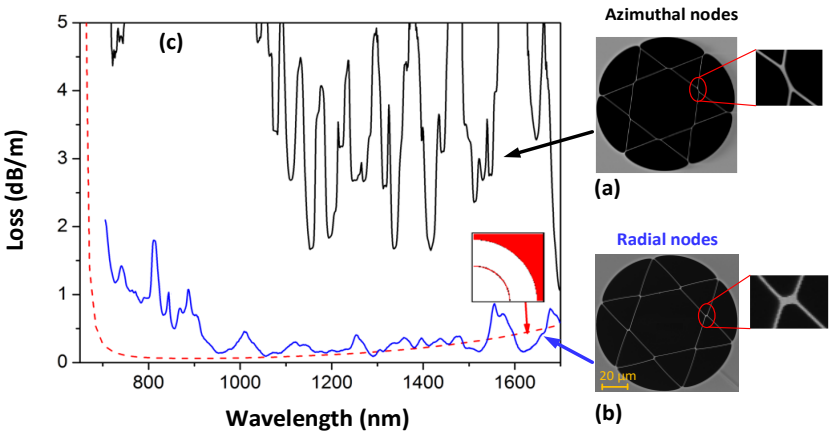

Figure A.1. SEM of anti-resonant hexagram HC fibres, **(a)** tilted nodes in azimuthal direction and **(b)** tilted nodes in the radial direction (54 µm core diameter, 0.31 µm web thickness), **(c)** the loss profile of the fibres alongside the modelled confinement loss for an idealized tube-jacket fibre (red dashed curve) with the same web thickness and core diameter.

Initially to investigate the effect of the nodes, a cross-section of the fibre has been modelled by the numerical toolbox developed as described in Chapter 3. In principle, it is very challenging to model the fibres with complex anti-resonant structures (i.e. Kagomé fibres) because of the resonance effects at sharp corners of the ideal structure and the sensitivity of the loss profile to a slight change in the web thickness throughout the fibre (see for example [67]). This phenomenon can be seen in **Figure A.2**, where the ideal structure of a fibre (with a core diameter of 50 µm, 0.32 µm web and node thickens of 0.83 µm) has been modelled in comparison to a more realistic form with filleted corners similar to real fabricated structure.

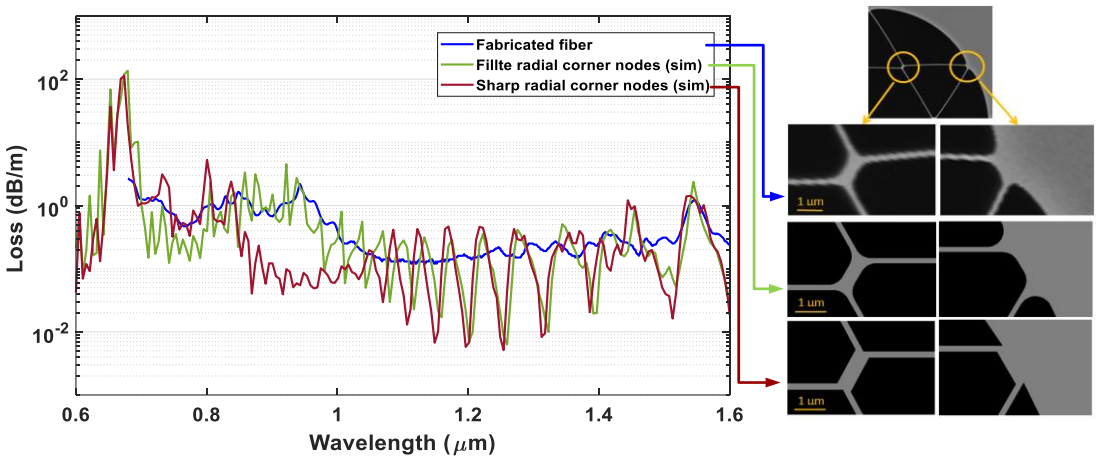

Figure A.2. Loss profile of a Hexagram HC fibre with ideal sharp web intersections and a fillet form compared to the fabricated fibre. All fibres have the same core diameter of 50 µm, 0.32 µm web thickness and node thickens of 0.83 µm.

Taking to account such effects in the modelling, the loss profile for radial and azimuthal nodes for the same fibre has been modelled and compared with the fabricated hexagram HC fibre with radial nodes as shown in **Figure A.3** (there is no fabricated fibre with an azimuthal node and the same core size). The simulation results for radial node fibre is in a very good agreement with experimental results for wavelengths less than 1 µm while the low loss features predicted by modelling at higher wavelengths disappear due to inconsistency of structure throughout the fabricated fibre, which, in practice, impose higher loss. More importantly, the simulation results for fibre with azimuthal nodes not only shows higher loss, but also exhibit the sharp fluctuation features in the loss profile observed in the experimental results in **Figure A.1**.

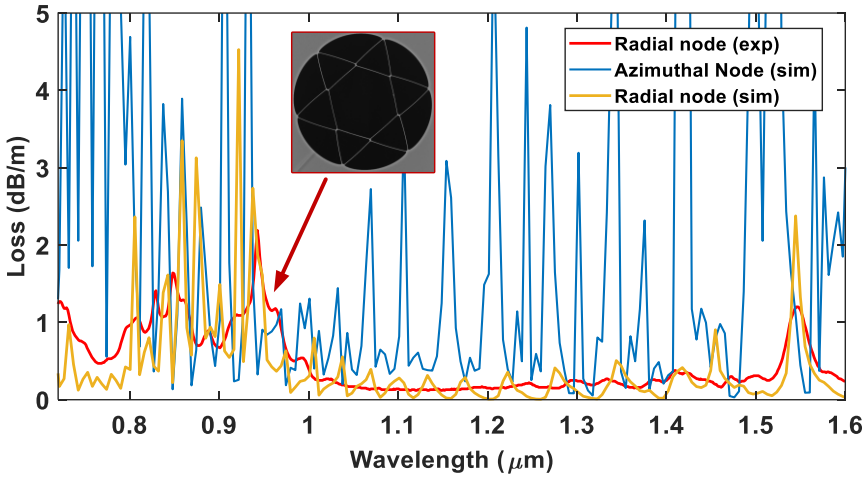

Figure A.3. The experimentally measured (exp) loss of anti-resonant hexagram HC fibre with radial nodes and simulation results for the same fibre with azimuthal and radial nodes. The fibre is similar to **Figure A.1** (core diameter of 50 µm, 0.32 µm web thickness and node thickens of 0.83 µm).

The simulation results on the power distribution with in different fibres show that despite the similar core size, web thickness and operating wavelength in both fibres, the leakage of the power to the cladding glass due to the azimuthal nodes is much higher than the alternative configuration shown in **Figure A.4**. This effect can be explained by the increase in overlap of the core field and core surrounding glass which leads to out-coupling of the core light into the jacket glass.

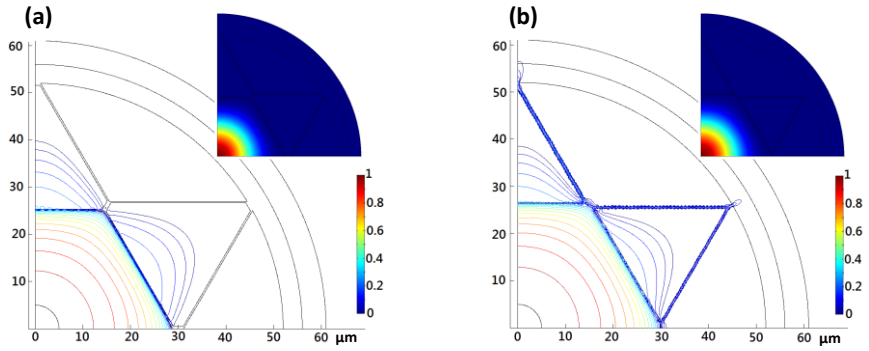

Figure A.4. Contour plot of normalized power for the fundamental mode in anti-resonant hexagram HC fibres with **(a)** radial nodes, **(b)** azimuthal nodes at 0.95 μm wavelength. They have a core diameter of 50 μm with 0.32 μm web thickness. The power leakage to the cladding can be seen in the azimuthal nodes fibre (contour lines are in 3 dB differences).

In order to examine the validity of this claim, simulations have been done considering the thickness of the radial nodes (*NT*). As is clear from **Figure A.5,** by increasing the thickness of the radial node in the azimuthal direction, the general trend of an increasing loss with increasing exposure of the core field to the glass and out-coupling of the field to the cladding glass. I , as a co-auther, have provided more detailed analysis of bend loss and the effect of structural enhancement on loss has been presented in [66].

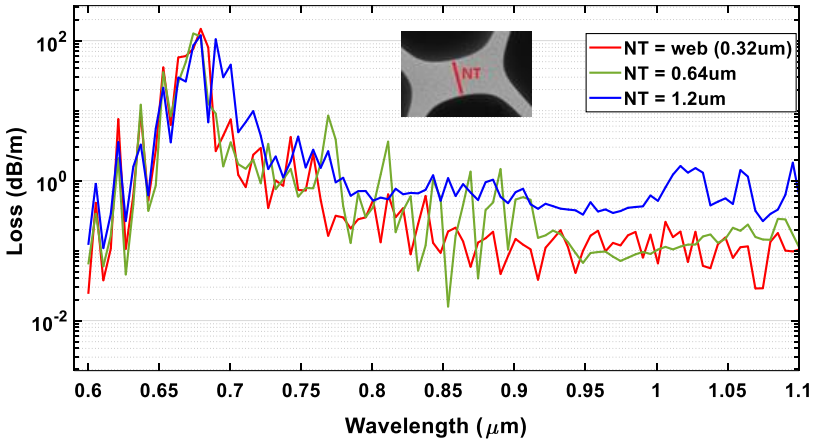

Figure A.5. FEM simulation of loss in anti-resonant hexagram HC fibre for different node thickness. The overall loss is increased by increasing the node thickness (all fibres have the same sizes in core diameter 50 μm, 0.32 μm web thickness).

Therefore, keeping the core field away from glass nodes seems a promising solution to decrease the CL. Similarly the effect of negative curvature core walls on loss and the dispersive properties of Kagomé lattice fibres has been demonstrated by B. Debord *et all* [63]. In this work, the influence of curvature of the core walls has been studied both theoretically and experimentally. It has been shown, by increasing the arc curvature of

the core-cladding interface it is possible to reduce the overlap between the core and cladding modes. **Figure A.6** represents experimental results for different curvature parameters (b) which has been defined as the ratio of the semi-minor to semi-major axis of core-cladding walls.

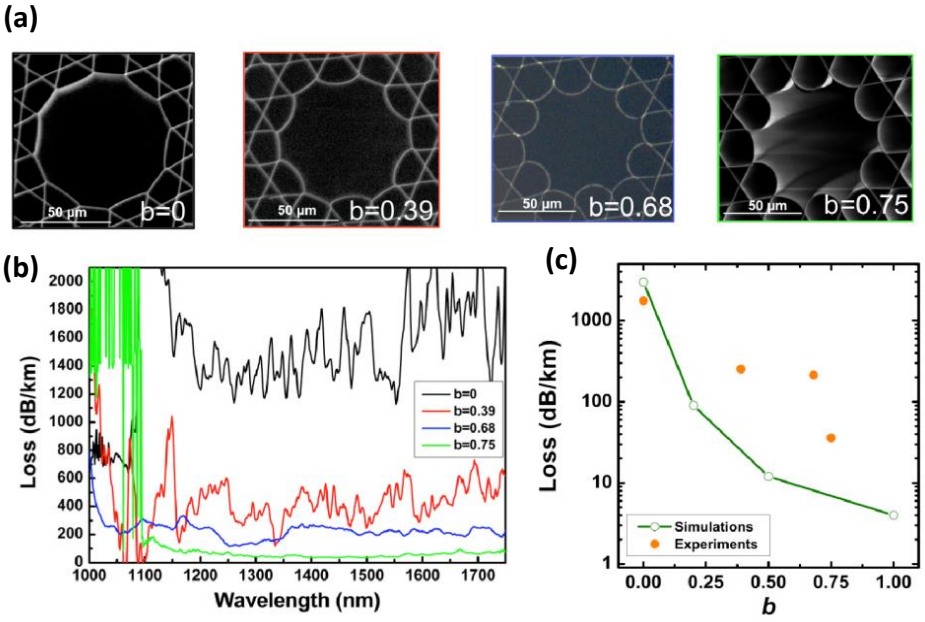

Figure A.6. Kagomé fibres with deferent curvature parameter (*b*), **(a)** SEM of hypocycloid-core Kagomé latticed HC-PCFs with different *b* parameter, **(b)** measured loss, **(c)** theoretical and an experimental loss vs *b* at 1.5 µm [after[63]].

Appendix B

Cylindrical bend adaptive PML

In this appendix the formulation used for circular bend adaptive PML in the modelling toolbox is represented.

The implemented PML in the developed toolbox is this thesis is based on anisotropic PML approach [117]. Unlike Beranger's type of PML [116], which needs certain modification in Eigen mode equation and consequently needs modified version of numerical solver, the anisotropic PML can be treated by the same numerical solver as the rest of the regions in the model without any extra computational burden (assuming the compatibility of solver to deal with anisotropic material similar to COMSOL) [117, 118].

In this type of PML, the layer is defined as an anisotropic material with permittivity tensor ($\bar{\bar{\varepsilon}}_{PML}$) and permeability tensor ($\bar{\bar{\mu}}_{PML}$) as follow [117, 118]:

$$\begin{aligned} \bar{\bar{\varepsilon}}_{PML} &= \tilde{\varepsilon}_{PML0}\bar{\bar{\Lambda}}, \\ \bar{\bar{\mu}}_{PML} &= \tilde{\mu}_{PML0}\bar{\bar{\Lambda}}. \end{aligned} \tag{B.1}$$

where $\tilde{\varepsilon}_{PML0}$ and $\tilde{\mu}_{PML0}$ are the permittivity and permeability of PML region at its interface with surrounding material. $\bar{\bar{\Lambda}}$ is the anisotropy matrix and defined according to the coordinate of PML. In principle, PMLs exhibit very high abortion in specific incident angle (e.g. perpendicular to its boundary) while their performance would degrades in other incident angles. Therefore, it is important to implement proper PML geometry and specifications according to propagation direction of outgoing field from the simulation domain. For instance, in the optical fibres the outgoing field mostly propagates in radial direction. Therefore, in order to have efficient absorption by rectangular PMLs, a substantial distance between the structure and rectangular PML is required to achieve planer outgoing field. On the other hand, cylindrical PML shows the best performance for radial outgoing field and can be a good option for optical fibre modelling. It is worth mentioning that although PMLs can be designed to exhibit high absorption in any direction regardless of their shape or defined coordinate, the most common form of PMLs exhibit their highest absorption at perpendicular angle of incident to their boundary.

Therefore, by choosing the cylindrical PML for the developed modelling toolbox the $\bar{\bar{\Lambda}}$ can be defined in the cylindrical coordinate as [117]:

$$\bar{\bar{\Lambda}}_{r\phi z} = \hat{r}\hat{r}\left(\frac{r_t}{r}\frac{S_z}{S_r}\right) + \hat{\phi}\hat{\phi}\left(\frac{r}{r_t}S_r S_z\right) + \hat{z}\hat{z}\left(\frac{r_t}{r}\frac{S_r}{S_z}\right), \qquad r_t = r_{\min} + \int_{r_{\min}}^{r} S_r(r')dr'. \tag{B.2}$$

where $\hat{r}$, $\hat{\phi}$ and $\hat{z}$ are the unit vectors of cylindrical coordinate and r, ϕ and z are the relative vector lengths.

The S_r can be defined by recalling from Eq. (3.5), as:

$$S_r \triangleq S = 1 - i\varsigma\left(\frac{r - r_{\min}}{w}\right)^m, \quad r \geq r_{\min}. \tag{B.3}$$

where $r_{\min}$ and w are the starting position of the PML and the thickness of the PML, as defined in **Figure B.1**, respectively. ς is a damping factor and must be positive number, m is the order of propagation loss in the PML which typically is $m = 2$ [121]. In general, the damping or absorbing coefficient ς should be frequency dependent ($\varsigma \propto 1/\omega$) in time or frequency domain analysis, but in the mode calculation, it should be frequency independent as all mode solutions are in the same frequency.

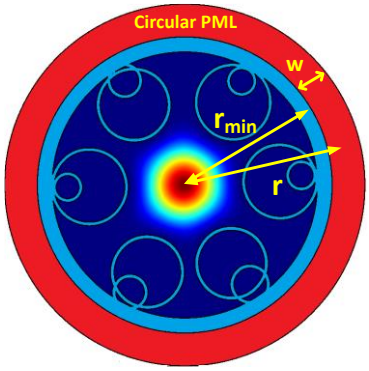

Figure B.1. The circular PML layer implemented in a hollow core modelling.

From Eq. (B.2) and Eq. (B.3):

$$r_t = r_{\min} + \left[1 - i\frac{\varsigma}{m+1}\left(\frac{r - r_{\min}}{w}\right)^m\right](r - r_{\min}). \tag{B.4}$$

The tensor representation of $\bar{\bar{\Lambda}}_{r\phi z}$ (Eq. (B.2)) by assuming $S_z = 1$ is in a form of :

$$\bar{\bar{\Lambda}}_{r\phi z}=\begin{pmatrix}\frac{r_t}{r}\frac{1}{S_r} & 0 & 0\\ 0 & \frac{r}{r_t}S_r & 0\\ 0 & 0 & \frac{r_t}{r}S_r\end{pmatrix} \tag{B.5}$$

The presented definition of cylindrical PML can be used in a cylindrical coordinate without any change in Maxwell's equations as long as the solver is implemented in the cylindrical coordinate as well. However, the other steps such as geometry definition, meshing, boundary definition, material definition and etc. are more convenient in the solver (i.e. COMSOL) to be in Cartesian coordinate. Therefore, it is essential to define the cylindrical PML in Cartesian coordinate while preserving its non-reflecting and absorbing attributes in the radial direction.

Using the coordinate transformation and invariance in Maxwell's equations, the material tensor property can be transformed from one coordinate to another one (i.e. cylindrical coordinate to Cartesian coordinate in the case of this study) by [222]:

$$\bar{\bar{\Lambda}}_{xyz}=\frac{\boldsymbol{J}_{rx}\bar{\bar{\Lambda}}_{r\phi z}\boldsymbol{J}_{rx}^{T}}{\det(\boldsymbol{J}_{rx})}. \tag{B.6}$$

where $\boldsymbol{J}_{rx}$ is the Jacobian matrix of transformation from cylindrical coordinate ($r\phi z$) to Cartesian coordinate (xyz) with $\boldsymbol{J}_{rx}^{T}$ and $\det(\boldsymbol{J}_{rx})$ as its transpose and its determinant, respectively. Using the Eq. (B.5) for $\bar{\bar{\Lambda}}_{r\phi z}$ and Eq. (B.6), the material tenser in Cartesian coordinate ($\bar{\bar{\Lambda}}_{xyz}$) is calculated as:

$$\bar{\bar{\Lambda}}_{xyz}=\begin{pmatrix}\frac{r_t}{r}\frac{1}{S_r}\cos^2(\phi)+\frac{r}{r_t}S_r\sin^2(\phi) & \sin(\phi)\cos(\phi)\left[\frac{r_t}{r}\frac{1}{S_r}-\frac{r}{r_t}S_r\right] & 0\\ \sin(\phi)\cos(\phi)\left[\frac{r_t}{r}\frac{1}{S_r}-\frac{r}{r_t}S_r\right] & \frac{r_t}{r}\frac{1}{S_r}\sin^2(\phi)+\frac{r}{r_t}S_r\cos^2(\phi) & 0\\ 0 & 0 & \frac{r_t}{r}S_r\end{pmatrix} \tag{B.7}$$

At the end, the PML can be defined as an anisotropic material, using Eq. (B.7) and Eq. (B.1) to define the permittivity and permeability of the layer in a Cartesian coordinate within the FEM solver (i.e. COMSOL).

As mentioned in Chapter 3, to achieve non-reflecting property in PML, the impendence matching condition should be satisfied at the boundary of PML and its surrounding material in a general form of:

$$\frac{\tilde{\mu}_{PML0}}{\tilde{\mu}_1} = \frac{\tilde{\varepsilon}_{PML0}}{\tilde{\varepsilon}_1}. \tag{B.8}$$

where $\tilde{\mu}_1$ and $\tilde{\varepsilon}_1$ are the complex permeability and permittivity of the material next to PML layer at their interface. The condition in Eq. (B.8) can be relaxed as $\tilde{\varepsilon}_{PML0} = \tilde{\varepsilon}_1$ and $\tilde{\mu}_{PML0} = \tilde{\mu}_1$. Although the presented PML can be accurately used for straight fibre simulation, in order to correctly model the bend loss, the impedance matching condition requires modification.

As discussed in Chapter 3, to implement the bend loss calculation in a 2D geometry instead of 3D geometry, the geometric transformation method has been used by applying a tilted refractive index approach Eq. (3.6). In this case, to preserve impedance matching at the interface of PML layer and simulation domains, while $\tilde{\mu}_{PML0}$ is 1, considering dielectric material for outer cladding layer of fibre (e.g. silica), the permittivity of PML defined as:

$$\tilde{\varepsilon}_{PML0} = n_1^2 e^{\frac{2x}{R_{eff}}}. \tag{B.9}$$

where n_1 is the tilted reactive index of surrounding material at the interface of PML (i.e. Eq. (3.6)). Implementing an anisotropic layer in the developed modelling toolbox with material defined though Eq. (B.1), (B.3), (B.4), (B.7) and Eq. (B.9) provides a circular bend adaptive PML. This PML facilitates the accurate modelling of straight and bend losses of fibres as well as improving the computation speed by reducing the wasted spaces between geometry and PML layer.

Appendix C

Chebyshev collocation method

In this appendix, the formulation of Chebyshev collocation method used in the calculation of dispersion operator in Chapter 6 is presented.

As mentioned in Chapter 6, even though introducing Eq. (6.6) provides an accurate form of dispersion operator by eliminating the need of truncating higher order dispersion derivatives (i.e. $\beta_n(\omega)$), the necessity of numerically calculating the derivative of dispersion and requirement of the dispersion value at the frequency grid points (i.e. $\beta(\omega_i)$) for the nonlinear modelling can still impose numerical error in the calculation of the dispersion operator from fibre modelling results.

On one hand, the calculation of dispersion for HC fibres at each frequency is computationally expensive, and on the other hand, the numerical modeming of nonlinear pulse propagation requires a very fine frequency grid to accurately model the dynamics of the pulse in nonlinear medium. Therefore, a balanced approach is required to achieve accurate dispersion profile (i.e. $\beta(\omega)$) at the frequency grid points of nonlinear pulse propagation modelling while reducing the number of FEM modelling of the fibre. The most common approach is to model the fibre by FEM mode solver for an equally spaced frequency domain grid (e.g. typically 100 points) with less points than frequency grid points required for the nonlinear pulse propagation modelling (e.g. 2^{24} points) and the required values at frequency grid points for nonlinear modelling are calculated by linear interpolation. However, it is well-know that equally spaced interpolation methods have high over-all error and require large number of points to achieve well-fitted curve and also have poor numerical derivative results [223]. Therefore, in this appendix, I have presented the Chebyshev polynomial interpolation, which is a well-known method in fluid dynamic [224], and more important, its capability to evaluate the derivative of a function (e.g. $\beta_n(\omega)$) in the form of matrix multiplication [223, 225].

A well-defined function $f(x)$ in domain $|x| \leq 1$ can be approximated by a N-order Chebyshev polynomial interpolation as:

$$f(x) \approx \sum_{k=0}^{N} a_k T_k(x) \tag{C.1}$$

where $T_K(x)$ are Chebyshev polynomial of first kind, which are defined as:

$$T_K(x) = \cos(K\cos^{-1}(x)) \tag{C.2}$$

In order to have a well-fitted interpolation polynomial, the collocation points are chosen as Chebyshev–Gauss–Lobatto points [223], which are defined as the roots of the polynomial $(1-x)T'_N$, where $T'_N = dT_N / dx$, these point can be expressed by [223]:

$$x_l = \cos(\frac{\pi l}{N}), \quad l = 0,1,\cdots N. \tag{C.3}$$

The expansion coefficients, a_k can be evaluated by the inverse relation:

$$a_k = \frac{2}{Nc_k}\sum_{l=0}^{N}\frac{f(x_l)}{c_l}\cos(\frac{k\pi l}{N}), \quad k = 0,1,\cdots N. \tag{C.4}$$

where $c_{l,k} = 1$ for $l,k = 1,2,\cdots N-1$ and $c_0 = c_N = 2$.

In addition to providing a well-fitted interpolation, this selection of collocation points (i.e. Eq. (C.3)) provide the ability to calculate the derivation of $f(x)$ by performing matrix multiplication rather than a simple two-point estimation (i.e. Newton's difference quotient) and avoid the sensitivity of numerical error to the direct derivation. In this approach, the Chebyshev-Lagrange collocation method [223] provides an Nth-order approximation of $f(x)$ as Lagrange interpolation using Chebyshev collocation points in Eq. (C.3)as:

$$(L_N f)(x) = \sum_{l=0}^{N} f(x_l)\psi_l(x) \tag{C.5}$$

where $\psi_l(x)$ are the *characteristic Lagrange polynomials* and have delta-function form of [ref]:

$$\psi_l(x) = \frac{(-1)^{l+1}(1-x^2)T'_N(x)}{c_l N^2(t-x_l)} \tag{C.6}$$

The polynomials $\psi_l(x)$ have the properties that $\psi_l(x_i) = 1$ for $l = i$ and $\psi_l(x_i) = 0$ for $l \neq i$. Due to such definition of $\psi_l(x)$, the $f(x)$ is analytically defined by $\psi_l(x)$ at x_l points and $(L_N f)(x_l) = f(x_l)$, consequently. Therefore, the derivative of $f(x)$ at collocation points (i.e. Eq. (C.3)) can be expressed analytically by:

$$\frac{df(x_l)}{dx} = \sum_{j=0}^{N} \frac{d\psi_j(x_l)}{dx} f(x_j) \tag{C.7}$$

Defining $D_{lj} = d\psi_j(x_l)/dx$ and using Eq. (C.6) for $\psi_l(x)$, the elements of the derivative matrix operator $\bar{\bar{\mathbf{D}}}$ can be expressed as [ref]:

$$D_{lj} = \begin{cases} \dfrac{c_l(-1)^{l+j}}{c_j(x_l - x_j)}, & l \neq j, \\ \dfrac{-x_j}{(1-x_j^2)}, & l = j = 1,2,\cdots,N-1, \\ \dfrac{2N^2+1}{6}, & l = j = 0, \\ -\dfrac{2N^2+1}{6}, & l = j = N, \end{cases} \tag{C.8}$$

By this formulation, the derivative of $f(x)$ can be calculated at the Chebyshev collocation points in the form of matrix multiplication defined as :

$$\begin{pmatrix} \dfrac{df(x_1)}{dx} \\ \dfrac{df(x_2)}{dx} \\ \vdots \\ \dfrac{df(x_N)}{dx} \end{pmatrix} = \bar{\bar{\mathbf{D}}} \begin{pmatrix} f(x_1) \\ f(x_2) \\ \vdots \\ f(x_N) \end{pmatrix} \tag{C.9}$$

The higher order derivatives at collocation points can be calculated following similar method by just multiplying the derivative matrix operator consequently.

The Chebyshev interpolation and Chebyshev-Lagrange collocation methods can be used to calculate the dispersion profile (i.e. $\beta(\omega)$) and its derivatives. Although the presented equations are in $|x| \leq 1$ domain, they can be extended to any arbitrary domain $a \leq x \leq b$ as long as $f(x)$ is well-defined in that domain and Chebyshev collocation points are defined as:

$$x_l = \frac{a+b}{2} + \frac{b-a}{2}\cos\left(\frac{\pi l}{N}\right), \quad l = 0,1,\cdots N. \tag{C.10}$$

List of publications

1. **S. A. Mousavi**, H. C. H. Mulvad, N. V. Wheeler, P. Horak, J. Hayes, Y. Chen, T. D. Bradley, S. U. Alam, S. R. Sandoghchi, E. N. Fokoua, D. J. Richardson, and F. Poletti, "Nonlinear dynamic of picosecond pulse propagation in atmospheric air-filled hollow core fibers," Opt Express **26**, 8866-8882 (2018).
2. **S.M.Abokhamis Mousavi**, S.R.Sandoghchi, D.J. Richardson, and F.Poletti, "Broadband high birefringence and polarizing hollow core antiresonant fibers," Opt. Express 24, 22943-22958 (2016),
3. **S. M Abokhamis Mousavi**, H. C. Hansen Mulvad, N. Wheeler, P. Horak, T. D. Bradley, S. Alam, J. Hayes, S. R. Sandoghchi, D. Richardson, F. Poletti, "Exploring nonlinear pulse propagation, Raman frequency conversion and near octave spanning supercontinuum generation in atmospheric air-filled hollow-core Kagomé fiber". Proc. SPIE 10088, Nonlinear Frequency Generation and Conversion: Materials and Devices XVI, 100880G (February 20, 2017).
4. **S.M.Abokhamis Mousavi**, D.J.Richardson, S.R.Sandoghchi, F.Poletti "First design of high birefringence and polarising hollow core anti-resonant fibre" 41st European Coference on Optical Communication (ECOC 2015) Valencia 27 Sept - 1 Oct 2015,
5. W. Talataisong, R. Ismaeel, T. H. R. Marques, **S. Abokhamis Mousavi**, M. Beresna, M. A. Gouveia, S. R. Sandoghchi, T. Lee, C. M. B. Cordeiro, and G. Brambilla, "Mid-IR Hollow-core microstructured fiber drawn from a 3D printed PETG preform," Sci Rep **8**, 8113 (2018).
6. J. Lousteau, **S. M. Abokhamis Mousavi**, P. Janicek, F. B. Slimen, N. White and F. Poletti, "Tellurite glasses and fibers for the development of coherent Mid-R supercontinuum source" presented in WSOF 2017.
7. N. V. Wheeler, J. R. HaXViyes, Y. Chen, T. D. Bradley, S. R. Sandoghchi, M. A. Gouveia, M. B. S. Nawazuddin, E. Numkam, G. T. Jasion, **S. M. Abokhamis Mousavi**, M. N. Petrovich, F. Poletti and D. J. Richardson, "Advances in Hollow Core Photonic Crystal Fiber Fabrication" in WSOF 2017.
8. W. Talataisong, R. Ismaeel, T. H. R. Marques, **S. M. Abokhamis Mousavi**, M. Beresna, M. Gouveia, S. R. Sandoghchi, A. Donko, T. Lee, C. M. B. Cordeiro and G. Brambilla, "3D-printed Hollow Core OmniGuide Bragg Fibres for Mid-IR Transmission" presented in WSOF 2017.
9. N. V. Wheeler, T. D. Bradley, J. R. Hayes, M. A. Gouveia, S. Liang, Y. Chen, S. R. Sandoghchi, **S. M. Abokhamis Mousavi**, F. Poletti, M. N. Petrovich, and D. J. Richardson, "Low-loss Kagome hollow-core fibers operating from the near- to the mid-IR," Opt. Lett. 42, 2571-2574 (2017).
10. L.Van Putten, E.Numkam Fokoua, **S.M.Abokhamis Mousavi**, W.Belardi, S.Chaudhuri, J.V.Badding, F.Poletti "Exploring the effect of the core boundary curvature in hollow antiresonant fibers", Photonic Technology Letters 2016 Vol.29(2) pp.263-266
11. L.Van Putten, E.Numkam Fokoua, F.Poletti, W.Belardi, **M.Abokhamis Mousavi** "Optimizing the curvature of elliptical cladding elements to reduce leakage loss in antiresonant hollow core fibres" 42nd European Conference and Exhibition on Optical Communications (ECOC '16) Dusseldorf 18-22 Sep 2016 (Poster)

12. S.R.Sandoghchi, D.R.Gray, Yong Chen, N.Wheeler, T.Bradley, J.R.Hayes, E.R.Numkam Fokoua, G.T.Jasion, **S.M.Abokhamis Mousavi**, M.N.Petrovich, F.Poletti "High dynamic range technique for discrete and distributed scattering loss measurement in microstructured optical fibres" European Conference on Optical Communication (ECOC'15) Valencia 27 Sep - 1 Oct 2015 Mo.3.1.4.,

13. S.R.Sandoghchi, M.N.Petrovich, D.R.Gray, Yong Chen, N.V.Wheeler, T.D.Bradley, N.H.L.Wong, G.Jasion, J.R.Hayes, E.Numkam Fokoua, M.Botelho Alonso, **S.M.Abokhamis Mousavi**, D.J.Richardson, F.Poletti "Optical side scattering radiometry for high resolution, wide dynamic range longitudinal assessment of optical fibers" Optics Express 2015 Vol.23 (21) pp.27960-27974,

14. E.Plum, **S.Abokhamis Mousavi**, Jinhui Shi, K.F.MacDonald, N.I.Zheludev "From coherent polarization control to chiral mirrors and perfect absorbers" Exeter Microwave Metamaterials Meeting Exeter 7-8 Dec 2015 (Invited),

15. J.R.Hayes, F.Poletti, **S.Abokhamis Mousavi**, N.V.Wheeler, N.K.Baddela, D.J.Richardson "Anti-resonant hexagram hollow core fibers" Optics Express 2015 Vol.23 (2) pp.1289-1299,

16. **S.Abokhamis Mousavi**, E.Plum, Jinhui Shi, N.I.Zheludev "Coherent control of optical polarization effects in metamaterials" Scientific Reports 2015 Vol.5 Article No.8977,

17. S.R.Sandoghchi, G.T.Jasion, N.V.Wheeler, J.P.Wooler, R.P.Boardman, N.Baddela, Yong Chen, J.R.Hayes, E.Numkam Fokoua, T.Bradley, T.Gray, **S.Abokhamis Mousavi**, M.N.Petrovich, F.Poletti, D.J.Richardson "X-ray computational tomography of hollow core photonic bandgap fibre" 3rd EPSRC Manufacturing the Future Conference Glasgow 23 Sep 2014,

18. S.R.Sandoghchi, G.T.Jasion, N.V.Wheeler, S.Jain, Z.Lian, J.P.Wooler, R.P.Boardman, N.Baddela, Yong Chen, J.R.Hayes, E.Numkam Fokoua, T.Bradley, D.R.Gray, **S.Abokhamis Mousavi**, M.N.Petrovich, F.Poletti, D.J.Richardson "X-ray tomography for structural analysis of microstructured and multimaterial optical fibers and preforms" Optics Express 2014 Vol.22 (21) pp.26181-26192,

19. S.R.Sandoghchi, G.T.Jasion, N.V.Wheeler, J.P.Wooler, R.P.Boardman, N.Baddela, Yong Chen, J.R.Hayes, E.Numkam Fokoua, T.Bradley, T.Gray, **S.Abokhamis Mousavi**, M.N.Petrovich, F.Poletti, D.J.Richardson "X-Ray Tomography for Structural Analysis of Microstructured Optical Fibres and Preforms" European Conference on Optical Communications (ECOC) Cannes 21-25 Sep 2014 Th.2.4.2.,

List of References

1. G. Agrawal, *Nonlinear Fiber Optics* (Academic Press, October 2012), p. 648.

2. G. P. Agrawal, *Applications of Nonlinear Fiber Optics* (Elsevier, 2008).

3. R. A. Ganeev, *Nonlinear Optical Properties of Materials* (Springer Netherlands, 2015).

4. H. Bach and N. Neuroth, *The Properties of Optical Glass* (Springer Berlin Heidelberg, 2012).

5. J. C. Travers, W. Chang, J. Nold, N. Y. Joly, and P. St. J. Russell, "Ultrafast nonlinear optics in gas-filled hollow-core photonic crystal fibers [Invited]," J. Opt. Soc. Am. B **28**, A11-A26 (2011).

6. P. Corkum, C. Rolland, and T. Srinivasan-Rao, "Supercontinuum Generation in Gases," Phys. Rev. Lett. **57**, 2268-2271 (1986).

7. T. Popmintchev, M.-C. Chen, P. Arpin, M. M. Murnane, and H. C. Kapteyn, "The attosecond nonlinear optics of bright coherent X-ray generation," Nat. Photonics **4**, 822-832 (2010).

8. L. Bergé, S. Skupin, R. Nuter, J. Kasparian, and J. P. Wolf, "Ultrashort filaments of light in weakly ionized, optically transparent media," Rep. Prog. Phys. **70**, 1633-1713 (2007).

9. S. E. Harris and A. V. Sokolov, "Broadband spectral generation with refractive index control," Phys. Rev. A **55**, R4019-R4022 (1997).

10. A. V. Sokolov, D. R. Walker, D. D. Yavuz, G. Y. Yin, and S. E. Harris, "Raman Generation by Phased and Antiphased Molecular States," Phys. Rev. Lett. **85**, 562-565 (2000).

11. F. Couny, F. Benabid, and P. S. Light, "Large-pitch Kagome-structured hollow-core photonic crystal fiber," Opt. Lett. **31**, 3574-3576 (2006).

12. P. Russell, "Photonic crystal fibers," Science **299**, 358-362 (2003).

13. J. C. Knight, "Photonic crystal fibres," Nature **424**, 847-851 (2003).

14. R. F. Cregan, "Single-Mode Photonic Band Gap Guidance of Light in Air," Science **285**, 1537-1539 (1999).

15. F. Benabid and P. J. Roberts, "Linear and nonlinear optical properties of hollow core photonic crystal fiber," Journal of Modern Optics **58**, 87-124 (2011).

16. A. R. Bhagwat and A. L. Gaeta, "Nonlinear optics in hollow-core photonic bandgap fibers," Opt. Express **16**, 5035-5047 (2008).

17. A. Nazarkin, A. Abdolvand, A. V. Chugreev, and P. St.J. Russell, "Direct Observation of Self-Similarity in Evolution of Transient Stimulated Raman Scattering in Gas-Filled Photonic Crystal Fibers," Phys. Rev. Lett. **105**, 173902 (2010).

18. A. Abdolvand, A. Nazarkin, A. V. Chugreev, C. F. Kaminski, and P. S. J. Russell, "Solitary Pulse Generation by Backward Raman Scattering in H_2-Filled Photonic Crystal Fibers," Phys. Rev. Lett. **103**, 183902 (2009).

19. D. G. Ouzounov, F. R. Ahmad, D. Muller, N. Venkataraman, M. T. Gallagher, M. G. Thomas, J. Silcox, K. W. Koch, and A. L. Gaeta, "Generation of megawatt optical solitons in hollow-core photonic band-gap fibers," Science **301**, 1702-1704 (2003).

20. K. F. Mak, J. C. Travers, P. Holzer, N. Y. Joly, and P. S. Russell, "Tunable vacuum-UV to visible ultrafast pulse source based on gas-filled Kagome-PCF," Opt Express **21**, 10942-10953 (2013).

21. B. H. Stuart, *Infrared Spectroscopy: Fundamentals and Applications* (Wiley, 2004).

22. F. K. Tittel, R. Lewicki, M. Jahjah, B. Foxworth, Y. Ma, L. Dong, R. Griffin, K. Krzempek, P. Stefanski, and J. Tarka, "Mid-infrared Laser Based Gas Sensor Technologies for Environmental Monitoring, Medical Diagnostics, Industrial and Security Applications," in Terahertz and Mid Infrared Radiation: Detection of Explosives and CBRN (Using Terahertz) (Springer Netherlands, 2014), 153-165.

23. A. Schliesser, N. Picqué, and T. W. Hänsch, "Mid-infrared frequency combs," Nat. Photonics **6**, 440-449 (2012).

24. M. N. Zervas and C. A. Codemard, "High Power Fiber Lasers: A Review," IEEE Journal of Selected Topics in Quantum Electronics **20**, 219-241 (2014).

25. Y. Yao, A. J. Hoffman, and C. F. Gmachl, "Mid-infrared quantum cascade lasers," Nat. Photonics **6**, 432-439 (2012).

26. M. Ebrahim-Zadeh, "Mid-Infrared Optical Parametric Oscillators and Applications," in *Mid-Infrared Coherent Sources and Applications*, M. Ebrahim-Zadeh and I. Sorokina, eds. (Springer Netherlands, 2008), pp. 347-375.

27. S. D. Jackson, "Towards high-power mid-infrared emission from a fibre laser," Nat. Photonics **6**, 423-431 (2012).

28. Z. Wang, W. Belardi, F. Yu, W. J. Wadsworth, and J. C. Knight, "Efficient diode-pumped mid-infrared emission from acetylene-filled hollow-core fiber," Opt Express **22**, 21872-21878 (2014).

29. A. M. Jones, C. Fourcade-Dutin, C. Mao, B. Baumgart, V. A. V. Nampoothiri, N. Campbell, Y. Y. Wang, F. Benabid, W. Rudolph, B. R. Washburn, and K. L. Corwin, "Characterization of mid-infrared emissions from C_2H_2, CO, CO_2, and HCN-filled hollow fiber lasers," **8237**, 82373Y (2012).

30. A. M. Jones, A. V. V. Nampoothiri, A. Ratanavis, T. Fiedler, N. V. Wheeler, F. Couny, R. Kadel, F. Benabid, B. R. Washburn, K. L. Corwin, and W. Rudolph, "Mid-infrared gas filled photonic crystal fiber laser based on population inversion," Opt. Express **19**, 2309-2316 (2011).

31. L. Ben Yehud and A. A. Ishaaya, "Highly efficient wavelength conversion in CF4-filled hollowcore photonic bandgap fibers," in *Lasers and Electro-Optics (CLEO), 2014 Conference on*, 2014), 1-2.

32. F. Benabid, G. Bouwmans, J. Knight, P. Russell, and F. Couny, "Ultrahigh Efficiency Laser Wavelength Conversion in a Gas-Filled Hollow Core Photonic Crystal Fiber by Pure Stimulated Rotational Raman Scattering in Molecular Hydrogen," Phys. Rev. Lett. **93**(2004).

33. B. M. Trabold, A. Abdolvand, T. G. Euser, and P. S. Russell, "Efficient anti-Stokes generation via intermodal stimulated Raman scattering in gas-filled hollow-core PCF," Opt Express **21**, 29711-29718 (2013).

34. F. Benabid, J. C. Knight, G. Antonopoulos, and P. S. Russell, "Stimulated Raman scattering in hydrogen-filled hollow-core photonic crystal fiber," Science **298**, 399-402 (2002).

35. F. Couny, F. Benabid, and P. Light, "Subwatt Threshold cw Raman Fiber-Gas Laser Based on H_2-Filled Hollow-Core Photonic Crystal Fiber," Phys. Rev. Lett. **99**(2007).

36. F. P. Kapron, D. B. Keck, and R. D. Maurer, "Radiation Losses in Glass Optical Waveguides," Appl. Phys. Lett. **17**, 423-425 (1970).

37. "Corning® SMF-28® Ultra Optical Fiber", retrieved https://www.corning.com/media/worldwide/coc/documents/Fiber/SMF-28%20Ultra.pdf.

38. M. Hirano, T. Haruna, Y. Tamura, T. Kawano, S. Ohnuki, Y. Yamamoto, Y. Koyano, and T. Sasaki, "Record Low Loss, Record High FOM Optical Fiber with Manufacturable Process," in *Optical Fiber Communication Conference/National Fiber Optic Engineers Conference 2013*, OSA Technical Digest (online) (Optical Society of America, 2013), PDP5A.7.

39. M. A. Terrel, M. J. F. Digonnet, and S. Fan, "Resonant fiber optic gyroscope using an air-core fiber," J. Lightwave Technol. **30**, 931-937 (2012).

40. F. Emaury, C. J. Saraceno, B. Debord, D. Ghosh, A. Diebold, F. Gerome, T. Sudmeyer, F. Benabid, and U. Keller, "Efficient spectral broadening in the 100-W average power regime using gas-filled kagome HC-PCF and pulse compression," Opt. Lett. **39**, 6843-6846 (2014).

41. B. Debord, M. Alharbi, L. Vincetti, A. Husakou, C. Fourcade-Dutin, C. Hoenninger, E. Mottay, F. Gerome, and F. Benabid, "Multi-meter fiber-delivery and pulse self-compression of milli-Joule femtosecond laser and fiber-aided laser-micromachining," Opt. Express **22**, 10735-10746 (2014).

42. J. Hu and C. R. Menyuk, "Understanding leaky modes: slab waveguide revisited," Advances in Optics and Photonics **1**, 58 (2009).

43. E. Yablonovitch, "Inhibited spontaneous emission in solid-state physics and electronics," Phys. Rev. Lett. **58**, 2059-2062 (1987).

44. S. John, "Strong localization of photons in certain disordered dielectric superlattices," Phys. Rev. Lett. **58**, 2486-2489 (1987).

45. T. A. Birks, D. M. Atkin, T. J. Shepherd, P. S. J. Russell, and P. J. Roberts, "Full 2-D photonic bandgaps in silica/air structures," Electron. Lett. **31**, 1941-1943 (1995).

46. F. Poletti, M. N. Petrovich, and D. J. Richardson, "Hollow-core photonic bandgap fibers: technology and applications," Nanophotonics **2** (2013).

47. F. Couny, F. Benabid, P. J. Roberts, P. S. Light, and M. G. Raymer, "Generation and photonic guidance of multi-octave optical-frequency combs," Science **318**, 1118-1121 (2007).

48. P. S. J. Russell, P. Hölzer, W. Chang, A. Abdolvand, and J. C. Travers, "Hollow-core photonic crystal fibres for gas-based nonlinear optics," Nat. Photonics **8**, 278-286 (2014).

49. O. H. Heckl, C. R. E. Baer, C. Kränkel, S. V. Marchese, F. Schapper, M. Holler, T. Südmeyer, J. S. Robinson, J. W. G. Tisch, F. Couny, P. Light, F. Benabid, and U. Keller, "High harmonic generation in a gas-filled hollow-core photonic crystal fiber," Appl. Phys. B **97**, 369-373 (2009).

50. J. C. Knight, J. Broeng, T. A. Birks, and P. S. J. Russell, "Photonic band gap guidance in gptical fibers," Science **282**, 1476-1478 (1998).

51. P. J. Roberts, F. Couny, H. Sabert, B. J. Mangan, D. P. Williams, L. Farr, M. W. Mason, A. Tomlinson, T. A. Birks, J. C. Knight, and P. S. J. Russell, "Ultimate low loss of hollow-core photonic crystal fibres," Opt. Express **13**, 236-244 (2005).

52. M. A. Duguay, Y. Kokubun, T. L. Koch, and L. Pfeiffer, "Antiresonant reflecting optical waveguides in SiO_2-Si multilayer structures," Appl. Phys. Lett. **49**, 13 (1986).

53. N. M. Litchinitser, A. K. Abeeluck, C. Headley, and B. J. Eggleton, "Antiresonant reflecting photonic crystal optical waveguides," Opt. Lett. **27**, 1592-1594 (2002).

54. F. Benabid, F. Gérôme, L. Vincetti, B. Debord, M. Alharbi, and T. Bradley, "Inhibited coupling hollow-core photonic crystal fiber," in *SPIE OPTO*, (SPIE, 2014), 6.

55. B. Debord, A. Amsanpally, M. Chafer, A. Baz, M. Maurel, J. M. Blondy, E. Hugonnot, F. Scol, L. Vincetti, F. Gérôme, and F. Benabid, "Ultralow transmission loss in inhibited-coupling guiding hollow fibers," Optica **4**, 209 (2017).

56. J. D. Joannopoulos, S. G. Johnson, and J. N. Winn, *Photonic Crystals: Molding the Flow of Light,* 2nd ed. (Princeton University Press, 2008).

57. F. Poletti, "Nested antiresonant nodeless hollow core fiber," Opt. Express **22**, 23807-23828 (2014).

58. G. J. Pearce, G. S. Wiederhecker, C. G. Poulton, S. Burger, and P. St. J. Russell, "Models for guidance in kagome-structured hollow-core photonic crystal fibres," Opt. Express **15**, 12680-12685 (2007).

59. A. Argyros and J. Pla, "Hollow-core polymer fibres with a kagome lattice: potential for transmission in the infrared," Opt. Express **15**, 7713-7719 (2007).

60. F. Couny, F. Benabid, P. J. Roberts, P. S. Light, and M. G. Raymer, "Generation and photonic guidance of multi-octave optical-frequency combs," Science **318**, 1118-1121 (2007).

61. J. L. Archambault, R. J. Black, S. Lacroix, and J. Bures, "Loss calculations for antiresonant waveguides," Lightwave Technology, Journal of **11**, 416-423 (1993).

62. M. Miyagi, "Bending losses in hollow and dielectric tube leaky waveguides," Appl. Opt. **20**, 1221-1229 (1981).

63. B. Debord, M. Alharbi, T. Bradley, C. Fourcade-Dutin, Y. Y. Wang, L. Vincetti, F. Gerome, and F. Benabid, "Hypocycloid-shaped hollow-core photonic crystal fiber Part I: Arc curvature effect on confinement loss," Opt Express **21**, 28597-28608 (2013).

64. N. V. Wheeler, T. D. Bradley, J. R. Hayes, M. A. Gouveia, S. Liang, Y. Chen, S. R. Sandoghchi, S. M. Abokhamis Mousavi, F. Poletti, M. N. Petrovich, and D. J. Richardson, "Low-loss Kagome hollow-core fibers operating from the near- to the mid-IR," Opt. Lett. **42**, 2571-2574 (2017).

65. M. Maurel, M. Chafer, A. Amsanpally, M. Adnan, F. Amrani, B. Debord, L. Vincetti, F. Gerome, and F. Benabid, "Optimized inhibited-coupling Kagome fibers at Yb-Nd:Yag (8.5 dB/km) and Ti:Sa (30 dB/km) ranges," Opt. Lett. **43**, 1598-1601 (2018).

66. J. R. Hayes, F. Poletti, M. S. Abokhamis, N. V. Wheeler, N. K. Baddela, and D. J. Richardson, "Anti-resonant hexagram hollow core fibers," Opt. Express **23**, 1289 (2015).

67. Y. Y. Wang, N. V. Wheeler, F. Couny, P. J. Roberts, and F. Benabid, "Low loss broadband transmission in hypocycloid-core Kagome hollow-core photonic crystal fiber," Opt. Lett. **36**, 669-671 (2011).

68. F. Poletti, J. R. Hayes, and D. Richardson, "Optimising the Performances of Hollow Antiresonant Fibres," in *37th European Conference and Exposition on Optical Communications*, OSA Technical Digest (CD) (Optical Society of America, 2011), Mo.2.LeCervin.2.

69. F. Yu, W. J. Wadsworth, and J. C. Knight, "Low loss silica hollow core fibers for 3?4 ?m spectral region," Opt. Express **20**, 11153-11158 (2012).

70. A. D. Pryamikov, A. S. Biriukov, A. F. Kosolapov, V. G. Plotnichenko, S. L. Semjonov, and E. M. Dianov, "Demonstration of a waveguide regime for a silica hollow - core microstructured optical fiber with a negative curvature of the core boundary in the spectral region > 3.5 μm," Opt. Express **19**, 1441-1448 (2011).

71. A. N. Kolyadin, A. F. Kosolapov, A. D. Pryamikov, A. S. Biriukov, V. G. Plotnichenko, and E. M. Dianov, "Light transmission in negative curvature hollow core fiber in extremely high material loss region," Opt. Express **21**, 9514-9519 (2013).

72. R. W. Boyd, *Nonlinear Optics (Third Edition)* (Academic Press, Burlington, 2008), p. 640.

73. C. V. Raman and K. S. Krishnan, "A New Type of Secondary Radiation," Nature **121**, 501-502.

74. G. S. Landsberg and L. I. Mandel'shtam, "A new phenomenon of light scattering," Zh. Rus. Fiz. Khim. Obshch. **60**, 335.

75. G. Placzek, "Rayleigh-Streuung und Raman-Effekt," in Handbuch der Radiologie **6**, 2.

76. E. J. Woodbury and W. K. Ng, "Ruby laser operation in the near IR," Proc. IRE **50**, 2367 (1962).

77. I. T. Sorokina, Vodopyanov, Konstantin L, *Solid-State Mid-Infrared Laser Sources*, Topics in Applied Physics (Springer-Verlag Berlin Heidelberg, 2003), Vol. 1, p. 89.

78. M. Maier, "Applications of stimulated Raman scattering," Applied Physics **11**, 209-231 (1976).

79. A. C. Albrecht and M. C. Hutley, "On the Dependence of Vibrational Raman Intensity on the Wavelength of Incident Light," The Journal of Chemical Physics **55**, 4438-4443 (1971).

80. M. G. Raymer and J. Mostowski, "Stimulated Raman scattering: Unified treatment of spontaneous initiation and spatial propagation," Phys. Rev. A **24**, 1980-1993 (1981).

81. J. T. Lin, "Theory of transient stimulated Raman scattering and four-wave-mixing processes in multiple-pump systems: A Hamiltonian approach," Phys. Rev. A **33**, 3210-3218 (1986).

82. M. Kolesik and J. V. Moloney, "Nonlinear optical pulse propagation simulation: from Maxwell's to unidirectional equations," Phys Rev E Stat Nonlin Soft Matter Phys **70**, 036604 (2004).

83. M. Kolesik, J. V. Moloney, and M. Mlejnek, "Unidirectional optical pulse propagation equation," Phys. Rev. Lett. **89**, 283902 (2002).

84. R. Khakimov, I. Shavrin, S. Novotny, M. Kaivola, and H. Ludvigsen, "Numerical solver for supercontinuum generation in multimode optical fibers," Opt Express **21**, 14388-14398 (2013).

85. F. Poletti and P. Horak, "Description of ultrashort pulse propagation in multimode optical fibers," J. Opt. Soc. Am. B **25** (2008).

86. J. M. Dudley and S. Coen, "Supercontinuum generation in photonic crystal fiber," Rev. Mod. Phys. **78**, 1135-1184 (2006).

87. M. F. Saleh, W. Chang, P. Hölzer, A. Nazarkin, J. C. Travers, N. Y. Joly, P. S. J. Russell, and F. Biancalana, "Theory of Photoionization-Induced Blueshift of Ultrashort Solitons in Gas-Filled Hollow-Core Photonic Crystal Fibers," Phys. Rev. Lett. **107**, 203902 (2011).

88. W. Chang, A. Nazarkin, J. C. Travers, J. Nold, P. Hölzer, N. Y. Joly, and P. S. J. Russell, "Influence of ionization on ultrafast gas-based nonlinear fiber optics," Opt. Express **19**, 21018-21027 (2011).

89. D. Ouzounov, C. Hensley, A. Gaeta, N. Venkateraman, M. Gallagher, and K. Koch, "Soliton pulse compression in photonic band-gap fibers," Opt. Express **13**, 6153-6159 (2005).

90. F. Gèrôme, P. Dupriez, J. Clowes, J. C. Knight, and W. J. Wadsworth, "High power tunable femtosecond soliton sourceusing hollow-core photonic bandgap fiber, andits use for frequency doubling," Opt. Express **16**, 2381-2386 (2008).

91. P. J. Mosley, W. C. Huang, M. G. Welch, B. J. Mangan, W. J. Wadsworth, and J. C. Knight, "Ultrashort pulse compression and delivery in a hollow-core photonic crystal fiber at 540 nm wavelength," Opt. Lett. **35**, 3589-3591 (2010).

92. F. Gérôme, K. Cook, A. K. George, W. J. Wadsworth, and J. C. Knight, "Delivery of sub-100fs pulses through 8m of hollow-core fiber using soliton compression," Opt. Express **15**, 7126-7131 (2007).

93. N. Y. Joly, J. Nold, W. Chang, P. Hölzer, A. Nazarkin, G. K. L. Wong, F. Biancalana, and P. S. J. Russell, "Bright Spatially Coherent Wavelength-Tunable Deep-UV Laser Source Using an Ar-Filled Photonic Crystal Fiber," Phys. Rev. Lett. **106**, 203901 (2011).

94. K. F. Mak, J. C. Travers, P. Hölzer, N. Y. Joly, and P. S. J. Russell, "Tunable vacuum-UV to visible ultrafast pulse source based on gas-filled Kagome-PCF," Opt. Express **21**, 10942-10953 (2013).

95. F. Guichard, A. Giree, Y. Zaouter, M. Hanna, G. Machinet, B. Debord, F. Gerome, P. Dupriez, F. Druon, C. Honninger, E. Mottay, F. Benabid, and P. Georges, "Nonlinear compression of high energy fiber amplifier pulses in air-filled hypocycloid-core Kagome fiber," Opt Express **23**, 7416-7423 (2015).

96. A. Abdolvand, A. M. Walser, M. Ziemienczuk, T. Nguyen, and P. S. J. Russell, "Generation of a phase-locked Raman frequency comb in gas-filled hollow-core photonic crystal fiber," Opt. Lett. **37**, 4362-4364 (2012).

97. S. A. Mousavi, H. C. H. Mulvad, N. V. Wheeler, P. Horak, J. Hayes, Y. Chen, T. D. Bradley, S. U. Alam, S. R. Sandoghchi, E. N. Fokoua, D. J. Richardson, and F. Poletti, "Nonlinear dynamic of picosecond pulse propagation in atmospheric air-filled hollow core fibers," Opt Express **26**, 8866-8882 (2018).

98. A. V. Gladyshev, A. F. Kosolapov, A. N. Kolyadin, M. S. Astapovich, A. D. Pryamikov, M. E. Likhachev, and I. A. Bufetov, "Mid-IR hollow-core silica fibre Raman lasers," Quantum Electronics **47**, 1078-1082 (2017).

99. A. V. V. Nampoothiri, A. M. Jones, C. Fourcade-Dutin, C. Mao, N. Dadashzadeh, B. Baumgart, Y. Y. Wang, M. Alharbi, T. Bradley, N. Campbell, F. Benabid, B. R. Washburn, K. L. Corwin, and W. Rudolph, "Hollow-core Optical Fiber Gas Lasers (HOFGLAS): a review [Invited]," Optical Materials Express **2**, 948-961 (2012).

100. W. B. Gardner, "Microbending Loss in Optical Fibers," Bcl] Syst. Tech. J. **54**, 457-465 (1975).

101. S. L. Jones, G. Murtaza, J. M. Senior, and N. Haigh, "Single-Mode Optical Fiber Microbend Loss Modeling Using the Finite Difference Beam Propagation Method," Optical Fiber Technology **4**, 471-479 (1998).

102. X. Jin and F. P. Payne, "Numerical Investigation of Microbending Loss in Optical Fibres," J. Lightwave Technol. **34**, 1247-1253 (2016).

103. P. J. Roberts, F. Couny, H. Sabert, B. J. Mangan, T. A. Birks, J. C. Knight, and P. S. J. Russell, "Loss in solid-core photonic crystal fibers due to interface roughness scattering," Opt. Express **13** (2005).

104. S. Johnson and J. Joannopoulos, "Block-iterative frequency-domain methods for Maxwell's equations in a planewave basis," Opt. Express **8**, 173 (2001).

105. R. Kotynski, M. Antkowiak, F. Berghmans, H. Thienpont, and K. Panajotov, "Photonic crystal fibers with material anisotropy," Optical and Quantum Electronics **37**, 253-264 (2005).

106. J. K. Ranka, R. S. Windeler, and A. J. Stentz, "Optical properties of high-delta air–silica microstructure optical fibers," Opt. Lett. **25**, 796 (2000).

107. T. P. White, B. T. Kuhlmey, R. C. McPhedran, D. Maystre, G. Renversez, C. M. de Sterke, and L. C. Botten, "Multipole method for microstructured optical fibers I Formulation," J. Opt. Soc. Am. B **19**, 2322 (2002).

108. A. Hochman and Y. Leviatan, "Calculation of confinement losses in photonic crystal fibers by use of a source-model technique," J. Opt. Soc. Am. B **22**, 474 (2005).

109. M. Koshiba and K. Saitoh, "Numerical verification of degeneracy in hexagonal photonic crystal fibers," IEEE Photonics Technology Letters **13**, 1313-1315 (2001).

110. D. Mogilevtsev, T. A. Birks, and P. S. J. Russell, "Localized function method for modeling defect modes in 2-D photonic crystals," J. Lightwave Technol. **17**, 2078-2081 (1999).

111. N. A. Issa and L. Poladian, "Vector wave expansion method for leaky modes of microstructured optical fibers," J. Lightwave Technol. **21**, 1005-1012 (2003).

112. J. M. Jin, *The Finite Element Method in Electromagnetics* (Wiley, 2015).

113. L. Vincetti and V. Setti, "Fano Resonances in Polygonal Tube Fibers," J. Lightwave Technol. **30**, 31-37 (2012).

114. W. Ding and Y. Wang, "Analytic model for light guidance in single-wall hollow-core anti-resonant fibers," Opt Express **22**, 27242-27256 (2014).

115. X. Yong, G. X. Ouyang, R. K. Lee, and A. Yariv, "Asymptotic matrix theory of Bragg fibers," J. Lightwave Technol. **20**, 428-440 (2002).

116. J.-P. Berenger, "A perfectly matched layer for the absorption of electromagnetic waves," J. Comput. Phys. **114**, 185-200 (1994).

117. F. L. Teixeira and W. C. Chew, "Systematic derivation of anisotropic PML absorbing media in cylindrical and spherical coordinates," IEEE Microwave and Guided Wave Letters **7**, 371-373 (1997).

118. W. Jo-Yu, D. M. Kingsland, L. Jin-Fa, and R. Lee, "A comparison of anisotropic PML to Berenger's PML and its application to the finite-element method for EM scattering," IEEE Trans. Antennas Propag. **45**, 40-50 (1997).

119. Z. S. Sacks, D. M. Kingsland, R. Lee, and L. Jin-Fa, "A perfectly matched anisotropic absorber for use as an absorbing boundary condition," IEEE Trans. Antennas Propag. **43**, 1460-1463 (1995).

120. F. L. Teixeira and W. C. Chew, "Systematic derivation of anisotropic PML absorbing media in cylindrical and spherical coordinates," Microwave and Guided Wave Letters, IEEE **7**, 371-373 (1997).

121. C. H. Lai and H. C. Chang, "Effect of perfectly matched layer reflection coefficient on modal analysis of leaky waveguide modes," Opt Express **19**, 562-569 (2011).

122. M. Heiblum and J. Harris, "Analysis of curved optical waveguides by conformal transformation," Quantum Electronics, IEEE Journal of **11**, 75-83 (1975).

123. A. B. Sharma, A. H. Al-Ani, and S. J. Halme, "Constant-curvature loss in monomode fibers: an experimental investigation," Appl. Opt. **23**, 3297-3301 (1984).

124. R. T. Schermer and J. H. Cole, "Improved Bend Loss Formula Verified for Optical Fiber by Simulation and Experiment," IEEE J. Quantum Electron. **43**, 899-909 (2007).

125. M. J. Ablowitz and H. Segur, *Solitons and the Inverse Scattering Transform* (Society for Industrial and Applied Mathematics, 1981).

126. L. Schoulepnikoff and V. Mitev, "Numerical method for the modeling of high-gain single-pass cascade stimulated Raman scattering in gases," J. Opt. Soc. Am. B **14**, 62 (1997).

127. J. C. Butcher, "A history of Runge-Kutta methods," Appl. Numer. Math. **20**, 247-260 (1996).

128. O. V. Sinkin, R. Holzlohner, J. Zweck, and C. R. Menyuk, "Optimization of the split-step fourier method in modeling optical-fiber communications systems," J. Lightwave Technol. **21**, 61-68 (2003).

129. A. F. Kosolapov, A. D. Pryamikov, A. S. Biriukov, V. S. Shiryaev, M. S. Astapovich, G. E. Snopatin, V. G. Plotnichenko, M. F. Churbanov, and E. M. Dianov, "Demonstration of CO_2-laser power delivery through chalcogenide-glass fiber with negative-curvature hollow core," Opt Express **19**, 25723-25728 (2011).

130. W. Belardi and J. C. Knight, "Hollow antiresonant fibers with low bending loss," Opt. Express **22**, 10091-10096 (2014).

131. L. Vincetti and V. Setti, "Waveguiding mechanism in tube lattice fibers," Opt. Express **18**, 23133-23146 (2010).

132. S. Liu, Y. Wang, M. Hou, J. Guo, Z. Li, and P. Lu, "Anti-resonant reflecting guidance in alcohol-filled hollow core photonic crystal fiber for sensing applications," Opt Express **21**, 31690-31697 (2013).

133. W. Ding and Y.-Y. Wang, "Hybrid transmission bands and large birefringence in hollow-core anti-resonant fibers," Opt. Express **23**, 21165-21174 (2015).

134. M. S. Habib, O. Bang, and M. Bache, "Low-loss single-mode hollow-core fiber with anisotropic anti-resonant elements," Opt Express **24**, 8429-8436 (2016).

135. O. Humbach, H. Fabian, U. Grzesik, U. Haken, and W. Heitmann, "Analysis of OH absorption bands in synthetic silica," J. Non-Cryst. Solids **203**, 19-26 (1996).

136. R. Kitamura, L. Pilon, and M. Jonasz, "Optical constants of silica glass from extreme ultraviolet to far infrared at near room temperature," Appl. Opt. **46**(2007).

137. I. A. Bufetov and E. M. Dianov, "A simple analytic model of a cw multicascade fibre Raman laser," Quantum Electronics **30**, 873-877 (2000).

138. E. A. J. Marcatili and R. A. Schmeltzer, "Hollow metallic and dielectric waveguides for long distance optical transmission and lasers," Bell Syst. Tech. J. **43**, 1783-1809 (1964).

139. A. Hartung, J. Kobelke, A. Schwuchow, K. Wondraczek, J. Bierlich, J. Popp, T. Frosch, and M. A. Schmidt, "Double antiresonant hollow core fiber--guidance in the deep ultraviolet by modified tunneling leaky modes," Opt Express **22**, 19131-19140 (2014).

140. S. A. Mousavi, S. R. Sandoghchi, D. J. Richardson, and F. Poletti, "Broadband high birefringence and polarizing hollow core antiresonant fibers," Opt Express **24**, 22943-22958 (2016).

141. M. I. Hasan, N. Akhmediev, and W. Chang, "Positive and negative curvatures nested in an antiresonant hollow-core fiber," Opt. Lett. **42**, 703-706 (2017).

142. M. S. Habib, O. Bang, and M. Bache, "Low-loss hollow-core silica fibers with adjacent nested anti-resonant tubes," Opt Express **23**, 17394-17406 (2015).

143. X. Feng, J. Shi, M. Segura, N. M. White, P. Kannan, W. H. Loh, L. Calvez, X. Zhang, and L. Brilland, "Halo-tellurite glass fiber with low OH content for 2-5microm mid-infrared nonlinear applications," Opt Express **21**, 18949-18954 (2013).

144. G. Epple, K. S. Kleinbach, T. G. Euser, N. Y. Joly, T. Pfau, P. S. J. Russell, and R. Löw, "Rydberg atoms in hollow-core photonic crystal fibres," Nat. Commun. **5**(2014).

145. A. D. Slepkov, A. R. Bhagwat, V. Venkataraman, P. Londero, and A. L. Gaeta, "Spectroscopy of Rb atoms in hollow-core fibers," Phys. Rev. A **81**, 053825 (2010).

146. X. Peng and L. Dong, "Fundamental-mode operation in polarization-maintaining ytterbium-doped fiber with an effective area of 1400 μm2," Opt. Lett. **32**, 358-360 (2007).

147. T. Hosaka, K. Okamoto, T. Miya, Y. Sasaki, and T. Edahiro, "Low-loss single polarisation fibres with asymmetrical strain birefringence," Electron. Lett. **17**, 530-531 (1981).

148. R. D. Birch, D. N. Payne, and M. P. Varnham, "Fabrication of polarisation-maintaining fibres using gas-phase etching," Electron. Lett. **18**, 1036-1038 (1982).

149. R. B. Dyott, J. R. Cozens, and D. G. Morris, "Preservation of polarisation in optical-fibre waveguides with elliptical cores," Electron. Lett. **15**, 380-382 (1979).

150. A. Hartung, J. Kobelke, A. Schwuchow, K. Wondraczek, J. Bierlich, J. Popp, T. Frosch, and M. A. Schmidt, "Double antiresonant hollow core fiber – guidance in the deep ultraviolet by modified tunneling leaky modes," Opt. Express **22**, 19131-19140 (2014).

151. A. D. Pryamikov, A. S. Biriukov, A. F. Kosolapov, V. G. Plotnichenko, S. L. Semjonov, and E. M. Dianov, "Demonstration of a waveguide regime for a silica hollow - core microstructured optical fiber with a negative curvature of the core boundary in the spectral region > 3.5 μm," Opt. Express **19**, 1441-1448 (2011).

152. W. Belardi and J. C. Knight, "Hollow antiresonant fibers with reduced attenuation," Opt. Lett. **39**, 1853-1856 (2014).

153. W. Belardi, "Design and properties of hollow antiresonant fibers for the visible and near infrared spectral range," J. Lightwave Technol. **33**, 4497-4503 (2015).

154. A. F. Kosolapov, G. K. Alagashev, A. N. Kolyadin, A. D. Pryamikov, A. S. Biryukov, I. A. Bufetov, and E. M. Dianov, "Hollow-core revolver fibre with a double-capillary reflective cladding," Quantum Electronics **46**, 267 (2016).

155. J. M. Fini, J. W. Nicholson, B. Mangan, L. Meng, R. S. Windeler, E. M. Monberg, A. DeSantolo, F. V. DiMarcello, and K. Mukasa, "Polarization maintaining single-mode low-loss hollow-core fibres," Nat. Commun. **5**, 5085 (2014).

156. S. A. Mousavi, D. J. Richardson, S. R. Sandoghchi, and F. Poletti, "First design of high birefringence and polarising hollow core anti-resonant fibre," in *Optical Communication (ECOC), 2015 European Conference on*, 2015), 1-3.

157. P. J. Roberts, "Birefringent hollow core fibers," in *Proc. SPIE 6782, Optoelectronic Materials and Devices II*, November 19, 2007), 67821R.

158. F. Poletti, N. G. R. Broderick, D. J. Richardson, and T. M. Monro, "The effect of core asymmetries on the polarization properties of hollow core photonic bandgap fibers," Opt. Express **13**, 9115-9124 (2005).

159. X.-L. Tang, B.-S. Sun, and Y.-W. Shi, "Design and optimization of low-loss high-birefringence hollow fiber at terahertz frequency," Opt. Express **19**, 24967-24979 (2011).

160. Y. Wang, F. Couny, P. J. Roberts, and F. Benabid, "Low loss broadband transmission in optimized core-shape kagome hollow-core PCF," in *Conference on Lasers and Electro-Optics 2010*, OSA Technical Digest (CD) (Optical Society of America, 2010), CPDB4.

161. P. J. Roberts, D. P. Williams, H. Sabert, B. J. Mangan, D. M. Bird, T. A. Birks, J. C. Knight, and P. S. J. Russell, "Design of low-loss and highly birefringent hollow-core photonic crystal fiber," Opt. Express **14**, 7329-7341 (2006).

162. J. Hayes, S. Sandoghchi, T. Bradley, Z. Liu, R. Slavík, M. A. Gouveia, N. Wheeler, G. Jasion, Y. Chen, E. Numkam-Fokoua, M. Petrovich, D. Richardson, and F. Poletti, "Antiresonant hollow core fiber with octave spanning bandwidth for short haul data communications," in *Optical Fiber Communication Conference Postdeadline Papers,* (Optical Society of America, 2016), p. Th5A.3.

163. C. Wei, R. A. Kuis, F. Chenard, C. R. Menyuk, and J. Hu, "Higher-order mode suppression in chalcogenide negative curvature fibers," Opt. Express **23**, 15824-15832 (2015).

164. M. Michieletto, J. K. Lyngsø, C. Jakobsen, J. Lægsgaard, O. Bang, and T. T. Alkeskjold, "Hollow-core fibers for high power pulse delivery," Opt. Express **24**, 7103-7119 (2016).

165. M. J. Weber, *Handbook of Optical Materials* (CRC Press 2002).

166. M. Wittmann, A. Nazarkin, and G. Korn, "New regime of fs-pulse stimulated Raman scattering," Appl. Phys. B **70**, S261-S267 (2000).

167. Y. Y. Wang, F. Couny, P. S. Light, B. J. Mangan, and F. Benabid, "Compact and portable multiline UV and visible Raman lasers in hydrogen-filled HC-PCF," Opt. Lett. **35**, 1127-1129 (2010).

168. E. R. Peck and S. Huang, "Refractivity and dispersion of hydrogen in the visible and near infrared," J. Opt. Soc. Am. **67**, 1550-1554 (1977).

169. L. Vincetti, "Empirical formulas for calculating loss in hollow core tube lattice fibers," Opt Express **24**, 10313-10325 (2016).

170. W. K. Bischel and M. J. Dyer, "Wavelength dependence of the absolute Raman gain coefficient for the Q(1) transition in H_2," J. Opt. Soc. Am. B **3** (1986).

171. K. Mochizuki, "Optical fiber transmission systems using stimulated Raman scattering: Theory," J. Lightwave Technol. **3**, 688-694 (1985).

172. Y. R. Shen and N. Bloembergen, "Theory of Stimulated Brillouin and Raman Scattering," Phys. Rev. **137**, A1787-A1805 (1965).

173. R. W. Ziolkowski and J. B. Judkins, "Nonlinear finite-difference time-domain modeling of linear and nonlinear corrugated waveguides," J. Opt. Soc. Am. B **11**(1994).

174. M. Alharbi, T. Bradley, B. Debord, C. Fourcade-Dutin, D. Ghosh, L. Vincetti, F. Gerome, and F. Benabid, "Hypocycloid-shaped hollow-core photonic crystal fiber Part II: Cladding effect on confinement and bend loss," Opt Express **21**, 28609-28616 (2013).

175. S. T. Bauerschmidt, D. Novoa, and P. S. Russell, "Dramatic Raman Gain Suppression in the Vicinity of the Zero Dispersion Point in a Gas-Filled Hollow-Core Photonic Crystal Fiber," Phys. Rev. Lett. **115**, 243901 (2015).

176. D. Hollenbeck and C. D. Cantrell, "Multiple-vibrational-mode model for fiber-optic Raman gain spectrum and response function," J. Opt. Soc. Am. B **19**, 2886-2892 (2002).

177. M. G. Raymer, I. A. Walmsley, J. Mostowski, and B. Sobolewska, "Quantum theory of spatial and temporal coherence properties of stimulated Raman scattering," Phys. Rev. A **32**, 332-344 (1985).

178. W. K. Bischel and M. J. Dyer, "Temperature dependence of the Raman linewidth and line shift for the Q(1) and Q(0) transitions in normal and para-H_2," Phys. Rev. A **33**, 3113-3123 (1986).

179. G. C. Corey and F. R. McCourt, "Dicke narrowing and collisional broadening of spectral lines in dilute molecular gases," The Journal of Chemical Physics **81**, 2318-2329 (1984).

180. S. Ghosh, *Control Systems: Theory And Applications* (Pearson Education, 2004).

181. L. Kotov, M. Likhachev, M. Bubnov, O. Medvedkov, D. Lipatov, A. Guryanov, K. Zaytsev, M. Jossent, and S. Février, "Millijoule pulse energy 100-nanosecond Er-doped fiber laser," Opt. Lett. **40**, 1189 (2015).

182. Y. Chen, Z. Wang, B. Gu, F. Yu, and Q. Lu, "Achieving a 1.5 mum fiber gas Raman laser source with about 400 kW of peak power and a 6.3 GHz linewidth," Opt. Lett. **41**, 5118-5121 (2016).

183. P. D. Drummond and J. F. Corney, "Quantum noise in optical fibers. I. Stochastic equations," J. Opt. Soc. Am. B **18**, 139-152 (2001).

184. C. Headley, III and G. P. Agrawal, "Noise characteristics and statistics of picosecond Stokes pulses generated in optical fibers through stimulated Raman scattering," Quantum Electronics, IEEE Journal of **31**, 2058-2067 (1995).

185. F. Vanholsbeeck, P. Emplit, and S. Coen, "Complete experimental characterization of the influence of parametric four-wave mixing on stimulated Raman gain," Opt. Lett. **28**, 1960-1962 (2003).

186. E. Golovchenko, P. V. Mamyshev, A. N. Pilipetskii, and E. M. Dianov, "Mutual influence of the parametric effects and stimulated Raman scattering in optical fibers," Quantum Electronics, IEEE Journal of **26**, 1815-1820 (1990).

187. T. Fevens and H. Jiang, "Absorbing Boundary Conditions for the Schrödinger Equation," SIAM Journal on Scientific Computing **21**, 255-282 (1999).

188. F. Couny and F. Benabid, "Optical frequency comb generation in gas-filled hollow core photonic crystal fibres," Journal of Optics A: Pure and Applied Optics **11**, 103002 (2009).

189. J. R. Hayes, S. R. Sandoghchi, T. D. Bradley, Z. Liu, R. Slavik, M. A. Gouveia, N. V. Wheeler, G. Jasion, Y. Chen, E. N. Fokoua, M. N. Petrovich, D. J. Richardson, and F. Poletti, "Antiresonant Hollow Core Fiber With an Octave Spanning Bandwidth for Short Haul Data Communications," J. Lightwave Technol. **35**, 437-442 (2017).

190. A. V. Gladyshev, A. F. Kosolapov, M. M. Khudyakov, P. Y. Yu, A. N. Kolyadin, A. A. Krylov, A. D. Pryamikov, A. S. Biriukov, M. E. Likhachev, I. A. Bufetov, and E. M. Dianov, "4.4-μm Raman laser based on hollow-core silica fibre," Quantum Electronics **47**, 491 (2017).

191. E. T. J. Nibbering, G. Grillon, M. A. Franco, B. S. Prade, and A. Mysyrowicz, "Determination of the inertial contribution to the nonlinear refractive index of air, N_2, and O_2 by use of unfocused high-intensity femtosecond laser pulses," J. Opt. Soc. Am. B **14**, 650-660 (1997).

192. M. Mlejnek, E. M. Wright, and J. V. Moloney, "Dynamic spatial replenishment of femtosecond pulses propagating in air," Opt. Lett. **23**, 382-384 (1998).

193. Q. Lin and G. P. Agrawal, "Raman response function for silica fibers," Opt. Lett. **31**, 3086 (2006).

194. K. F. Mak, J. C. Travers, N. Y. Joly, A. Abdolvand, and P. S. Russell, "Two techniques for temporal pulse compression in gas-filled hollow-core kagome photonic crystal fiber," Opt. Lett. **38**, 3592-3595 (2013).

195. A. R. Bhagwat and A. L. Gaeta, "Nonlinear optics in hollow-core photonic bandgap fibers," Opt. Express **16**, 5035 (2008).

196. Y. P. Yatsenko, E. N. Pleteneva, A. G. Okhrimchuk, A. V. Gladyshev, A. F. Kosolapov, A. N. Kolyadin, and I. A. Bufetov, "Multiband supercontinuum generation in an air-core revolver fibre," Quantum Electronics **47**, 553-560 (2017).

197. B. Debord, F. Gérôme, C. Hoenninger, E. Mottay, A. Husakou, and F. Benabid, "Milli-Joule energy-level comb and supercontinuum generation in atmospheric air-filled inhibited coupling Kagome fiber," in *CLEO: 2015 Postdeadline Paper Digest*, (Optical Society of America, 2015), JTh5C.4.

198. B. Debord, M. Alharbi, L. Vincetti, A. Husakou, C. Fourcade-Dutin, C. Hoenninger, E. Mottay, F. Gérôme, and F. Benabid, "Multi-meter fiber-delivery and pulse self-compression of milli-Joule femtosecond laser and fiber-aided laser-micromachining," Opt. Express **22**, 10735-10746 (2014).

199. Y. P. Yatsenko, A. A. Krylov, A. D. Pryamikov, A. F. Kosolapov, A. N. Kolyadin, A. V. Gladyshev, and I. A. Bufetov, "Propagation of femtosecond pulses in a hollow-core revolver fibre," Quantum Electronics **46**, 617-626 (2016).

200. P. Jaworski, F. Yu, R. R. Maier, W. J. Wadsworth, J. C. Knight, J. D. Shephard, and D. P. Hand, "Picosecond and nanosecond pulse delivery through a hollow-core Negative Curvature Fiber for micro-machining applications," Opt Express **21**, 22742-22753 (2013).

201. C. Li, K. P. Rishad, P. Horak, Y. Matsuura, and D. Faccio, "Spectral broadening and temporal compression of approximately 100 fs pulses in air-filled hollow core capillary fibers," Opt Express **22**, 1143-1151 (2014).

202. F. Emaury, C. F. Dutin, C. J. Saraceno, M. Trant, O. H. Heckl, Y. Y. Wang, C. Schriber, F. Gerome, T. Sudmeyer, F. Benabid, and U. Keller, "Beam delivery and pulse compression to sub-50 fs of a modelocked thin-disk laser in a gas-filled Kagome-type HC-PCF fiber," Opt Express **21**, 4986-4994 (2013).

203. Y. Chen, H. C. Mulvad, S. Sandoghchi, E. Numkam Fokoua, T. Bradley, J. Hayes, N. Wheeler, G. Jasion, S.-U. Alam, F. Poletti, M. Petrovich, and D. J. Richardson, "First Demonstration of Low Loss, Bend Insensitive 37-Cell Hollow-Core Photonic Bandgap Fiber at 1μm for High Power Delivery Applications," in *Conference on Lasers and Electro-Optics*, OSA Technical Digest (2016) (Optical Society of America, 2016), STu4P.1.

204. L. Chen, G. J. Pearce, T. A. Birks, and D. M. Bird, "Guidance in Kagome-like photonic crystal fibres I: analysis of an ideal fibre structure," Opt Express **19**, 6945-6956 (2011).

205. F. Yu and J. C. Knight, "Negative Curvature Hollow-Core Optical Fiber," IEEE Journal of Selected Topics in Quantum Electronics **22**, 146-155 (2016).

206. M. A. Finger, N. Y. Joly, T. Weiss, and P. S. Russell, "Accuracy of the capillary approximation for gas-filled kagome-style photonic crystal fibers," Opt. Lett. **39**, 821-824 (2014).

207. A. Börzsönyi, Z. Heiner, M. P. Kalashnikov, A. P. Kovács, and K. Osvay, "Dispersion measurement of inert gases and gas mixtures at 800 nm," Appl. Opt. **47**, 4856-4863 (2008).

208. "TruMicro Series 5000", retrieved http://www.uk.trumpf.com/en/products/laser-technology/products/solid-state-lasers/short-pulsed-lasers/trumicro-series-5000.html.

209. G. P. Agrawal, *Nonlinear Fiber Optics* (Academic Press, 2007).

210. A. V. Gorbach and D. V. Skryabin, "Soliton self-frequency shift, non-solitonic radiation and self-induced transparency in air-core fibers," Opt. Express **16**, 4858-4865 (2008).

211. J. Lægsgaard and P. J. Roberts, "Modeling of High-Power Pulse Compression and Soliton Formation in Hollow-Core Photonic Bandgap Fibers," IMG1 (2009).

212. K. J. Blow and D. Wood, "Theoretical description of transient stimulated Raman scattering in optical fibers," IEEE J. Quantum Electron. **25**, 2665-2673 (1989).

213. J. M. Brown and A. Carrington, *Rotational Spectroscopy of Diatomic Molecules* (Cambridge University Press, 2003).

214. A. P. Hickman, J. A. Paisner, and W. K. Bischel, "Theory of multiwave propagation and frequency conversion in a Raman medium," Phys. Rev. A **33**, 1788-1797 (1986).

215. J. R. Penano, P. Sprangle, P. Serafim, B. Hafizi, and A. Ting, "Stimulated Raman scattering of intense laser pulses in air," Phys Rev E Stat Nonlin Soft Matter Phys **68**, 056502 (2003).

216. W. D. Brewer, H. Haken, and H. C. Wolf, *Molecular Physics and Elements of Quantum Chemistry: Introduction to Experiments and Theory* (Springer Berlin Heidelberg, 2013).

217. L. Martinsson, P. E. Bengtsson, M. Aldén, S. Kröll, and J. Bonamy, "A test of different rotational Raman linewidth models: Accuracy of rotational coherent anti-Stokes Raman scattering thermometry in nitrogen from 295 to 1850 K," The Journal of Chemical Physics **99**, 2466-2477 (1993).

218. A. M. Zheltikov, "Raman response function of atmospheric air," Opt. Lett. **32**, 2052-2054 (2007).

219. L. A. Rahn and R. E. Palmer, "Studies of nitrogen self-broadening at high temperature with inverse Raman spectroscopy," J. Opt. Soc. Am. B **3**, 1164 (1986).

220. M. E. Kooi, L. Ulivi, and J. A. Schouten, "Vibrational Spectra of Nitrogen in Simple Mixtures at High Pressures," International Journal of Thermophysics **20**, 867-876 (1999).

221. B. M. Walsh, H. R. Lee, and N. P. Barnes, "Mid infrared lasers for remote sensing applications," J. Lumin. **169**, 400-405 (2016).

222. W. Yan, M. Yan, Z. Ruan, and M. Qiu, "Coordinate transformations make perfect invisibility cloaks with arbitrary shape," New Journal of Physics **10** (2008).

223. *Spectral Methods*, Scientific Computation (2006).

224. C. Canuto, M. Y. Hussaini, A. Quarteroni, and T. A. Zang, *Spectral Methods in Fluid Dynamics* (1988).

225. P.-J. Chiang, C.-P. Yu, and H.-C. Chang, "Robust Calculation of Chromatic Dispersion Coefficients of Optical Fibers From Numerically Determined Effective Indices Using Chebyshev–Lagrange Interpolation Polynomials," J. Lightwave Technol. **24**, 4411-4416 (2006).